Optical Spectroscopy on Semiconductor Nanocrystals: Emission Dynamics on a Nanoscale

Dissertation
zur Erlangung des Grades eines
Doktors der Naturwissenschaften
des Fachbereichs Physik
der Technischen Universität Dortmund

vorgelegt von
Dipl.-Phys. Oliver Schöps
aus Dortmund

technische universität
dortmund

Experimentelle Physik IIb

Dezember 2008

Vom Fachbereich Physik der Technischen Universität Dortmund
als Dissertation angenommen.

Tag der mündlichen Prüfung:	12.12.2008
Dekan:	Prof. Dr. B. Spaan
Erster Gutachter:	Prof. Dr. U. Woggon
Zweiter Gutachter:	Prof. Dr. K. Lischka
Dritter Gutachter:	Prof. Dr. A. Eychmüller
Vertretung der promovierten wissenschaftlichen Mitarbeiter:	Dr. B. Siegmann.

List of Publications

Articles in refereed Journals:

1. **Dot-in-a-dot: electronic and photonic confinement in all three dimensions** U.Woggon, R. Wannemacher, M.V. Artemyev, B. Möller, N. LeThomas, V. Anikeyev, O. Schöps; Applied Physics B 77, 469-484 (2003)

2. **Exciton Fine Structure in Single CdSe Nanorods** N. LeThomas, E. Herz, O. Schöps, M.V. Artemyev, U. Woggon; Physical Review Letters 94, 016803 (2005)

3. **Hybrid Epitaxial-Colloidal Semiconductor Nanostructures** U. Woggon, E. Herz, and O. Schöps, M. V. Artemyev, Ch. Arens, N. Rousseau, D. Schikora, K.Lischka, D. Litvinov,D. Gerthsen; Nano Letters 2005 Vol. 5, No. 3 483-490

4. **Colloidal nanocrystals integrated in epitaxial nanostructures: structural and optical properties** Ch. Arens, N. Roussau, D. Schikora, K. Lischka, O. Schöps, E. Herz, U. Woggon, D. Litvinov, D. Gerthsen, M. V. Artemyev; Physica status solidi (c) 3, No. 4, 861-864 (2006)

5. **Cavity QED with Semiconductor Nanocrystals** N. Le Thomas, U. Woggon, O. Schöps, M. V. Artemyev, M. Kazes, U. Banin; Nano Letters 2006 Vol. 6, No. 3 557-561

6. **Recombination Dynamics of CdTe/CdS Core-Shell Nanocrystals** O. Schöps, N. Le Thomas, U. Woggon, M. V. Artemyev; Journal of Physical Chemistry B 2006, 110, 2074-2079

7. **DNA-Directed Assembly of Supramolecular Fluorescent Protein Energy Transfer Systems** Florian Kukolka, Oliver Schoeps, Ulrike Woggon, and Christof M. Niemeyer; Bioconjugate Chemistry 2007, 18, 621-627

8. **Exciton-Plasmon-Photon Conversion in Plasmonic Nanostructures** Y. Fedutik, V. V. Temnov, O. Schöps, U. Woggon, M. V. Artemyev; Physical Review Letters 2007, 99,13

9. **Surfactant-Mediated Variation of Band-Edge Emission in CdS Nanocomposites** C. O'Dwyer, V. Lavayen, N. Mirabald, M. A. Santa Ana, E. Benavente, S. Ormazabal, G. González, Z. Lopez, O. Schöps, C. M. Sotomayor Torres, U. Woggon; Photonics and Nanostructures - Fundamentals and Applications 5 (2007) 45-52

10. **A Self-Assembled Donor Comprising Quantum Dots and Fluorescent Proteins for Long-Range Fluorescence Resonance Energy Transfer** H. Lu, O. Schöps, U. Woggon, C.M. Niemeyer; Journal of the American Chemical Society, 130 (14), 4815 -4827, 2008

Conference Contributions:

1. **Time Resolved Luminescence of CdSe Nanocrystals** O. Schöps, U. Woggon, W. Langbein, N. LeThomas, B. Möller, M.V. Artemyev; Application talk for the Graduiertenkolleg 726 "Materialien und Konzepte zur Quanteninformationsverarbeitung", Jul. 29, 2003; Dortmund, Germany (oral presentation)

2. **Optical Properties of CdSe Nanocrystals - Control Through Size, Shape and Temperature** O. Schöps, N. LeThomas, W. Langbein, U. Woggon, M.V. Artemyev; PMP Network Conference, Oct. 04, 2004; Paderborn, Germany (oral presentation)

3. **Low-Temperature Spectroscopy of Single CdSe Nanorods: Fine Structure and Polarization Properties** O. Schöps, N. LeThomas, E. Herz, W. Langbein, U. Woggon, M.V.Artemyev; MRS Fall Meeting, Nov. 29, 2004; Boston, MA (oral presentation)

4. **Optical Properties of CdSe Nanocrystals - Size, Shape and Temperature Dependence of Luminescence Dynamics** O. Schöps, E. Herz, N. LeThomas, W. Langbein, U. Woggon, M.V.Artemyev, Ch. Arens, D. Schikora, K. Lischka, D. Litvinov, D. Gerthsen; DPG Frühjahrstagung, Mar. 07, 2005; Berlin, Germany (oral presentation)

5. **Colloidal Nanocrystals in Epitaxial Nanostructures: Towards Low Denstity Integrated Emitters** O. Schöps, E. Herz, N. LeThomas, W. Langbein, U. Woggon, M.V.Artemyev, Ch. Arens, D. Schikora, K. Lischka,

D. Litvinov, D. Gerthsen; 2nd Workshop of the GK 726: Materials and Concepts for QIP, Sep. 23, 2005; Riezlern, Austria (oral presentation)

6. **Colloidal Nanocrystals Integrated in Epitaxial Nanostructures: Structural and Optical Properties** O. Schöps, E. Herz, U. Woggon, M.V.Artemyev, Ch. Arens, D. Schikora, K. Lischka, D. Litvinov, D. Gerthsen; QD 2006 Quantum Dots Conference, May 05, 2006; Chamonix-Mont Blanc, France (oral presentation)

7. **Colloidal Quantum Dots, Fluorescent Proteins and Organic Dyes in a Self-Assembled Structure for Lang-Range Energy Transfer** O. Schöps, H. Lu, C.M. Niemeyer, U. Woggon; International Workshop on Optical Properties of Coupled Semiconductor and Metallic Nanoparticles, Jul. 23, 2008; Dresden, Germany (oral presentation)

8. **CdSe doped Micro-Spheres: Candidates for a Thresholdless Laser** N. Le Thomas, O. Schöps, M. V. Artemyev, U. Woggon; 304th WE-Heraeus Seminar: "Elementary Quantum Processors"; Oct. 14, 2003; Bad Honnef, Germany (poster presentation)

9. **Lumineszenzeigenschaften von CdSe-Nanokristallen** O. Schöps, N. Le Thomas, W. Langbein, B. Möller und U. Woggon; Berichtskolloquium des Graduiertenkollegs 726 "Materialien und Konzepte zur Quanteninformationsverarbeitung"; Feb. 03, 2004; Dortmund, Germany (poster presentation)

10. **Excitonic fine structure of colloidal II-VI nanocrrystals: Size and shape dependent recombination dynamics** O. Schöps, N. Le Thomas, M.V. Artemyev, U. Woggon; QD2006 May 05, 2006; Chamonix-Mont Blanc, France (poster presentation)

11. **Exciton fine structure in single CdSe nanorods** N. LeThomas, O. Schöps, M.V. Artemyev, U. Woggon; NOEKS 2006, Feb. 22, 2006; Münster, Germany (poster presentation)

12. **CdS Nanocomposites with Tunable Band-Gap Energies** O. Schöps, C. O'Dwyer, V. Lavayen, N. Mirabald, M. A. Santa Ana, E. Benavente, S. Ormazabal, G. González, Z. Lopez, C. M. Sotomayor Torres , U. Woggon; Phoremost meeting, Mar. 21, 2007; Rome, Italy (poster presentation)

13. **A Self-Assembled Donor Comprising Quantum Dots and Fluorescent Proteins for Long-Range Energy Transfer** Oliver Schöps, Huachang Lu,

Christof M. Niemeyer, Ulrike Woggon; The 5th International Conference on Semiconductor Quantum Dots, May 13, 2008; Gyeongju, Korea (poster presentation)

Contents

Motivation

One of the most important technologies available today is semiconductor technology, and within this technology, an important trend is miniaturization. The attempt to increase the packing density, that is, to implement more and more transistors or other p-n-junction based electronic circuits on the same area, resembles a top-down approach towards a size regime, in which the structures consist of only a small number of tens to thousands of atoms. Considering todays photo-lithographic micro-chip fabrication techniques operating at structure sizes down to 50 nm, the quantum size regime is already touched at the present day.

The complementary problem which could be denoted as bottom-up view, is the question at what stage the properties of an atom or molecule transform into what we consider bulk semiconductor properties.

Both approaches imply the investigation of the properties of semiconductors that exist in sizes in the range of a few nanometers. The engagement in what might therefore be called nanotechnology is consequently a necessity for both, applied and fundamental research.

A formerly not existing compatibility with biological systems is achieved when dealing with semiconductor nanostructures, since the size regime investigated here corresponds to physical dimensions ranging from the size of a single protein to that of a virus.

Structurally probing material of such small measurements is the domain of electron microscopy and x-ray diffraction methods. For the investigation of the energetic structure, optical means are the method of choice, since the energy scale that needs to be addressed corresponds to the photon energies of visible light. Accessing the finer energy scale of energy level splittings within such samples is possible by manipulating the occupations of the levels by controlling the temperature of the sample down to a few Kelvin.

The mayor effects on the properties of semiconductors that are observed when dealing with nanometer sized objects, stem from the fact that the particle size becomes comparable

to the extension of the wave function of electron and hole in the given material. If the size of a semiconductor sample confines the wave function in one, two or three dimensions a quasi two-, one-, or zero-dimensional semiconductor is created. One effect of manipulating the effective dimensionality on the semiconductor properties is the modification of the density of states (DOS). The dependence of the DOS on the square root of energy in bulk, is modified to a step function in two-dimensional quantum well structures, an inverse square root in one-dimensional quantum rods or quantum wires, and a series of delta functions in the case of complete confinement in all three spatial dimensions. The latter case being referred to as a zero dimensional quantum dot. The states available for electron and hole become discrete and their energetic position depends on the confining size. A more in-depth analysis reveals an additional dependence of the optical recombination selection rules on the dimensionality as well as the size.

The results of the early work in this field has shown already that the observed effects are of exploitable magnitude which has paved the way for a number of new applied and fundamental research fields:

The modified density of states changes the absorption of light in a such a way, that many optical excitations can be stored in a small energy interval, which could be exploited for example in low threshold quantum dot lasers. The variety of nanocrystals available allows a systematic study of the influence of, for example the transition from one- to two-dimensional structures. The optical properties, like size tunable emission wavelength as well as the reduced photo degradation have made nanocrystals ideal markers in biological labeling applications with a number of advantages over conventional organic dyes. Moreover the semiconductor nature offers a certain degree of compatibility with existing silicon technologies, which paves the way for the use in integrated structures. The confinement of single electron-hole pairs which resembles a storage capability for both charge and spin is also interesting for applications in quantum information processing.

All of the above mentioned topics are linked not only to the existence of discrete energy levels in a nanocrystal, but to the question how energy actually migrates within a structure to allow for the radiative recombination. This is for example the case, when excited continuum states, that are typically situated at energies corresponding to near UV wavelength, transfer energy to lower lying states out of which radiative combination occurs which can be probed at visible light wavelength. Moreover the absorbing and emitting states can be spatially separated in complex light harvesting structures. The elucidation of these processes and their dynamics are the problems this work is dedicated to.

This thesis is therefore organized as follows:

The first chapter will briefly review the basic concepts underlying the description of semiconductors in general as well as the peculiarities of nanocrystals. Two complementary approaches towards the fabrication of nanometer sized objects will be introduced: Molecular beam epitaxy and colloidal chemistry. The theoretical basics to describe the resulting characteristics with special focus on the optical properties will be described at the end of this chapter.

The second chapter will deal with the possibilities of energy migration between such nanoparticles, especially the dipole-dipole coupling or Förster resonance energy transfer (FRET).

In chapter three the experimental methods used for the investigation of the different sample structures will be introduced.

While the first three chapters are of an introductory character, the following parts can be understood as the results and discussion section, in which a number of sample systems are treated.

Chapter four lists the properties of nanocrystals consisting of cadmium and selenium, with particular focus on the influence of the size and shape, and the resulting temperature dependence of the luminescence properties. The quantum electrodynamic effects that occur when coupling these emitters to a cavity are reviewed.

The fifth chapter includes cadmium telluride in the list of investigated materials, and deals with the differences that influence the recombination dynamics.

In chapter six, the results of an attempt to merge the two introduced complementary approaches towards the nanoscale are presented. Here, colloidally grown cadmium selenide nanocrystals are incorporated in a semiconductor matrix obtained with molecular beam epitaxy and similar methods. The resulting hybrid systems are investigated regarding both the optical and the structural properties.

Chapter seven reviews the results of an interdisciplinary effort to make use of the unique features of semiconductor nanocrystals as energy donors in a biochemical system comprising fluorescent proteins, DNA, and organic dyes. Different approaches, both theoretical and experimental are taken to investigate the energy migration in this organic-inorganic structure. This could be an important tool for spectroscopic studies in biological environments, joining the advantages of both material systems.

1. Introduction

This first chapter introduces some of the basic concepts needed to describe the solid state, in a size regime, that implies quantum confinement effects. Though the introduction starts with a description of crystal structures and its physical properties in general, it is limited to a selection of topics that apply to this work in particular and therefore by far not complete. For a full understanding of the theory, standard literature, that was also used as a guideline for this text should be referred to ([58],[57],[56],[6]).

1.1 Basic Concepts

1.1.1 The Solid State

Joining many atoms to form a crystal leads to a splitting of the eigenenergies of the electrons and hence the formation of energy bands. The splitting of the bands depends on the overlap integral of neighboring atoms and therefore on the underlying crystallographic structure.

At a hypothetical temperature of 0 K, the electrons of the crystal are distributed among the available states following the Pauli principle. The energetically lowest, completely filled band is referred to as the valence band and the band above the conduction band. The filling of these bands and the gap E_g between them allows a classification of the solid state: A partially filled conduction band leads to metallic properties. Completely filled valence bands with a large gap define an insulator. Semiconductors exhibit a band gap smaller than 4 eV, which can be bridged for example by the irradiation with photons of equal or higher energy.

A further distinction in different semiconductor classes is made by comparing the positions of the valence band maximum and the conduction band minimum in k-space. If the two extrema coincide in k-space, a transition from one band to another can occur without the participation of a quasi particle that enables momentum conservation. The

semiconductor is referred as a direct band gap material, as it is the case for CdSe, CdTe, ZnSe, and ZnS. If the band extrema are at different positions in k-space, a momentum carrying phonon needs to be involved in the transition. Semiconductor of this class are referred to as indirect semiconductors, like silicon.

The absence of an electron in an otherwise completely filled valence band can be used to define the "*hole*", a quasi particle with opposite charge with respect to the missing electron. This enables the use of hole spin and hole effective mass in a description complementary to that of the electron, sketched in the following.

When a large number of individual atoms is brought in close proximity, the behavior of electrons in the forming crystal is governed by the interaction of the outer electrons with the nucleus and the innermost electrons bound to it. The mathematical description is based on the solution of the according Schrödinger equation, which, due to the large number of atoms in a solid state sample relies on a number of simplifications.

The Hamiltonian describing kinetic terms for electrons and cores as well as the coulombic interaction of cores, electrons and between electrons and cores is:

$$\widehat{H} = -\frac{\hbar^2}{2}\sum_{j=1}^{M}\frac{1}{M_j}\Delta_{R_j} - \frac{\hbar^2}{2m_0}\sum_{i=0}^{N}\Delta_{r_i} + \\ + \frac{1}{4\pi\epsilon_0}\Big(\sum_{j>j'}\frac{e^2 Z_i Z_{i'}}{|\boldsymbol{R}_j - \boldsymbol{R}_{j'}|} + \sum_{i>i'}\frac{e^2}{|\boldsymbol{r}_i - \boldsymbol{r}_{i'}|} + \sum_{i,j}\frac{e^2 Z_j}{|\boldsymbol{R}_j - \boldsymbol{r}_i|}\Big). \tag{1.1}$$

Here Z_j Is the effective charge of the ion core j with mass M_j and coordinate $\boldsymbol{R}_j$. The equivalent parameters for the electrons are e, m_0 and $\boldsymbol{r}_i$. The indices j and i include all M ion cores an N electrons

The mass ratio of electron and ion core justifies the assumption, that the electrons react upon movements of the ion cores instantaneously, while the cores themselves can be considered fixed to their positions. In this *adiabatic* or *Born-Oppenheimer-approximation*, the wave functions factorize as

$$\phi(\boldsymbol{r}_i, \boldsymbol{R}_j) = \phi(\boldsymbol{r}_i) \cdot \phi(\boldsymbol{R}_j) \tag{1.2}$$

An additional simplification is the one-electron-approximation in which these fixed ion cores produce a periodic potential landscape in which a test charge like the electron under consideration moves without distorting the spatial ordering. The functions suited for

the description of such a conception are Bloch waves, comprising a term expressing the periodicity of the lattice, multiplied with a plane wave part.

$$\phi_{k,i}(\boldsymbol{r}) = e^{i\boldsymbol{k}\boldsymbol{r}} u_{k,i}(\boldsymbol{r}), \qquad \text{with} \qquad u_{k,i}(\boldsymbol{r}) = u_{k,i}(\boldsymbol{r} + \boldsymbol{R}) \tag{1.3}$$

where $\boldsymbol{k}$ is the wave vector and i the band index. A shift of a reciprocal wave vector $\boldsymbol{G}$ does not change the wave function nor the energy eigenvalues, as expressed by:

$$E(\boldsymbol{k}, i) = E(\boldsymbol{k} + \boldsymbol{G}, i) \qquad \text{and} \qquad \phi_{k,i}(\boldsymbol{r}) = \phi_{k+G,i}(\boldsymbol{r}). \tag{1.4}$$

This enables the reduction of the energy dispersion $E(\boldsymbol{k})$, as well as other k-dependent parameters to the first Brillouin-zone ($k \in [-\frac{\pi}{a}, +\frac{\pi}{a}]$).

The influence of a weak periodic potential changes the energy dispersion of the free electron, $E(\boldsymbol{k}) = \frac{\hbar^2 k^2}{2m}$, and leads to the formation of allowed and forbidden regions, the bands and band gaps.

The concept of the effective mass is well suited to describe the effect of external fields on the motion of quasi particles in a crystal. Instead of the infinitely extended Bloch functions, a superposition that forms a wave packed referred to as Wannier functions is used:

$$\phi_{k_0}(\boldsymbol{r}) = \sum_k a_k e^{i\boldsymbol{k}\boldsymbol{r}} u_k(\boldsymbol{r}). \tag{1.5}$$

The energy of a particle whose motion is described by such a wave packet is changed by an external force acting along an infinitesimal path $d\boldsymbol{s}$

$$dE(\boldsymbol{k}) = \boldsymbol{F} \cdot d\boldsymbol{s} = \boldsymbol{F} \cdot \boldsymbol{v}_g dt \tag{1.6}$$

with the group velocity

$$\boldsymbol{v}_g = \frac{1}{\hbar} \mathrm{grad}_k E(\boldsymbol{k}), \tag{1.7}$$

or, limited to the 1 dimensional case

$$v_g = \frac{1}{\hbar} \frac{dE}{dk}. \tag{1.8}$$

since furthermore

$$dE(\boldsymbol{k}) = \frac{dE(\boldsymbol{k})}{d\boldsymbol{k}} \cdot d\boldsymbol{k} = \hbar \boldsymbol{v}_g d\boldsymbol{k}, \tag{1.9}$$

one finds for the time derivative of the crystal momentum $\hbar\boldsymbol{k}$

$$\hbar \frac{d\boldsymbol{k}}{dt} = \boldsymbol{F} = \dot{\boldsymbol{p}}, \tag{1.10}$$

which corresponds to Newton's second law of motion.
For the acceleration the following equation holds:

$$\boldsymbol{a} = \frac{d\boldsymbol{v}_g}{dt} = \frac{1}{\hbar} \frac{\partial^2 E}{\partial k \partial t} = \frac{1}{\hbar} \frac{\partial^2 E}{\partial k^2} \frac{d\boldsymbol{k}}{dt} = \frac{1}{\hbar^2} \frac{\partial^2 E}{\partial k^2} \boldsymbol{F}. \tag{1.11}$$

In accordance with the second law of motion:

$$\boldsymbol{a} = \frac{1}{m} \cdot \boldsymbol{F}, \tag{1.12}$$

the effective mass is defined as

$$\frac{1}{m_{\text{eff}}} = \frac{1}{\hbar^2} \frac{\partial^2 E}{\partial k_i \partial k_j}; \qquad i, j = x, y, z. \tag{1.13}$$

and is in this general form a tensor, which means that the inertia an electron or hole presents towards an acceleration depends on the direction. Close to the extremal points of the bands, the shape of the bands can be approximated as a parabola. The essence of the effective mass approximation is the treatment of electrons or holes as free particles, whose mass is defined with the use of equation (1.13).

1.1.2 Crystal Structures

From the large variety of crystal structures, only those relevant for this work shall be briefly introduced and reviewed, namely those of the binary compounds CdSe, CdTe, ZnSe and ZnS.

In these crystal structures, the lattice is occupied by two atomic species. The bonds between them have a significant ionic character. At the center of the Brillouin zone, the conduction band is primarily formed by the s electrons of the metal, while the valence band mainly consists of the p electrons of the non-metal [49].

The zinc-blende (figure 1.1, right) structure of CdTe, ZnSe, and the alpha modification of zinc sulfide (α-ZnS) are of cubic symmetry, similar to the face centered cubic lattice

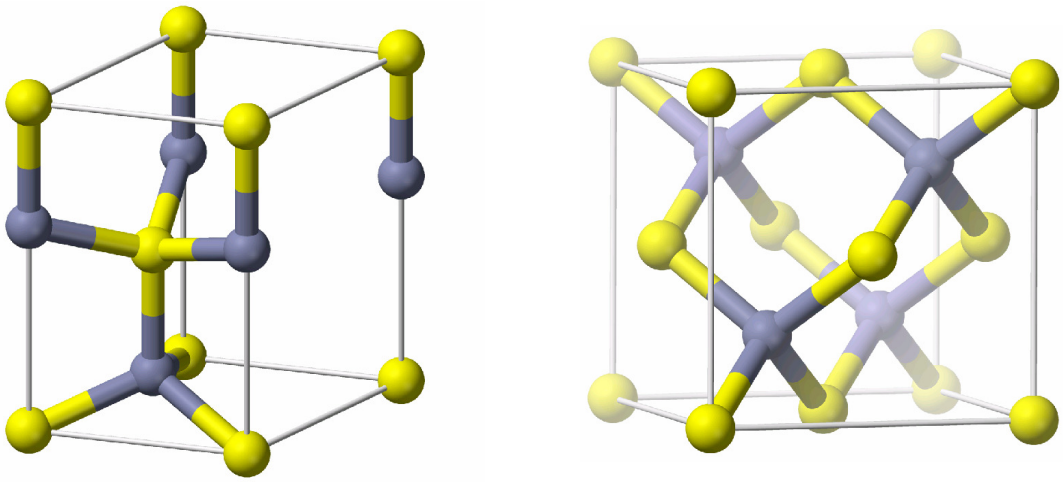

Figure 1.1: Wurtzite (left) and zinc-blende (right) crystal structure. Adapted from http://en.wikipedia.org/wiki/Wurtzite and http://en.wikipedia.org/wiki/Zinc_blende

	CdSe	CdTe	ZnSe	ZnS
stable structure at RT	wurtzite	zinc blende	zinc blende	zb and w
zinc blende a_0 (nm)	0.605	0.648	0.567	0.541
wurtzite a_0	0.430	NA	0.400	0.382
wurtzite c_0	0.701	NA	0.654	0.626
effective electron mass m_e^*/m_0	0.13	0.11	0.141	0.275
effective hole mass m_h^*/m_0	0.45	0.4	0.6	0.5
energy gap E_g (eV)	1.751	1.43	2.67	3.57
refractive index (550 nm)	2.6	2.72	2.43	2.387

Table 1.1: Material Properties of selected II-VI compounds at 300 K. Adapted from [74]

of diamond, with the carbon atoms of one layer substituted with cadmium (zinc), and in every second layer with tellurium (selenium, sulfur). It can also be visualized as two face centered cubic lattices, one for the metal and one for the non-metal, which are displaced by a quarter of the room diagonal, that is the vector $\frac{1}{4}(1,1,1)$. This leads to equivalent layers in the structure in the sequence ABCABC.

The wurtzite structure displayed in figure (figure 1.1, left), represents a member of the hexagonal crystal system. As in the zinc-blende structure, every atom is tetrahedrally surrounded by 4 atoms of the other kind in the binary compound. The layering can be enumerated as ABABAB. The distinctive property of the wurtzite structure is the existence of a distinguished c-axis that lowers the symmetry and gives rise to a built in crystal field. The II-VI compounds under investigation that display wurtzite crystal structure are cadmium selenide (CdSe), and the less frequently occurring beta modification of zinc sulfide (β-ZnS).

A selection of the crystallographic and electronic properties of II-VI compounds is listed in table 1.1.

Figure 1.2 shows the band structure of hexagonal CdSe as well as that for cubic CdTe. Since in experiments with optical excitation, the momentum transferred to the crystal is comparably small, the relevant region in k-space is limited to the vicinity of the gamma point. There, a parabolic approximation of the bands is valid for the majority of applications. The approximated band structures for both crystal types is displayed in figure 1.3. Using the conventional labeling of the states, the main difference is the degeneracy of light hole (lh) and heavy hole (hh) bands in the zinc blende structure at the gamma point. The according bands in the wurtzite structure are labeled A and B bands, and lack this degeneracy.

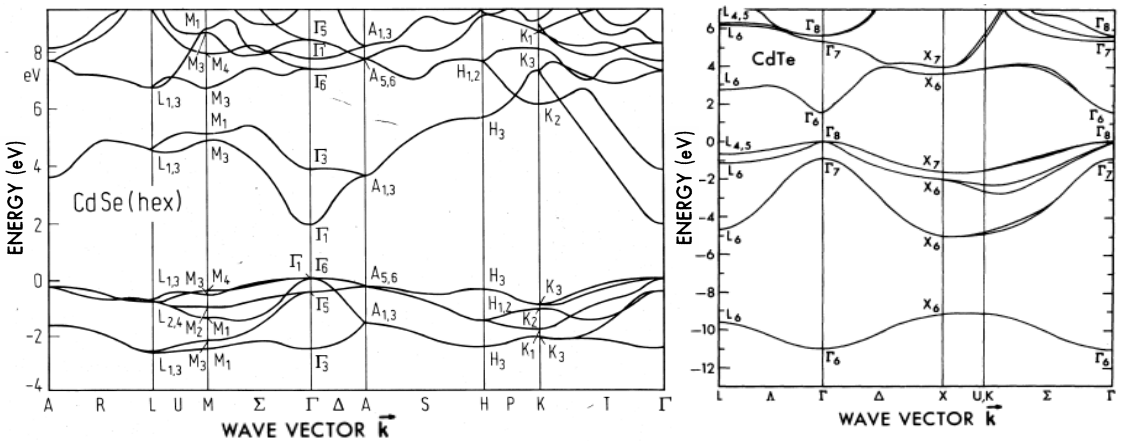

Figure 1.2: Calculated band structure of hexagonal CdSe [16] and zinc blende CdTe [74].

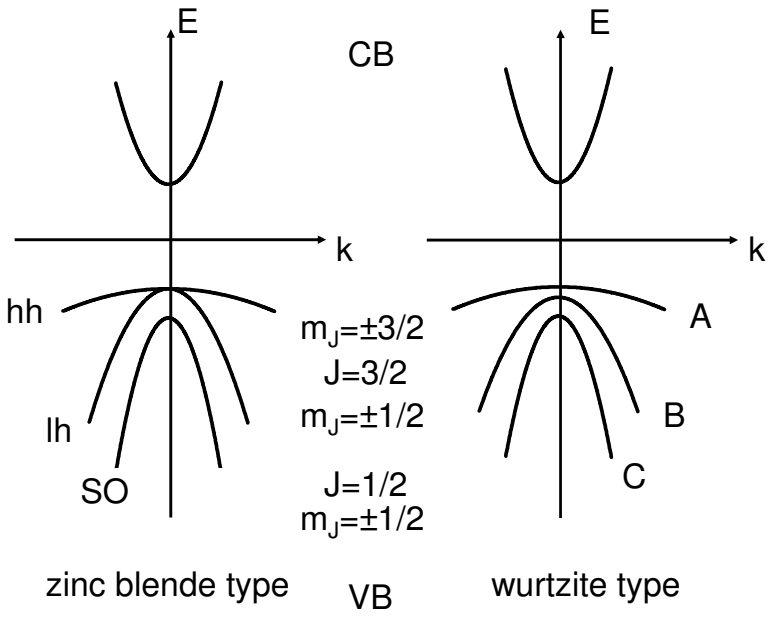

Figure 1.3: Nomenclature of parabolically approximated bands in wurtzite and zinc blende structures (not to scale). The hole state $J = 3/2$, $m_J = \pm 3/2$ is referred to as the heavy hole state in zinc blende and the A band in wurtzite structures. $J = 3/2$, $m_J = \pm 1/2$ is labeled light hole or B band. The $J = 1/2$, $m_J = \pm 1/2$ states are referred to as the split-off (SO) band, or C band in wurtzite.

1.1.3 Excitons

The concept of electronic excitations leading to an electron in the conduction and a hole in the valence band, treats both quasi particles as independent. Taking into account the Coulomb interaction, an attractive force between the oppositely charged particles lifts this independence, and creates a situation similar to the hydrogen atom or the positronium. The Coulomb potential, which in SI units is of the form

$$V(|\boldsymbol{r}_e - \boldsymbol{r}_h|) = -\frac{e^2}{4\pi\varepsilon_0\epsilon|\boldsymbol{r}_e - \boldsymbol{r}_h|} \tag{1.14}$$

leads to the formation of bound states below the bad gap - the exciton states. Within the approximation of parabolic bands in direct semiconductors, the relative motion of electron and hole can be separated from the center of mass motion, which leads to an energy dispersion of the form

$$E_{\text{exc}}(n_B, \boldsymbol{K}) = E_g - Ry^* \frac{1}{n_B^2} + \frac{\hbar^2 \boldsymbol{K}}{2M} \tag{1.15}$$

using the following definitions:

$n_B = 1, 2, 3, ...$	:	primary quantum number
$Ry^* = \frac{\mu}{m_0 \varepsilon^2} \cdot 13,6\text{eV}$	:	exciton binding energy
$M = m_e + m_h$	:	combined mass
$\boldsymbol{K} = \boldsymbol{k}_e + \boldsymbol{k}_h$	:	wave vector of the center of mass
$\mu = \frac{m_e m_h}{m_e + m_h}$	:	reduced mass

In typical semiconductors, the exciton Rydberg energies vary between 1 meV and 200 meV, while the exciton Bohr radii, calculated by

$$a_B^{\text{exc}} = \frac{\varepsilon \hbar^2}{\mu e^2} \tag{1.16}$$

are between 1 and 50 nm. The values obtained for the exciton radius are significantly larger than the typical 0.5 nm for the inter-atomic spacing in a semiconductor crystal. This means that the orbit of electron and hole around the center of mass extends over more than one lattice constant. Excitons of such a kind are referred to as Mott-Wannier excitons, in contrast to excitons described by a formalism introduced by Frenkel, which treats electrons and holes bound to the same atomic core. In the case of Mott excitons,the wave function is of the form:

$$\phi(\boldsymbol{K}, n_B, l, m) = \frac{1}{\sqrt{\Omega}} e^{i\boldsymbol{K}\cdot\boldsymbol{R}} \phi_e(\boldsymbol{r}_e)\phi_h(\boldsymbol{r}_h)\phi^{env}_{n_B,l,m}(\boldsymbol{r}_e - \boldsymbol{r}_h) \tag{1.17}$$

With the center of mass:

$$\boldsymbol{R} = \frac{(m_e \boldsymbol{r}_e + m_h \boldsymbol{r}_h)}{m_e + m_h}. \tag{1.18}$$

The plane wave $e^{i\boldsymbol{K}\cdot\boldsymbol{R}}$ describes the motion of the quasi particle through the crystal, while the envelope part $\phi^{\text{env}}_{n_B,l,m}(\boldsymbol{r}_e - \boldsymbol{r}_h)$ deals with the relative motion of electron and hole. For $n_B \to \infty$, the excitonic levels approach the continuum states of the unbound electron and hole $E_{\text{exc}}(n \to \infty) = E_g$, which again shows close similarity to the hydrogen atom, which is considered ionized for $n \to \infty$.

1.2 Quantum Confined Structures

The above considerations rely on the assumption that a semiconductor is in its bulk form, that consists of a large number of atoms. When the size of the system is reduced in one or more spatial directions, the effective dimensionality of the system is changed. This has a drastic effect on the electronic density of states (DOS), that is, the number of available electronic states per unit volume and unit energy.

The density of states is calculated by comparing the volume of an n-dimensional spherical shell of radius k and thickness dk to the unit volume in k-space. One of these electronic states can be occupied by two electrons of opposite spin, which accounts for an additional factor of 2.

In the bulk case, where n=3, the DOS is proportional to the square root of the energy of the state. Confinement in one direction resulting in a two-dimensional structure modifies the DOS to become independent of the energy. One-dimensional structures created by a two-dimensional confinement show an DOS dependence on the reciprocal of the square root of the energy. If confinement is present in all three spatial dimensions, resulting in a zero-dimensional structure, the DOS is expressed by a delta function. With increasing confinement the DOS maxima are enhanced. When higher quantum states indexed by i are taken into account for the DOS of quantum confined structures, the 2d-DOS appears as a staircase like function, while the 1d and 0d functions appear as sequences of the inverse square root and delta functions respectively. This is expressed by the introduction of the Heaviside function $\Theta(E - E_i)$ into the equations 1.33 and visible in the quasi periodicity of the DOS in figure 1.4.

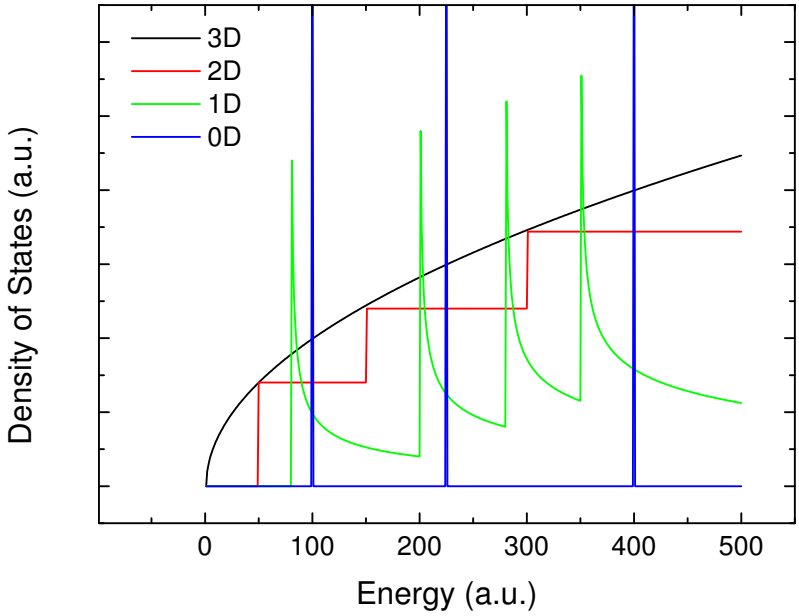

Figure 1.4: Density of states as a function of the dimensionality.

$$g_{3D}(E) = \frac{1}{2\pi^2}\left(\frac{2m^*}{\hbar^2}\right)^{\frac{3}{2}}(E-E_0)^{\frac{1}{2}} \tag{1.19}$$

$$g_{2D}(E) = \frac{1}{2\pi}\left(\frac{2m^*}{\hbar^2}\right)\sum_i \Theta(E-E_i) \tag{1.20}$$

$$g_{1D}(E) = \frac{1}{\pi}\left(\frac{2m^*}{\hbar^2}\right)^{\frac{1}{2}}\sum_i \left(\Theta(E-E_i)\cdot(E-E_i)^{-\frac{1}{2}}\right) \tag{1.21}$$

$$g_{0D}(E) = \sum_i 2\delta(E-E_i) \tag{1.22}$$

Apart from the modification of the DOS, the spatial confinement leads to an additional effect. The magnitude of the expected confinement can be classified by comparing the size of the structure, represented by the radius R, to the exciton Bohr radius a_B^{exc} in the material [65]. In very small structures ($R \ll a_B^{\text{exc}}$), the movement of the electron and the hole are quantized, which is refered to as strong confinement. An intermediate confinement can be realized when the to quantities are comparable ($R \approx a_B^{\text{exc}}$). Here the effective mass of the hole is typically larger than that of the electron. The separation of the quantized center of mass motion from the relative motion of the electron and hole is possible when the particles are only weakly confined ($R \gg a_B^{\text{exc}}$).

The confining potential realized by a matrix, surrounding a semiconductor sphere of radius R, can be modeled as a potential well of infinite barrier height for distances $r > R$. When the semiconductor sphere consists of enough atoms to make the typical periodic crystal structure observable, the assumption is valid, that the wave function can be built from Bloch functions that are equal on both sides of the barrier ($u_{\nu,k}(\boldsymbol{r})_{\text{sphere}} = u_{\nu,k}(\boldsymbol{r})_{\text{matrix}} = u_{\nu,k}(\boldsymbol{r})$), and an envelope part. In the simplest case, the envelope is described in the single parabolic band approximation. Neglecting Coulomb interactions, this yields

$$\widehat{\boldsymbol{H}} = -\frac{\hbar^2}{2m_e}\nabla_e^2 - \frac{\hbar^2}{2m_h}\nabla_h^2 + V_e(\boldsymbol{r}_e) + V_h(\boldsymbol{r}_h). \tag{1.23}$$

with the confining potential

$$V_i(\boldsymbol{r}_i) = \begin{cases} 0 & \text{for} \quad \boldsymbol{r}_i < R \qquad (i = e, h) \\ \infty & \text{for} \quad \boldsymbol{r}_i > R \qquad (i = e, h). \end{cases}$$

In this non-interacting particle approximation, the envelope can be assumed to be a product of the one-particle wave functions. The according solution is attained by taking into account the boundary condition of a vanishing wave function at the boundary of the confining potential ($r = R$) as :

$$\phi^i_{nlm}(\boldsymbol{r}) = Y_{lm}\sqrt{\frac{2}{R^3}}\frac{J_l(\chi_{nl}\frac{r}{R})}{J_{l+1}(\chi_{nl})}. \tag{1.24}$$

with

$$-l \leq m \leq l \qquad l = 0, 1, 2, \ldots \qquad n = 1, 2, 3, \ldots$$

The Y_{lm} are the spherical harmonics, and the J_l the Bessel functions, with χ_{nl} as the n-th root of the Bessel function of l th order. The boundary condition

$$J_l\Big(\chi_{nl}\frac{r}{R}\Big)\Big|_{R=r} = 0 \tag{1.25}$$

yield the energy eigenvalues

$$E^{e,h}_{nl} = \frac{\hbar^2}{2m_{e,h}}\frac{\chi^2_{nl}}{R^2}. \tag{1.26}$$

This leads to the quantization energy of the lowest state with $n = 1$ and $l = 0$:

$$E^i_{10} = \frac{\hbar^2}{2m_i}\frac{\pi^2}{R^2}. \tag{1.27}$$

This means, that the quasi particle in the spherical potential possesses discrete energy eigenvalues that scale with the inverse of the square of the particle size. In relation to the native band gap of the material, the transition energy is shifted by:

$$\Delta E = \frac{\hbar^2}{2\mu}\frac{\pi^2}{R^2} \tag{1.28}$$

With the reduced exciton mass:

$$\mu = \frac{m_e m_h}{m_e + m_h}. \tag{1.29}$$

The formation of an exciton in a quantum confining structure therefore occurs, unlike in the bulk semiconductor, even without the inclusion of the Coulomb interaction. The size dependence of the transition energy is the key for the size tunable emission wavelength obtained from nanoparticles [12].

1.2.1 Optical Transitions

Within the effective mass approximation, the probability of a dipole-allowed radiative transition is given by [126]:

$$\alpha(\omega) \propto |\langle \Psi_f | \boldsymbol{e} \cdot \widehat{\boldsymbol{p}} | \Psi_i \rangle|^2.$$

where $\boldsymbol{e} \cdot \widehat{\boldsymbol{p}}$ is the dipole operator and Ψ_i und Ψ_f are the initial and final states of the transition. With

$$|i\rangle : \Psi_i(\mathbf{r}) = u_{\nu_i} \phi_i(\boldsymbol{r}),$$

$$|f\rangle : \Psi_f(\mathbf{r}) = u_{\nu_f} \phi_f(\boldsymbol{r})$$

and the limitation to interband transitions, that is $\nu_i \neq \nu_f$ the overlap integral is

$$\langle f | \boldsymbol{e} \cdot \widehat{\boldsymbol{p}} | i \rangle = \underbrace{\langle u_{\nu_f} | \boldsymbol{e} \cdot \widehat{\boldsymbol{p}} | u_{\nu_i} \rangle}_{p_{cv}} \langle \phi_f | \phi_i \rangle.$$

With p_{cv} as the size independent transitions dipole matrix element, which is also retrieved in the bulk case from the integration of the Bloch part. The correction introduced by the confinement is given by the product $\langle \phi_f | \phi_i \rangle$. Due to the symmetry of the ϕ^i_{nlm} and their orthonormality this yields delta functions. For non-interacting electron and hole states, all n and l conserving transitions, namely $1s_e \rightarrow 1s_h$, $1p_e \rightarrow 1p_h$, $1d_e \rightarrow 1d_h$ and so on are allowed.

The oscillator strength of these transitions is proportional to $2l + 1$ due to the contributions from states with $-l \leq m \leq +l$. The absorption is therefore described by a series of delta functions

$$\alpha \propto |p_{cv}|^2 \frac{1}{\frac{4\pi}{3} R^3} \sum_{n,l} (2l+1) \delta(\hbar\omega - E^e_{nl} - E^h_{nl}). \tag{1.30}$$

The line spectrum defined by equation 1.30 is idealized. Apart from the limitations of the line width due to the finite lifetime expressed as a homogeneous broadening, ensembles of nanostructures undergo an inhomogeneous broadening as the dominant broadening

effect. A realistic ensemble of nanocrystals represents a distribution of sizes, rather than a single, fixed radius, which results in a distribution of the individual transition energies. With $P(R)$ as the probability of a nanoparticle of radius R in the ensemble, the ensemble absorption becomes:

$$\alpha(\omega) \propto \int_0^\infty P(R) \cdot \alpha_R(\omega) dR. \tag{1.31}$$

In the case of strong confinement, the ansatz of the non-interacting electron-hole systems is sufficient. In the intermediate confinement regime, the larger effective mass of the hole allows a description that leaves the hole confined at the center of the nanoparticle. In the weak confinement limit, the exciton can be described as a single composite particle that undergoes confinement effects. The absorption is then described by

$$\alpha(\omega) \propto |\langle \Psi_{pair} | \boldsymbol{e} \cdot \widehat{\boldsymbol{p}} | 0 \rangle|^2.$$

When beyond that, the Coulomb interaction should be included in the Hamiltonian, variational calculations and perturbation theory approaches have to be employed, which use a finite confinement potential.

$$\widehat{\boldsymbol{H}} = -\frac{\hbar^2}{2m_e}\nabla_e^2 - \frac{\hbar^2}{2m_h}\nabla_h^2 - \frac{e^2}{4\pi\varepsilon_0\varepsilon|\boldsymbol{r_e} - \boldsymbol{r_h}|} + V_e(\boldsymbol{r}_e) + V_h(\boldsymbol{r}_h) \tag{1.32}$$

A further refinement of the model is the inclusion of realistic band structures, beyond the parabolic approximation. Since in II-IV semiconductors like CdSe or CdTe, the conduction bands origin from the s-orbitals of the metal, the description as a twofold spin-degenerate band holds. The inclusion of spin-orbit coupling in the valence bands however complicates the description. In crystals of the zinc-blende type, the combination of an orbital angular momentum of 1 and the spin of 1/2 creates of a valence band with a total angular momentum of $J = 3/2$ that is fourfold degenerate at the gamma point. Away from the gamma point, the bands split into the light hole (lh) band with $m_J = \pm 1/2$, and the heavy hole band (hh) with $m_J = \pm 3/2$. Furthermore, a two-fold degenerate band with $J = 1/2$, separated from the other two bands at the gamma point by Δ_{SO} is referred to as the split-off band (SO)

In the wurtzite crystal structure, the distinguished c-axis lowers the symmetry. The intrinsic crystal field lifts the lh-hh degeneracy at the gamma point. The corresponding bands are referred to as the A, B and C bands (see figure 1.3).

Due to the confinement of carriers, a wave function overlap occurs that leads to a mixing of states. The hole wave function consists of linear combinations of the valence band wave functions and therefore exhibits a mixed s-d type symmetry. This enables transitions that were otherwise dipole forbidden.

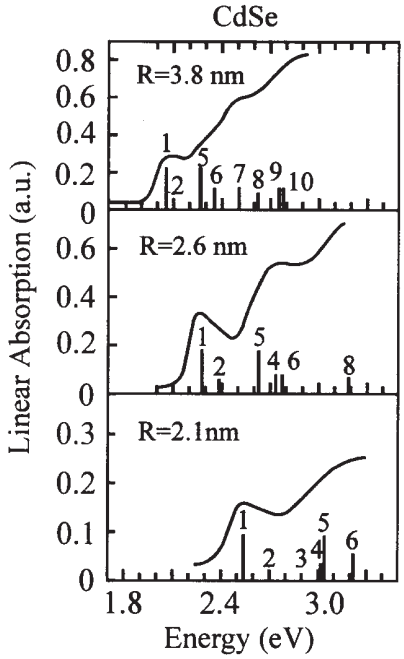

No.	Transition
1	$1S_{3/2} - 1s_e$
2	$2S_{3/2} - 1s_e$
3	$1S_{1/2} - 1s_e$
4	$2S_{1/2} - 1s_e$
5	$1P_{3/2} - 1p_e$
6	$1P^{l}_{1/2} - 1p_e$
7	$3S_{1/2} - 1s_e$
8	$2S_{3/2} - 2s_e$
9	$1P^{SO}_{1/2} - 1p_e$
10	$4S_{3/2} - 2s_e$

Figure 1.5: Calculated linear absorption of CdSe nanocrystals as a function of size, adapted from [126] and [30]. The effects included are Coulomb interaction, band degeneracy, non-parabolic bands and inhomogeneous broadening

For strongly confined systems, the short range exchange interactions further complicates the description of the system.

The result of a calculation taking into account the effects mentioned above is displayed in figure 1.5, adapted from [126]. For the ground state luminescence which is probed in most of the experiments of this work, the responsible transition is that from the $(1S_{3/2}, 1s_e)$ state to the ground state.

A nomenclature applicable for the lowest excitonic states is presented in the following [85]:

The electron is represented by its spin quantum number $s = 1/2$ with the projections $m_s = \pm 1/2$. For the hole state including valence band mixing, the quantum number $F = L + J$ applies. The possible projections of the $1S_{3/2}$ state are $m_F = -3/2, -1/2, +1/2, +3/2$. The composite pair state is described by the quantum number $N = F + s$ and the projections N_m. For the eight possible combinations, the following

names are used:

$$
\begin{array}{rll}
1^U & \text{for} & |1,1\rangle \text{ and } |1,-1\rangle \\
0^U & \text{for} & |1,0\rangle \\
1^L & \text{for} & |2,1\rangle \text{ and } |2,-1\rangle \\
0^L & \text{for} & |2,0\rangle \\
2 & \text{for} & |2,2\rangle \text{ and } |2,-2\rangle
\end{array}
$$

The crystal field and deviations from the exact sphere shape lift the degeneracy and split the states in the A and B groups. The B states, which are situated some ten meV above the A states can split further, when the deviations from the sphere shape are strong. The A group, which is especially important for the recombination dynamics, is split by exchange interaction into two pair states with $N_m = \pm 1$ and $N_m = \pm 2$. Since the angular momentum has to be conserved in radiative recombination processes, but the photon can only carry a spin of 1, the lowermost state with spin projection $N_m = \pm 2$ is named *dark state* or A_F. Consequently the $N_m = \pm 1$ state is labeled *bright state*, *allowed state*, or A_T, as shown in figure 1.6.

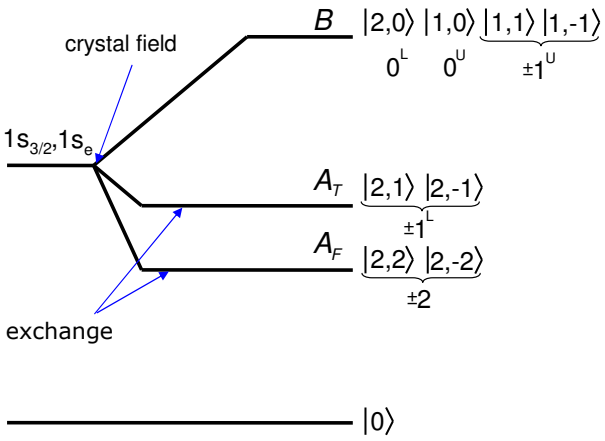

Figure 1.6: Splitting of exciton states (not to scale) and nomenclature.

1.3 Growth Techniques

A number of preparation methods to obtain quantum confined structures of lowered dimensionality are available. The growth of a thin film of a thickness that is smaller than the exciton Bohr radius in the material results in a quasi two dimensional structure. The

confinement in one direction produces a potential that is flat in the non confined dimensions and displays a pronounced valley in the confined direction, which has coined the term *quantum well*. Further processing, of such a structure (by etching or lithography) into a narrow stripe brings confinement in a second dimension. The quasi one dimensional structure obtained is referred to as *quantum wire*. Confinement in all three dimensions reduces the structure to zero dimensions. The term *quantum dot* (QD) is commonly used for these structures.

Instead of processing three-dimensional bulk semiconductors into confined structures of lowered dimensionality a controlled growth to build up the samples from a molecular scale is favorable.

Structures of low dimensionality can be obtained from chemical preparation routines, in which a small nanocrystal (NC) is grown either spherically or elongated to form *nanodots* or *nanorods*. Controlled chemical deposition of material on a substrate results in quantum well structures.

The nanocrystals under investigation in this work are obtained from these wet chemical syntheses. In chapter 6, the attempt to incorporate these colloidal nanoparticles in a semiconductor matrix, grown by molecular beam epitaxy (MBE), is described. Since the MBE process itself is also one of the important fabrication methods for nanostructures, the general principle shall be described here as well [46].

1.3.1 Colloidal Nanocrystals

In the colloidal or wet chemistry, II-VI nanocrystals are synthesized in a high temperature growth from metallic and organometallic precursors in highly coordinating solvents [81] [47].

The reaction is in principle a precipitation of the nanocrystals. The ligand acts, similar to processes in emulsions, as a molecule that attaches to the nanoparticle with one end and floats in the solution with the other end, thereby covering the surface and moderating the growth kinetics. A reduction of the growth speed at the very early state of the synthesis effectively separates the nucleation of small nanocrystals from the subsequent growth of larger ones. This is an important feature of the growth procedure to prevent a constant formation of new nanocrystal seedlings, which would result in a very large distribution of nanoparticle sizes. In the protocols used, precursor concentration and temperature are the parameters to control the outcome of the synthesis.

Following the synthesis, the ensemble of differently sized particles can be fractionated by making use of the fact that larger particles - as in the case of molecules - have a smaller solubility. Adding a solvent in which the nanocrystals are not soluble leads to the precipitation of the largest particles first, which can be removed by centrifuging and filtering. By iterating these methods one can fractionize the reaction batch into almost mono disperse sub-ensembles, that is- nanocrystal samples of only a few percent size distribution.

1.3.2 Self Assembled Semiconductor Quantum Dots - The Stranski-Krastanov Growth Mode

Epitaxy describes the deposition of adatoms onto a highly crystalline substrate under continuation of the atomic ordering. While, in general, the adatoms may originate from a vapor-phase or a liquid-phase, in molecular beam epitaxy, heated effusions cells are used as the source of a beam of atoms that travel through a high vacuum and condense on the substrate in a characteristic growth mode [46].

The Stranski-Krastanov growth mode takes place under conditions at the transition between the island deposition of the Volmer-Weber growth and the fully formed layer depositing Frank-van der Merwe growth mode [110] [7]. It occurs at a critical layer thickness that depends on the surface energies and the lattice mismatch. It is this method that allows the fabrication of nanometer sized objects by choosing parameters that lead to a self assembly of quantum dots. The substrate is covered with atoms of a latticed mismatched material like CdSe (a=0.6126) on ZnSe (a=0.5662, pseudomorphously strained on GaAs at 280°C), forming a fully strained wetting layer (WL). The continued deposition of CdSe layers leads to a growing strain due to the lattice mismatch of -7.57 %. At a critical coverage of 2 to 3 ML, the strain is released by forming a roughly dome shaped structure of growing inter-atomic distance until the native CdSe lattice parameters are recovered. The concept of strain release by quantum dot formation is sketched in figure 1.7.

During the growth of the ZnSe buffer layer as well as the growth of the CdSe wetting layer and quantum dot, the effusion cells for zinc and selenium or cadmium and selenium are opened permanently. The subsequent overgrowth of the CdSe QD with ZnSe, the selenium source is opened permanently, while the zinc flux is added periodically. This supports a migration of adatoms on the surface that favors the growth of smooth layers with less defects. Consequently this growth mode is called migration enhanced epitaxy (MEE).

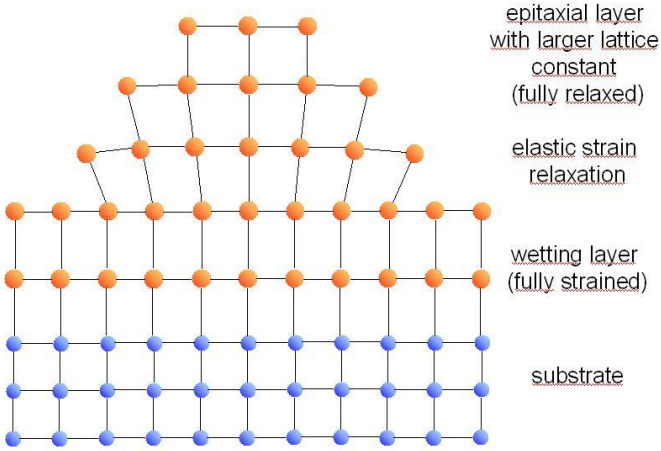

Figure 1.7: Schematic of the concept of strain relaxation leading to the formation of islands in the Stranski-Krastanov growth mode

It should be mentioned here that the wet chemical growth and the Stransky-Krastanov mode in MBE are not the only fabrication routes to obtain structures capable of confining excitons on a nanometer scale. In addition to the bottom-top approach of assembling small scale structures, various methods for a top-down approach of structuring macroscopic templates into nanometer sized objects exist. Among these are the wet chemical etching or focussed ion beam lithography to achieve structures like mesas or micro-pillars. Even a growth interruption in a layer by layer deposition like MBE can lead to interface roughness in, for example, a GaAs/InGaAs/GaAs heterostructure. The resulting thickness fluctuations of the quantum well lead to local potential variations that can confine electron-hole pairs. These structures are referred to as "Gammon dots" [38]. An interdiffusion process that leads to cadmium rich islands is another mechanism that results in quantum confining structures.

In the following the discussion is limited to the colloidal semiconductor nanocrystals (NCs).

1.4 Optical Properties

1.4.1 Size Tunability of the Luminescence

Light is emitted by a semiconductor, when an electron in the lowest normally empty conduction band and a hole in the highest normally occupied valence band recombine under emission of a photon (more than one in nonlinear processes allowed), whose energy

equals that of the band gap.

In quantum confined structures, this energy is increased by the quantization energy, which enables a tuning of the emission wavelength via the particle size. In CdSe the accessible wavelength range extends from about 500 nm to 700 nm. The lower wavelength limit is defined by the smallest size below which the nanocrystals can no longer be kept in suspension. The upper limit is the bulk value of the band gap.

One of the main advantages of using nanoparticles instead of other fluorophores is the decoupling of the emission wavelength from other material properties. The synthesis can therefore be optimized for the material system in use, and the emission wavelength is determined by the size of the particle, which is controlled by the temperature and the growth kinetics.

Figure 1.8: Photograph of CdSe/ZnS NCs of different size in solution under excitation with an unfocused laser beam of 409 nm wavelength. The red (green) emission stems from NC of approximately 2.3 nm (4 nm) core diameter.

While in the simplest approximation, the shift of the lowest quantum confined exciton level, with respect to the bulk value, scales with the inverse of the nanocrystal radius like $\Delta E = \frac{\hbar^2}{2\mu}\frac{\pi^2}{R^2}$, phenomenological description of the wavelength of the first absorption peak as a function of the particle size have been developed. Peng and coworkers for example introduced a polynomial function of fourth order in reference [134], that allows to extract the mean diameter d_{NC} of the NCs from the spectral position λ of the first exciton absorption peak of the ensemble.

$$d_{NC} = (1.6122 \cdot 10^{-9})\lambda^4 - (2.6575 \cdot 10^{-6})\lambda^3 +$$

$$+ (1.6242 \cdot 10^{-3})\lambda^2 - (0.4277)\lambda + (41.57) \tag{1.33}$$

1.4.2 Surface Capping

The formation of structural defects, that can enable radiationless recombination or trapping of carriers that later recombine under emission of a photon of reduced energy, is favored by the high surface to volume ratio of nanoparticles. Moreover, dangling bonds on the surface can give rise to trap states that additionally reduce the quantum yield. To counteract this tendency, colloidal NCs are capped with a larger band gap material and/or organic ligands to increase the confinement and passivate surface states [89]. Quantum yields of 70% at room temperature can be obtained by applying this kind of capping. The quantum confinement that leads to the size dependence of the excitonic levels is defined by the boundaries of the semiconductor core. In other problems, like the estimation of spatial arrangements of a nanoparticle, the existence of a semiconductor shell as well as a shell of ligands has to be taken into account. The resulting effective or hydrodynamic diameter therefore differs from the above definition.

1.4.3 Recombination Dynamics

The dynamic behavior of the luminescence obtained from NC samples strongly depends on the recombination mechanism. Upon non-resonant excitation, excitons form and relax on a picosecond time scale. Fast capture into trap states as well as energy transfer processes from small nanocrystal within the ensemble to larger ones takes place at comparable times. The radiative recombination time is typically on the order of hundreds of picoseconds to tens of nanoseconds, if the transition is optically allowed. Dark state luminescence is observed at decay times that are one to two orders of magnitude larger than the corresponding bright state recombinations. Luminescence stemming from trap states is red shifted with respect to the exciton recombination and typically decays with a time constant in the order of hundreds of nanoseconds. This decay time is often not well defined. As a consequence the observed decay is multi-exponential when measuring on NC ensembles.

1.4.4 Luminescence Intermittency - Blinking

An effect that is observed when monitoring the luminescence of single nanocrystals on a time scale of seconds, is a sudden and drastic reduction or even vanishing of the PL signal for a limited time, until it recovers to the original value. This *blinking* can be attributed to two different mechanisms [62], [82], [108].

An effect present in nanocrystals is the non-radiative transfer of energy from one electron-hole pair to another exciton, which is thereby ionized and dissociated. Since the nanocrystal is now in an effectively charged state, it is not able to emit photons until the recapture of the missing charge carrier. This Auger-type effect leads to a switching between an "on" and an "off" state of the emission of the nanocrystal. Small ensembles of nanocrystals thereby show a small fluctuation of the emission intensity. If this intensity is additionally spectrally dispersed with sufficient resolution, the center wavelength and overall shape of the spectrum can change in time, since the individual nanocrystals of the ensemble possess non degenerate resonance energies due to small size and shape deviations. With a growing number of NCs in the ensembles, the effect is averaged out. A reduction of the number of NCs adding to the observed emission leads to more drastic relative changes of the intensity with the extremal case of only a single NC emitting. In that particular case a switching between only two discrete levels of intensity is observed. This "on" and "off" blinking is widely considered a proof for the presence of only one optically active emitter within the sample area out of which light is collected. Figure 1.9 shows snapshots and a transient of the luminescence obtained from a sample containing isolated NCs as well as agglomerates.

A second explanation for the observed behavior is based on the fine structure of the excitonic states. If a dark state is energetically close to a state out of which radiative recombination is allowed, a phonon assisted switching of the nanocrystal from one state into the other is possible. Since the dark state emits light only weakly or not at all, the switching between two quantum mechanical states can account for the observed blinking, even if the ionization effect described above is not present or less strong. Nevertheless, the considerations regarding the connection between luminescence blinking and ensemble size also hold here, that is, a bimodal distribution can be used as a fingerprint of a single NC.

1.4.5 Jitter

Another temporal change in emission of the NC is useful for the identification and assignment of individual transitions within ensembles. This is especially useful if the existence of a lowest attainable nanoparticle density prevents the light collection from only one emitter [116]. Local fields in the vicinity of the particle can introduce a Stark-shift of the emission lines, which is changing on a time scale of seconds [31]. Since the local electric fields change little over distances of the size of the particle, it can be expected that all lines stemming from one particle are subject to the same electric field and thereby "jitter" in the same way. High resolution spectroscopy at temperatures low enough to produce

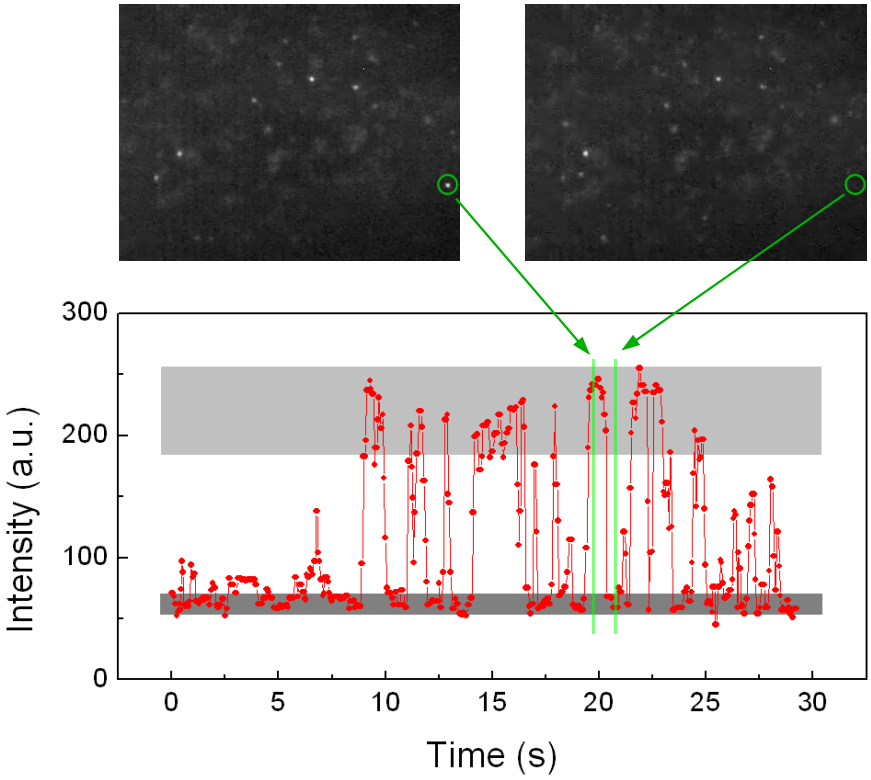

Figure 1.9: The temporal behavior of the NC PL. The snapshots show an area of 40 μm diagonal of a sample containing NC embedded in polymer. The circle marks an area in which the intensity was monitored over time to produce the trace seen below. The Intensity shows a bimodal distribution between "on" and "off" represented by the grey areas.

narrow emission lines is therefore a well suited tool for the identification of lines belonging to the fine structure of a single nanoparticle.

2. Energy Transfer Mechanisms

In this section the theoretic background of energy transfer is introduced, and the necessary formalism for the evaluation and quantification derived. This follows closely the derivation originally published by Theodor Förster [37] as well as reviews of this and related works [118].

2.1 Intra System Energy Transfer

Strictly speaking, energy transfer is almost always present, when a sample is excited optically. The non-resonant excitation usually applied in luminescence experiments creates carriers at energies above that of the state out of which radiative recombination occurs. It was anticipated, that the relaxation process from the absorbing down to the emitting states could be inefficient, unless the energetic difference that has to be overcome equals a multiple of the systems LO-phonon energy. This so called phonon bottleneck however was not observed experimentally in colloidal NCs or NCs embedded in a glass matrix [127]. The models explaining the unexpected fast relaxation include vibrations of the surface of the NC [21] [22] or even in the surrounding ligand molecules [44]. The energy transfer from the higher, absorbing to the lower, emitting states is reported to be on a sub picosecond time scale, which is well below that of the radiative and non-radiative processes.

A rather unwanted mechanism, which effectively transfers energy, is the trapping of carriers in crystallographic defect levels or unpassivated dangling bonds. The energy is drawn out of the exciton system, stored and dissipated radiatively or non-radiatively. in the former case trap state luminescence, which is red-shifted with respect to the exciton recombination wavelength, can be observed. This enables the identification of trap state luminescence, which can also serve as a criterion for the quality of the NC.

While the above mechanisms occur within even a single isolated NC, the energy transfer mechanisms under investigation here are inter-chromophore events, described in the following.

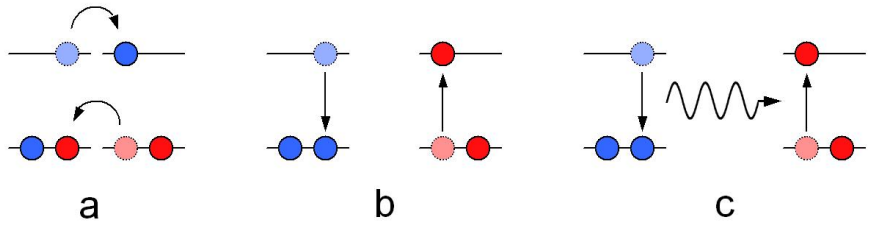

Figure 2.1: Transfer mechanisms, acting at different separations: If donor and acceptor are separated by less than one nanometer, charge carrier exchange can occur (a, Dexter transfer). At distances above, dipole-dipole coupling transfers energy radiationless (b). At macroscopic distances, emission and subsequent reabsorption of a photon transfers energy (c).

2.2 Inter System Energy Transfer

Energy transfer between fluorophores is defined as a process in which a donor (Don) in an excited state relaxes to the ground state neither by radiative combination (k_{rad}) nor by an internal, non-radiative conversion (k_{nrad}), but by shifting the energy to a thereby excited acceptor (Acc) via a transfer process (k_{transf}). This is commonly sketched like:

$$\mathrm{Don}^* + \mathrm{Acc} \overset{k_{transf}}{\longrightarrow} \mathrm{Don} + \mathrm{Acc}^*$$

where the asterisk marks the species in the excited state. Depending on the distance between donor and acceptor, this can take place in a variety of ways.

2.2.1 Reabsorption

The largest distance can be bridged by employment of a photon ($h\nu$) that relays energy from a donor chromophore to an acceptor. This transfer involves a donor excitation, after which the spontaneous emission of a photon occurs. If the acceptor species has an absorption window in the spectral region of the emitted photon, it can absorb the photon and thereby changes to an exited state itself.

$$\mathrm{Don}^* + \mathrm{Acc} \overset{k_{rad}}{\longrightarrow} \mathrm{Don} + h\nu + \mathrm{Acc} \qquad \mathrm{Don} + \mathrm{Acc} + h\nu \longrightarrow \mathrm{Don} + \mathrm{Acc}^*$$

The distances involved in such a reabsorption transfer are large, compared to the wavelength of the emitted light and in principal have no upper limit, if the photon involved is free to propagate.

In practice, this kind of energy transfer is often an unwanted effect, that has to be avoided in experimental situations. This can be achieved by using diluted samples, in which the concentration of the fluorophores is low enough to make reabsorption events unlikely. Likewise, using cuvettes of small volume and short optical path length limits the reabsorption probability.

The presence of reabsorption effects can be identified by red shifts of the PL in the concentrated samples, with respect to the samples of higher dilution, because photons emitted from the high energy part of the NC ensemble spectrum are reabsorbed by larger particles, which subsequently emit the transferred energy at a longer wavelength. In addition, the magnitude of this red shift is depending on the traversed sample thickness, which can give additional proof for the presence of such a mechanism. Since the emission of photons, and therefore the release of energy from the donor, is governed by its radiative recombination rate only, the donor PL life time is not changed in a reabsorption scenario.

2.2.2 Charge Carrier Migration - Dexter Transfer

At distances below 1 nm, the charge carrier wave functions of donor and acceptor can overlap. In that case, the Dexter transfer mechanism leads to a simultaneous transfer of charge carriers: An electron in an excited state of the donor is transferred to the acceptor, which in turn transfers a ground state electron to the donor. After the carrier exchange, the donor is left deactivated, while the acceptor is in an excited state, from which it can relax by radiative recombination.

$$\mathrm{Don}^* + \mathrm{Acc} \xrightarrow{k_{Dexter}} \mathrm{Don} + \mathrm{Acc}^*$$

For intermediate distances, coulombic interactions, especially the dipole-dipole interaction play the main role in the exchange of energy. Since this is the basis for the transfer system described in chapter 7, the according theory is described in the following in more detail.

2.2.3 Dipole-Dipole Coupling - Fluorescence Resonant Energy Transfer

The idea that the electro magnetic field surrounding a dipole can influence the state of a second nearby dipole was treated by Theodor Förster [37] already sixty years ago. His theory became known as *fluorescence resonant energy transfer* or *Förster resonance energy transfer* abbreviated FRET. Although written in the light of inter-chromophore

energy transfer between organic compounds, the description also holds for NCs as the emitting species.

Taking into account, that both, the donor emission, and the acceptor absorption, have a significant bandwidth, it is reasonable, to approximate their internal structures as a set of dipoles, oscillating in a range of frequencies. The theoretic description makes use of classical concepts like the harmonic oscillator. Next to this classical approach quantum mechanical calculations exist, that lead to the same result [118].

To calculate the energy taken up by a single charge carrier in an electro magnetic field, the model of a forced, undamped oscillator is used. Starting with the initial condition of an electron at rest, and at minimum displacement at $t = 0$, and from there on being accelerated by a sinusoidal field $E = E_0 \cdot \sin(\omega_0 t)$, the systems energy is converted from kinetic to potential energy and back with twice the frequency of the driving field. Finding the maximum displacement (when the kinetic fraction of the energy balance is zero) therefore enables the calculation of the energy uptake.

The eigen frequency ν_0 of a charge e with mass m , tied to its zero position by a spring of constant k, is given by $\nu_0 = \frac{1}{2\pi}\sqrt{\frac{k}{m}}$. With the driving field E, the equation of motion for this system is

$$m\frac{d^2}{dt^2}x = -m\omega_0^2 x + eE_0\cos(\omega t) \tag{2.1}$$

With the above boundary conditions, the solution of this equation is given by:

$$x = -\frac{2eE_0}{m(\omega^2 - \omega_0^2)}\sin(\frac{\omega - \omega_0}{2}t)\sin(\frac{\omega + \omega_0}{2}t) \tag{2.2}$$

Close to the resonance ($\omega \approx \omega_0$), which is the only case in which considerable displacements can be achieved, the sine functions can be approximated with their arguments, and the sum of the resonance frequency and ω is approximately twice the resonance frequency. This simplifies the problem to:

$$x \approx -\frac{eE_0}{2m\omega_0}t \cdot \sin(\omega_0 t) \tag{2.3}$$

The above holds for a narrow frequency intervall around the resonance, defined by $\omega_0 - \pi/t < \omega < \omega_0 + \pi/t$. The maximum displacement, reached at times, when the argument to the sine is a multiple of $\pi/2$ then is:

$$\hat{x} = \pm\frac{eE_0}{2m\omega_0}t$$

which can now be inserted into the potential energy:

$$W = \frac{1}{2}k\hat{x}^2 = \frac{1}{2}k\frac{e^2E_0^2}{4m^2\omega_0^2}t^2 = \frac{e^2E_0^2}{8m}t^2 \tag{2.4}$$

The considerations so far are valid for a one dimensional problem. If in the general case, the energy uptake is to be calculated, the orientation of the driving field has to be taken into account. The relative orientations of the field produced by the energy-donating transition dipole, the accepting transition dipole, and the vector connecting the donor and acceptor centers, commonly are accounted for by the orientational factor κ^2. It is defined as:

$$\kappa^2 = \left(\hat{d} \cdot \hat{a} - 3(\hat{d} \cdot \hat{r})(\hat{a} \cdot \hat{r})\right)^2 \tag{2.5}$$

with $\hat{d}$, $\hat{a}$, and $\hat{r}$ denoting the unit vectors for the donor dipole, the acceptor dipole, and the interconnecting vector respectively. It varies from a maximum of 4, when all dipoles are aligned end on end, to a minimum of zero. For randomly oriented dipoles, like it is the case in solutions and solid samples, without any preferred orientation of the chromophores, κ^2 equals $\frac{2}{3}$.

The amplitude of the driving field E in 2.4 can be rewritten as the field produced by a donor dipole as:

$$E_0 = \frac{\kappa e a}{n^2 r^3} \tag{2.6}$$

where a refers to the displacement of the charge e oscillating in the donor system, and r is the donor-acceptor distance. The dielectric effect of the medium in which donor and acceptor are embedded is expressed by the refractive index n. This results in the acceptor energy uptake to be:

$$W_{\mathrm{Acc}} = \frac{\kappa^2 e^4 a^2}{8 n^4 m r^6} t^2 \tag{2.7}$$

Similar to the harmonic oscillator description of the acceptor, the energy of the donor dipole can be expressed as:

$$W_{\mathrm{Don}} = \frac{1}{2} m \omega^2 a^2 \tag{2.8}$$

This allows to replace the donor oscillation amplitude a, to yield the following relationship between donor and acceptor energies:

$$W_{\mathrm{Acc}} = \frac{\kappa^2 e^4}{4 n^4 m^2 \omega^2 R^6} W_{\mathrm{Don}} \cdot t^2 \tag{2.9}$$

Since, as mentioned above, the donor and acceptor system can be understood as ensembles of oscillators with different resonance frequencies, the oscillator strength of both species $f_{\mathrm{Don}}(\omega)$ and $f_{\mathrm{Acc}}(\omega)$, and their overlap in frequency space have to be taken into account. The overlap has to be considered within the frequency interval $[\omega_0 - \frac{\pi}{t}; \omega_0 + \frac{\pi}{t}]$ in which the approximation of the sine functions, made in the derivation so far, holds. The resonance, necessary for energy uptake by the acceptor fraction $f_{\mathrm{Acc}}(\omega)d\omega$ is only

given for the donor fraction $f_{\mathrm{Don}}(\omega) \cdot \frac{2\pi}{t}$. Taking this into account, and integrating over all frequencies, yields:

$$W_{\mathrm{Acc}} = \frac{\kappa^2 e^4}{4n^4 m^2 \omega^2 r^6} 2\pi W_{\mathrm{Don}} t \int_0^\infty f_{\mathrm{Don}} f_{\mathrm{Acc}} \frac{d\omega}{\omega^2} \tag{2.10}$$

The time derivative of this energy is the power transferred, which, since we only consider a lossless transfer, is equal to both,the power lost by the donor, and the power taken up by the acceptor. This can in turn be understood as the energy transferred in a given time interval, or the product of the energy and the transfer rate:

$$\frac{d}{dt} W_{\mathrm{Don}} = k_{transf} \cdot W_{\mathrm{Don}} = \frac{\pi \kappa^2 e^4}{2n^4 m^2 \omega^2 R^6} W_{\mathrm{Don}} \int_0^\infty f_{\mathrm{Don}} f_{\mathrm{Acc}} \frac{d\omega}{\omega^2} \tag{2.11}$$

The introduced oscillator strength can be accessed by the spectral properties of the chromophores. In the case of the acceptor, the oscillator strength is connected with the molar extinction coefficient $\varepsilon_{\mathrm{Acc}}(\nu)$, given by:

$$f_{\mathrm{Acc}}(\nu) = \frac{3000 n (\ln 10) mc}{\pi N_{AV} e^2} \varepsilon_{\mathrm{Acc}}(\nu) \tag{2.12}$$

where c is he vacuum speed of light. The donor oscillator strength is connected with the emission spectrum accessible by photoluminescence measurements, and denoted as $I_{\mathrm{Don,norm}}(\nu)$, since it is normalized on the frequency scale as $\int I_{\mathrm{Don}}(\nu) d\nu = 1$. Additional parameters are the donor quantum yield η_{Don}, and its native (i.e. in the absence of a transfer partner) fluorescence lifetime τ_{Don}.

$$f_{\mathrm{Don}}(\nu) = \frac{3mc^2 \eta_{\mathrm{Don}} I_{\mathrm{Don,norm}}(\nu)}{8\pi n e^2 \tau_{\mathrm{Don}} \nu^2} \tag{2.13}$$

Extracting the transfer rate k_{transf} out of 2.11, changing from the angular frequency to the frequency, and substituting the expressions for the oscillator strengths, results in:

$$k_{transf}(r) = \frac{9000 (\ln 10) \kappa^2 \eta_{\mathrm{Don}}}{128\pi^5 n^4 N_{AV} \tau_{\mathrm{Don}} r^6} \cdot J \tag{2.14}$$

with the overlap integral in the wavelength form

$$J = \int I_{\mathrm{Don,norm}}(\lambda) \varepsilon_{\mathrm{Acc}}(\lambda) \lambda^4 d\lambda \tag{2.15}$$

Figure 2.2 illustrates the calculation of the spectral overlap integral J out of the normalized donor emission and acceptor absorbance in the wavelength representation.

Förster defined the radius R_0 as the distance between donor and acceptor, at which the transfer rate equals the inverse fluorescence decay time of the donor in the absence of an acceptor and therefore in the absence of any transfer. This corresponds to a situation

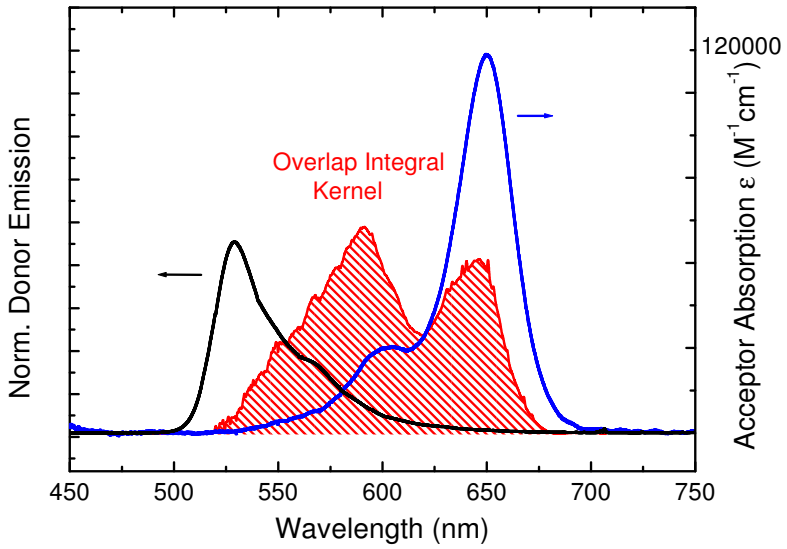

Figure 2.2: The overlap integral Kernel (red) is the product of the normalized donor emission (black) and the acceptor absorption (blue) multiplied by the fourth power of the wavelength. Integration over all relevant wavelength yields the overlap integral J, which linearly enters the calculation of the energy transfer rate of a given FRET pair

where equal amounts of energy are transferred to an acceptor, as are dissipated by radiative and non-radiative transitions to the donor ground state. The mathematic formulation of this definition is

$$k_{transf}(R_0) = k_{rad} + k_{nrad} = \frac{1}{\tau_{\mathrm{Don}}} = \frac{9000(\ln 10)\kappa^2\eta_{\mathrm{Don}}}{128\pi^5 n^4 N_{AV}\tau_{\mathrm{Don}}R_0^6} \cdot J \tag{2.16}$$

Extraction of the argument R_0 yields the definition of the Förster radius:

$$R_0^6 = \frac{9000(\ln 10)\kappa^2\eta_{\mathrm{Don}}}{128\pi^5 n^4 N_{AV}} \cdot J \tag{2.17}$$

The dependence of the transfer rate on the sixth power of the inverse distance enables a number of equivalent representations of the magnitude of energy transfer:
The efficiency of energy transfer can be defined as the ratio of the transfer rate to all other rates of deactivation: [1]

$$E = \frac{k_{transf}}{k_{rad} + k_{nrad} + k_{transf}} \tag{2.18}$$

[1] In some publications covering FRET, the transfer channel is included in the non-radiative channel. In the frame of this work, radiative, non-radiative, and transfer transitions are distinguished and always named explicitly.

With the definition of R_0, the transfer rate can also be written as:

$$k_{transfer} = (k_{rad} + k_{nrad})\Big(\frac{r}{R_0}\Big)^6 \tag{2.19}$$

Inserting this in the definition of the efficiency results in the distance dependence of the FRET efficiency:

$$E(r) = \frac{R_0^6}{R_0^6 + r^6} \tag{2.20}$$

The above definition of the efficiency has some similarity to the definition of the quantum yield, as the ratio of emitted photons to those absorbed by a fluorophore:

$$\eta = \frac{k_{rad}}{k_{rad} + k_{nrad} + k_{transf}} \tag{2.21}$$

This can be interpreted as a change in the donor quantum yield in the presence of transfer, or in the presence of a transfer enabling acceptor species. This redefines the efficiency as:

$$E = 1 - \frac{\eta_{\mathrm{Don,Acc}}}{\eta_{\mathrm{Don}}} \tag{2.22}$$

This has practical implications, since, if the non-radiative rates stay unchanged, the above definition directly links the donor PL intensity in the absence and the presence of an acceptor to the efficiency

$$E = 1 - \frac{I_{\mathrm{Don,Acc}}}{I_{\mathrm{Don}}} \tag{2.23}$$

If only one energy transfer channel is present, and the decay of the donor fluorescence can be described by a single time constant, the change in this constant in the presence and absence of transfer is another means of extracting the efficiency out of experimental data:

$$E = 1 - \frac{\tau_{\mathrm{Don,Acc}}}{\tau_{\mathrm{Don}}} \tag{2.24}$$

An alternative way for the determination of the transfer efficiency, out of time integrated spectroscopic data, is the comparison of the acceptors PL intensity, in the presence $I_{\mathrm{Acc,Don}}$, and absence I_{Acc} of a energy transfer providing donor. Here, the acceptor PL, purely due to transfer, that is the difference between the acceptor PL in the presence and the absence of the donor ($I_{\mathrm{Acc,Don}} - I_{\mathrm{Acc}}$) is set into relation to the overall acceptor PL in the absence of a donor (I_{Acc}). Since all intensities are measured under excitation with a fixed wavelength (λ'), the difference in donor and acceptor absorbance ($A_{\mathrm{Acc}}(\lambda')$, $A_{\mathrm{Don}}(\lambda')$), at the particular excitation wavelength, is taken into account as a correcting pre factor:

$$E = \frac{A_{\mathrm{Acc}}(\lambda')}{A_{\mathrm{Don}}(\lambda')}\left[\frac{I_{\mathrm{Acc,Don}}(\lambda') - I_{\mathrm{Acc}}(\lambda')}{I_{\mathrm{Acc}}(\lambda')}\right] = \frac{A_{\mathrm{Acc}}(\lambda')}{A_{\mathrm{Don}}(\lambda')}\left[\frac{I_{\mathrm{Acc,Don}}(\lambda')}{I_{\mathrm{Acc}}(\lambda')} - 1\right] \tag{2.25}$$

The above equations shows that fluorescence energy transfer or Förster Transfer or simply FRET, as it will be referred to in the following, can be efficiently quantified by spectroscopic investigations. Values for the transfer efficiency can be deduced from measurements in the presence and the absence of the respective transfer partner. The quantities to measure are the donor or acceptor PL intensity. For samples showing mono-exponential PL decays, also the change in the PL decay time yields efficiency values.

The prerequisite for the successful determination of distances out of efficiency data is the knowledge of the Förster radius, which requires donor emission and acceptor absorbance spectra to be acquired.

3. Experimental Techniques

The following pages are intended to illustrate the particularities of the experimental techniques that were used for the acquisition of spectroscopic data. Very basic experiments employed for characterization purposes are described in the beginning, in order to lay the foundation for the more complex experiments described thereafter.

3.1 Absorption and Emission Spectroscopy

3.1.1 Absorption Spectroscopy

The ability of a sample to absorb light is proportional to the optical path length traversed, that is, the thickness of the sample, the concentration of individual absorbers within the sample, as well as the quantum mechanical transition probability between two states upon the irradiation of light of a given wavelength λ. This transition probability is expressed by the absorption cross section [66]. Phenomenologically, the decrease in intensity observed when light travels through a sample is described by the Lambert-Beer law:

$$I(d) = I_0 \cdot e^{-\alpha \cdot c \cdot d} \Leftrightarrow A = -\ln(\frac{I}{I_0}) \tag{3.1}$$

or

$$I(d) = I_0 \cdot 10^{-\alpha' \cdot c \cdot d} \Leftrightarrow A' = -\log_{10}(\frac{I}{I_0}) \tag{3.2}$$

With I_0 and $I(d)$ denoting the light intensity before entering the sample, and after having traveled the distance d within the sample of concentration c. A and A' are the absorbances and α and α' the absorption coefficients. Both representations, that imply an exponential decay of the light intensity are generally valid and used in chemistry and physics communities. The concentrations can be given as a mole fraction, that is, a dimensionless fraction, or in moles per unit volume. The units of the absorption coefficients are of reciprocal length.

In an experimental situation, a tunable, monochromatic beam of light passes through the sample, after which its intensity is measured as a function of the wavelength λ and

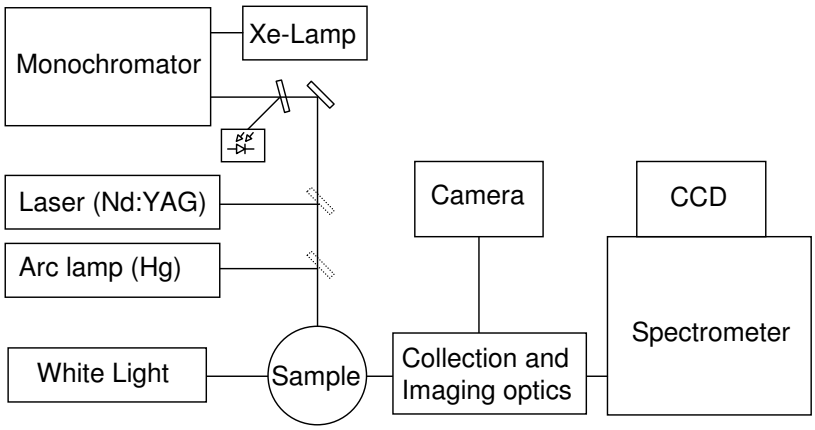

Figure 3.1: Setup for transmission, PL, and PLE measurements (imaging optics not shown)

compared with the intensity transmitted through a blank sample. An alternative realization is to pass white light of low intensity through the sample and to record the transmitted light intensity spectrally dispersed.

Figure 3.1 shows such a transmission spectroscopy setup with a tungsten lamp as the source of collimated white light. The sample can be contained in a cuvette for measurements on liquids, or a polymeric carrier film on a quartz plate for nanocrystal samples. The latter can additionally be measured at low temperatures, when contained in a cryostat. The collimating and focusing optics are left out of this and the following descriptions of experimental setups for simplicity.

Measuring the ratio of incident light and transmitted light gives access to a number of sample properties. The energy at which the onset of the absorption occurs, marks the band gap energy of a bulk sample. In NC samples, the absorption shows a peak of lowest energy, which corresponds to the first excitonic transition. This spectral position can be used to determine the average size of the contained NC following equation 1.33. The spectral dependence of the absorption of a species acting as an acceptor in an energy transfer scenario is of major importance for the determination of the spectral overlap with a given donor emission spectrum. Both quantities will be investigated in chapter 7. If the absorption cross section per single absorbing entity is known, the absolute absorbance value can be used to determine the concentration of absorbers contained in the sample, as it will be the case in the determination of NC densities in chapter 6.

3.1.2 Photoluminescence Spectroscopy

Instead of probing the unoccupied states in a system, as it is the case in absorption experiments, photoluminescence spectroscopy is dealing with the radiative recombination from populated excited states to the ground state. Light from a source of sufficiently high photon energy to populate levels above the ground state, is focussed onto the sample. The light emitted upon recombination of the excited carriers is separated from scattered excitation light, by spectral or spatial filtering, and recorded with a CCD, spectrally dispersed by a spectrometer. In the case of a setup like the one sketched in figure 3.1, the available excitation ranges from UV (367 Hg-line, xenon lamp), over violet (409 nm GaInN laser) and green (532 nm, Nd:YAG laser) to red (632 HeNe laser) and infrared (xenon lamp).

Similar to absorption spectroscopy, PL spectroscopy can give insight to NC size by recording the emission wavelength, as well as the sample concentration, or number of NC, by monitoring the emission intensity. In the following paragraphs, several extensions of PL spectroscopy to more powerful techniques are discussed.

3.1.3 Photoluminescence Excitation Spectroscopy

A modification of PL measurements is the monitoring of the emission of a sample while changing the excitation wavelength. These measurements can be understood as a combined absorption and emission probing, since a measured intensity is influenced by the samples absorbance at that particular excitation wavelength and the recombination probability at the emission wavelength under investigation. It is of particular interest to record PLE spectra not only at a fixed emission wavelength, but over a wavelength range. The measured PLE intensities can then be represented in a map-like plot with excitation and detection wavelength as the axes, which gives rise to the name multichannel or two-dimensional PLE (2d-PLE).

Figure 3.1 shows a setup capable of recording 2d-PLE graphs. A xenon lamp attached to a computer-controlled monochromator acts as an excitation source, tunable from 350 to 900 nm. A fraction of the emerging light is redirected to a photo diode, which records the intensity. The main part of the excitation light is focussed onto the sample. The luminescence light is collected and scattered excitation light suppressed by choosing a suited geometry, using crossed polarizers or long pass color filters. After focusing onto a detection spectrometer, the luminescence spectrum for a given excitation wavelength is recorded by a cooled CCD detector, before the next excitation wavelength is approached.

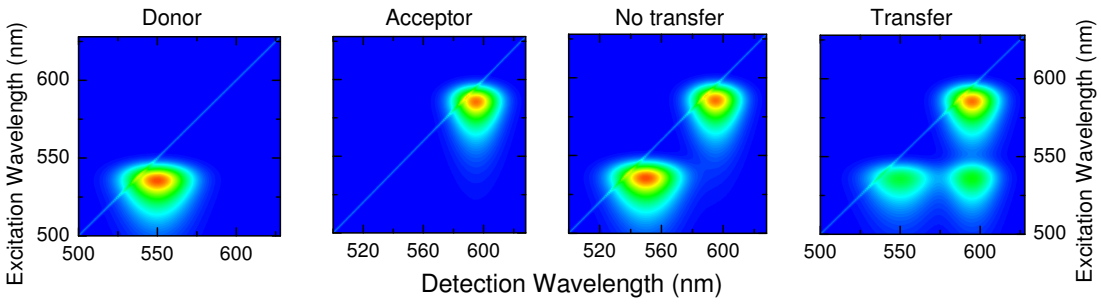

Figure 3.2: Simulated 2d-PLE emission map. The simulated emission intensity is color-coded from blue (low intensity) to red (high intensity) and shown as a function of detection wavelength (x-axis) and excitation wavelength (y-axis). The signature of a hypothetical donor with an absorption centered at 535 nm, and an emission at 550 nm as well as an acceptor with absorption and emission maxima centered at 585 nm and 595 nm respectively are displayed in the two left panels. An sample containing both fluorophores, without transfer emits a superposition of the two former signatures. In the presence of transfer, an off-diagonal peak at the donor absorption and the acceptor emission peak position is found (right panel). The efficiency of transfer was simulated at 50 %. The expected stray light line at positions where the detection wavelength equals the excitation wavelength is included in all panels.

In this way a set of luminescence spectra, each for a single excitation wavelength, is obtained. Since the emission of the xenon lamp exhibits a strong spectral dependence, the excitation intensity is recorded for every spectrum. Moreover, a single exciting photon can only trigger the emission of a single luminescence photon - neglecting nonlinear effects, which can only occur at much higher excitation intensities. Therefore each spectrum is normalized to a factor proportional to the incident photon flux. This is calculated by taking into account the measured intensity, the photo diode characteristic and the corresponding photon energy.

The energetic shift between absorbing and emitting states - the Stokes shift - is evidenced in a 2d-PLE plot as signal off the diagonal line, that represents the case of absorption wavelength being equal to emission wavelength. This line is typically visible due to small amounts of scattered excitation light. The stokes-shifted, off-diagonal signal is already visible in measurements on a single chromophore. The utility of the 2d-PLE measurements is however most evident in samples displaying a pronounced inter-chromophore energy transfer, as examplified in figure 3.2. In the presence of energy transfer between a donor and an acceptor species, the 2d-PLE plot will show a high intensity at the preferential acceptor recombination wavelength, while exciting at wavelengths that correspond to pronounced donor absorption, as it is subject of investigation in chapter 7. There,

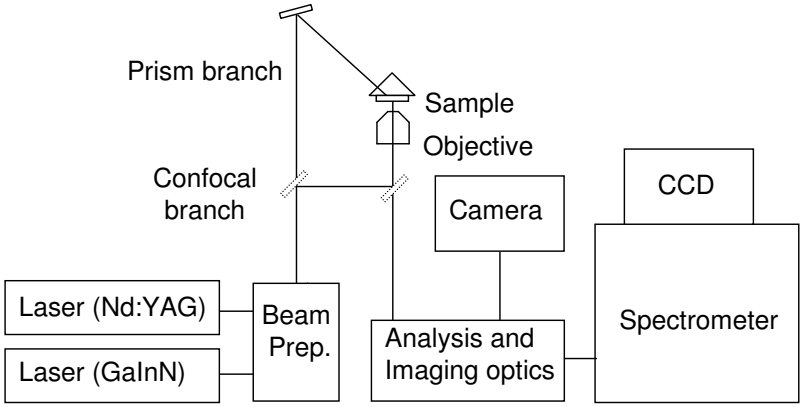

Figure 3.3: Block diagram of the setup for room temperature micro photoluminescence. The beam preparation includes selection, attenuation, and polarization control of the available laser sources. The removable mirror (dashed) allows for an easy switching between the prism geometry (upper optical path) and the confocal excitation geometry.

off-diagonal transfer peaks of this type will be used as an energy transfer fingerprint and analyzed quantitatively.

3.2 Micro Photoluminescence Spectroscopy

Spatial resolution and optimization of the light collection efficiency have not been considered up until now. As a justification for the utilization of a more complex setup for micro photoluminescence (μ-PL), like sketched in figure 3.3, these issues shall be addressed in the following in the light of the numerical aperture (NA) as the decisive parameter. The numerical aperture is defined by $NA = n \cdot \sin(\alpha)$ with the refractive index n between the optical element and the sample, and α half of the opening angle. In the case of diffraction limited imaging, most properties of the imaging depend on this numerical aperture.

3.2.1 Light Collection Efficiency

While in general in optical experiments as much of the signal light as possible should be collected by an objective lens, a distinction has to be made, whether the sample is an extended, or a point-like source of light. When investigating an ensemble of NCs, or a cuvette containing a liquid sample, both of which resembling an extended light source, an optimization implies a trade-off between collection efficiency and collection area.

The collection efficiency depends on the opening angle of the objective lens for the acceptance of light. The planar opening angle for light collection is connected with the NA via

$$NA = n \cdot \sin(\alpha) \Leftrightarrow \alpha = \arcsin(NA/n) \tag{3.3}$$

The solid angle connected with this opening angle is

$$\Omega(\alpha) = 4\pi \cdot \sin^2\Big(\frac{\alpha}{2}\Big) \tag{3.4}$$

The fraction of a full solid angle of 4π that can be used for light collection might be called angular light collection efficiency

$$Eff(NA) = \sin^2\Big(\frac{\arcsin(NA/n)}{2}\Big) \tag{3.5}$$

These algebraic considerations suggest using an objective of highest numerical aperture.

On the other hand, the collected light has to be relayed to the detection scheme, which typically includes, that it has to pass through the entrance slit of a spectrometer. Typical spectrometer f-numbers, that is, the ratio of focal length to element diameter, range from 4 to 10. This translates into numerical apertures of 0.125 to 0.05. The necessary matching of the incoupling optics to the NA of the spectrometer, results in a net magnification, given by the ratio of the numerical apertures. When the sample emits a constant number of photons per sample area, and these photons are emitted at random directions, gathering light from a maximal area is favorable. For a fixed spectral resolution, that is a fixed entrance slit width, and a fixed detector height, the net magnification of the system limits the sample area that can be imaged into the spectrometer, which contradicts the use of a collection objective with high numerical aperture. As a consequence, for a given sample size and spectral resolution, the collection optics have to be adapted, which often results in the use of large diameter achromatic lenses of focal length of a few cm.

A somewhat different situation is the collection of light emitted from point sources, which is the case in single NC PL measurements. Here, the light emitting area is the NC surface. Since this is smaller than the wavelength of light, it cannot be resolved. Moreover, since ideally only one NC is present in the field of view, a larger collection area does not increase the number of collected signal photons. This is why in this case the highest possible NA is the sole criterion of importance, which results in microscope objectives being used in such an investigation, which however account for some additional issues to consider.

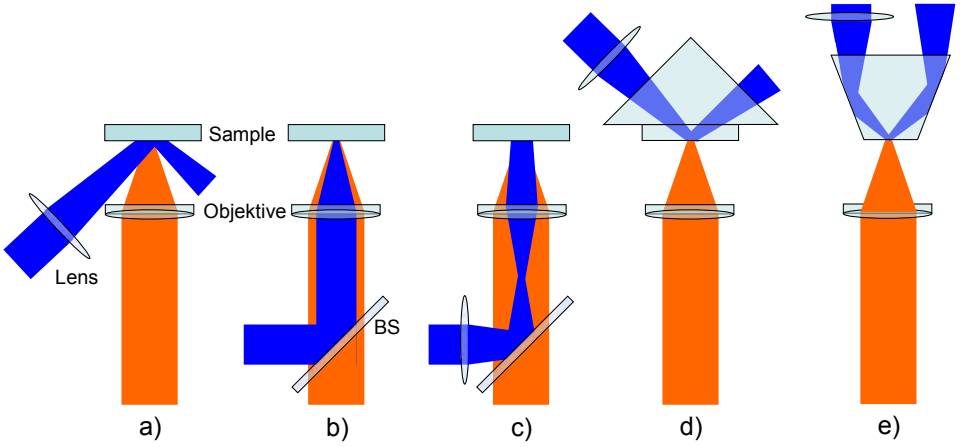

Figure 3.4: Excitation incoupling geometries. a) separated focusing of excitation laser (blue) and collection of luminescence (orange). b) confocal excitation, BS=beam splitter. c) confocal excitation with prefocused excitation. d) prism geometry. e) modified prism geometry.

3.2.2 Excitation Geometries

Figure 3.4 sketches some variations of optics for focusing excitation light onto a sample. If an objective with large working distance is used, space is normally sufficient to decouple the excitation from the collection optics by placing an additional lens, that is most suited for the desired excitation density (3.4, a).

For microscope objectives this is typically not possible, due to the space limitations of a small working distance, and the excitation is therefore focused onto the sample by the same objective that also collects the luminescence. To do so, a beam splitter of appropriate reflection/transmission ratio is placed in the collimated beam before the objective (3.4, b). In this geometry, the excitation is focused into a small spot which, in the ideal case, can be diffraction limited, that is half the wavelength in diameter.

When point like emitters are distributed across the field of view, a homogeneous distribution of the excitation light over a larger area is favored over a small area of excitation. Additional pre-focusing of the excitation leads to different z-positions of the focal planes, effectively enlarging the excitation spot size to tens of μm (3.4, c).

Another geometry enabling a separated adjustment of the excitation spot size and position makes use of a quartz prism to direct the light (3.4, d). The focused excitation laser enters through a short side of a right triangle prism, with an angle of incidence close to 0°. The NC are dispersed in a polymer film, attached to the hypotenuses of the prism. At room temperature, and for quick sample exchange, a quartz plate, acting as a carrier for the NC containing film, can be attached to that side of the prism with immersion oil, instead of

using the prism surface itself. The non absorbed laser light is mostly reflected from the boundary to air, effectively reducing the amount of scattered excitation light entering the collection optics. For low temperature applications, the geometry has to be matched to the positions of the cryostat windows. This can be achieved with a parallelogram prism inside the cryostat, and the excitation light entering from the side opposite to the collection optics, as sketched in figure (3.4, e).

3.2.3 Resolution

Spatial Resolution

If the maximum of the diffraction pattern of one object does not yet overlap the first minimum of it's neighbors diffraction pattern, one considers them to be optically resolved. This is expressed by the Rayleigh criterion for the achievable angular separation α, or its equivalent connecting the NA with the minimum linear separation d that can be resolved.

$$\alpha \approx 1.22 \cdot \frac{\lambda}{d} \Leftrightarrow d = \frac{0.61 \cdot \lambda}{NA} \tag{3.6}$$

While the resulting resolving power is by far to low to resolve individual NCs, it gives an idea of the required accuracy of the objective positioning. As the more crucial, limiting value the depth of focus can be used, which in a diffraction limited imaging is calculated as

$$d_z = \frac{\lambda}{2n \sin^2(\alpha)} \tag{3.7}$$

where α is the aperture angle, λ is the wavelength, and n is the index of refraction of the surrounding medium. For the microscope objectives in use, the numerical apertures are between 0.4 and 0.95. This translates to depth of focus values of 300 nm to 1.7 μm for green light of 550 nm wavelength. A precise positioning, that makes full use of the z-contrast due to the small depth of focus is therefore crucial. While at room temperature commercial, piezo-driven xyz-translation stages are used for this purpose (PI Piezo systems, Jena), a customized solution was developed for low temperatures.

The additional imaging optics towards the used spectrometer or camera were designed for net magnifications the range from 50-fold to 150-fold. The field of view observable with a video camera as the detector corresponded to a spot on the sample of roughly 150 μm to 50 μm diameter.

Spectral Resolution

The spectral resolutions obtained from the spectrometers used varied. The excitation wavelength in PLE experiments was typically chosen with a spectral bandwith of 1 nm. The monochromator used had a focal length of 1 m, which allowed an operation with rather wide input and output slits of 1.2 mm, to increase the light throughput. Depending on the experimental requirements, the luminescence was recorded with suited spectrometer-detector combination. In detail, a multichannel analyzer, attached to a monochromator of 0.25 m focal length was used for overview spectra. A medium resolution was obtained from a liquid nitrogen cooled CCD array of 1024x256 pixel attached to a 0.46 m imaging spectrometer, yielding 0.2 nm spectral resolution. Higher resolution spectra were obtainable from a thermo-electrically cooled CCD of 1024x256 pixel and a 0.85 m imaging corrected spectrometer enabling 0.1 nm resolution. The best spectral resolution of 0.003 nm was obtained with a imaging spectrometer of 2m focal length.

3.2.4 Cryogenic Temperatures

Cooling a sample to cryogenic temperatures is advantageous in a number of aspects. Lowering the phonon occupation number reduces the depopulation of excited states by temperature dependent non-radiative processes. As a consequence, the quantum yield of most NC samples is higher at low temperatures. Non-resonant excitation, far above the band gap, which is necessary to access a large density of states for absorption, and also supports a complete separation of the luminescence signal from the excitation light, leads to the deposition of excess energy in the sample. This local heating can damage the sample and cause a degradation of the NCs with time. Lowering the temperature acts as a protection of the NCs against such light induced damage.

While the above stated issues suggest a cooling to an arbitrary, low temperature, the precise control of the temperature and thereby the phonon occupation number, allows a tuning of the occupation of closely spaced energy levels in order to study the transition dynamics between those levels.

When trying to combine the light collection efficiency and spatial resolution of a μ-PL setup with the benefits of keeping the sample at cryogenic temperatures, one has to overcome the difficulties connected with the small working distance (distances between focal point and first surface of the objective). Figure 3.5 sketches two solutions to this issue. If moderate light collection efficiencies are sufficient, the sample can be contained in a flow cryostat with a short distance between cooling finger and optical window. A

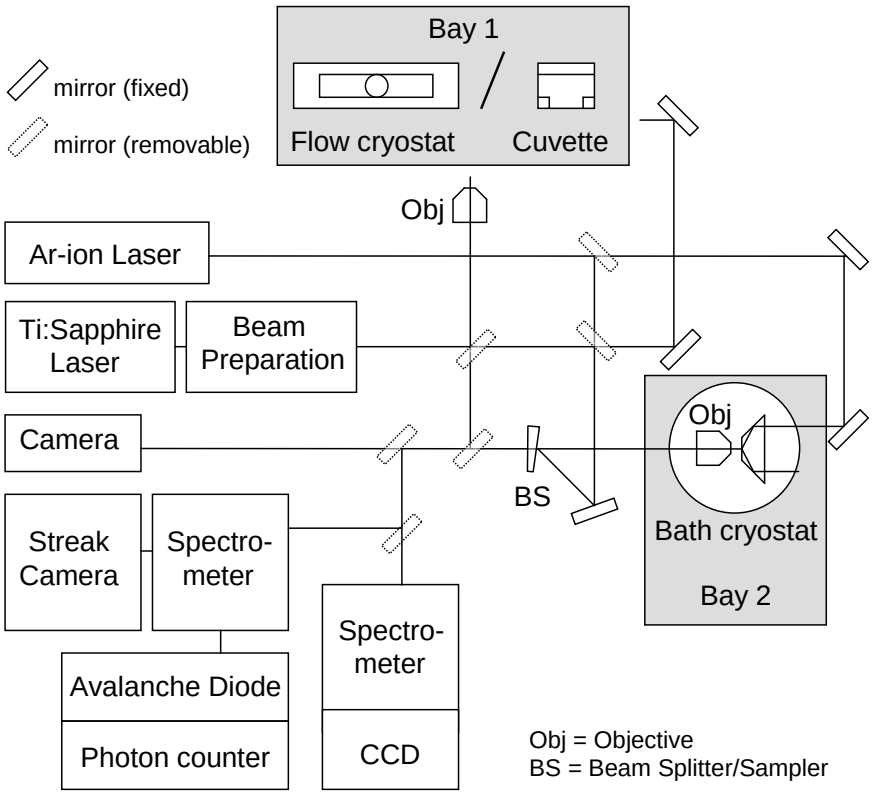

Figure 3.5: Block diagram of the setup for various time-resolved and low temperature PL measurements. The beam preparation for the pulsed Ti:sapphire laser includes a second harmonic generation and repetition rate control based on an acousto-optical modulator (AOM). The lasers can be used for experiments in two different sample bays. Bay one can be equipped with a either flow cryostat or a cuvette for liquid samples. Bay two hosts a bath cryostat which enables the excitation in confocal and prism geometry, as well as a high collection efficiency, due to a high NA microscope objective inside the cooled chamber (detailed description: see text).

microscope objective, designed for long working distance of approximately 8 mm (Zeiss, LD Plan Neofluar) can be used, which comprises a numerical aperture of 0.4. Liquid helium is used as a cooling agent, that evaporates inside a cooling finger, contained in an isolation vacuum of sufficiently low pressure (below $5 \cdot 10^{-4}$ mbar). A helium gas pump is employed to draw the exhaust gas out of the cryostat, thereby creating the suction power needed to draw liquid helium from the helium container through the transfer tube into the cryostat. After sufficient time to equilibrate the temperature between cooling finger and sample, temperatures of 5 K, at a coolant consumption of about 2 liters per hour, can be achieved, with a stability of $\pm$ 0.1 K.

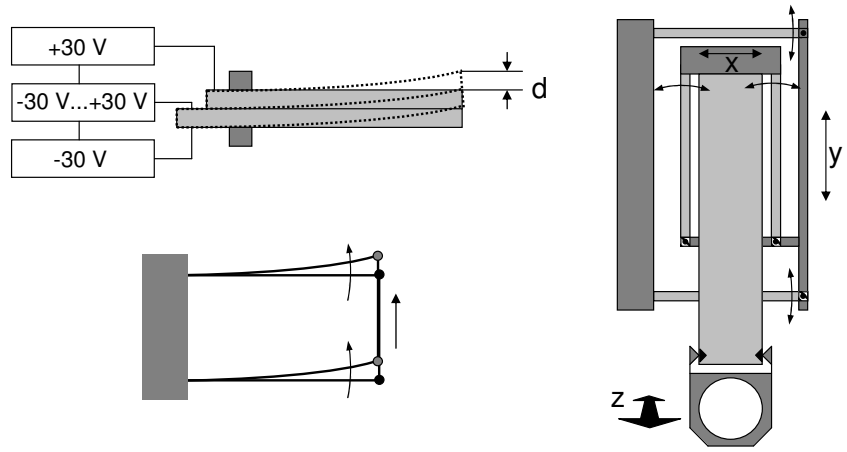

Figure 3.6: Left: Piezo actuator (bender) working principle. Right: Piezo translation stage. The ceramic piezo benders (light gray) shift the frame (dark gray) and the objective holder up to ± 0.25 mm, ± 0.4 mm, and ± 1 mm in x-,y-, and z-direction (focus)

For experimental applications that require the collection of light emitted from single NCs, a larger numerical aperture has proven to be necessary. Objectives designed to meet this requirements typically exhibit working distances well below 1 mm, and therefore have to be mounted inside the sample chamber of the cryostat. To allow for control of the focus (z) as well as the x- and y-position of the objective with sufficient accuracy, piezo actuators (PI-Systems, Jena) are used, whose bending motions are translated into linear shifts by a parallelogram based construction sketched in figure 3.6.

The enlarged space requirements for a translational stage like this, as well as the need to cool a rather large device, requires the cooling in a coolant gas flow, which can be achieved in a bath cryostat rather than a flow cryostat which provides a controlled temperature only for the closest proximity to the cooling finger. A bath cryostat (Cryovac, type KontiIT Spectro) with a large center bore of 50 mm and combined liquid nitrogen, liquid helium cooling provides the necessary stable operation conditions for many hours. The four quartz windows allow access to the sample in the confocal excitation/detection geometry. A specially designed prism furthermore enables to usage of the prism geometry at low temperatures. The fact that the piezo electric effect is reduced dramatically at low temperatures, reduces the travel of the piezo translation stage to about 10 % of the room temperature value. This has to be taken into account when operating at low temperatures. A redesigned μ-PL holder for cryogenic temperatures will contain a nanopositioner that retains a total travel of 5 mm even at 4 K, for the focusing direction (AttoCube).

3.3 Time-resolved Photoluminescence Spectroscopy

For a number of questions not only intensity and spectral position of a PL signal are of interest, but also it's evolution in time. Figure 3.5 includes a sketch of the setup for time-resolved measurements.

3.3.1 Beam Preparation

Many consecutive excitations of the sample system, each of which are short in time, can be achieved with the output of a mode-locked Titanium-sapphire (Ti:Sa) laser as the pulsed laser source. The laser outputs light of a wavelength between 750 nm and 980 nm with a temporal width of approximately 150 fs, as measured by auto-correlation, at a repetition rate of 75.4 MHz. To attain a wavelength suited for off-resonant excitation, a β-barium borate crystal generates the second harmonic (375...490 nm) with little temporal pulse broadening. If necessary, the repetition rate is reduced, by selectively deflecting only every n-th (n=20...5000) pulse emitted by the laser towards the main experiment by the use of an acousto-optic modulator (AOM). The so prepared laser beam can be used at the same sample bays and in the same excitation geometries like an argon ion laser, or other continuous wave (cw) excitation lasers, by simple exchange of kinematically mounted mirrors. As in time integrated experiments, the signal light is collected, bearing in mind the above considerations, and fed into a 0.5 m imaging spectrometer to attain spectral dispersion. When using a multichannel detection, like the streak camera system described below, the spectral information is preserved in the following temporal dispersion. When using a single diode as a detector, an output slit at the spectrometer is employed, yielding a single output wavelength at a time. The grating is then scanned slowly , while multiple time resolved traces are recorded. Both techniques allows for the acquisition of luminescence intensity maps with spectral and temporal dispersion, but differ in the temporal resolution and the accessible time range.

3.3.2 Temporal Dispersion

For medium temporal resolution, the light can be detected with a fast response avalanche photo diode (APD). With one electronic signal synchronized to the impinging excitation laser as a start event, and a second signal triggered by the detection of a luminescence photon as a stop event, a time of flight analysis can be carried out. A photon counting card correlates the counted photon arrivals events with their individual arrival times. This yields a representation of the number of counts versus the arrival time with 0.5

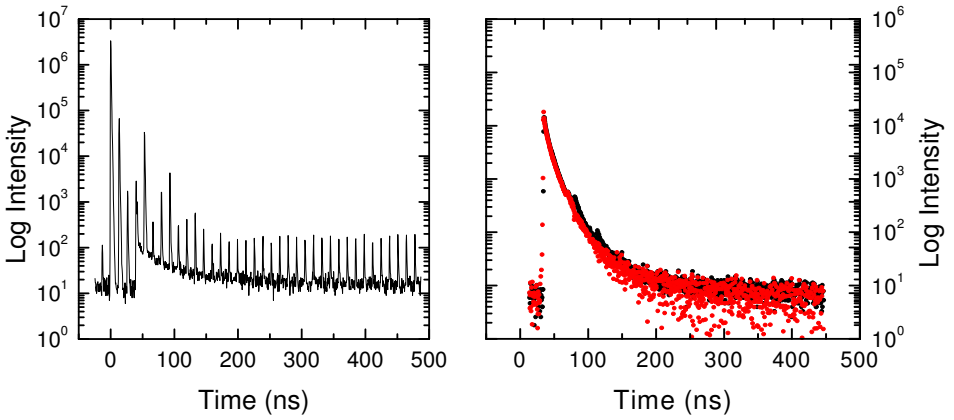

Figure 3.7: Left: A laser spectrum recorded with the TCSPC setup, used for deconvolution of recorded PL spectra. Right: Raw data (black) and deconvoluted data (gray) of a PL decay spectrum.

ns resolution. Due to the high detection efficiency this technique is referred to as "time correlated single photon counting" (TCSPC). Data acquired this way needs to be processed to account for the system response, which is influenced by a number of factors [99]. The actively quenched electronics of the APD produce a hold off time in which the detector is not sensitive to incoming photons. After this hold off time of 42 ns, which is necessary to prevent the electron avalanche from damaging the detector, the bias is applied again. The possibility of carriers still present in the active region of the APD produces a high probability of a counting event directly following the detector dead time [23]. This effect is referred to as the after pulsing effect [48]. In addition, the reduction of the repetition rate by selective beam deflection creates a finite contrast of about 1:250 between the selected and the suppressed pulses. A time-resolved spectrum of the attenuated laser pulse train is therefore recorded and treated as the combined system's response to a delta like excitation. When recording the actual luminescence decay data, this reference spectrum is taken as the response function in a numerical deconvolution algorithm, to attain corrected spectra. Figure 3.7 shows such a laser profile used for deconvolution and an exemplary PL decay curve as recorded, and after deconvolution.

A second detection scheme for time resolved measurements with higher resolution makes use of a streak camera (Hamamatsu model C5680). Here, the spectrally dispersed photons are converted into electrons, when hitting a horizontally aligned photo cathode. The photo cathode marks one end of an electron tube, through which the electrons are guided by magneto optics, to be imaged onto a phosphor coated multi channel plate at

the opposite end. When an alternating electric field is applied in vertical direction, the electrons arrive at different heights of the phosphorous screen at different times. A CCD camera monitoring the phosphorous screen therefore records spectral information along the x-axis and temporal information contained in the streaks along the y-axis with a resolution down to 2 ps per pixel. Geometrical path length differences reduce the theoretical temporal resolution, given by the time deflection in y direction and the pixel size. This results in a realistic resolution of 25 ps if no further measures are taken. Reducing the horizontal extension of the beam within the spectrometer by masking off the outer parts of the grating, results in a partial recovery of the temporal resolution on the expense of light gathering power. Since the laser has a temporal width of 150 fs, it can be considered to be delta-like for both used time resolving setups. The deformation into a 25 ps long pulse can be accounted for by convoluting theoretical data by a gauss-function of appropriate width.

3.3.3 Data Interpretation

The results of a decay time analysis can be used in a number of ways. The decay of the PL intensity with time is not only governed by the inverse of the radiative recombination rate k_{rad}, but is also strongly influenced by the presence of non-radiative depopulation channels k_{nrad} for the exited state under investigation, as described by equation 3.8.

$$\tau = \frac{1}{k_{\mathrm{rad}} + \sum k_{\mathrm{nrad}}} \tag{3.8}$$

The rates k_{nrad} can be non-radiative recombinations into the ground state, transitions to other states of the same excited species, including capture into trap states, or transitions to a proximal energy transfer acceptor. The summation of all depopulation processes involved in the depletion of an excited state, leads to a decay with a characteristic time constant τ. However, the overall behavior of the decay curve will still be mono-exponential:

$$I(t) = I_0 \cdot e^{-\frac{t}{\tau}} \tag{3.9}$$

Since the quantum yield of a sample is connected to the radiative and non-radiative recombination rates via:

$$\eta = \frac{k_{\mathrm{rad}}}{k_{\mathrm{rad}} + k_{\mathrm{nrad}}} \tag{3.10}$$

in the absence of inter-chromophore transfer, fluorescence lifetime measurements can be used to determine the rate of non-radiative recombination channels if the quantum yield is known. The quantum yield typically can be extracted from a comparative PL intensity measurement with a sample of known chromophore concentration and quantum yield, like Rhodamine 6G as a standard.

Even in more complex systems, that include transfer and refilling mechanisms and may therefore lack the mono-exponential behavior described by equation 3.9, the internal transitions can be modeled by rate equations. If we assume two levels denoted **1** and **2** above a ground state **0**, which are initially populated, then at a given temperature T, the according set of partial differential equations can be written as:

$$\dot{n_2} = -n_2 k_{2\to 0} - n_2(1 + N_{\Delta_{1,2}})k_{1\to 2} + n_1 k_{2\to 1} N_{\Delta_{1,2}} \tag{3.11}$$

$$\dot{n_1} = -n_1 k_{1\to 0} + n_2(1 + N_{\Delta_{1,2}})k_{1\to 2} - n_1 k_{2\to 1} N_{\Delta_{1,2}} \tag{3.12}$$

Here k denotes a radiative rate from the highest state **2** to the ground state **0**, or the lower state **1** to the ground state. The rate $k_{1\to 2} = k_{2\to 1}$ is the transition probability per unit time between the levels **1** and **2**. While these rates can be considered to be constant, the temperature dependence of the population dynamics of such a system is introduced by the phonon occupation number, given by the Bose function

$$N_{\Delta_{1,2}} = \frac{1}{e^{\frac{\Delta_{1,2}}{k_B T}} - 1} \tag{3.13}$$

with Boltzmann's constant k_B and the energetic spacing $\Delta_{1,2}$ between the levels **1** and **2**. The solutions for the dynamic variables $n_1(t)$ and $n_2(t)$ then translate into an measurable intensity.

$$I(t) \propto n_1(t)k_{1\to 0} + n_2(t)k_{2\to 0} \tag{3.14}$$

If the excitation is due to an ultra short laser pulse, and the relaxation to the states **1** and **2** is fast, the dynamics of the absorption can be neglected in the modeling, and equal populations of both states can be used as an initial condition. Escape processes, or temperature dependent non-radiative processes can be included in the modeling by additional terms. These terms are omitted here, since colloidal NCs lack the barrier that surrounds epitaxially grown quantum dots, and non-radiative processes can be approximated to be constant, when the experiments are carried out at temperatures below 100 K.

A set of temperature dependent transients of the PL intensity, fitted to the solutions of a differential equation system like the one above, can therefore give access to the transition rates and energetic level spacing within the system. Knowledge of the recombination dynamics and the corresponding decay curves allows an identification of emitters with higher confidence than the observation of PL intensity within the corresponding spectral window, alone. The temporal evolution of the PL is therefore used as an investigative tool whenever the emitted intensity allows for such an experiment.

FRET in biological samples, like the ones dealt with in chapter 7, is typically examined at room temperature, which rules out the phonon occupation number as a tuning

parameter. A sample set will therefore comprise a variety of inter-chromophore distances in order to change the transfer rates among the samples of a set. The transfer channel can serve as an additional channel of population or depopulation, depending on whether the chromophore under investigation is a donor or acceptor in the system. Especially in more complex multi-FRET systems, the decay curves can deviate from mono-exponential behavior. If the rates and lifetimes involved are within a suited range, a rise of PL intensity after the arrival of the exciting laser pulse can be observed, which can serve as a prominent fingerprint of strong energy transfer towards the examined chromophore.

3.4 Structural Characterization Methods

For a better understanding of the information obtained from optical measurements, a comparison with structural properties like size, composition, and ordering is of great value. The techniques employed to gather these additional parameters are therefore described in the following.

3.4.1 Reflection High Energy Electron Diffraction RHEED

The standard method for in situ growth monitoring in MBE is the diffraction of electrons of high kinetic energy off the surface of the growing structure. Here an electron beam of some ten keV is incident on the sample at a grazing angle of less than one degree. The diffracted electrons produce electro luminescence on a phosphorous screen on the opposite side of the sample, which is monitored with a CCD camera.

Starting with a substrate with a nearly atomically smooth surface, the intensity of the 0-th diffraction order, the specular spot, is high. The deposition of additional material roughens the surface which can be observed by a reduction of the intensity of the specular spot. After crossing a minimum in intensity, when the coverage of the surface with newly deposited islands is close to one half, the intensity rises again until the next maximum is reached upon the completion of a full layer. Keeping track of these RHEED oscillations enables an accurate growth rate monitoring.

In addition to the determination of the amount of deposited material, RHEED enables a characterization of the surface morphology. Due to the energy, and the grazing angle of the incident electrons, only the first few layers of the material contribute to the formation of the diffraction pattern. Therefore a perfectly smooth, two-dimensional surface lacks the diffraction conditions in the dimension perpendicular to the sample surface. The

reciprocal lattice of such a structure can be considered as a number of lines in contrast to points in the reciprocal lattice of a three dimensional real space lattice. In realistic experimental conditions the aforementioned lines actually have to be considered to be of finite thickness. Similarly, the shell of the Ewald sphere is not infinitely thin. As a consequence, the intersection of both is not a single point in reciprocal space, but a volume of elongated shape.

Since a RHEED pattern basically resembles an image of the reciprocal space, a line pattern can therefore be interpreted as stemming from a flat surface, while the transition to a point like pattern marks the admixture of three dimensional features on the sample surface. This interpretation of RHEED measurements will be used in the evaluation of hybrid colloidal-epitaxial samples in chapter 6.

3.4.2 High Resolution X-ray Diffraction HRXRD

Reciprocal space maps, ω - 2θ scans, and "rocking curves" were acquired for the samples manufactured by MBE, in order to evaluate their structural properties. These tools allow the evaluation of the layer thickness, lattice mismatch, layer tilt or misorientation, and the dislocation content. This is enabled by probing the angular distribution of the intensity of x-rays, Bragg-reflected by the sample.

For the acquisition of rocking curves, the probing wavelength is λ=0.15 nm, detected around the direction of the (004) reflex, that is, the detector is fixed to $2\times\theta_{Bragg}$ while the sample is rocked. The deviations from a perfect crystal due to dislocations cause a broadening of the reflex peaked at the sample angle ω, to a FWHM of $\Delta\omega$. This value can be linked to the square root of the density of dislocations.

Rotating the detector about the sample additionally with twice the angle of the sample rotation, is used for the recording of an ω - 2θ scan. The layer thicknesses present in the sample can be inferred from the periodicity of the detected scattered intensity.
Displaying the recorded scattered x-ray intensity in two dimensions of the reciprocal space shows peaks at positions characteristic for the used materials and allows an evaluation of strain and relative tilt between the layers.

These measurements were carried out by C. Arens under supervision of Prof. D. Schikora and Prof. K. Lischka at the university of Paderborn, department of physics.

3.4.3 Electron Microscopy

Structural analysis on an atomic scale was of special interest in the attempt to incorporate colloidal nanocrystals in an epitaxial matrix, since here the identification of embedded nanoparticles in the host material of different lattice parameter as well as dislocations, stacking faults, and interfaces are of importance. Following the spectroscopic investigation and imaging with a scanning electron microscope (SEM), the samples were thinned and investigated in a high resolution transmission electron microscopy (HRTEM) setup.

These experiments have been carried out at the university of Karlsruhe by D. Litvinov at the laboratory for electron beam microscopy under the direction of Prof. D. Gerthsen.

4. CdSe Nanocrystals

From the large variety of semiconductor nanocrystals, those representing the main focus of this work exhibit an excitonic emission wavelength in the visible range of the spectrum. This is the case for a number of material systems, out of which here cadmium selenide was chosen.

While general studies on the luminescence properties of mainly spherical nanodots have been carried out since a long time, this chapter focuses on the particularity of elongated nanocrystals - the nanorods. The excitonic fine structure that depends crucially on not only the size, but also the shape is investigated. Since the underlying formalism for the understanding of the nanorods' properties is an extension of the methods developed for the description of spherical nanocrystals, a brief introduction into theory and experiment on those nanocrystals will be given as well, following earlier work of the author and published literature.

4.1 Sample Preparation: Rods and Dots

General Mechanism

The underlying mechanisms for the formation of nanorods or nanodots can be explained in the light of growth kinetics [88], moderated by suited surfactants. After injection of cadmium and selenium precursors into a surfactant solution, nucleation of the NCs occurs within one second. The simultaneous cooling of the mixture due to the injection of the precursor solutions stops the nucleation process. Subsequently the growth period sets in, during which surfactant molecules ad- and desorb onto the NC seedlings. Coordinating solvents moderate the growth kinetics and prevent an agglomeration or fusion of multiple NC seedlings during the growth process.

When the precursor monomer concentration is high, smaller nanoparticles grow faster, their size therefore catching up with the larger ones. When the growth process is stopped,

by cooling the reaction vessel, before the monomer concentration has dropped below a critical value, a narrow size distribution can be achieved. Leaving the reaction running will lead to a stage at which the smaller NCs are dissolved in favor of the larger ones. This "Oswald ripening" stage of the growth leads to a broadening of the size distribution [90].

Controlling the precursor concentration as well as the reaction temperature, and thereby the growth kinetics furthermore allows for a control of the shape of the resulting NC [88]. This is due to the anisotropy of the CdSe wurtzite crystal lattice, which favors growth along the c-axis of the system. The crystallographic (001) and (00-1) planes, which are perpendicular to the c-axis, correspond to the top and bottom of an idealized, perfect NC. They consist of one atomic species only, while the surface atoms of the side walls comprise a mixture of cadmium and selenium atoms.

At a slow growth rate in a coordinating solvent like trioctylphosphine-oxide (TOPO, $[CH_3(CH_2)_7]_3PO$), the decisive parameter for the emerging shape is the surface area. In this case a spherical shape of the NC is favored because of its minimized surface energy.

Kinetically overdriving the system by increasing the monomer concentration leads to a strongly enhanced growth along the c-axis, resulting in elongated NCs. Since the high growth rate also enhances the increase of the waist size, that is, the dimension perpendicular to the c-axis, the NC would increase in size up to a point where no quantum confinement is present anymore, if no further measures were taken.

An effective shielding of the crystallographic planes other than (00-1) can be achieved by the addition of a surfactant that binds to the metal ions stronger than TOPO alone, which is tetradecylphosphonic acid (TDPA, $C_{14}H_{31}O_3P$) in this case. Its affinity to the metal ion dresses the nanocrystal site-selectively. The selenium terminated facet is almost free of surfactant molecules, which allows for an efficient deposition of cadmium [53]. The consequential charge reversal now leaves the facet with one unsaturated valences of the cadmium, which can be shielded by the surfactants. The mixed surfaces of the other crystallographic planes are shielded effectively as well, which halts the growth of the NC waist diameter. The three dangling bonds of the cadmium present on the (001) facet can however not be passivated completely by the TDPA. Therefore the growth is unidirectional, along the c-axis, resulting in a NC with high aspect ratio - the nanorod.

Obviously the delicate balance between the growth rates at different crystallographic planes that has to be maintained for an efficient growth of high quality NCs, allows only for small deviations from the ideal values for precursor and surfactant concentration, reaction temperature, and reaction time. The CdSe nanocrystals investigated in this section were synthesized by Dr. Mikhail Artemyev.

Dots

For the growth of CdSe/ZnS core-shell nanodots, the following synthesis protocol, similar to that published in reference [81], was used:

Into a solvent mixture consisting of TOPO and hexadecylamin (HDA, $N(C_{16}H_{33})H_2$) kept at 340°C, solutions of the cadmium and selenide precursors were added. These consisted of dimethylcadmium ($(CH_3)_2Cd$) and selenium powder dissolved in trioctylphosphine (TOP). At this temperature the dimethylcadmium decomposes, releasing the elemental cadmium, which reacts with elemental selenium to form cadmium selenide crystallites. The surface of these nanocrystallites binds to the oxygen atom of TOPO, thereby creating the stabilizing ligand shell. The concentration of the precursors, the temperature at which the synthesis is carried out, and the overall reaction time govern the resulting NC size.

For the subsequent shell growth, the NCs are again brought into a solvent mixture of HDA and TOPO at 220°C, and precursors of zinc and sulfur are injected (diethylzinc, $(C_2H_5)_2Zn$ and hexamethyldisilathian, $C_6H_{18}SSi_2$). The CdSe core now acts as a seedling for the growth of a ZnS shell. The TOPO ligands attach to the zinc contained in the shell, which is typically 1 to 2 monolayers in thickness.

Rods

The CdSe nanorods were synthesized, following the protocols published by Mokari and coworkers [80]. In a first step CdSe nanorods were grown and in a second step covered with a ZnS shell at moderate temperatures in the presence of trioctylphosphine-oxide and hexadecylamine as coordinating solvents.

A TOPO-TDPA mixture at 360 °C, stirred and kept under argon atmosphere was used as the surfactant solution for the rod core growth. After the cadmium and selenium precursor injection, the mixture cools to 290 °C. In the following minutes more precursors were added drop wise.

For the ZnS capping, the rod suspension was mixed with HDA, heated to 190°C and the shell precursor solution was introduced drop wise.

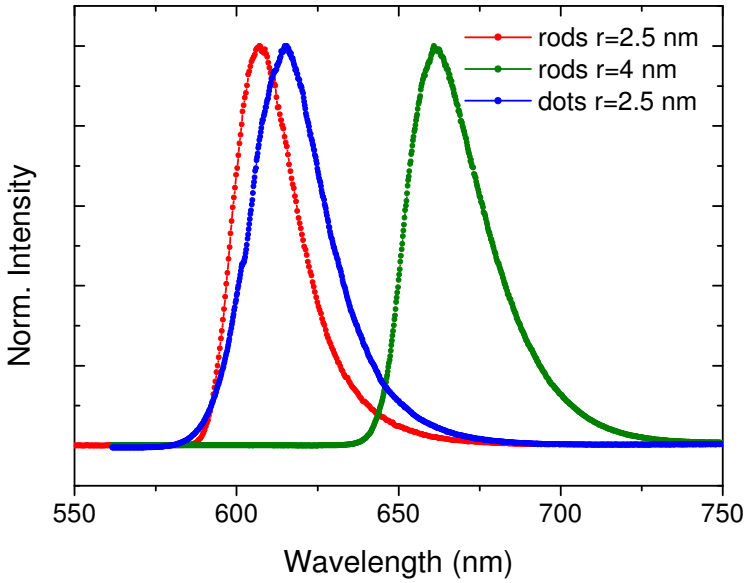

Figure 4.1: PL of ensembles of CdSe nanorods of two different sizes, and nanodots, recorded at room temperature.

Post Synthesis Processing

From all synthesis batches, aliquots were extracted at different stages of the synthesis, yielding nanocrystal suspensions of different average size. After cooling of the reaction vessel, the nanocrystals are suspended in toluene. Addition of methanol, in which the NCs are less soluble, leads to a size selective precipitation of the NC. Separation of the precipitate by centrifugation and subsequent resuspension in toluene leads to a reduction of the size distribution of one sample. Several repetitions of this purification method lead to a size distribution well below 10 %.

The nanocrystal suspensions were investigated by absorption and luminescence spectroscopy to determine the absorption and emission peak positions. While these can be used for the determination of the average size, additional TEM analysis were carried out to confirm the values. The samples measured on here are "small nanorods" with a waist radius r $\approx$ 2.5 nm, and an average length of L $\approx$ 25 nm, and a room temperature PL centered at 607 nm with an inhomogeneous broadening of FWHM= 23 nm and "big nanorods" with a waist radius r $\approx$ 4 nm, and an average length of L $\approx$ 35 nm, whose room temperature PL is centered at 661 nm with an inhomogeneous broadening of FWHM= 29 nm. For comparison, the results of earlier measurements on CdSe dots of 2.5 nm radius emitting at 615 nm with a FWHM of 27 nm are quoted here as well.

For spectroscopic studies at cryogenic temperatures, a diluted suspension of the nanocrystals in trichlorethylene or toluene is mixed with a polymer (polymethylmethacrylate, PMMA) and deposited on a quartz substrate to produce a sample for ensemble measurements. Figure 4.1 shows the normalized luminescence obtained from such samples. Dilution of the stock solution enables a deposition of well spaced NCs for experiments on a single NC level.

4.2 Shape Dependence of the Excitonic Fine Structure

A derivation of the excitonic fine structure in spherical nanocrystals was already given in chapter 1.2.1. The main features are the lifting of the degeneracy of the excitonic spin states due to the wurtzite crystal field and the further splitting of the lowermost group by exchange interaction. Figure 4.2 plots the energy levels for spherical CdSe nanodots as a function of particle radius, following calculations published by Efros and coworkers [29]. The calculated energies of the $s_e S_{1/2}$ and $s_e S_{3/2}$ states are plotted versus the nanodot radius, and relative to the $s_e S_{1/2}$ state with no exchange interaction. The most important result is the nature of the ground state. For all sizes, the lowest excitonic state has a spin quantum number of ± 2, and is therefore a dark state [29][85].

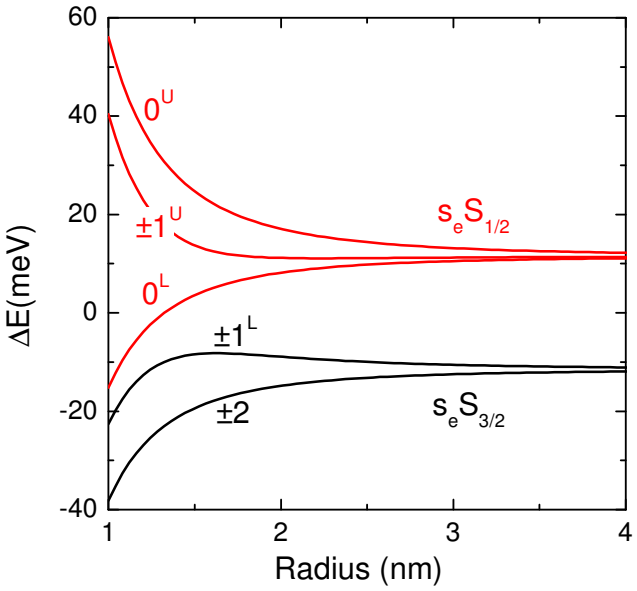

Figure 4.2: Size dependence of the excitonic level fine structure in CdSe dots.

The energy-level scheme describing the excitonic fine structures of elongated nanoparticles can be calculated by taking into account the quasi one-dimensional nature of the structure, following a formalism developed by Sercel and coworkers [106]. The energetic

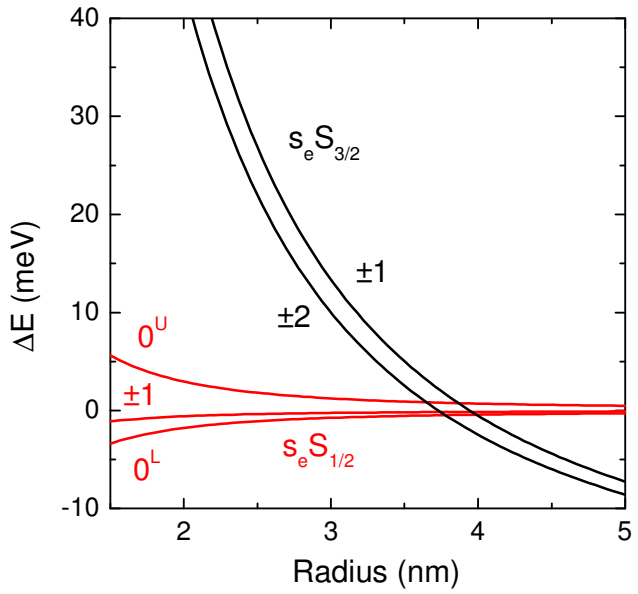

Figure 4.3: Size dependence of the excitonic level fine structure in CdSe rods.

degeneracy of the hole states $S_{1/2}$ and $S_{3/2}$ is lifted by the cylindrical quantum confinement in two dimensions. In addition, the wurtzite structure, which in bulk contributes a crystal field splitting of these states of 25 meV, is taken into account as a perturbation of the Luttinger Hamiltonian [72]. The electron-hole pair energy is obtained by a variational calculation following [45]. After deriving the one-dimensional exciton parameters, the electron-hole exchange interaction is calculated following the theory of invariants as described in [29].

The result is a splitting of the states of light hole type or $s_e S_{1/2}$, which are otherwise fourfold degenerate. The modified term scheme consists of three energetically separated levels. The combinations of opposite orientation of the electron and hole spin sum up to a total angular momentum projection along the rod axis of zero, and construct the states denoted upper and lower state (0^{U} and 0^{L}). Their energetic spacing increases with decreasing nanocrystal size up to approximately 12 meV at a radius of 1.5 nm. The combinations of equal spin orientation form two states, whose projection of the total angular momentum along the rod axis is +1 and -1. Their energies are equal and located between the 0^{U} and 0^{L} states.

The heavy hole type states, comprising the electron spin 1/2 and the hole spin 3/2 are split into two doubly degenerate states, referred to as the ± 1 and the ± 2 states. Again, like in the case of spherical symmetry, the ± 2 state is not optically active and referred to as the dark state in this system.

Figure 4.3 shows the dependence of the level spacing and ordering as a function of the radius of the rod. The striking feature is the crossing of the light and heavy hole type states at a critical radius r_{crit}, which in this system is at approximately 3.7 nm. The level crossing has an important effect on the recombination dynamics, since for radii above the critical, the lowermost state is the ± 2 state, which is of low optical activity. In contrast, the lowest state for nanorods below the critical radius is the 0^{L} state, which has a vanishing oscillator strength [68]. However, the close proximity of the other light hole type states 0^{U} and ± 1, allows for a thermal population of these states, out of which radiative recombinations are allowed, even at moderate cryogenic temperatures.

4.3 Temperature Dependent Time-resolved Luminescence

In order to compare the results of the above calculations to the real nanocrystals, temperature dependent, time-resolved photoluminescence studies were carried out on all samples with the instrumentation described in section 3.3. Varying the temperature changes the population ratio between the dark and bright exciton levels, which effects the observable luminescence dynamics.

A far off-resonant, that is, high above the band gap excitation was chosen, to allow for a relaxation of the excited carriers down to the levels out of which radiative recombination occurs.

The luminescence was recorded temporally and spectrally resolved to be able to narrow the size of the inhomogeneously broadened ensemble by performing spectrally narrow cuts on the recorded emission maps.

In order to assure a probing of the excitonic population, rather than recombinations influenced by multi exciton complexes, the dependence of the PL intensity on the excitation power was monitored over a wider range. A regime in which the dependence was found to be linear was chosen for the experiments, which typically translates to intensities below 1 mWcm^{-2}.

Since the spectral distribution of the luminescence resembles the size distribution as well as the distribution among different states in a single NC, the spectral cuts were performed on the low energy side of the recorded spectrum. This should assure, that the lowest excitonic transition in the largest NCs within the ensemble is probed, rather than a mixture of luminescence stemming from the ground state of small, and higher excited states of large NCs.

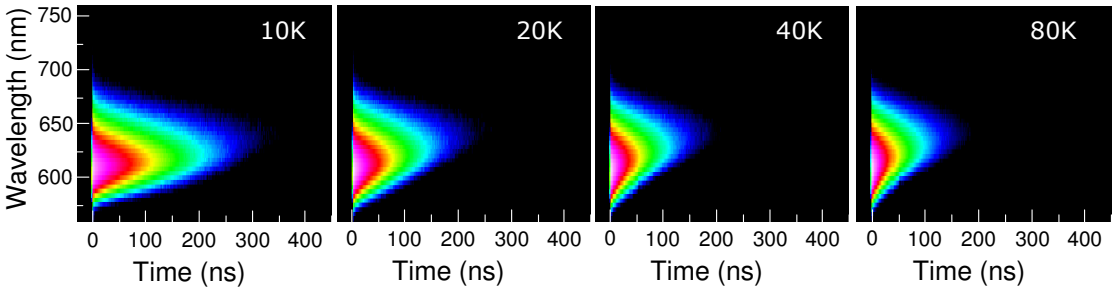

Figure 4.4: Spectrally and temporally resolved PL of CdSe nanorods at various temperatures. The logarithmic color scale spans the first three orders of magnitude of luminescence intensity. The temperature induced filling of the higher bright state results in the accelerated PL decay at elevated temperatures.

4.3.1 CdSe Dots

Figure 4.4 shows the spectrally and temporally dispersed luminescence of CdSe nanodots at different temperatures. PL traces extracted at 624 nm (1.98 eV) with a resolution of 4 nm (13 meV), which corresponds to the low energy sided of the ensemble, as mentioned above are shown in figure 4.5. At the lowest temperatures, a fast initial PL decay is followed by a slower mono-exponential decrease in intensity. At higher temperatures, the two parts of the decay curve merge. The underlying dynamic behavior of the exciton population is modeled in the following way:

When the excitation process and subsequent relaxation is fast, compared to the dynamic processes that are to be modeled, the excitation dynamics as can be understood as a fast absorption of the exciting photons in states high above the band gap, followed by a fast relaxation into the lowest excitonic states. Non-radiative losses can be treated as an overall reduction of the available excitations. The starting point of the modeling is therefore a situation of equal population of the two levels under the consideration as the initial condition. The coupled differential equation system 4.1a, 4.1b then describes the situation in which, during the time interval ∂t, the number of excitons in the bright state n_b is reduced due to radiative recombination to the ground state ($n_b \cdot k_{b,rad}$) and transitions to the dark state ($n_b \cdot k_{bd}(N_{\Delta E}+1)$), while thermally activated transitions from the dark state ($n_d \cdot k_{db} N_{\Delta E}$) increase the population. In a complementary way, the population of the dark state n_d is reduced by the less frequent radiative transition to the ground state ($n_d \cdot k_{d,rad}$), and thermally activated transitions to the above lying bright state, while the

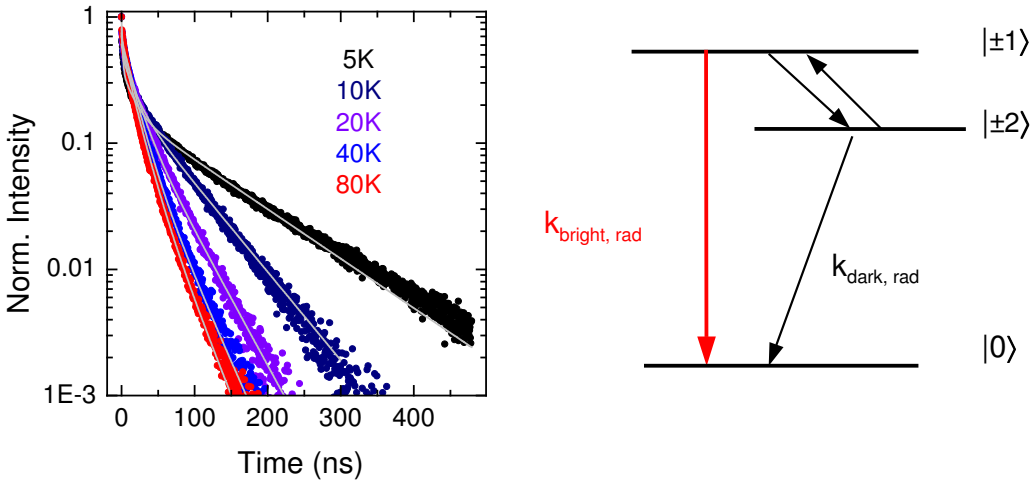

Figure 4.5: TRPL of CdSe nanodots at various temperatures. The luminescence decay traces obtained from spectral cuts of the 2d-data displayed in figure 4.4 are shown together with the fitted curves. The acceleration of the PL decay can be explained with temperature activated filling of a bright $|\pm 1\rangle$ state from a dark $|\pm 2\rangle$ state, as sketched on the right side.

transitions from the bright state fill the exciton reservoir of the dark state.

$$\frac{\partial n_b}{\partial t} = -n_b \cdot k_{b,rad} - n_b \cdot k_{bd}(N_{\Delta E} + 1) + n_d \cdot k_{db} N_{\Delta E} \tag{4.1a}$$

$$\frac{\partial n_d}{\partial t} = -n_d \cdot k_{d,rad} + n_b \cdot k_{db}(N_{\Delta E} + 1) - n_d \cdot k_{db} N_{\Delta E} \tag{4.1b}$$

The thermally activated transition is governed by the number of phonons N, with energies that allow them to bridge the energy gap ΔE between dark and bright state:

$$N_{\Delta E} = \frac{1}{e^{\frac{\Delta E}{k_B T}} - 1} \tag{4.2}$$

Under the assumption that the transitions between dark and bright state are symmetric ($k_{bd} = k_{db}$), and their respective radiative recombination rates $k_{b,rad}$ and $k_{d,rad}$ are constant, the set of differential equations can be solved analytically, yielding expressions for the occupation numbers $n_b(t)$ and $n_d(t)$. The PL intensity measured in an experiment, that records emission from both states simultaneously is then proportional to the occupation numbers multiplied with the respective radiative recombination rates, as given by:

$$I(t) \propto n_b(t) \cdot k_{b,rad} + n_d(t) \cdot k_{d,rad} \tag{4.3}$$

The results of a least square fitting routine for the temperature dependent data and the model explained above showed poor numeric agreement. A consistent fit was achieved by the inclusion of an additional thermally activated decay channel with a recombination rate equal to that of the bright state, according to:

$$I(t) \propto (n_b(t) \cdot k_{b,rad} + n_d(t) \cdot k_{d,rad}) \cdot (1 - P_T) + P_T \cdot \exp(-k_{b,rad} \cdot t) \tag{4.4}$$

With this model and the following fit parameters, the curves shown in figure 4.5 were obtained:

$$k_{db} = 0.7 \text{ ns}^{-1} \qquad k_{b,rad} = 0.065 \text{ ns}^{-1} \qquad k_{d,rad} = 0.007 \text{ ns}^{-1} \qquad \Delta E = 1.4 \text{ meV},$$

with the temperature dependent weighting factor P_T for the admixture of the additional mono-exponential decay channel

$T(K)$	5	10	20	40	80
P_T	0.192	0.354	0.507	0.68	0.75

For the interpretation of the parameter P_T, two possibilities are discussed: A capture of carriers in trap states would deplete the system and act as a reservoir that feeds the recombination, when the temperature is high enough to reactivate the carriers out of the trap states. Another decay channel that is known to display a recombination rate similar to that of the exciton, but does not undergo a dark-bright state splitting, is that of the charged exciton or trion [86]. While the exact nature of the admixed mono-exponential decay channel is still unclear, the dark-bright dynamics found are consistent with literature [85]. The agreement between the dynamic model and the recorded luminescence decay data is evidenced in figure 4.5

4.3.2 CdSe Rods

In contrast to spherical nanocrystals, nanorods exhibit not only a size dependent emission wavelength, but additionally a size dependent ground state symmetry, as was shown in the above calculations. The impact on the recombination dynamics can be seen in the spectrally and temporally resolved PL intensity plots shown in figure 4.6.

Spectral cuts of these plots, again performed on the lower energy side to exclude contributions from higher excited states are shown in figure 4.7. In order to describe the

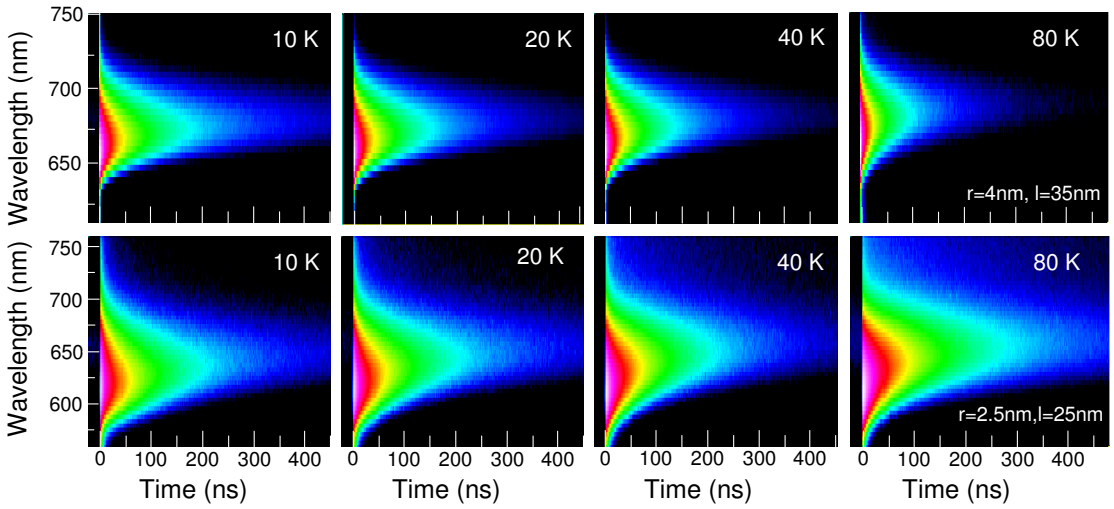

Figure 4.6: Spectrally and temporally resolved PL of CdSe nanorods at various temperatures. The logarithmic color scale spans the first three orders of magnitude of luminescence intensity. The top row shows the behavior of the larger nanorods, whose emission decay speeds up with growing temperature. Small nanorods exhibit the contrary behavior, namely a decelerated PL decay, as depicted on the lower line.

observed PL decay traces, mono-, bi- and stretched exponential functions were tested. A good fit to the data was achieved only by the use of a two component stretched exponential function of the form:

$$I_{PL}(t) \propto A_1 \cdot \exp\left[-\left(\frac{t}{\tau_1}\right)^{\beta_1}\right] + A_2 \cdot \exp\left[-\left(\frac{t}{\tau_2}\right)^{\beta_2}\right] \tag{4.5}$$

The presence of a slow component can be explained by slowly recombining dark and trap states within the nanorods. Since the shape of a nanorod in reality deviates from a perfect cylindrical form, one can assume the rod to exhibit a distribution of confining waist diameters. This can explain why for both components of the decay describing functions, stretched exponentials need to be employed, since they resemble a decay according to a distribution of mono-exponential decay functions. A parameter suited for comparison of the decays is the therefore the average decay time $\langle\tau\rangle$ calculated according to equation 4.6 with Γ denoting the gamma function [70].

$$\langle\tau\rangle = \frac{\tau}{\beta} \cdot \Gamma\left(\frac{1}{\beta}\right) \tag{4.6}$$

Table 4.1 lists the values found to produce a good fit to the obtained data and the resulting average decay times. The contrary behavior of small and large nanorods is

Radius	T (K)	A_1	τ_1 (ns)	β_1	$\langle\tau_1\rangle$ (ns)	A_2	τ_2 (ns)	β_2	$\langle\tau_2\rangle$ (ns)
4 nm	10	0.87	6.1	0.65	6.05	0.013	70.6	0.7	89.4
	40	0.88	1.75	0.43	4.82	0.012	36.9	0.58	58.1
	80	0.86	0.94	0.5	1.88	0.014	21.3	0.67	28.2
2.5 nm	5	0.886	1.3	0.486	2.74	0.114	38.1	0.63	54.0
	40	0.834	1.49	0.413	4.54	0.166	45.5	0.649	62.3
	80	0.86	6.45	0.474	14.3	0.14	70	0.7	88.6

Table 4.1: PL decay fit parameters of CdSe nanorods. The increase (decrease) in PL decay time in big (small) rods with rising temperature, as evidenced by the averge decay time $\langle\tau_1\rangle$.

evidenced in the decay time dependence on temperature.

The PL of nanorods above the critical radius is slow at low temperatures due to the dark state nature of the lowest excitonic state. With increasing temperature, the above lying allowed states become populated, and the optical transition probability therefore rises. This behavior is similar to the situation in spherical nanocrystals as shown before.

Rod shaped nanocrystals with a radius below the critical value of 3.7 nm do not display the acceleration of the PL decay with rising temperature. In contrast, a deceleration of the PL decay is found in these nanorods. A mechanism that is complementary to the dark-bright dynamics observed in spherical nanodots and larger nanorods would rely on a thermally activated population of higher lying dark states. Their slow recombination would explain a combined PL decay that slows down with rising temperature. However, the splitting of the ± 2 states with respect to the $s_e S_{1/2}$ manifold is large (tens of meV) compared to the thermal energy in these nanorods. This is why an alternative explanation proposed by Citrin and coworkers, that is focusing on the temperature dependence of the radiative decay itself, seems more likely [19].

In the model proposed, the occupation of the lowest excitonic levels as a function of temperature is taken into account. It is assumed, that free excitons in a one-dimensional structure like the nanorods under investigation, have a k-vector along the long axis of the rod k_z. However, neglecting other processes, only those with $k_z < \kappa$, with κ the photon momentum, can recombine radiatively. Therefore a thermalization among the free excitons leads to a higher occupation of states that can not contribute to efficient radiative recombination, thereby prolonging the effective PL decay constant. Averaging over the participating states' oscillator strengths and their respective occupancy at a given thermal energy of the system, results in a dependence of the decay time on the square root of the temperature. This effect is visible only, when the bright state dynamic is directly

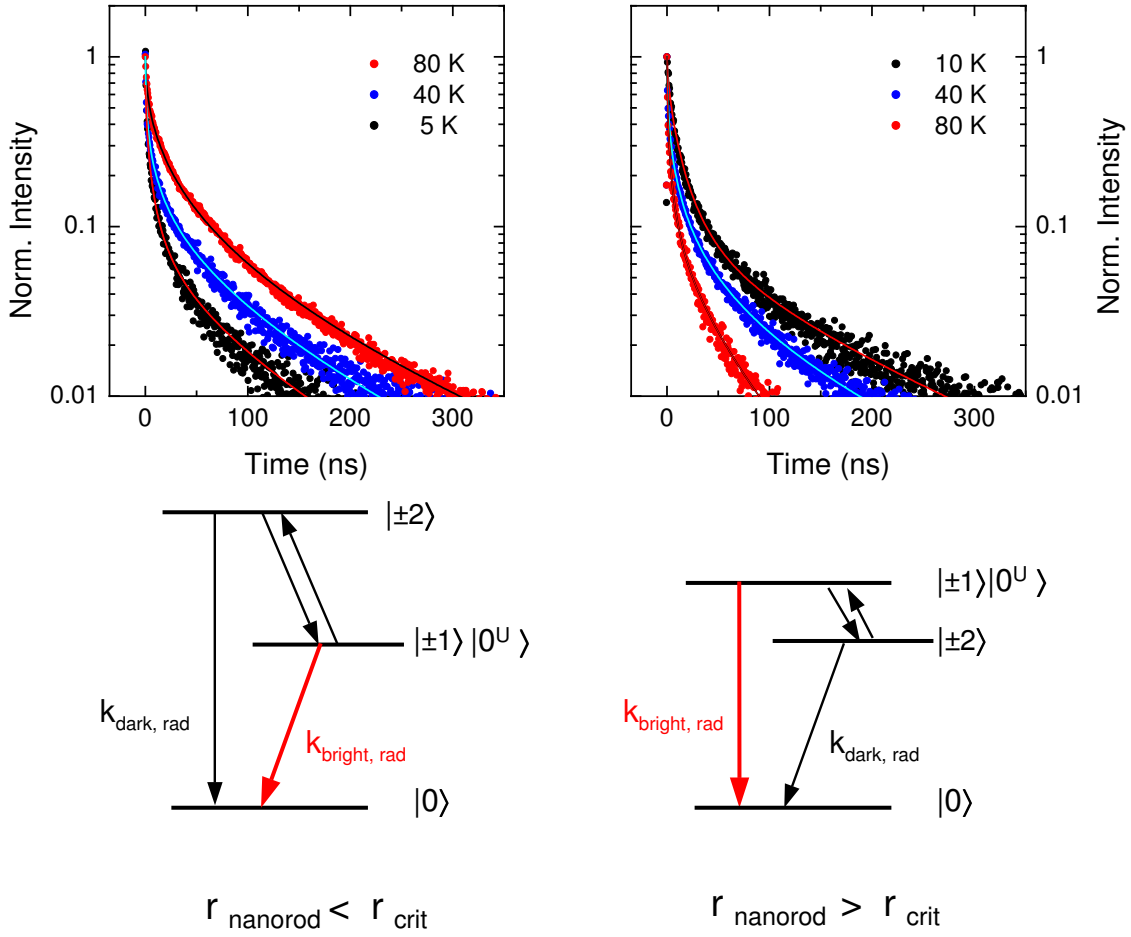

Figure 4.7: The decay of the PL as a function of nanorod size measured at different exemplary temperatures. Solid lines represent the fits according to the parameters listed in table 4.1. The case of nanorods with a waist diameter smaller than the critical radius r_{crit} is displayed on the left. An increase in temperature leads to a deceleration of the PL decay (left). When the nanorod size exceeds the critical radius, the lowermost state is a dark state, resulting in a slow recombination at low temperatures (right). Raising the temperature populates the bright state and leads to an accelerated PL decay.

accessible as it is the case for nanorods with $r < r_{crit}$. For bigger nanorods this effect might be overcompensated by the dynamics between dark and bright excitonic levels.

In the case at hand, fitting the average decay constant $\langle\tau\rangle$ of the faster of the two components describing the PL decay for five different temperatures yields a relation of $\tau(T) = 1.15\sqrt{T}$ ns, as depicted in figure 4.8.

The results obtained from the temperature-dependent, time-resolved photoluminescence experiments on CdSe nanocrystals can be summarized as follows: The fine structure

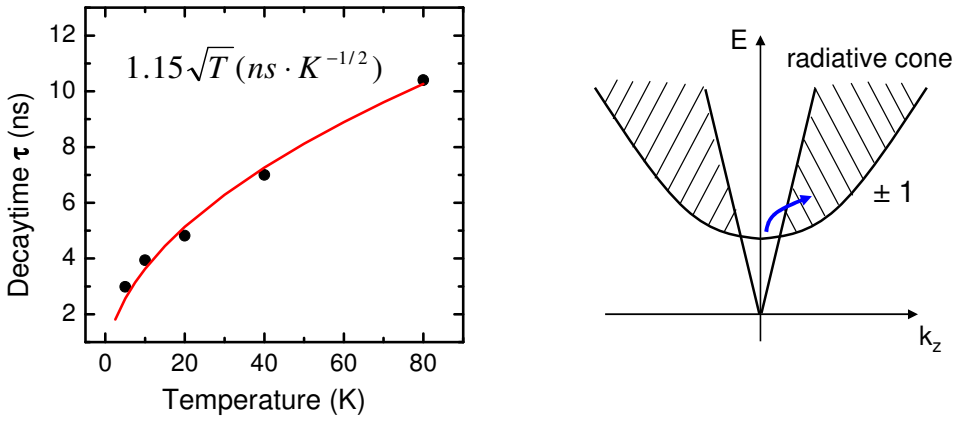

Figure 4.8: Temperature dependence of the fast component of the PL decay of nanorods with a waist size $r < r_{crit}$. The increase in the fast lifetime component of the PL decay is proportional to the square root of the sample temperature. The underlying mechanism is an increased scattering of excitons that leads to a population of states involving k_z vectors outside of the radiative cone. These excitons can not recombine radiatively under k-conservation. The thermal distribution among the states with different k vectors leads to a prolonged lifetime.

of the exciton levels of lowest energy is determined by exchange interaction and the crystallite shape. In the case of spherical nanodots, the dynamics are governed by temperature mediated population changes between dark and bright states. An acceleration of the PL decay is found in spherical nanodots and elongated nanorods above a critical radius of 3.7 nm, since in both the lowest state is a dark state. Nanorods with smaller radius possess a bright ground state, whose radiative recombination parameters are directly accessible in PL experiments.

4.4 Nanocrystals in Cavities - Towards Strong Coupling

The previous sections have shown, that the optical properties of CdSe NC are strongly influenced by size, shape and surface capping properties, which allows for a tailoring of the transition dipole moment.

However, the above considerations resemble a classical approach towards the optical properties of isolated emitters, that is, a photon is emitted with a probability given by the transition dipole moment, into vacuum. If the emitting nanocrystal is coupled to a resonator, the system undergoes modifications that are classified by the strength of the emitter-cavity coupling. In the *weak coupling regime*, the spontaneous emission rate is enhanced by the presence of a resonator mode, as described by the *Purcell factor* [117]. It

is given by the ratio of the emission rate in the presence of a cavity mode and the emission rate into vacuum

$$F_{Purcell} = \frac{\gamma_{Resonator}}{\gamma_{Vacuum}} = \frac{3Q\lambda^3_{Resonator}}{4\pi^2 n^3 V_C} \tag{4.7}$$

Here Q denotes the quality factor of the cavity, given by the ratio of the resonance frequency and the width of the resonance $Q = \frac{\omega_C}{\Delta\omega_C}$, $\lambda_{Resonator}$ is the wavelength corresponding to this resonance, n is the refractive index and V_C is the mode volume.

When experimental conditions are suited, the confinement of the light field enables a reabsorption of the emitted photon leading to a *strong coupling* of the emitter-photon system. This can be interpreted in the picture of exchange of energy between the resonator modes and the population in a two level system. If the rate of exchange is higher than the loss rates of cavity photons and two-level excitations, the strong coupling condition can be fulfilled. The cavity photon has to be able to complete a sufficient number of round trips through the cavity, in order to couple to the two-level system again. The now reversible emission-absorption cycle performed by the excitation then corresponds to a coherent state of the coupled system, described by the non-classical cavity quantum electrodynamics (cavity QED). The fingerprint of the strong coupling regime is the observation of the vacuum *Rabi splitting*, explained in the following.

Cavity quantum electrodynamic systems are of interest since they enable fundamental studies of coherent interactions of confined electromagnetic fields - the cavity photons - and microscopic dipoles - the single nanoemitters [94, 41]. The first cavity QED experiments such as the measurements of the vacuum Rabi splitting [114, 11] stimulated an intensive search for atom-photon entanglement in cavity QED systems of atomic physics. Coherent interactions of atom-photon quantum systems are proposed to realize a variety of quantum protocols [87, 18, 28, 73] in quantum information science. The vacuum Rabi splitting, which was originally observed with atom beams only, has been measured with epitaxially grown InGaAs quantum dots in micropillars [97], photonic crystals [133], and with localized GaAs excitons in microdisks [93].

Chemically synthesized colloidal nanocrystals, are another promising class of photon emitting two-level systems that possess a large optical transition dipole moment, compared with atoms, and can be incorporated in polymer, glass, or semiconductor microcavities. This should allow for an optimization of the coupling strength g, which scales like

$$g \propto \mathbf{d} \cdot \mathbf{E} \tag{4.8}$$

since with nanorods of an appropriate size, the dipole element $\mathbf{d}$ can be optimized, and the emitter placed at a position in the cavity with the highest possible field strength $\mathbf{E}$.

In the following, such a strongly coupled cavity QED system, realized by coupling a CdSe nanocrystal to a single photon mode of a polymer microsphere is introduced [69].

4.4.1 Theoretical Background

A theoretic model describing the situation of a two-level system coupled to a single resonator mode was introduced by E. Jaynes and F. Cummings in 1963 [51]. Here, both, the cavity modes as well as the light field are treated quantum mechanically. The Hamiltonian consists of a part for the light field (LF), given by

$$H_{\mathrm{LF}} = \frac{1}{2}\int(\varepsilon_0\mathbf{E}^2 + \mu_0\mathbf{H}^2)d^3r = \sum_m \hbar\omega_m(a_m^\dagger a_m + \frac{1}{2}) \tag{4.9}$$

with the field operators $\mathbf{E}$ and $\mathbf{H}$, the creation and annihilation operators $a_m^\dagger$ and a_m and the vacuum dielectric constant and permeability ε_0 and μ_0.

When only the coupling to a single cavity mode (with resonance frequency ω_C) is considered, the sum vanishes and the Hamiltonian simplifies to

$$H_{\mathrm{LF}} = \hbar\omega_C(a^\dagger a + \frac{1}{2}) \tag{4.10}$$

The quantum state $|n\rangle$ of the field is characterized by the number of photons n in this mode.

The emitting quantum mechanical system is modeled to consist of two levels, an excited state ($|\mathrm{ES}\rangle$) above a ground state ($|\mathrm{GS}\rangle$) with the energetic spacing $\hbar\omega_{\mathrm{EG}}$. It is represented by states in a two-dimensional Hilbert space, in which Pauli matrices build up the operators, that is, the operators $\sigma_\pm = \frac{1}{2}(\sigma_x \pm \sigma_y)$ describe transitions from the ground to the excited and from the excited to the ground state respectively. The Hamiltonian for the two-level system (2LS) with the projector definition $\sigma_{\mathrm{EE}} = |\mathrm{ES}\rangle\langle\mathrm{ES}|$ is given by

$$H_{\mathrm{2LS}} = \hbar\omega_{\mathrm{EG}}\sigma_{\mathrm{EE}} \tag{4.11}$$

The coupled system comprises the above contributions of the cavity and two-level subsystems and the interaction between them, expressed by H_{int}. When limiting the treatment to the quasi resonant condition of $\omega_C \approx \omega_{\mathrm{EG}}$ and the lossless case when the annihilation of one photon switches the two-level system to its excited state, while a transition to the ground state creates one photon, the interaction part is given by

$$H_{\mathrm{int}} = \hbar g(a\sigma_+ + a^\dagger\sigma_-) \tag{4.12}$$

In the dipole approximation, the coupling strength g is expressed by

$$g = \frac{\mathbf{d} \cdot \mathbf{E}}{\hbar} = d\sqrt{\frac{\hbar\omega_C}{2\varepsilon_0 V_C}} \tag{4.13}$$

Here V_C denotes the mode volume and $\mathbf{d} \cdot \mathbf{E}$ is the product of the dipole transition matrix element and the electric field strength.

The full Jaynes-Cummings Hamiltonian then sums up to

$$H_{\mathrm{JC}} = \hbar\omega_c(a^\dagger a + \frac{1}{2}) + \hbar\omega_{\mathrm{EG}}\sigma_{\mathrm{EE}} + \hbar g(a\sigma_+ + a^\dagger\sigma_-) \tag{4.14}$$

The states of a system described by this Hamiltonian no longer factorize. The distinction between a pure two-level system and a pure light field is no longer possible. The eigenstates coupled by the above Hamiltonian , differ in photon number only by one, and are also referred to as dressed states, defined by:

$$|\pm, n\rangle = \frac{1}{\sqrt{2}}\big(|\mathrm{GS}, n\rangle \pm |\mathrm{ES}, n-1\rangle\big) \tag{4.15}$$

Vacuum Rabi Splitting

In the strong coupling regime, the degeneracy of the $|\mathrm{GS}, n\rangle$ and $|\mathrm{ES}, n-1\rangle$ states is lifted. More precisely, when the condition

$$g > |\gamma_{2LS} - \gamma_C|/4 \tag{4.16}$$

with γ_{2LS} and γ_C as the irreversible decay rates of the emitter and the confined photon mode, is fulfilled, the coherent emitter-photon interaction is evidenced by a doublet structure in the spontaneous emission spectrum of the coupled system [2, 15, 115, 94, 101]. At the exact resonance, the doublet is split by the Rabi energy

$$\hbar\Omega = 2\hbar\sqrt{g^2 - (\gamma_{2LS} - \gamma_C)^2/16} \tag{4.17}$$

The system oscillates between the two states with a frequency corresponding to this splitting energy. The Rabi oscillation might also be interpreted as a time-dependent energy transfer between the two subsystems.

Introducing the oscillator strength $f = \frac{2m\omega_{\mathrm{EG}}d^2}{e^2\hbar}$, with e and m as charge and mass of the oscillating carrier, into equation 4.17 results in

$$\hbar g = |\mathbf{d} \cdot \mathbf{E}| \propto \sqrt{\frac{f}{V_C}} \tag{4.18}$$

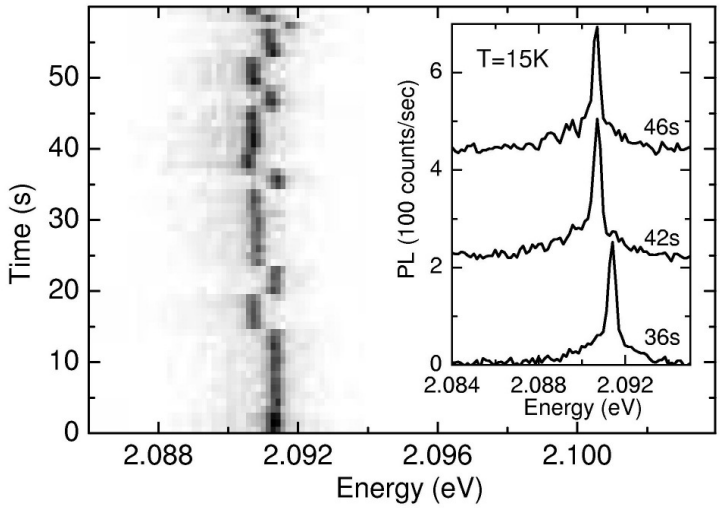

Figure 4.9: PL Jitter and line width of a single CdSe nanorod with dimensions $r \approx 2.5$ nm and $L \approx 25$ nm measured at 15 K and 1 s acquisition time for a single spectrum. Intensity is plotted as a function of time and energy in a linear grey scale. The inset shows exemplary spectra illustrating a spectral jump of 700 μeV.

for the dependence of the coupling constant on the design parameters of the experiment. A large Rabi splitting can therefore be achieved by the use of an emitter with large dipole moment, which is placed close to the maximum of the electrical field, and a cavity of high Q factor and small mode volume V_C.

4.4.2 Experimental Implementation

Modifications in the spontaneous emission rate, that is, the Purcell effect [117], as an indication of weak exciton-photon interactions, have already been experimentally demonstrated for CdSe and CdTe nanocrystals [61, 34, 4, 129].

The two-level system for this cavity QED implementation was chosen to be ZnS capped CdSe nanorods with a radius of $r = 2.5$ nm and a length of $L \approx 25$ nm. The radius is below the critical radius, introduced in the previous section, which makes the lowest excitonic level a bright state. Therefore a high oscillator strength [107], evidenced by the radiative decay rate of ≈ 1 ns and no blurring dark-bright state dynamics are to be expected. The nanorods' very sharp zero-phonon line (ZPL) of a few μeV (FWHM) enables the matching to only one cavity mode.

Figure 4.9 shows the spectrum of a single nanorod and the long term stability of its emission at low temperature. After excitation with the 488-nm line of an Ar-ion laser

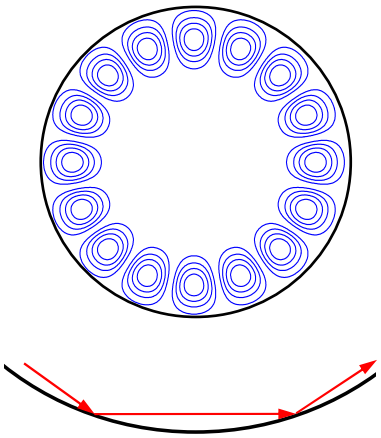

Figure 4.10: Principal of the origin of whispering gallery modes in a perfectly spherical microsphere. The picture of geometric optics, where a ray of light (red) at grazing incidence to the sphere/air interface (black) is reflected totally (lower panel), explains the appearance of WGM around the outer edge of the microsphere. The blue contours sketch the intensity of the light field of a WGM.

and collection with an achromatic objective (NA=0.85, x60) inside a bath cryostat, the emission is detected with a liquid nitrogen cooled CCD attached to a 0.5 m spectrometer (spectral resolution 100 μeV). The nanorod emission is linearly polarized parallel to the c-axis [49]. It consists of a sharp, spectral resolution-limited zero-phonon line and an acoustic phonon sideband, which is attributed to a localized exciton interacting with the acoustic phonon spectrum of the semiconductor nanostructure [68]. As explained in section 1.4.5, and illustrated in figure 4.9, the spectral position of the nanocrystal emission is stable for a period of several seconds, before a spectral jump occurs, due to charge fluctuations in the surroundings [32]. This amount of spectral stability is sufficient to observe a spectral matching of the cavity mode and the emitter emission. In addition, the spectral jitter is used as a natural tool to tune the single nanorod resonance energy of the ZPL, since the temperature can not be used as a resonance tuning parameter because of the effect of spectral wandering and the narrow free spectral range of the cavity mode set [97, 133]. Instead, the nanorod-cavity spectra are measured over a long time interval and the line shape is analyzed for on/off resonant nanorod emission for a consecutive sequence of spectra. Another argument for the choice of nanorods as emitters for this cavity QED experiment is the relative ease with which they can be incorporated in polymeric structures, since the cavity is realized by a micrometer sized dielectric polymer sphere.

In such spherical structures, the light confinement within the resonator can be understood as a total internal reflection of the light at a grazing incidence angle on the inside of the sphere (see figure 4.10). This leads to the formation of modes that exhibit a field localization close to the sphere surface, referred to as *whispering gallery modes*. These modes exhibit high Q factors, for diameters in the range of μm. For a strong coupling application, a compromise between Q factor and the rather large mode volume V_C has to be found [10, 13].

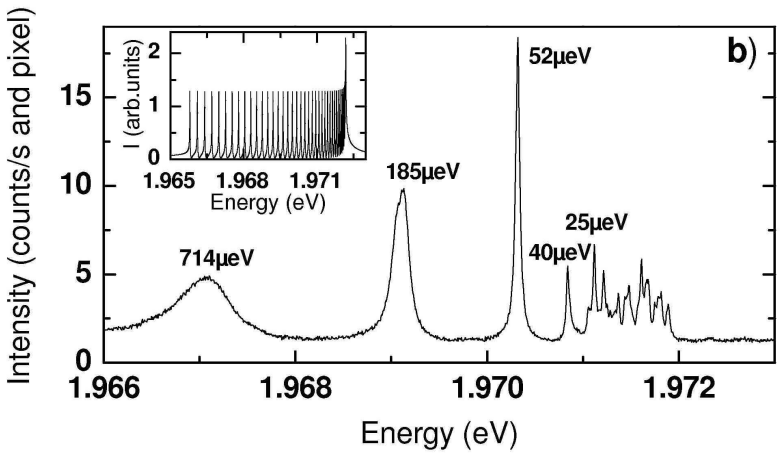

Figure 4.11: Line width of scattering modes of a single polymer sphere with a diameter of 6 μm. The spectrum was recorded from a diffraction limited detection spot on the sphere and displays the degeneracy lifting of the $l = 41$ mode. The inset shows the theoretical spectrum for a slightly oblate sphere.

In a perfectly spherical resonator, the whispering gallery modes around the sphere center are degenerate in energy, even if the are aligned in different planes, that is, if they differ in azimuthal or polar angle. A slight deformation, which is present in all real microspheres, lifts this degeneracy, allowing for an isolation of a single mode, if sufficient spectral resolution is applied.

The nanorod emitters can easily be positioned at the electromagnetic field maximum of the cavity to maximize the coupling strength g, by an electrostatic attachment method. Due to the fabrication process, polystyrene microspheres carry a surface layer of sulphate groups, which adds a negative surface charge to the microspheres in the suspension. Nanorods carrying a positive surface charge attach electrostatically to the microsphere surface leading to a tangential alignment of the nanorods.

The microcavities used here are commercial polystyrene spheres with a diameter of $d = 6 \pm 0.3\,\mu$m, a size optimal for obtaining both a high Q factor and still a comparably small mode volume. The cavity modes are characterized by angular, azimuthal and radial photon mode numbers l, m, and n for the transverse electric ($\mathrm{TE}^n_{l,m}$) and transverse magnetic ($\mathrm{TM}^n_{l,m}$) field modes. For a given radial mode number n, for example $n = 1$, the free spectral range is much larger than the tens of μeV homogeneous line broadening of the single CdSe nanorod spectrum. As a result, a single nanorod couples only to photon modes with a given n and l mode number. For the mode number m, the $(2l+1)$- fold degeneracy is lifted by a deviation from a perfect sphere shape.

Figure 4.11 shows a spectral characterization of the $(2l + 1)$ modes of a TE^1_{41} photon state for a deformed microsphere, demonstrating the degeneracy lifting. The spectrum of this "empty" sphere, that is, without emitters, was excited by a 150-fs pulse of an optical parametric oscillator (OPO) centered at 620 nm and evanescently coupled into the sphere by focusing on the contact point between the sphere and the substrate. The scattered light from the sphere was collected with a high numerical aperture objective (NA = 0.95) and recorded with a high-resolution imaging spectrometer and a CCD camera. The inset shows the theoretical spectrum for a slightly deformed (oblate) sphere with a relative difference of approximately 0.5 % between the polar and equatorial radii calculated by first-order perturbation theory [64]. The effect of natural shape deformation (symmetry invariance breaking) and the translation invariance breaking due to the sphere/substrate contact point allows the observation of scattered light from different m modes. By selecting a proper spatial region, we measure a minimum mode line width of 20 μeV, which corresponds to a quality factor $Q \approx 10^5$. The calculated spectrum predicts a Lorentzian line shape with 5 μeV width (FWHM) for the different m, while the experimental homogeneous line widths of the individual photon modes vary between 20 and 714 μeV. For the m modes at energies, E_{mode}, smaller than 1.970 eV, the larger line broadening might be explained by an efficient photon escape into the substrate.

After characterization of the spectral properties of the cavity modes and the nanorod emitter separately, the combined system and its coherent interaction is studied. By positioning the nanorods tangentially aligned on the sphere surface, predominantly TE modes with $m = \pm 1$ will be excited, with the photon quantization axis defined perpendicular to the emitter polarization [79]. With the spectral jitter of the nanorods in mind, which is larger than the m mode line width, a Rabi splitting can only be detected during a certain transit time and at temperatures below 15 K. The samples, held together with the microscope optics inside a bath cryostat, are again excited with the 488-nm line of an Ar-ion laser. The emission from single modes is spatially selected by imaging spectroscopy using a high-resolution imaging spectrometer with a focal length of 2 m, a spectral resolution of 7 μeV and read out of only a few selected CCD channels (signal-to-noise ratio N $\approx$ 10). For about 200 cavity modes a sequence of 100 spectra with an acquisition time of 4 s each is recorded, which, on one hand, is sufficiently long to have a detection intensity above the noise level and, on the other hand, short enough to be within a time range without spectral jumps. For about 5 % of the modes, a mode line shape was found that splits into a doublet symmetrically around a center energy with values for the splitting energy, $\hbar\Omega_{exp}$ between 30 and 45 μeV. The unlikeliness of the existence of two or more completely identical nanorods performing identical spectral jumps strongly supports the interpretation of

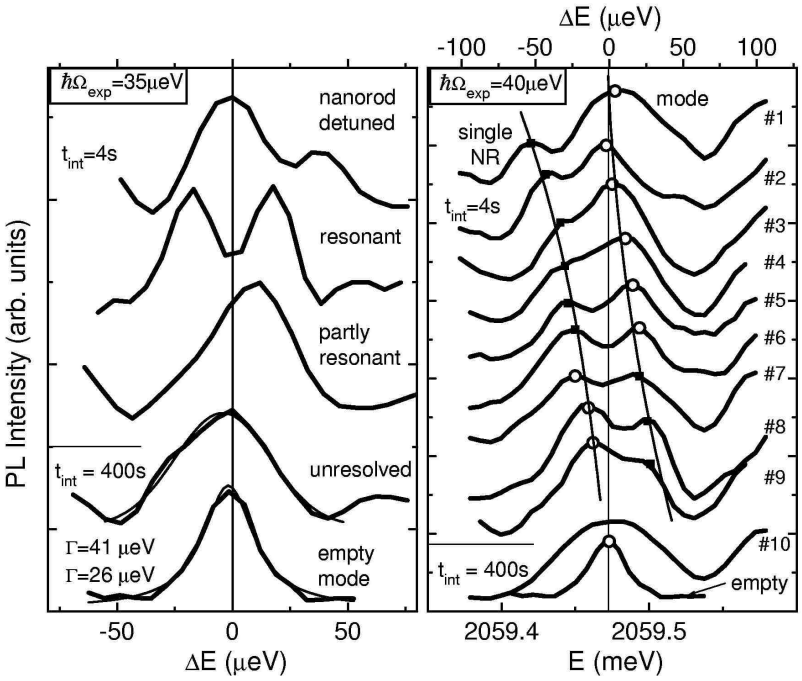

Figure 4.12: PL as a function of the detuning between cavity mode and nanorod emission. Left: exemplary spectra for different stages of detuning. The line width obtained from a gaussian fit (thin solid line) is denoted with Γ. Right: Spectra aligned with respect to their nanorod detuning energy demonstrating the avoided level crossing behavior.

the spectra as stemming from single nanorods coupling to non-degenerate photon modes.

In Figure 4.12 two exemplary sets of spectra from different microspheres with CdSe nanorods electrostatically attached to the surface are shown. The left panel displays for one sphere the four typical stages of nanorod detuning that are observable during the recording time with a clear line splitting for the nanorod in resonance. In contrast, the reference sphere without nanorods shows a much smaller mode line width and unchanged resonance energy with time. In Figure 4.12 (right), the spectra are not plotted according to their acquisition number, but arranged with respect to their nanorod detuning energy, allowing the reconstruction of the avoided level crossing behavior expected for the strong coupling regime.

From the average of the experimental splittings, $\hbar\Omega_{exp} = 37\mu$eV, the coupling constant g_{exp} can be deduced, and compared it with theoretical predictions. In the present system, the lifetime broadening of the emitter spectra $\hbar\gamma_{2\mathrm{LS}}$ is expected to be small with respect to $\hbar\gamma_{\mathrm{C}}$ and can be neglected compared to the experimental photon line width $\hbar\omega_{\mathrm{C}} \approx 20\mu$eV as deduced from radiative lifetime measurements [68]. The estimate

$\hbar g_{exp} \approx \sqrt{(\hbar\Omega_{exp})^2 + (\hbar\gamma_C)^2/16}$ results in $\hbar g_{exp} = 19\,\mu$eV, showing that the strong coupling condition $g > |\gamma_{2LS} - \gamma_C|/4$ is well satisfied. For comparison, the coupling constant g_{theo} is calculated using

$$g_{theo} = \lambda/2\pi\sqrt{\pi c(2n_C^2 + n_E)/(2n_C^3\tau_{rad}V_C)} \tag{4.19}$$

according to reference [115], with the emission wavelength λ, the emitter radiative decay time in free space τ_{rad}, the effective mode volume V_C, the refractive indices of the emitter n_E, and of the polymer sphere n_C, and the vacuum velocity of light c. The mode volume was approximated by a torus with a length equal to the sphere perimeter and a section radius of λ/n_C, which gives $V_C \approx 8\,\mu m^3$. To obtain consistency between g_{exp} and g_{theo}, the nanorods' radiative decay times τ_{rad}, have to span the range between 1.6 ns and 0.7 ns, which is in agreement with photoluminescence decay time measurements on these CdSe nanorods, as shown in section 4.3.2.

It should be noted here, that at T = 5 K the acoustic phonon sideband is still a non-negligible contribution to the spectrum (see Figure 4.9). In references [125] and [135] it has been shown theoretically that if there is a perfect matching between the cavity mode and the ZPL then the Rabi frequency is exponentially suppressed by a factor $\exp(-S/2)$ as a result of exciton-phonon coupling, where S is the Huang-Rhys parameter. This parameter, deduced from the intensity ratio of the first LO replica and the ZPL from the CdSe nanorod μPL spectra, ranges between 0.04 and 0.16. It implies only a small correction of the Rabi splitting energy by the exciton-phonon coupling. However, the ZPL is most of the time not in resonance with the 20 μeV wide mode and the emission from the acoustic phonon sideband, which spreads over 5 meV, can flow through the mode in a weak coupling regime. For this reason the mode is always "switched on" and can be detected even without being in the strong coupling regime.

Since the line width is connected to the decay time, the above analysis can be supported by decay time measurements. If no inhomogeneous broadening mechanisms are present, the shape of a transition in the frequency domain is given by a Lorentzian line shape

$$g(\nu) = \frac{\Delta\nu/2\pi}{(\nu - \nu_0)^2 + (\Delta\nu/2)^2} \tag{4.20}$$

with $\Delta\nu = \frac{1}{2\pi\tau}$ and $\Delta\nu = \frac{\Delta E}{h}$. The lifetime of a transition connects to its line width as $\tau = \frac{h}{2\pi\Delta\nu}$, Which results in the easy to use relation:

$$\tau(\text{ps}) = \frac{659}{\Delta E(\mu\text{eV})} \tag{4.21}$$

To make use of this dependence, the photon lifetime for microspheres with and without nanorods at T = 5 K were measured (Figure 4.13). A 120-fs pulse of the OPO was

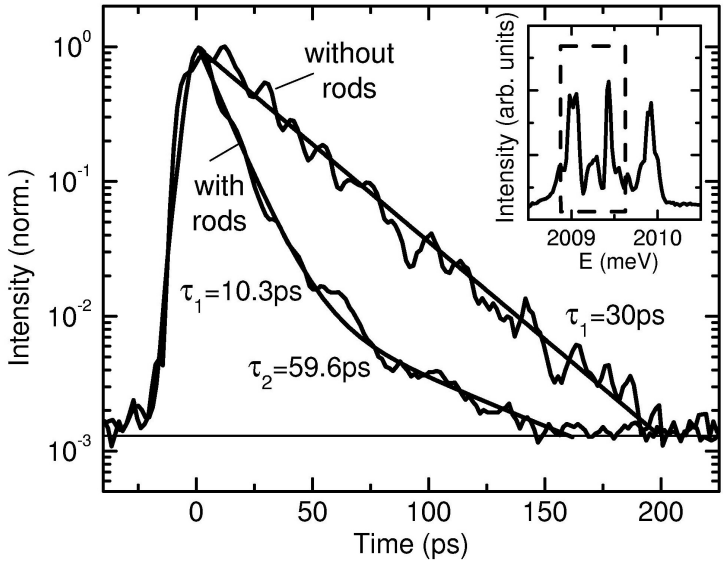

Figure 4.13: Decay time a of sphere mode (TE^1_{42}) with and without nanorod, extracted from an ensemble measurement by spectral selection. The inset shows the excited energy range, which covers a set of several m-degenerated cavity modes. The solid lines are the curves obtained with the given fit parameters.

tuned in resonance to a set of cavity m-modes having the same n and l mode number within a narrow spectral window (see inset of Figure 4.13). For the detection of both the empty microsphere and nanorod-microsphere photon lifetime, a spectrometer and a streak camera with a time resolution of 5 ps was employed. When no emitters are on the sphere, the cavity photon decay is mono-exponential with a decay time of approximately 30 ps, implying that all excited modes have roughly the same homogeneous line width of 22 μeV, in agreement with the empty-sphere spectral line width measured, for example, in Figure 4.12. For the spheres covered with nanorods, two decay regimes are observed: a fast, almost mono-exponential decay of 10 ps followed by a slow exponential decay of 60 ps. The fast decay is assigned to modes that are not in the strong coupling regime. For this majority of modes, a FWHM between 50 and 70 μeV was measured, which is in good agreement with a 10 ps photon lifetime component. The slower decay is attributed to the decay of the 5 % modes in the strong coupling regime. For these modes the decay time is two times longer than the decay of the same modes without nanorods, which is a striking signature of the strong coupling regime. From the average line broadening (FWHM) of the Rabi doublet given by $\frac{1}{2}(\hbar\gamma_C + \hbar\gamma_{2LS})$, [2, 15] and assuming $\gamma_C >> \gamma_{2LS}$, the change in

photon lifetime with and without coupling to nanoemitters is just the factor of 2 measured in the experiment.

Summarizing, a study of the strong coupling regime of cavity QED with semiconductor nanocrystals in microsphere cavities using spectrally and time-resolved imaging spectroscopy was successfully conducted. With colloidal CdSe nanorods, a new material class, for which solid-state-based cavity QED was implemented, was added.

5. CdTe Nanocrystals

A material system exhibiting similarities to the CdSe nanocrystals studied in the previous chapter is cadmium telluride (CdTe). The comparably small band gap of 1.43 eV gives rise to an emission which can be tuned from the near infrared (870 nm), across the visible range of the spectrum, down to a wavelength corresponding to blue-green emission, by the same size-dependent quantum confinement effects.

CdTe nanocrystals have been fabricated by several groups [95, 81, 76, 113, 134], and their luminescence properties have been tested [52, 132, 131] extensively. With applications in mind, ranging from solar cells, in-vivo biomedical detections, or donor/acceptor pairs in systems designed for efficient energy-transfer [36], larger size CdTe NCs, emitting in the deep red or near IR are of particular interest. Large sizes of CdTe NCs were obtained by growth in coordinating [81] or non-coordinating solvents [134], by making use of S-Te exchange reaction by capping CdTe by CdS shells [105], or by preparing nanocrystalline CdTe films by electrodeposition [75]. Several strategies of improvement of the PL efficiency of capped CdTe nanocrystals have been developed [95, 81, 39, 40, 9].

The photoluminescence dynamics of CdTe NCs are governed by the zinc-blende type crystal symmetry which leads to a distinctly different behavior than found in II-VI nanocrystals with wurtzite crystalline structure, like CdSe. The analysis of the optical properties of CdTe NCs will give insight to the fundamental properties of this material system.

In detail, CdTe/CdS core-shell nanocrystals with radii $r > 3$ nm, which emit in the deep-red spectral range are investigated. The temperature-dependence of the position, intensity and decay of the photoluminescence and the influence of the ground state exciton fine structure on the radiative decay times for a nanocrystal material with cubic crystal structure are the main focus.

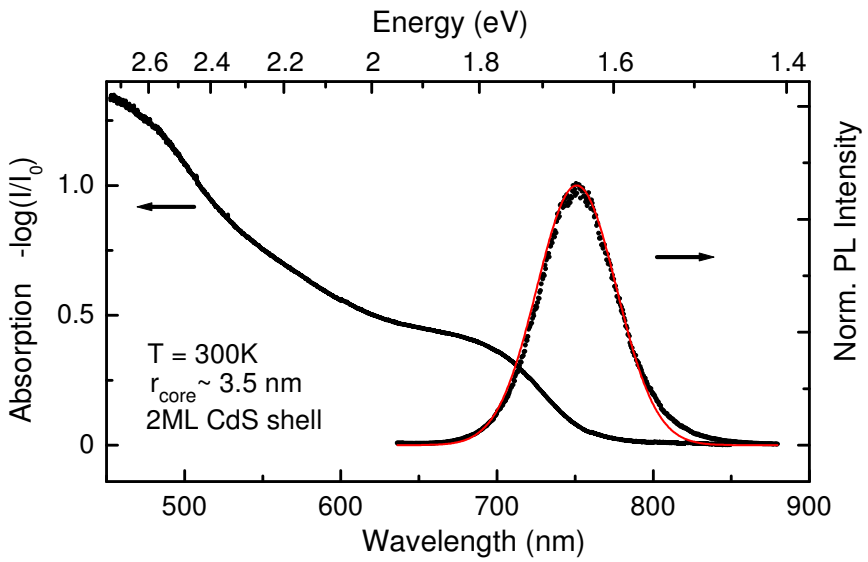

Figure 5.1: Absorption and Luminescene of CdTe nanocrystals.

5.1 Sample Preparation

The CdTe core nanocrystals have been synthesized by Dr. Mikhail Artemyev according to the standard high-temperature reaction as reported for CdSe NCs [81]. Equimolar amounts (0.1-0.5 mmol) of elemental tellurium and dimethylcadmium were dissolved in 2 ml of trioctylphosphine TOP and quickly injected into the mixture of 1.5 g trioctylphosphine oxide (TOPO), 2.5 g hexadecylamine (HDA) and 5 ml octadecene at 200°C under intensive stirring. The growth of the CdTe NCs was controlled by monitoring the spectral position of the NCs PL-band, until the desired size was reached.

In order to increase the quantum yield of the so obtained core NCs, a shell consisting of a higher band gap material, that is, CdS was grown. The isolated CdTe core NCs in toluene solution were therefore injected into a fresh portion of a TOPO/HDA mixture to which the precursors for the CdS shell (1 mmol of cadmiumethylhexanoate, $Cd(CH_3(CH_2)_4COOC_2H_5)_2$ and 1 mmol of thiourea, $(NH_2)_2CS$ in TOP) were added dropwise at 180°C. The finalized CdTe/CdS core-shell NCs were purified and redissolved in chloroform.

Figure 5.1 shows the room temperature absorption and emission spectrum of the prepared CdTe/CdS core-shell NCs. The ensemble is characterized by an absorption shoulder at 710 nm and an emission peak at 750 nm. No apparent defect emission at longer wavelength was observed [104].

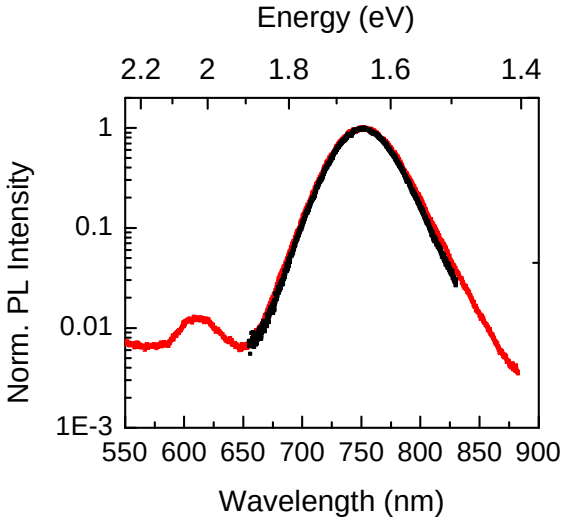

Figure 5.2: CdTe NCs in solution (red) and dispersed in polymer (black). The identity of the PL spectra evidences the absence of energy transfer, which would lead to a red-shifted emission in the solid sample. The small peak at 610 nm is caused by luminescence of a small amount of CdTe precursors in the solution [9].

The samples for the temperature dependent optical investigations were prepared by dispersing a diluted stock solution in a polymer (PMMA) and depositing a small volume on a quartz substrate, where it was left to dry. Great care was taken in preparing an ensemble of diluted, non-interacting nanocrystals. The identity of the PL spectra of the low-concentrated nanocrystals in solution and after drying on the substrate indicates that no aggregates or close-packed layers of coupled nanocrystals are formed as evidenced in figure 5.2. An interacting ensemble would result in spectral red shifts of the emission with respect to a diluted NC suspension [42, 5, 3]. The small luminescence peak visible at 610 nm in figure 5.2 is due to a small amount of residual CdTe precursors in the solution [9].

Since for NCs of larger sizes, numerical methods based on effective mass approximations (EMA) work still well, we can estimate a radius of $r = 3.5$ nm by a simple EMA-based modeling of the size-dependent absorption maximum. This assignment is in good agreement with absorption data and structural data from literature [95, 81, 75, 134].

5.2 Temperature Dependence of the Photoluminescence

The sample was mounted onto the cooling finger of a helium flow cryostat to allow for temperature dependent measurements between 15 K and room temperature. The excitation source for both, time integrated as well as time-resolved measurements was a frequency doubled titanium sapphire laser, providing an excitation wavelength of 430 nm. Time integrated PL was measured with the μ-PL setup described in section 3.2 with 0.2 nm spectral resolution. Focusing of the attenuated excitation light onto a spot of 20 μm in

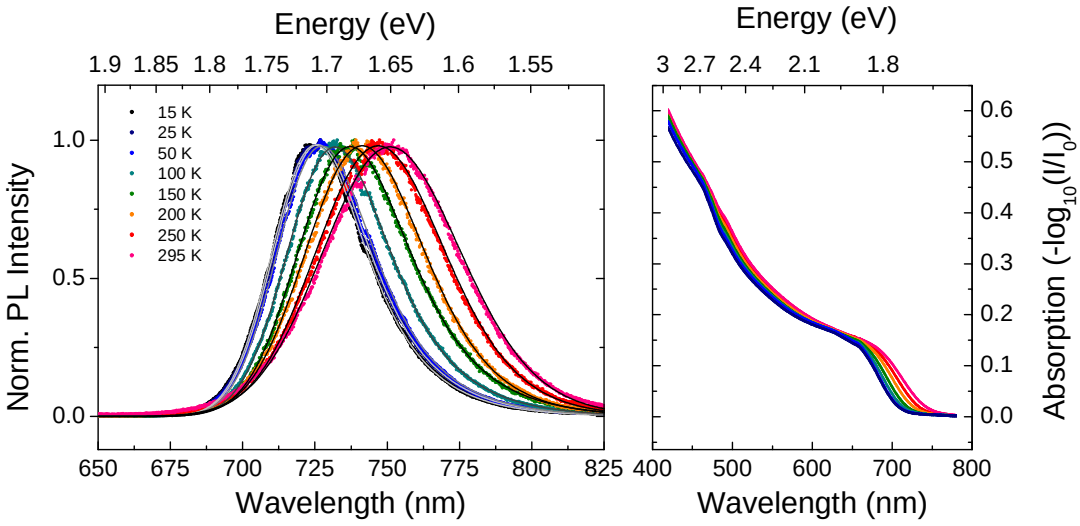

Figure 5.3: Temperature-dependent shift of absorption (right) and emission (left) of CdTe NCs. The color index indicating the temperature is valid for both graphs.

diameter resulted in pump intensities below 1 Wcm^{-2}. This was done to ensure a low density of excitons (on average less that one per NC), to neglect multi exciton processes.

The influence of temperature on the emission peak is shown in figure 5.3, left panel. The emission band shifts towards longer wavelength and simultaneously broadens from a FWHM of 38 nm at 15 K to 54 nm at room temperature. This shift can be fitted to a linear dependence of the emission energy on the temperature given by $E_{\mathrm{Em}} = 1.714\,\mathrm{eV} - 0.215\,\mathrm{meV}\cdot\mathrm{K}^{-1}$. The slope of $-0.215\,\mathrm{meV}\cdot\mathrm{K}^{-1}$ is similar to the temperature dependent band gap shift of bulk CdTe of $-0.3\,\mathrm{meV}\cdot\mathrm{K}^{-1}$ [14], indicating that the phonon-mediated shift of the band gap is similar for nanocrystals and bulk CdTe. The linear fit of the observed shift is represented in figure 5.4.

A similar behavior as for the recombination energy can be expected for the absorption properties. Figure 5.3 shows the absorption of CdTe NCs as a function of temperature on the right panel. The half value of the absorption shoulder was used to determine the shift of the absorption since it can be determined with higher accuracy. The corresponding energy is plotted alongside the emission energy in figure 5.4. Again a linear fit function was employed, yielding $E_{\mathrm{Abs}} = 1.816 - 0.242\,\mathrm{meV}\cdot\mathrm{K}^{-1}$. The slope of $-0.242\,\mathrm{meV}\cdot\mathrm{K}^{-1}$ compares well with that of the observed PL peak shift.

In order to measure accurately the PL intensity as a function of temperature, a number of possible sources of error should be accounted for. For the here projected measurements, a sample of diluted NCs embedded in a polymer was needed to assure independent emission without any cross-talk or energy transfer. In addition to a smooth deposition on the quartz

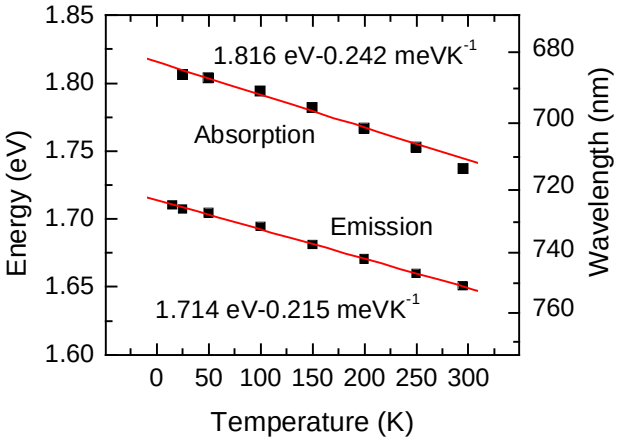

Figure 5.4: Temperature-dependent PL and absorption shift of CdTe. The energetic position of the emission peak and the half value of the low energy absorption shoulder can be fit to linear functions of temperature.

substrate, careful calibration of the positioning was performed in order to assure a probing of exactly the same sample spot in every measurement. The duration of the time-resolved measurements was on average 30 minutes to attain the three orders of magnitude decay dynamics. Although in the time required to change the sample temperature, the laser was blocked, even the moderate pump fluences lead to an inevitable degradation, especially at elevated temperatures. To correct for this effect, the time-integrated PL before and after every time-resolved measurement was recorded, and the data corrected for the degraded luminescence.

The corrected intensities as a function of sample temperature are plotted in figure 5.5. The error bars displayed are calculated according to error propagation based on an estimated uncertainty of 10 % in the determination of the degradation effect. In the temperature range between 15 and 25 K, a slight increase by a factor of 1.2 is observed, followed by a steady decrease for temperatures above 50 K. The data shown is superimposed with a sum of two Boltzmann distribution functions with activation/deactivation energies of 1 and 3 meV, respectively, as a guide to the eye. As will be discussed in more detail in the following, the slight increase in efficiency at low temperatures can be assigned to a thermally induced population change among the allowed exchange-split exciton states having different oscillator strength. At temperatures between 50 and 295 K, the increasing phonon population (both confined acoustic phonons and LO phonons) supports non-radiative recombination which results in a decrease of fluorescence intensity by a factor of approximately 8, a similar factor as measured for the fastening of the decay time τ_1 in the same temperature range.

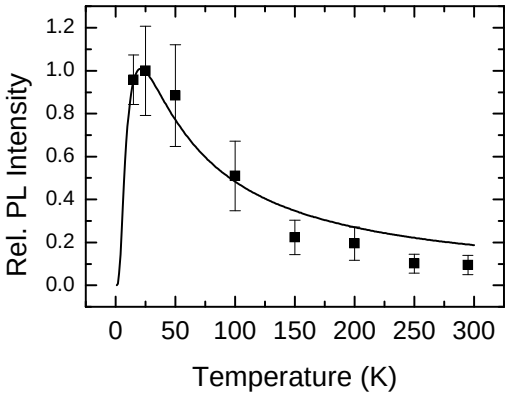

Figure 5.5: Temperature dependence of the PL intensity of CdTe NCs. The emission intensity rises with temperature initially, and then decreases. As a guide to the eye, the sum of two exponential activation and a deactivation terms described by $I \propto \left[\exp\left(-1.0\,\mathrm{meV}/k_bT\right) - \exp\left(-3.0\,\mathrm{meV}/k_bT\right)\right]$ is included. The error bars are estimates based on the uncertainties introduced by the degradation correction.

5.3 Temperature Dependence of PL Decay Times

To investigate the PL dynamics, the same laser system as in the time integrated measurements was used. The pulses of 150 fs length were originally emitted with a repetition rate of 75.4 MHz. After frequency-doubling, using a BBO crystal, the excitation light was passed through a pulse picker to reduce the repetition rate to 1.2 MHz. This is necessary to ensure a full depletion of all states excited before the arrival of the next excitation pulse. Focusing the laser light as well as collecting the luminescence signal was performed with the same optics as before. The time-resolved detection was employed by switching kinetically mounted mirrors to redirect the light onto an avalanche photo diode attached to a 0.5 m scanning spectrometer (0.7 nm resolution). A photon counting card provided a temporal resolution of 500 ps. The resulting data sets were deconvoluted as described in section 3.3 to yield response corrected data for three orders of magnitude of decay dynamics. Out of the so obtained spectrally and temporally resolved emission maps, spectrally narrow cuts were extracted at the low energy side of the ensemble, following routines and considerations discussed in section 4.3. The resulting data, displayed in figure 5.6, was analyzed with temperature as the external parameter and decay times were derived, which will be discussed within a qualitative model.

To extract the radiative lifetime from the PL decay time, usually a suited kinetic model has to be applied providing a reasonable fitting function. The current studies in the literature refer to luminescence decays that are highly non-exponential [52, 103, 27, 35]. For CdTe NCs, as will be discussed below, the microscopic origin of this multi-exponential decay behavior has still to be clarified. The CdTe nanocrystals studied here are well isolated and cannot interact with each other which excludes microscopic hopping and migration processes as the origin for stretched exponential decays. This mechanism is used to explain the non-exponential PL decay found in disordered system, such as porous

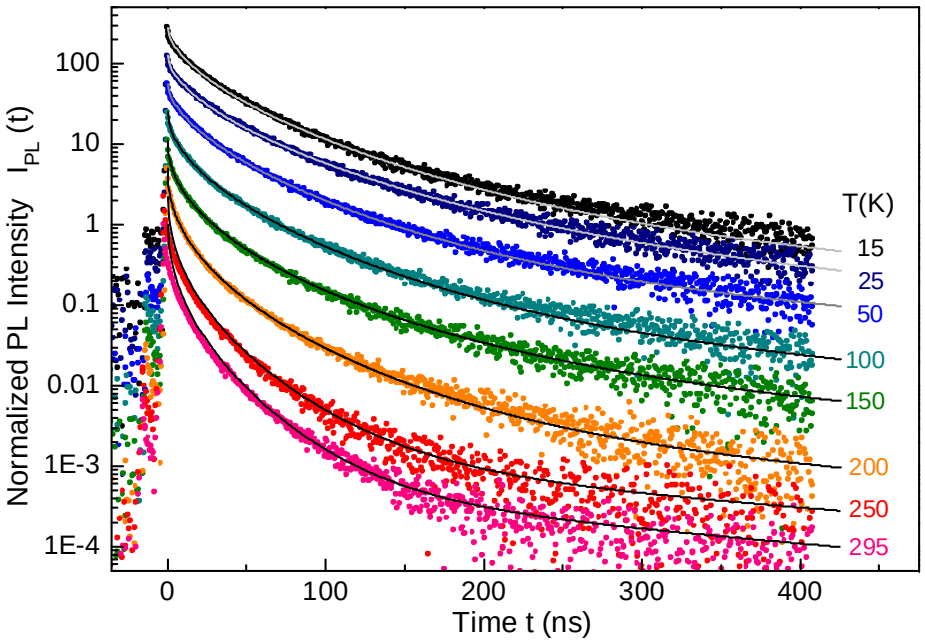

Figure 5.6: Temperature dependence of the PL decay in CdTe. The normalized decay curves are vertically displaced for better visibility. Clearly observable is an initial decay component that speeds up with rising temperature and emerges in an slow part, that is less sensitive to temperature. The solid lines are fits with the parameters given in table 5.1

silicon, where excitons can migrate inside a landscape of local potentials. In such systems, stretched exponential decay behaviors can be observed, however, the microscopic origin of the stretched exponential fitting function is there a broad distribution in decay times due the dispersive motion of exciton.

The decay curves measured here show best-fitting parameters by using stretched exponential functions. The fitting functions applied for spherical CdSe nanocrystals in section 4.3, caused by a thermally induced bright state filling from dark states could not be used to describe the CdTe decay dynamics. Different fit routines were tested, both bi- and multi-exponential fit functions as well as a single-exponent stretched exponential decay. The best fit is obtained with a two-component function $A_1 \exp(-t/\tau_1)^{\beta_1} + A_2 \exp(-t/\tau_2)^{\beta_2}$ using two stretched exponentials with coefficients β_1 and β_2. Although the applied fit model starts with these two stretched exponential functions, the best fits resulted in $\beta_2 = 1$, which means the second, long decay component is essentially a mono-exponential decay. The parameters A_1 and A_2 characterize the relative weighting of the fast and slow decay component. The value of β implies information about the spread in the decay time distri-

T (K)	A_1	τ_1 (ns)	β_1	$\langle\tau_1\rangle$ (ns)	A_2	τ_2 (ns)	β_2
15	0.99600	13.195	0.585	20.536	0.0040	350	1
25	0.99422	13.725	0.580	21.615	0.0057	314	1
50	0.99452	12.080	0.587	18.735	0.0055	316	1
100	0.99762	7.749	0.535	13.773	0.0024	328	1
150	0.99850	4.548	0.478	9.908	0.0015	333	1
200	0.99945	2.800	0.462	6.552	0.0006	333	1
250	0.99950	2.1737	0.480	4.699	0.0005	300	1
295	0.99950	2.250	0.500	4.500	0.0005	260	1

Table 5.1: Fit parameters derived for different temperatures using the fitting function $A_1 \exp(-t/\tau_1)^{\beta_1} + A_2 \exp(-t/\tau_2)^{\beta_2}$. The average decay time corresponding to the τ_1 and β_1 values has been calculated with $\langle\tau\rangle = \tau/\beta \cdot \Gamma(1/\beta)$.

bution, that is, the smaller β, the larger the variation in τ. From the stretched exponential fit of the decay curve we can derive an average lifetime $\langle\tau\rangle = \tau/\beta \cdot \Gamma(1/\beta)$, as already used in the previous section. The parameters used for the curves shown in figure 5.6 are given in table 5.1. The decay traces are dominated by a stretched exponential component, describing 99.5% to 99.95% of the observed decay. The extracted average decay time decreases from 20.5 ns at 15 K to 4.5 ns at room temperature. The minor contribution is described by a mono-exponential decay that accelerates moderately from 350 ns to 260 ns when the temperature is increased, as shown in figure 5.7.

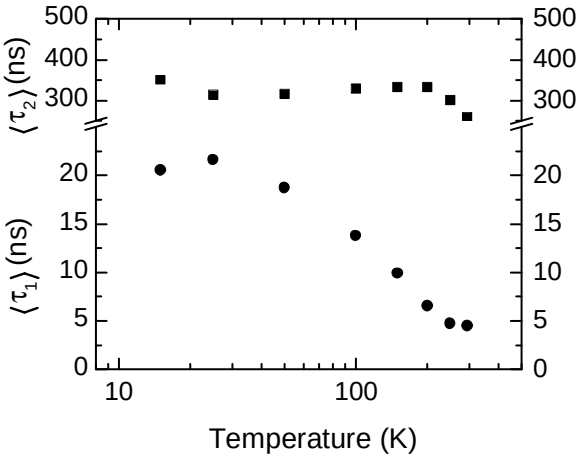

Figure 5.7: Temperature dependence of the average PL decay times in CdTe. The lower part of the plot displays the reduction in decay time from 21.6 ns to 4.5 ns, after an initial increase from 15 K to 25 K. The parameter $\langle\tau_2\rangle$ is displayed above the axis-break and shows less sensitivity to the temperature.

5.3.1 Influence of Exchange Splitting and Exciton Fine Structure

In zinc blende CdTe, the conduction and valence bands are made from s orbitals of cadmium and p orbitals of tellurium, respectively, in first approximation. The orbital angular momentum is mixed with the spin angular momentum, and the valence band is split into the topmost J = 3/2 band and the split-off J = 1/2 band. Since CdTe has the largest spin-orbit splitting of 0.927 eV among CdS, CdSe, and CdTe, the split-off band is expected to mix only weakly with the topmost valence band. The energies of the lowest electron-hole pair transitions have been computed for CdTe NCs using different methods based on EMA or tight-binding calculations [33, 26, 96, 98, 67, 92, 50]. In experiments, the quantized electronic levels are observed to shift monotonically with decreasing size without any crossing or anticrossing, reflecting the rather simple valence band structure of CdTe [76, 26]. Therefore, a likewise simple EMA model was used to estimate the theoretical exciton band edge structure of the CdTe NCs neglecting the thin CdS shell and assuming complete strain relaxation. These computations were carried out by Dr. Nicolas LeThomas. The inset of Figure 5.8 shows the size dependence of the first absorption peak position at T = 295 K. On the basis of the size-dependent absorption and the data from TEM, the radius of r = 3.5 nm is used as a base for the discussion of effects of electron-hole exchange interaction in our CdTe NCs in the following.

For the CdTe nanocrystals studied here, the electron-hole exchange interaction is modeled following the theory of invariants of reference [29]. The 8-fold degenerate exciton ground state $s_eS_{3/2}$ is then split into a group of lower levels of dark 0^L, $\pm1^L$, and ±2 exciton states and a group of upper levels of bright states with total angular momentum projection 0^U and $\pm1^U$. To calculate the splitting between the dark and bright states, the ratio of the light to heavy hole effective masses is assumed to be 0.23, the bulk exciton Bohr radius 6.5 nm and the bulk exciton splitting $\omega_{ST}^{3D} = 0.07$ meV [120].

In figure 5.8, the calculated energies of the exciton band edge structure are plotted versus the NC radius r and relative to the $s_eS_{3/2}$ state with no exchange interaction. As can be seen, in zinc-blende-type CdTe NCs, the ground-state exciton is split by exchange interaction. The fine structure is different from that known for wurtzite-type CdSe NCs with five states. In CdTe NCs two groups of energetically degenerate exciton states are obtained, both of which have contributions from allowed optical transitions. Their energy splitting is smaller and amounts to only a few meV, in particular in the size range of r > 3 nm, allowing a simultaneous, thermal population of all states, even at cryogenic temperatures. Important consequences of that excitonic fine structure on the emission dynamics of excitons in CdTe are:

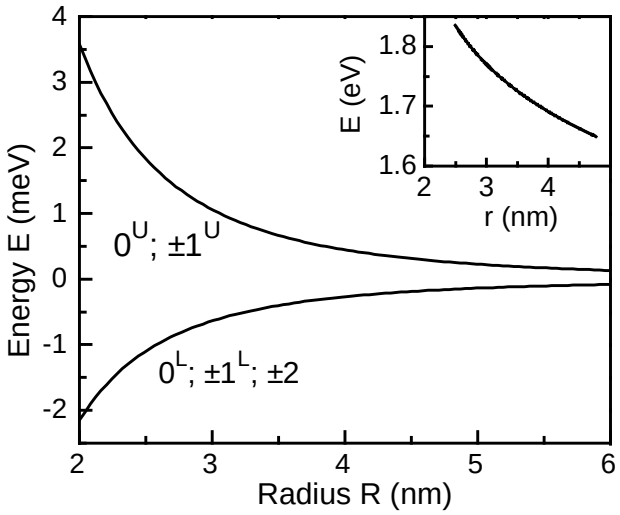

Figure 5.8: Radius dependent exchange Splitting in zinc-blende CdTe NCs. The parameters used for the calculation are $\omega_{ST}^{3D} = 0.07\,\text{meV}$, $a_{exc} = 6.5$ nm, and the Luttinger parameters $\gamma_1 = 4.8$, $\gamma_2 = 1.5$. The relative oscillator strengths are 2 and 1 for the $\pm1^U$ and 0^U states and 0 and 1 for the $\pm1^L$ and 0^L states, while the $\pm$ 2 state is a dark state. The inset shows the size dependence of the lowest excitonic absorption at room temperature, calculated within an EMA model.

(i) The lack of a temperature-dependent change in population as usually observed in CdSe nanocrystals [8, 85, 34, 63, 24], that is, the population of a single bright $\pm1^U$ exciton state thermally filled from a single, energetically nondegenerated ±2 dark exciton state.

(ii) The energy degeneracy of allowed exciton states with different oscillator strength can result in a decay with different radiative lifetimes, meaning that a stretched exponential decay is possible already for a single CdTe NC.

(iii) The specific exciton fine structure of zinc-blende-type CdTe nanocrystals suggests an increase in quantum efficiency due to contributions of the upper $\pm1^U$ and 0^U bright states, in particular in the low temperature range between 5 and 50 K. This is indeed observed up to a certain temperature where the effect is then overcompensated by the increase in phonon population (see figure 5.7). The activation energy of ≈ 1 meV coincides with the energy difference between the lower exciton group ($\pm1^L$, 0^L, ±2) and the upper $\pm1^U$ and 0^U bright states in a cubic CdTe nanocrystal (Figure 5.8).

For the explanation of features i and ii derived from the experimental data in figure 5.6 and table 5.1, it is likely, that for CdTe NCs the total decay is determined by a superposition of several decay times which is one of the possible origins for the strong non-exponential decay behavior. On the basis of the results presented in figure 5.6, likewise an explanation for the variation in τ_1 and in the parameter β_1 from 0.58 to 0.5 for temperatures

above 50 K can be derived. According to reference [29], the optically allowed exciton states have different oscillator strengths, which vary, relative to that of the 0^U state. The values assigned to the three states $\pm 1^U$, 0^U, and $\pm 1^L$ are factors of 2, 1, and 0 for the ideal spherical NC and 1.6 (1.4), 1, and 0.4 (0.6) for oblate (prolate) NCs. The PL decay is then expected to exhibit multi-exponential dynamics due to the thermally induced population of states with different oscillator strength with a tendency of a fastening of the radiative recombination with higher temperatures.

The above-discussed effect of the exchange interaction on the PL dynamics, however, can not explain why in some reports on room temperature PL decay measurements mono-exponential decay curves of several tens of nanoseconds are observed [102, 131, 121]. Likewise it can not explain the observation of a temperature-independent decay component of $\tau_2 = 315$ ns observed in this study. Recombination times of this magnitude are often attributed to the recombination from dark exciton states. The low value of the stretched exponential coefficient β_1 of 0.5 indicates a much larger variation in the radiative lifetime τ_1, over more than 1 order of magnitude, than can be explained by the variation in oscillator strength of the different contributing bright states. To understand these facts, a closer look to the surface-related contributions to the emission dynamics, which will be taken in the following, is necessary.

5.3.2 Influence of the CdTe/CdS Surface Boundary

The discussion in the subsection above is valid for ideal exciton states, meaning that both, electron and hole are localized in the CdTe core surrounded by vacuum. Uncapped CdTe core NCs prepared via a high-temperature reaction in organic solvents, however, have a very low quantum efficiency caused by surface-related non-radiative recombination centers. To increase the quantum yield, the CdTe core can be capped by thin shells of various materials, such as CdS, CdSe, or HgTe [105, 9, 54, 55, 100]. Core/shell CdTe/CdSe nanocrystals are grown in reference [55] and introduced as structures with spatially indirect band gap, so-called type-II quantum dots.

Figure 5.9 illustrates the conduction and valence bands for type-I and type-II quantum structures as a function of distance from the NC center. In conventional type-I structures, like CdSe/CdS, the shells energy levels envelop those of the core. In type-II structures, the conduction and valence band levels are nested in alternation, meaning that the lowest level belongs to the shell, the above lying to the core, the one above again to the shell, and the highest to the core again. This leads to a preferred localization of the hole in the core and of the electron in the shell. The reduced wave function overlap decreases the

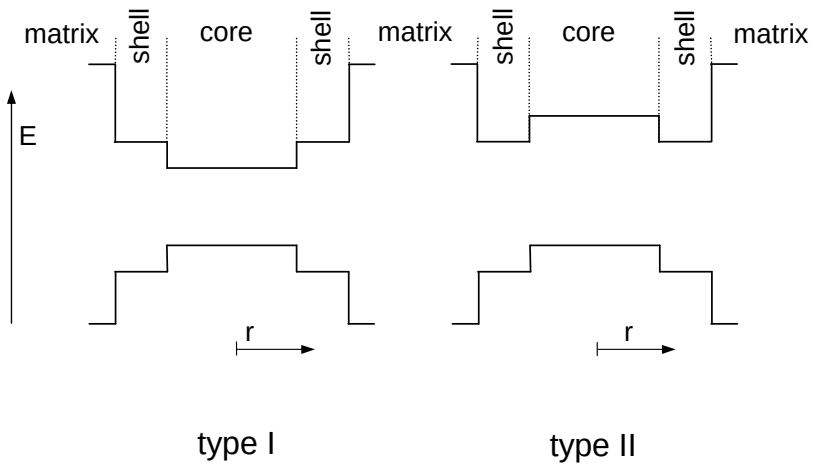

Figure 5.9: Energy structure of type-I and type-II quantum dots. In type-I dots, like CdSe/CdS, the shells energy levels envelop those of the core. In type II structures, the conduction and valence band levels are nested in alternation, leading to a preferred localization of the electron in the shell and of the hole in the core.

probability of radiative recombination.

In literature [105, 40, 9, 100], it has been proposed that thiol-capped CdTe nanocrystals represent a kind of naturally sulfur-capped surface (CdS shell) created by mercapto[1] groups covalently attached to the surface cadmium atoms. Such a structure results not only in the removal of dangling bonds of tellurium atoms from the surface, but moreover leads to the formation of a core-shell-like structure. However, until now, the discussion of optical properties of CdTe/CdS core-shell structures is done in the context of surface stabilization and suppression of non-radiative processes, and no analysis of the influence of a CdS shell on the electronic states is done.

An exact calculation of the spatial probability of the electron and hole wave function for a CdTe NC completely capped by a closed CdS shell needs the knowledge of the band alignment parameters and of the lattice-mismatch-induced strain. Strain might be negligible as reported in references [105] and [100], and explained by an incomplete CdS shell causing a release of the strain. In concern of the band alignments, the current literature provides different data sets, both from theory and experiments [1, 83, 123, 124]. A simple estimate for a possible radial distribution of the electron and hole wave functions in a CdTe/CdS core-shell NC (CdS shell thickness 0.6 nm, CdTe core radius 3.5 nm) is illustrated with the sketch in figure 5.10. For the shown calculation, strain has been

[1] Thiols, also referred to as mercaptans, contain a functional group composed of a sulfur atom and a hydrogen atom (HS-R, R=Rest)

neglected and the band parameter of reference [1] are used.

The most important result for even this very simplified picture is that under certain conditions a CdTe/CdS core-shell NCs can develop an indirect-type exciton, that is, the hole is then predominantly confined to the CdTe core, while the electron is predominantly localized in the CdS shell. The idea of either electron or hole localization inside the NC shell of a type-II quantum dot has been formulated already for other material combinations of CdTe/CdSe(Core/Shell) and CdSe/ZnTe(Core/Shell) NCs [55].

As mentioned above, the spatial separation of electron and hole can result in a decrease of the wave function overlap and thus longer radiative lifetimes. Although the model of a CdTe nanoparticle which is fully coated by a CdS bulk like monolayer is not exactly valid in our CdTe/CdS sample (the growth of a complete CdS shell around large NCs is still subject of intensive investigations and the shell produced in this study is still an incomplete one), the result from figure 5.10 has implications for the understanding of the PL dynamics.

When the electron is localized closer to the CdTe/CdS boundary and is subject to a higher probability to get trapped by a defect, the stretched exponential behavior of the PL decay could be explained by a fluctuating non-radiative decay rate of each single nanocrystal as demonstrated in references [103] and [35], which resulted in a multi-exponential decay behavior already for a single CdSe/ZnS nanocrystal in that case.

Taking into account that individual members of the measured NC ensemble might exhibit different configurations of the CdTe/CdS boundary, and consequentially, differently localized electron and hole states, might also serve as an explanation for the broad distribution of decay times expressed by the low β_1-value. The observed temperature-dependent change in decay times τ_1 from 13 to 2.25 ns however can not be explained by a thermally activated change in electron localization from shell to core states. The thermal activation energy necessary for such a direct-indirect exciton transformation is much higher than the provided thermal energy and the observed change in decay times does not correspond to the decay time difference expected for a transformation from an indirect-type core-shell exciton towards a direct-type core exciton state.

The effect of the core-shell boundary adds to the spread in radiative lifetimes which arises already from the exchange interaction, lowering the β_1 value in the stretched exponential function further.

One might summarize the findings of this chapter as follows: In zinc-blende-type, deep-red emitting CdTe/CdS nanocrystals, the PL decay time is characterized by stretched

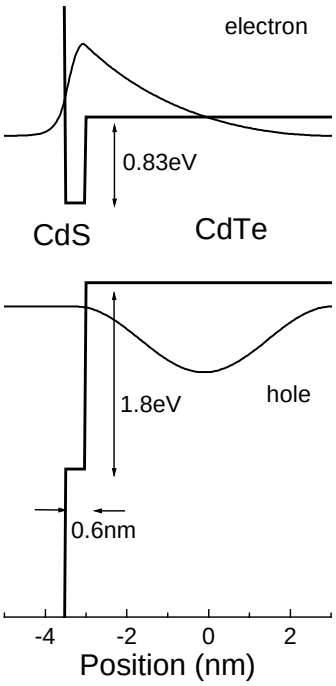

Figure 5.10: Schematic plot of the electron and hole wave functions using the sketched band alignment following reference [1] for an indirect-type CdTe/CdS core-shell structure. The resulting spatial localization of carriers, that is that of the electron in the shell and that of the hole mainly in the core reduces the wave function overlap and leads to an extended recombination time for the indirect exciton.

exponential decay curves. The stretched exponentials are the result of a broad distribution in decay times due to a nearly energy-degenerated bright and dark state superposition and variations in the electron-hole overlap caused by a (partly incomplete) CdTe/CdS core-shell structure. The average decay time of the bright exciton states changes from 20 to 5 ns when the temperature is increased from 15 to 295 K. At low temperatures $T < 25$ K, the emission intensity slightly increases by a factor of 1.2 when the temperature is increased from 15 to 25 K which can be assigned to a thermally induced population change among the allowed exchange-split exciton states having different oscillator strength. At higher temperatures ($50 > T > 295$ K), the increasing phonon population supports non-radiative recombination resulting in a decrease of emission intensity. The mono-exponential, almost temperature-independent decay of 315 ns observed for later times is either due to the decay of the optically forbidden ± 2 dark exciton state, by a deep trap decay or caused by indirect excitons formed in some of the CdTe/CdS core-shell nanocrystals.

6. Hybrid Colloidal-Epitaxial Structures

The preparation of nanocrystals (NC) in colloidal wet chemistry, or quantum dots (QD) by self assembly in the Stransky-Krastanov growth mode, can be seen as complementary approaches to obtain nanometer sized semiconductor particles, both of which exhibit advantages and disadvantages.

The MBE growth of QDs is fully compatible with existing semiconductor technologies. The fabricated structures can be enclosed in epitaxial layers of high crystalline quality, which enables the growth of Bragg mirrors above and below the emitters to form a resonator structure. Additional doping of the neighboring layers allows for a PIN diode type chemical potential profile for electrical charge carrier injection. The nucleation and growth of the nanoparticles in the Stranski-Krastanov growth mode is governed by the temporal evolution of the material deposition. An interruption of the buffer layer growth followed by the deposition of a lattice mismatched material leads to the formation of a fully strained epitaxial wetting layer. Further deposition of this material triggers the nucleation and growth of the QD, and subsequent resumption of the original growth forms an epitaxial cap layer. In this procedure, the parameters responsible for the epitaxial buffer and cap layer growth, and the wetting layer and QD formation are the same, namely the substrate temperature and the atomic fluxes out of the source effusion cells. Therefore the QD characteristics, like the density, variations in size and shape, and the choice of the QD material itself can only be varied within a certain span, in order to maintain the epitaxial character of the structure. In practice, only QDs of a fixed composition can be grown at a time, whose surface density can not be tuned below 1×10^8 cm^{-2}. This requires additional post growth structuring (mesas, masks) for experiments on a single QD scale.

In the wet chemical preparation of NC, the variation of the growth parameters allows for a tuning of the size and shape within a wide range. In addition, the materials can be changed easily which, among others, extends the accessible range of emission wavelength.

The synthesis is carried out with high purity raw materials in a solution of coordinating solvents at high temperatures.

An interesting, but challenging endeavor is therefore the combination of both of the above methods to obtain a new kind of hybrid colloidal-epitaxial structure. In this material, the preparation of the optically active emitters and the epitaxial host material are effectively decoupled, allowing for a separated optimization of the colloidal NC synthesis and the epitaxial growth of the host matrix. Earlier attempts to combine the two methods, relying on organometallic chemical vapor deposition (OMCVD) succeeded only in the encapsulation of NC in an amorphous cap layer [25]. The new approach will comprise a growth interruption during which the NCs, suspended in an appropriate solvent, are deposited on the buffer, a heat treatment that cleanses the substrate from organic contaminations, and a cap layer growth to enclose the NCs in the host material. The resulting samples are tested for their optical as well as structural properties.

6.1 Compatibility of Wet Chemistry and Molecular Beam Epitaxy

In order to combine two technologies that are widely considered to be incompatible, a number of questions needs to be addressed.

The colloidal NCs obtained from the organo-metallic precursors by growth in a highly coordinating solvent mixture of trioctylphosphine (TOP) and hexadecylamin (HDA), exhibit the passivating, and therefore stabilizing, and quantum yield enhancing layer of trioctylphosphine oxide (TOPO) ligands. An introduction of these substances to a MBE system will prevent an epitaxial overgrowth or at least limit the cap layer quality. Therefore a ligand exchange has to replace the TOPO shell with a substance that can be removed in the high temperature, high vacuum (10^{-10} mbar residual gas pressure) environment of the MBE chamber. The material deposited in the MBE process has to be of high crystallinity in order to preserve the epitaxial character of the structure. A low defect density is furthermore necessary to avoid quantum yield limiting non-radiative recombination as well as parasitic radiative recombination that introduces and unwanted luminescence background.

At the same time this new ligand has to preserve the NCs' stability in suspension, and a new ligand should preserve as much of the quantum yield as possible. The NCs furthermore have to sustain the applied high temperatures, and be resistant against the presence of the atomic species present during the MBE growth, that is, selenium and zinc.

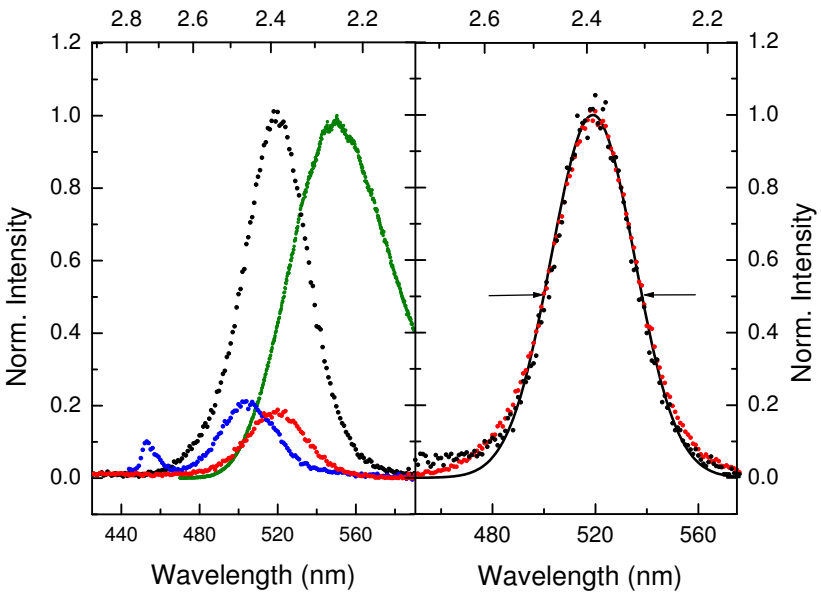

Figure 6.1: CdSe NC ensemble before (black) and after (red) heating to 240°C in vacuum. While the intensity decreases, a normalization (right panel) shows that the PL before and after the treatment can be fitted to a gaussian distribution function, centered at 519 nm with a FWHM of 38 nm. The blue curve in the left panel shows the PL after the heat treatment, taken at 10 K. The same annealing procedure with applied selenium overpressure results in a weakened and red shifted emission that is broadened by 50 % (green).

6.1.1 Nanocrystals in an MBE Environment

The organic solvent pyridin (C_5H_5N) with a vapor pressure of 20.5 hPa at 20°C, and a boiling point of 115°C meets the requirements stated above. A strong affinity of the excess electron pair of the pyridines nitrogen atom to the surface metal atoms of the NCs gives rise to the ability to fully replace the TOPO shell, while simultaneously limiting the tendency of the NCs to aggregate.
Starting from a stock suspension of TOPO covered CdSe or CdSe/ZnS core-shell NCs in trichlorethylene, a number of consecutive precipitation-resuspension cycles with methanol and toluene is used to reduce the content of residual TOPO in the NC suspension to a minimum. After the final precipitation the NCs are suspended in pyridine and stored for at least 24 hours to allow for the ligand exchange to be completed.

With the epitaxial growth preventing TOPO replaced by pyridine, the NCs were deposited onto a freshly grown ZnSe buffer layer. A heat treatment causes the highly volatile

pyridine to evaporate in the low pressure environment of the MBE chamber. Additionally the atomic fluxes used in the later overgrowth, namely a selenium to zinc ratio of 3:1 and a stoichiometric 1:1 ratio were applied.

Figure 6.1 shows the PL of an ensemble of NCs deposited out of a pyridine suspension before and after the treatment described above. A drop of the liquid was left to dry on a quartz substrate and the PL at room temperature was recorded. After a heat treatment at 240°C, the PL intensity has dropped by a factor of 5, which is not only due to degradation, but might also be related to a lowered quantum yield of the NCs, which are unprotected after the ligand removal. A normalization of the intensities reveals that the spectral position of the PL maximum, as well as the distribution around this wavelength are unchanged, since both can be fitted by the same gaussian distribution function. The preservation of the spectral shape implies that the degradation is effecting all NCs in the ensemble equally, instead of, for example damaging the larger particles more than the smaller ones.

In the presence of excess selenium vapor the observed degradation was stronger as compared to a metal-nonmetal equilibrium. In the case of higher selenium partial pressure, the degradation is accompanied by a red shift of the emission of almost 50 nm, and broadening of the ensemble PL by more than 50 %.

6.1.2 MBE in the Presence of Nanocrystals

Another important prerequisite that has to met in order to attempt a hybrid sample assembly is the compatibility of the pyridine involvement with the matrix growth. The structural and optical properties of an "empty" hybrid structure were therefore examined. A 45 nm thick ZnSe buffer layer, that was exposed to pyridine prior to the overgrowth with a 22 nm thick cap layer of ZnSe, was investigated by RHEED and XRD. Figure 6.2 shows the rocking curves as well as the in situ measured RHEED pattern obtained from a sample which, during a growth interruption, has been wetted with pyridine of 99.9+ % purity (biotech grade). The width of the rocking curve of 25 arc seconds, as well as the streak features of the RHEED pattern confirm a structural quality which is sufficient to still identify the structure as epitaxial. For comparison, control experiments were carried out on samples exposed to air and samples that were kept under high vacuum during a growth interruption of equal duration. The FWHM values amount to 7.2 arc seconds and 6.8 arc seconds respectively.

While the electron beam and x-ray investigations suggest a sufficiently high crystalline quality, the sample was additionally investigated in the micro PL setup described in section

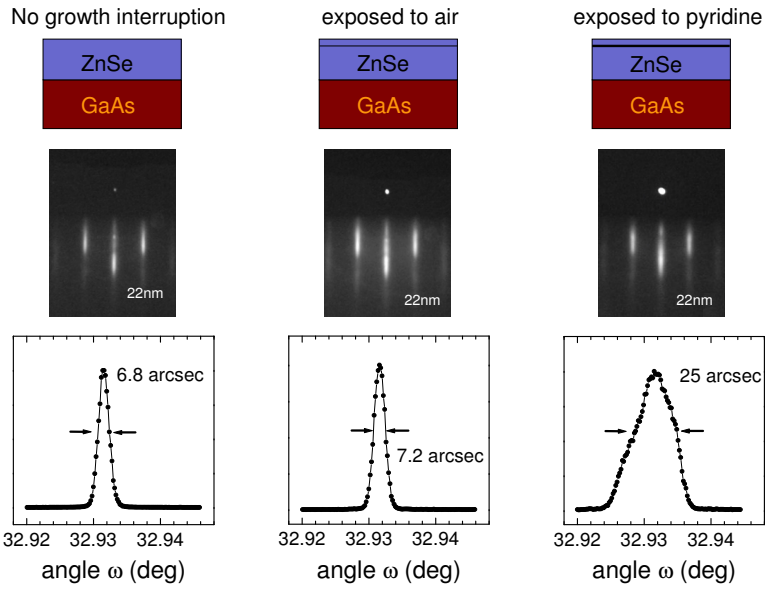

Figure 6.2: Effect of pyridine on the crystalline cap layer quality. The interruption of the growth after deposition of 45 nm of ZnSe on GaAs at 240°C in MEE mode, and the consecutive deposition of additional 22 nm of ZnSe results in the reference sample (left column). The RHEED pattern in the middle shows streaks, indicating a two dimensional growth. The according rocking curve has a FWHM of 6.8 arc seconds. Middle column: the effect of exposure to air during a growth interruption in an otherwise identical growth shows a similar RHEED pattern and a marginally broadened rocking curve of 7.2 arc seconds. The additional exposure of the buffer surface to 99.9+% pyridine does not interfere with a two dimensional overgrowth and increases the rocking curve FWHM to 25 arc seconds (right column).

3.2 at room temperature and 15 K. Under laser excitation at 430 nm and 60 μW, the sample shows the emission characteristic shown in figure 6.3. The emission peaks visible are the y-defect at 472 nm (2.63 eV) of the ZnSe buffer layer, which is more pronounced at cryogenic temperatures. The origin of this peak is attributed to defects and dislocations [43]. The signal stemming from the direct band gap recombination of the Znse follows the same trend in intensity, and is centered at 458 nm (2.7 eV) and 442 nm (2.8 eV) at room temperature and 15 K respectively. Only at cryogenic temperatures, a broad band of low intensity, centered around 555 nm is visible. The absence of strong defect induced PL bands corroborates the classification of the grown structure to be of sufficient crystalline and optical quality for the incorporation of colloidal NCs. It should be mentioned here, that when using pyridine of lower purity, a defect emission band, centered around 545 nm with a width of approximately 80 nm develops.

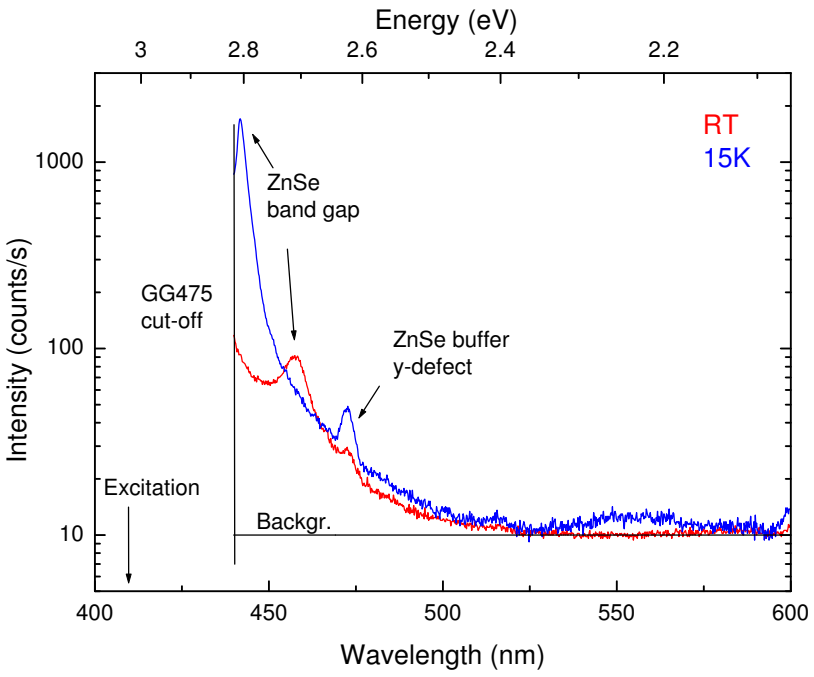

Figure 6.3: Effect of pyridine on the ZnSe PL. The only signatures visible are the y-defect of the ZnSe buffer and the band gap recombination of ZnSe. Even at cryogenic temperatures, only a minor signal, centered at 555 nm is above the detection background of 10 cts^{-1}.

6.2 Hybrid Colloidal-Epitaxial Samples

With the NCs surviving the conditions of the MBE environment, and the chosen solvent proven to be compatible with the growth procedure, the fabrication of the hybrid colloidal-epitaxial structures in a manner sketched in figure 6.4, was approached.

The choice of the NCs for actual incorporation into the hybrid samples was made following a number of considerations. The incorporation of the NC should not prevent the distinction from the host material by means of structural characterization. In order to obtain a high contrast, not only in lattice parameters, but also in the crystal structure itself, rod shaped CdSe NCs with a mean diameter of 7 nm and an average length of approximately 35 nm, with a room temperature emission wavelength of 670 nm, were chosen. The samples were designed to comprise various cap layer thicknesses, starting from a very thin covering ZnSe layer, amounting from less than the NC radius to three times the NC diameter. In this way the incorporation of the NCs can be monitored stepwise. The same approach was chosen for the incorporation of spherical CdSe/ZnS core-shell NCs, with a mean core diameter of 2.3 nm and a cladding of 1-2 ML of ZnS. These NCs were chosen because of their smaller size which should perturb the MBE or

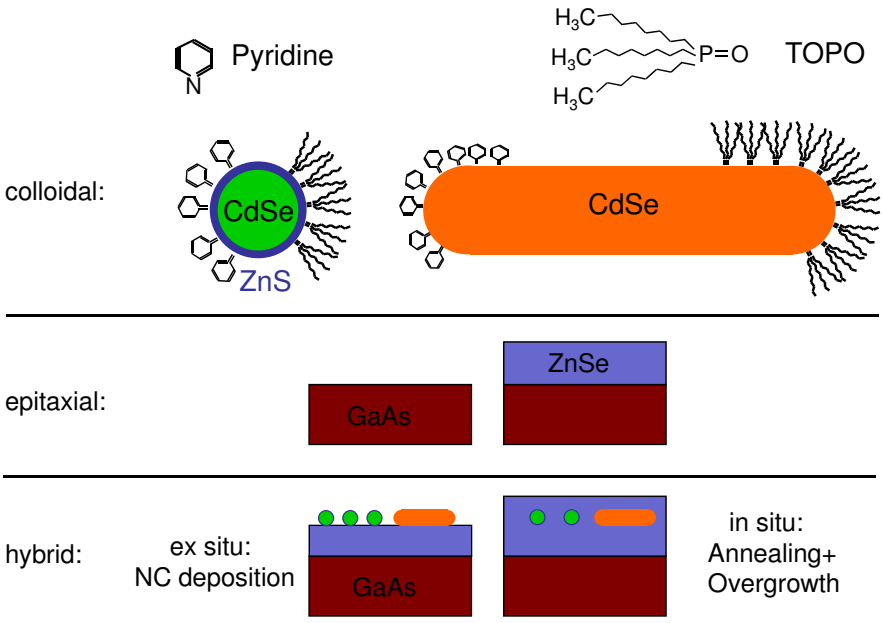

Figure 6.4: Concept for hybrid colloidal epitaxial growth: *Colloidal:* The TOPO coated NC are transferred into a pyridin solution, which replaces the organic ligand shell (here depicted are spherical and rod shaped CdSe/ZnSe and CdSe NCs, with both possible ligands sketched as partial shells). *Epitaxial:* An epitaxial ZnSe buffer layer is grown onto a GaAs wafer. *Hybrid:* The pyridin NC suspension is deposited on the buffer layer. A heat treatment evaporates the solvent and leaves the pure semiconductor NCs on the buffer. The ZnSe deposition is resumed and incorporates the colloidal NC in the epitaxial ZnSe host material.

MEE cap layer growth to a minimum. Additionally CdSe/ZnS core-shell NCs exhibit a large quantum yield and are widely studied. The room temperature luminescence of the CdSe/ZnS dots was centered at 530 nm.

6.2.1 Structural Properties

A scanning electron micrograph (SEM) of a sample of CdSe nanorods covered with a 6 nm thin layer of ZnSe is shown in figure 6.5. The overgrowth was carried out in the migration enhanced epitaxy mode (MEE) at 240°C at a growth rate of approximately 0.255 ML/s. In this growth mode, the enhanced mobility of adatoms on the buffer surface supports the incorporation of the three-dimensional objects into a structure that, with increasing cap layer thickness, should transform into a two-dimensional flat surface again. At the stage

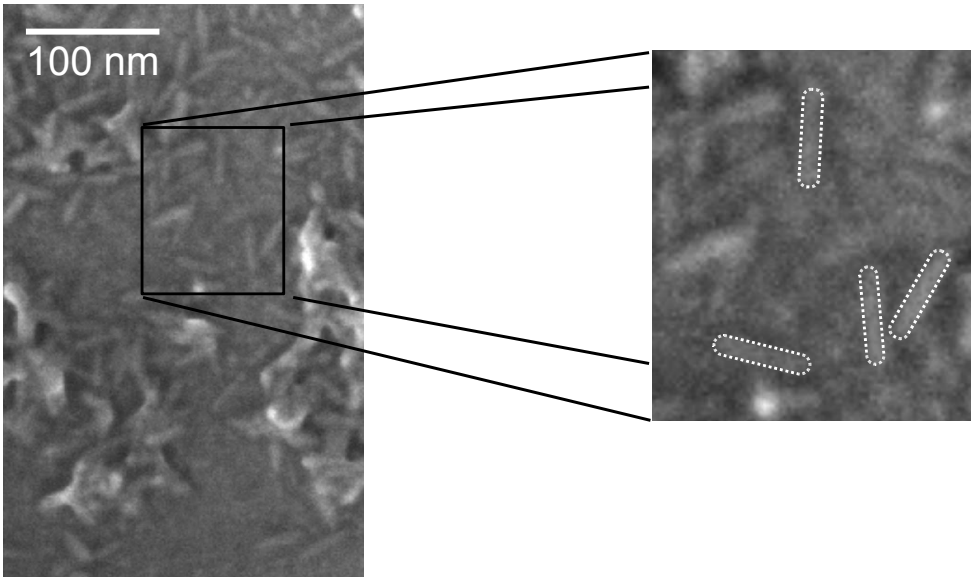

Figure 6.5: Scanning electron micrograph of CdSe nanorods overgrown with a 6 nm cap layer. The rods highlighted in the zoomed area on the right have a length of 34.7 ± 0.5 nm, and a diameter of 6.7 ± 0.5 nm, close to their original dimensions before overgrowth.

depicted in this figure, the silhouette of the nanorods is still visible and shows an almost unaltered shape and size compared to the originally deposited NCs.

The further evolution of the cap layer crystallinity, that is, the transition from a 3 dimensional surface consisting of a flat buffer impregnated with NCs, towards a 2 dimensional flat surface of NCs buried underneath a cap layer, is monitored by RHEED, as shown in figure 6.6. When the cap layer thickness approaches the NC diameter, the surface quality improves, as evidenced by the development of the streak features in the RHEED pattern, characteristic for two dimensional surfaces. This development can also be seen on the decrease of the FWHM of the first order diffraction streak.

Since a selenium to zinc flux ratio of 3:1 is known to produce (001)-ZnSe layers of highest perfection and smallest defect density, this condition was employed for the cap layer growth. However, the stability of NC annealed in the MBE chamber was weakened in the presence of a selenium overpressure, which is why the cap layer growth was performed under a stoichiometric flux ratio additionally. It turns out, that the stoichiometric condition, favorable in terms of NC stability, also produces a better cap layer quality, in the presence of NCs. While the quality improves with growing cap layer thickness under both atomic flux ratios, the improvement is more pronounced in the case of a selenium to zinc ratio of 1:1.

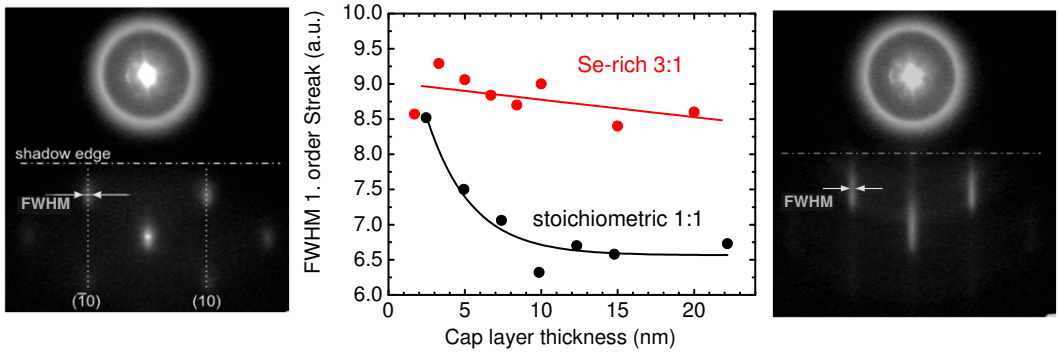

Figure 6.6: Crystalline quality of a cap layer grown with Zn to Se Flux ratios of 1:1 and 1:3. The FWHM value of the first order electron diffraction streak was monitored as a function of cap layer thickness. The extreme cases of streak patterns encountered are exemplified on the far left and right. The solid lines represents exponential and linear fit functions as a guide to the eye.

Since different kinds of NCs were used in the incorporation experiments, HRXRD measurements were carried out for both, the spherical CdSe/ZnS core-shell NCs and elongated CdSe rods. Although one could assume, that the larger volume of the rods ($L \approx 35$ nm, $d \approx 7$ nm) should give rise to inferior crystallinity as compared to the smaller spherical NC ($d \approx 2.3$ nm), the rocking curve in figure 6.7 shows a peak width of 27 arc seconds for the sample comprising incorporated CdSe rods, while the spherical NCs lead to a stronger broadening. The most likely explanation is that the cap layer quality is governed rather by the NC density, than merely the NC size and shape, assuming that the overall size stays below a certain limit. Under ideal conditions, the quality of a NC covering cap layer can be comparable to the quality obtained when overgrowing the buffer after exposure to pyridine, which was found to exhibit a rocking curve of 25 arc seconds FWHM in section 6.1.2.

A higher resolution investigation by HRTEM of a sample comprising a thin cap layer over the nanorods is shown in figure 6.8. The ZnSe buffer / ZnSe cap interface has been extrapolated from a larger scale overview TEM. The crystallographic axes of the matrix itself are indicated, defining the view to be in [1 -1 0] direction. Parallel to this direction is the c-axis of a CdSe rod, whose cross section is visible above the buffer layer. The hexagonal wurtzite crystal system of the CdSe rod viewed along the (0001) axis contrasts the cubic zinc blende lattice of the ZnSe host. The capping is incomplete and about 1 nm in thickness. This allows a monitoring of the onset of the overgrowth procedure, which fastens the NC to the buffer layer without the formation of gaps. The further incorporation takes place without deposition below the NC, which would leave it floating on the additional material. The material deposition furthermore is not hindered by a shadow effect of the

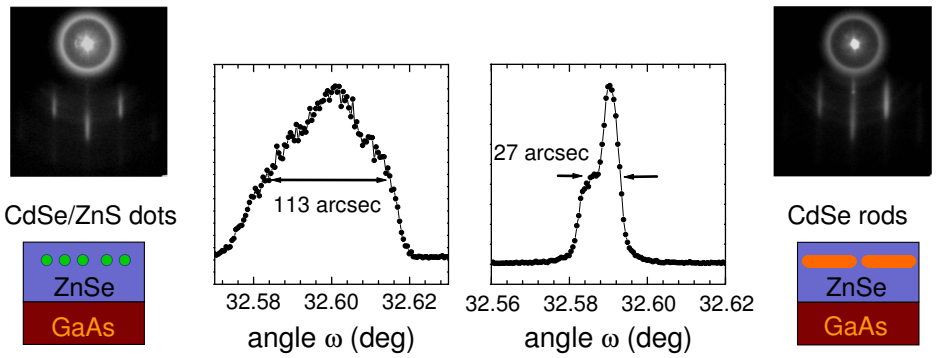

Figure 6.7: The structural quality of a 22 nm ZnSe cap layer grown in MEE mode on top of CdSe/ZnS dots (left) and CdSe rods (right). The rocking curves show a broadening that, in contrast to size considerations, is smaller for the larger rods. The cap layer quality seems to be determined by the amount of NC deposited and can ideally be comparable to the case of overgrown pyridine, without any NCs (see fig. 6.2)

NCs.

In figure 6.9 a high resolution TEM overview of a sample comprising CdSe rods and a 12 nm ZnSe cap layer grown at 240°C in MEE is shown. Here the different growth scenarios encountered are represented. In the absence of a NC, the ZnSe buffer layer is capped with epitaxial, defect free ZnSe as visible on the far right and left. A CdSe nanorod is visible in the middle of the field of view. It is perfectly connected to the buffer, as already observed

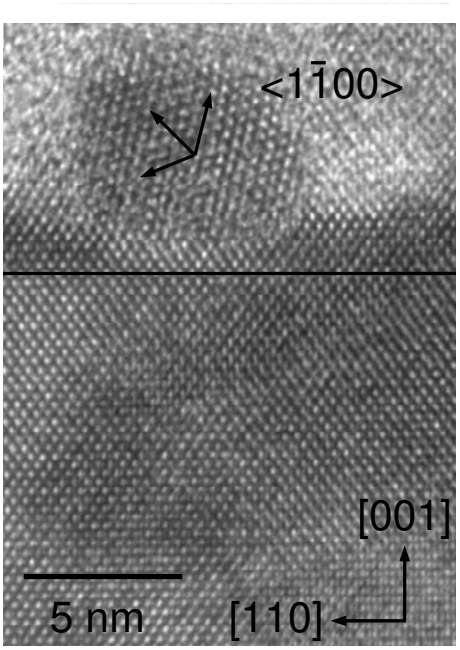

Figure 6.8: TEM of a CdSe nanorod in cross sectional view, overgrown with a thin cap layer. The onset of the overgrowth is accompanied by a fastening of the NC to the buffer layer, without the formation of gaps. The crystallographic axes of the host ZnSe matrix as well as the guest CdSe nanorod are indicated. The buffer-cap boundary that was extrapolated from a larger field of view TEM is indicated as a black line.

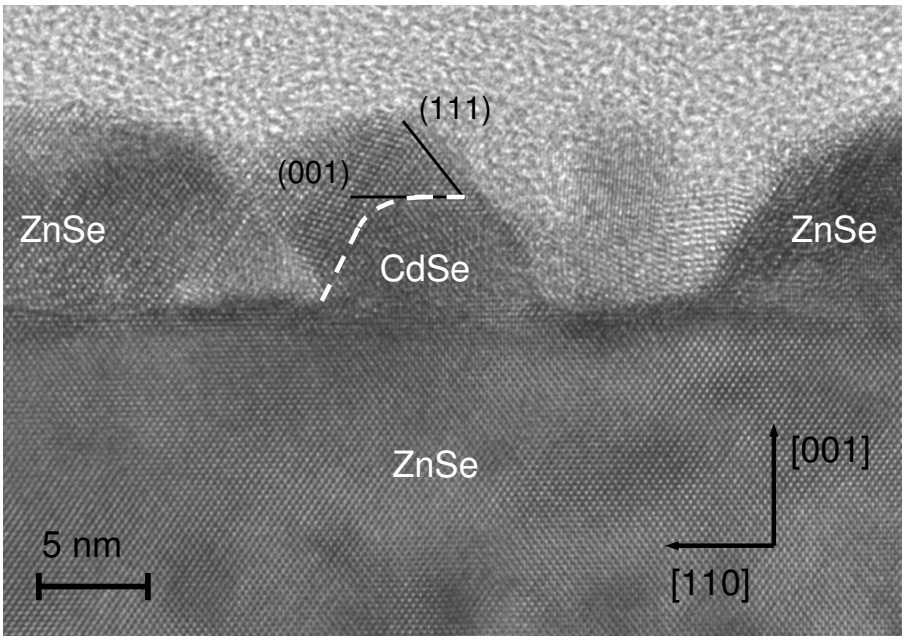

Figure 6.9: Overgrowth modes of ZnSe on a CdSe nanorod. A 7 nm diameter nanorod overgrown with 12 nm ZnSe is attached perfectly to the underlying ZnSe buffer. The connection to the ZnSe cap layer is epitaxial on top and to the left on the NC, defects form at a distance of a few nm to the left. Incomplete overgrowth is encountered on the right side of the NC, while in its absence to the far right and left, the cap layer again is epitaxially attached to the ZnSe buffer.

in a sample resembling the onset of the overgrowth process. Left and above the NC, the incorporation in the host matrix is evidenced by the fact that the matrix was grown in the same orientation as the buffer layer, without any defects. While in the growth direction, this defect free matrix can be traced up to the sample surface, strain relaxation in the lateral direction introduces defect lines a few nm away from the NC. The region to the right of the nano rod shows an impeded overgrowth, most likely due to the presence of an additional NC, hardly visible in the HRTEM, because it is not aligned along a low index zone axis.

6.2.2 Hybrid Samples - Optical Properties

With the structural characterization confirming an incorporation of the NC in the semiconductor matrix, the same samples were examined for their optical properties in the μ-PL setup . The excitation wavelength was chosen to correspond to an energy above both, the band gap of the ZnSe matrix, and the quantum confined ground state level of the CdSe

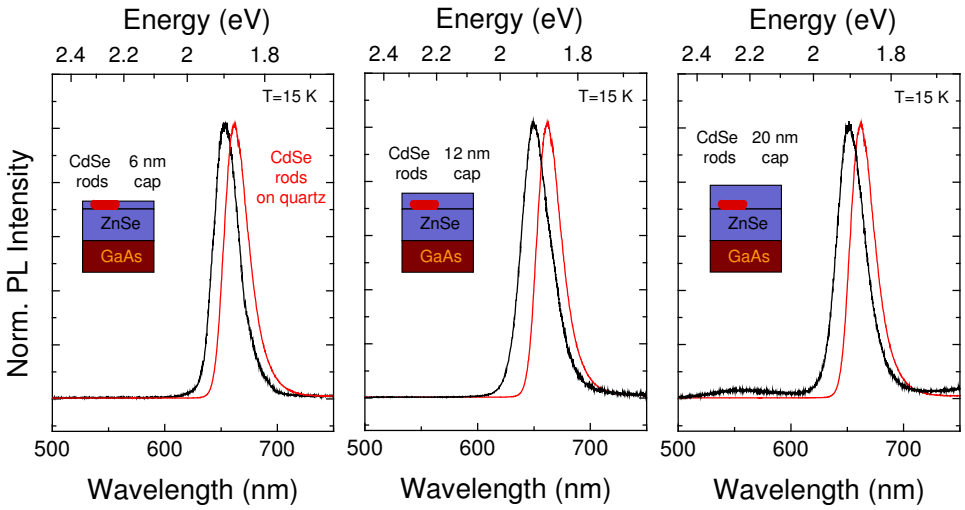

Figure 6.10: Normalized PL of CdSe rods before and after overgrowth at 240°C in MEE mode with stoichiometric Se to Zn flux ratio. The Emission at 15 K is shown in normalized graphs. The emission maximum is blue shifted by 10-12 nm from its original peak position at 662 nm. The FWHM of 25 nm is only marginally broadened to 26 nm. When increasing the cap layer thickness to 20 nm, defect luminescence at 555 nm appears.

nanorod. In this way, excitations are created in the host matrix, from which they can be transferred by relaxation into the NC, and the NC itself, allowing for a large abundance of charge carriers for radiative recombination, even at moderate pump powers of 50 μW, corresponding to excitation intensities of around 30 Wcm^{-2}. To additionally limit the effects of photo degradation, the samples were kept at 15 K in a flow cryostat, while the luminescence was collected with a high NA, long working distance microscope objective outside the cryostat.

Figure 6.10 compares the emission of CdSe rods before and after incorporation into a ZnSe matrix of growing cap layer thickness. The luminescence of the samples, kept at 15 K, was recorded upon excitation at a wavelength of 435 nm. The PL peak position is shifted from 662 nm before, to 651-653 nm after application of the overgrowth procedure. The FWHM value of 25 nm is preserved, indicating no changes in the size distribution of the ensemble. The observed blue shift can be linked to a small reduction of the mean diameter of the nanorods. The spectral shift of 10 nm corresponding to 30 meV energetic shift, translates into a radius change of less than an monolayer of CdSe, if the simple quadratic size to emission energy relation given in the introduction is used. This is consistent with the slight radius changes observed in the TEM analysis.

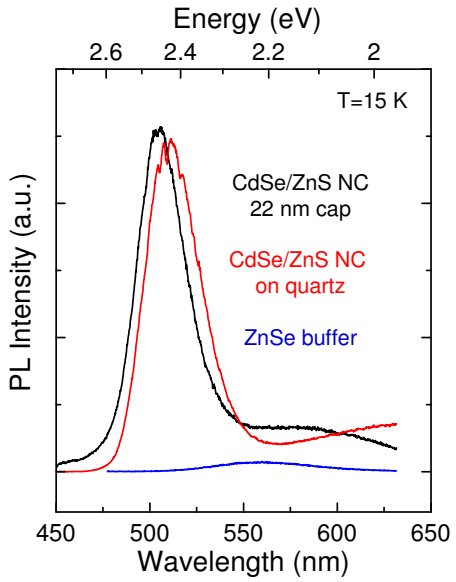

Figure 6.11: PL of spherical CdSe/ZnS NC on quartz and after incorporation in ZnSe, measured at 15 K upon excitation with 50 μW at 430 nm. The emission maximum is shifted from 510 nm to 504 nm, while the FWHM stays constant at 33-34 nm. The onset of a trap state related band centered at 650 nm is visible in the case of uncapped dots (red). The PL of the overgrown dots (black) exhibits only the quantum confined band edge emission and a contribution from defects in the ZnSe matrix (blue)

Another effect that might explain the observed red shift in NC emission is the change in dielectric confinement. It is known, that a high contrast between the dielectric constant inside and around the NCs can lead to a reduced emission energy [126]. This is the case when the NCs are characterized, embedded in a polymer or in vacuum. The encapsulation in a semiconductor matrix like ZnSe reduces the dielectric contrast and can thereby partially lift this effect. As a result, the overgrown NCs' emission is observed at higher energies than that of the NCs in polymer or vacuum.

In addition to the excitonic recombination, a defect related emission band appears at 555 nm, when the cap layer is extended to 20 nm, at the onset of relaxation via the introduction of structural defects. Due to the inhomogeneous wetting of the buffer layer, a comparison of the PL intensity is not possible, since the number of emitters probed by detecting over a certain detection area is not known well enough.

The overgrowth procedure was also applied to spherical CdSe/ZnS core shell NCs. The mean size of the NCs was chosen to be approximately 2.3 nm. The geometry of these smaller NCs should interfere less with the crystal growth, if comparable amounts of NCs are deposited on the buffer layer. The 1-2 ML of ZnS are applied in order to improve the confinement and therefore enhance the quantum yield of the NC emission at 525 nm. Figure 6.11 shows the recorded PL of such a sample and the corresponding NC before overgrowth. At cryogenic temperatures, the native NC PL is centered at 510 nm, and shifts to 504 nm after overgrowth. The FWHM stays constant as it was observed in the case of nanorods as the active emitters. A further opportunity the incorporation in epitaxial matrices offers is evidence by the disappearance of a trap related band visible in

the PL of uncapped CdSe/ZnS dots centered at about 650 nm. This feature is not visible in the luminescence of dots capped with 22 nm of ZnSe, where the only defect related signal seems to stem from the ZnSe matrix. This might also serve as an additional prove of the good connection of the NC to the host matrix and probable passivation effects on the NCs' surface.

Time-resolved Luminescence

As an additional probing of the optical properties of buried NCs, the dynamics of the radiative recombination were addressed in a time-resolved luminescence experiment, as described in section 3.3, and compared to the original, uncapped NCs' properties. Like in the time-integrated experiments before, the excitation condition was chosen to be far off-resonant, that is, above the band gaps present in the system. As the pulsed excitation source, the frequency doubled output of a Ti:Sapphire laser with a pulse duration of 150 fs was used.

Since the decay traces suggest the presence of a decay time component beyond the resolution of the photon counting apparatus, the system response was included in the data fitting in the following way: The decay was assumed to be of a bi-exponential character, with an additional distribution of the two recombination times around their mean values. This is modeled by the use of a two component stretched exponential function 6.1.

$$I_{PL}(t) \propto A_1 \cdot \exp\left[-\left(\frac{t}{\tau_1}\right)^{\beta_1}\right] + A_2 \cdot \exp\left[-\left(\frac{t}{\tau_2}\right)^{\beta_2}\right] \tag{6.1}$$

The result of a simulation of the PL decay according to this equation was then convoluted with the response function of the system, and compared to the measured decay traces. The response function itself was obtained by measuring the laser pulse intensity with the same apparatus. Since the laser pulse duration is short, compared to the temporal resolution of the used system, and therefore would appear as a delta function in an ideal time-resolved measurement, a fit of the actually measured laser intensity to a gaussian distribution function 6.2 yields the system response.

$$I_{Laser}(t) \propto \exp\left[-\left(\frac{t-t_0}{w}\right)^2\right] \tag{6.2}$$

The FWHM of equation 6.2 is connected to the parameter w by $2w\sqrt{\ln 2}$. The values found to be consistent with the measured responses are FWHM = 830 ps for the low res-

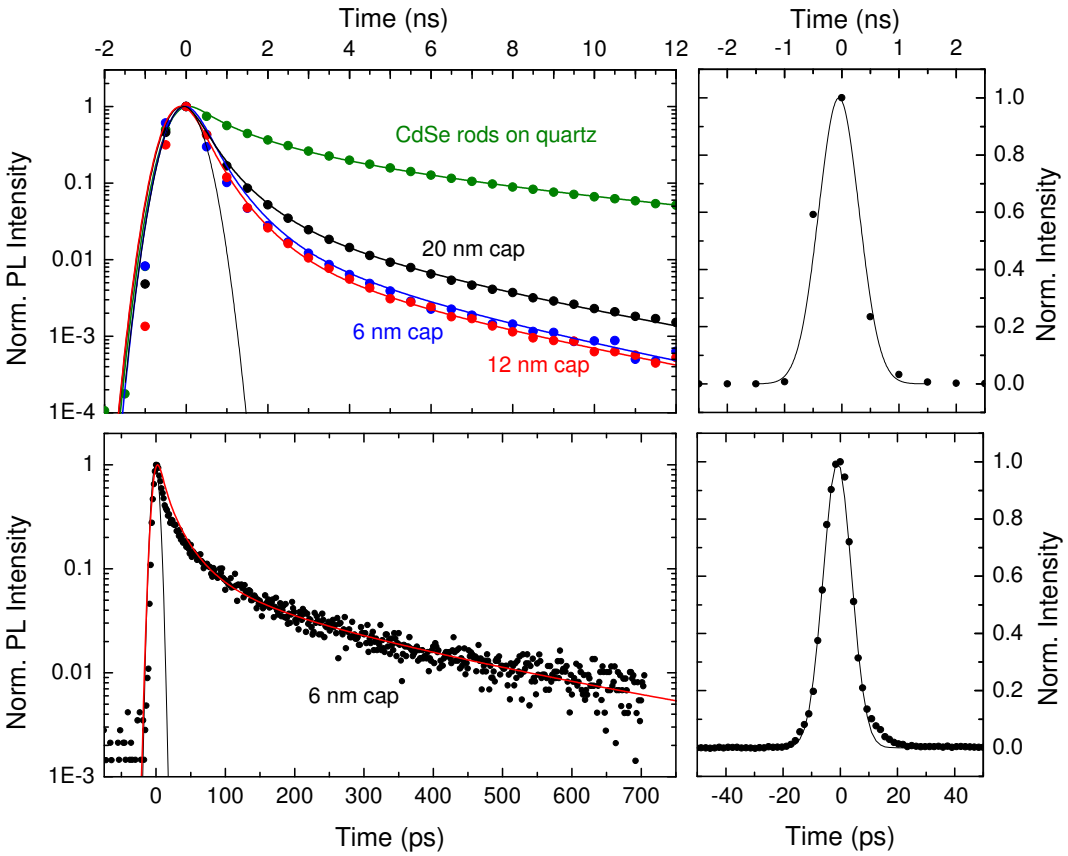

Figure 6.12: Time-resolved PL of CdSe rods before and after overgrowth at 15 K. The top left panel shows the PL of CdSe rods before overgrowth (green), and after capping with 6 nm (blue), 12 nm (red), and 20 nm (black). The lower left panel shows the PL trace of the sample capped with 6 nm recorded with higher temporal resolution. The solid lines are obtained from a convoluted fit function with the parameters listed in table 6.1. The right panels show the measured exciting laser intensity and a gauss-shaped fit resembling a FWHM of 830 ps (top) and 12 ps (bottom).

olution and FWHM = 12 ps for the high resolution setup. These values enter a numerical algorithm, based on the definition of the convolution as:

$$(f \circ g)(t) = \int_{-\infty}^{+\infty} f(\tau) \cdot g(t-\tau) d\tau \tag{6.3}$$

The discrete version of the convolution then follows:

$$(f \circ g)(n) = \sum_{m=-\infty}^{\infty} f[m] \cdot g[n-m] \tag{6.4}$$

In practice, the convolution is performed by a C-based program written in "LabWindows". The main calculation is realized by the nested loop:

cap layer	A_1	τ_1 (ps)	β_1	$<\tau_1>$ (ps)	A_2	τ_2 (ps)	β_2	$<\tau_2>$ (ps)
20 nm	0.965	120	0.65	164	0.035	600	0.6	902
12 nm	0.988	100	0.65	136	0.012	550	0.6	827
6 nm	0.982	100	0.65	136	0.018	500	0.6	752
0	0.72	300	0.62	433	0.28	1700	0.6	2560
6 nm (fast)	0.95	5	0.6	7.5	0.05	95	0.7	120

Table 6.1: PL decay fit parameters. The last line represents the data obtained from a streak camera based experimental setup with faster temporal resolution.

```
for(i=0;i<maxtime;i++) {
  for(j=0;j<(maxtime-i);j++) {
    convolution[i+j]=convolution[i+j]+decay[j]*response[i];
  }
}
```

The cell index i is scaled with the time resolution of the according setup to obtain the correct x-axis values. The variable *maxtime* represents the number of data points for which the convolution is performed. The variables *decay* and *response* carry the decay function and the response function defined by 6.1 and 6.2 respectively. Table 6.1 lists the parameters that produce the fitting curves displayed in figure 6.12.

Since the use of a stretched exponential decay function resembles a decay according to a distribution of mono-exponential decay functions, a parameter suited for comparison of the decays is the average decay time $<\tau>$ calculated according to equation 6.5 [70].

$$<\tau>=\frac{\tau}{\beta}\cdot\Gamma\left(\frac{1}{\beta}\right) \tag{6.5}$$

The PL decay of the CdSe nanorods deposited on quartz comprises average decay times of 430 and 2560 ps. After the incorporation in a ZnSe matrix, the decays found exhibit significantly faster decays, described by a fast component around 150 ps and a slower component ranging from 750 ps to 900 ps. Since the fast component is beyond the resolution of the TCSPC setup, the sample with the fastest decay was additionally examined in a streak camera system of faster temporal response (see also section 3.3). While a component of 120 ps average decay time was confirmed, even here an ultra fast component on the scale of 7.5 ps was found. These very fast PL decays are most likely linked to trapping of excitations and non-radiative recombination processes. The influence of the cap layer thickness is evident in the increase of one of the PL decay times from 750 ps to 830 ps and 900 ps, when the covering layer thickness is increased from 6 nm to 12 nm and 20 nm.

Since the changes introduced to the optically active material by incorporation in a new matrix can be expected to be significant, a number of possible interpretations of the observed modifications should be taken into account.

The PL intensity is proportional to the product of the population of excitonic levels and their characteristic recombination time. The population itself is depleted by radiative and non-radiative recombinations, while it is increased by the exciting laser pulse as well as by a possible excitation transfer from the ZnSe matrix. An accelerated PL decay (with respect to the non overgrown NC) can be linked to both, a decreased radiative recombination time, and a decreased non-radiative recombination time. Even a reduction in the amount of energy transferred from the surrounding matrix can account for such a PL modification.

Since there is no energy transfer present, when the NCs are placed on a quartz substrate, only an increase in transfer is possible, when switching to the semiconductor matrix. This rules out the last point as an explanation for the accelerated PL decay.
An increase in the number of non-radiative recombination channels, or a decrease of their respective time constants should be accompanied by a reduction in PL intensity, since these channels act as additional means of excitation depopulation.
An increase of the radiative recombination rate in contrast should be evidenced by an increase of the PL intensity, since more excitons recombine radiatively per time interval. However, the PL intensity is not suited as an additional source of information about the recombination efficiency, since the number of emitters within a given detection area is unknown. This motivates the effort to achieve homogeneous NC distributions on the buffer layer, as it will be discussed in the next section.

At this stage the modifications in the PL dynamics may be interpreted in the following way: NCs covered with a thin cap layer show an accelerated PL decay, fittable to a two component stretched exponential function. The fact that the decay is not mono-exponential strongly hints towards the presence of multiple recombination channels influencing the PL dynamics. An accelerated radiative recombination of excitons can be expected in the case of NCs embedded in a ZnSe matrix, since the reduced contrast in the dielectric function (compared to NCs in air) allows a further extension of the excitonic wave function, leading to a larger transition dipole moment. Considering the model case of an excited atom emitting into vacuum, the influence of parameters affected by the overgrowth procedure can be estimated, when considering the connection to the radiative decay time [71].

$$\tau = \frac{1}{k_{rad}} = \frac{3c^3\varepsilon_0 h}{16\pi^3\nu^3\mu^2} \tag{6.6}$$

While Planck's constant h and the speed of light c are naturally constants, the dielectric properties of the environment have to be taking into account by the introduction of ε_r in addition to the vacuum dielectric constant ε_0. Also the induced transition dipole moment μ can be changed due to a modified overlap of the electron and hole wave function, which can extend into the surrounding matrix material. To a smaller extend, the shift in emission wavelength can influence the recombination time via the frequency ν.

The fact that the acceleration of the NC PL decay is most pronounced in the case of the thinnest cap layer, and approaches larger values with growing cap layer thickness suggests, that stronger non-radiative recombination is enabled by defects, formed in the early stages of the overgrowth. These defects play a less important role when the layer thickness is increased. The lack of a recovery of the original PL decay time, even at relatively thick cap layers can be interpreted as a proof for the actual modification of the excitonic wave functions' extension and thereby the induced transition dipole moment.

An interesting observation was made when monitoring the PL intensity of buried NC ensembles over a time of several minutes to hours. When investigating the PL of NC ensembles that are either completely unprotected, surrounded by a TOPO ligand shell, or even embedded in polymer, the PL intensity typically decays on a time scale of several seconds to minutes. This process is faster at room temperature than at cryogenic temperatures and attributed to photo degradation [119]. In the hybrid colloidal-epitaxial structures, in contrast, an increase of the PL intensity by a factor of two was encountered, when the optical excitation was carried out with a HeCd laser emitting at 325 nm (3.8 eV), as displayed in figure 6.13. This could be caused by laser induced annealing, which heals out defects and non-radiative recombination centers, increasing the quantum yield of the buried NC over time. While the detailed investigation of this phenomenon was beyond

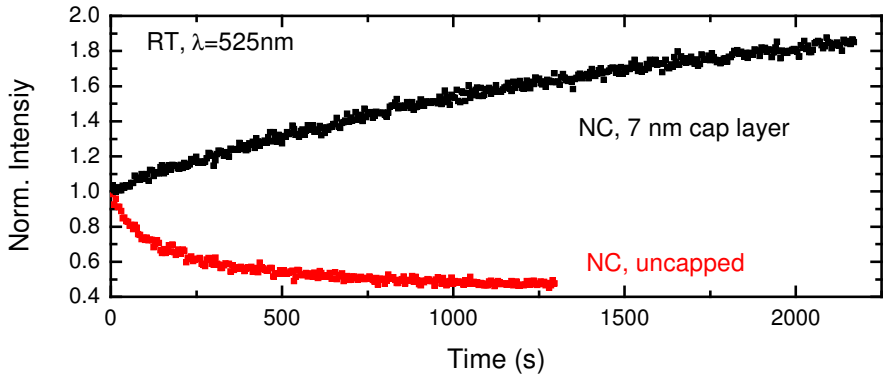

Figure 6.13: Evolution of the PL intensity of buried and uncapped NC.

the scope of this work, it demonstrates the additional opportunities for optimization of semiconductor opto-devices by hybrid colloidal-epitaxial growth technology.

6.3 The Low Density Limit - Towards Buried Single Emitters

The decoupling of the NC synthesis from the embedding in an epitaxial semiconductor structure shown in the previous section enables a large variety of new applications and improvements [128]. One of them is the chance to go beyond the minimal areal density of about 1×10^8 cm^{-2} encountered in self organized QD growth. This limit should not apply to the hybrid colloidal-epitaxial growth mode, since arbitrary amounts of NCs can be deposited. This brings the limit of low emitter densities into reach.

6.3.1 Wetting of Buffer Layers with Nanocrystals

In order to achieve an even distribution of NCs across the sample with a controllable areal density, the wetting properties of various buffer layers and deposition methods were tested before the actual overgrowth. To this end, the GaAs substrates with ZnSe buffer layers of varying thickness were impregnated with NCs by drop casting or spin coating as described in detail below, and the wetting judged by optical measurements.

Drop Casting

A straight forward approach is the deposition of NCs out of a droplet of NC suspension on the substrate, which is then left to dry. The NC carrying solvent of a droplet of approximately 10 μl wets the full sample area of typically 3×5 mm. The evaporation, which is completed on a time scale of seconds to minutes, leads to a shrinking of the droplet. The air-liquid boundary sweeps across the surface, accumulating the NCs in a smaller area, which finally exhibits the highest areal density of NCs. This method is suited for the preparation of samples with a variation of NC densities on the surface, namely a low concentration of NC at the outer parts, and a higher concentration in the position of the final solvent evaporation. While this is desirable if various NC densities should be examined on one sample, other methods need to be employed in order to obtain a good predictability and reproducibility of the result.

A number of additional methods of NC deposition were tested and found to produce similarly uneven wettings. These include the pressing of a wetted stamp onto a substrate,

and heating a NC wetted conductive filament by applying a current, in close proximity to the substrate, which causes the NCs to spray off the filament onto the buffer.

Spin Coating

A method derived from standard procedures for covering, for example, semiconductor wavers with thin films of photoresist, was employed for reproducible surface coverages of NCs on the substrate. Here, the sample substrate was mounted on the rotary table of a spin coater. It is then wetted with a measured volume of NC suspension. Subsequently the table is rotated while controlling the parameters acceleration, revolutions per minute and overall spinning time. The process of deposition is thereby altered in a way that the centrifugal force over-compensates the surface tension of the evaporating solvent, removing the remaining liquid quickly. It therefore can be assumed, that the final distribution of nanoparticles on the surface is not governed by the drying process, but by the adhesion of the NC to the sample surface in the short time before the solvent is removed. In this way the decisive parameters are the number of available NC for deposition, given by the NC concentration and suspension volume, and the buffer surface properties composition and roughness. This interpretation is supported by the fact that a set of parameters, suited for a given NC areal density on one substrate, can be unsuitable when the substrate properties are changed. This was encountered, when changing the substrates from quartz to GaAs and finally ZnSe.

Another promising deposition method for reproducable and even, low areal densities makes use of a high efficiency nebulizer, through which a NC suspension is sprayed onto the surface. This method is currently tested and might be employed in future overgrowth experiments.

Method of Surface Coverage Evaluation

The PL signal obtained from these samples was recorded with a μ-PL setup as described in section 3.2. Since the GaAs waver absorbs the blue and green laser lines suited for the excitation of the NCs, the confocal excitation geometry was chosen. A pre-focusing of the beam displaces the actual excitation focus along the optical axis with respect to the focus of detection. The slightly out of focus excitation illuminates a larger sample area of 10-20 μm diameter, to enable an estimation of the NCs' areal density. For reference and further data processing the spatially resolved PL signal, detected with a high sensitivity CCD camera, was recorded with a video card.

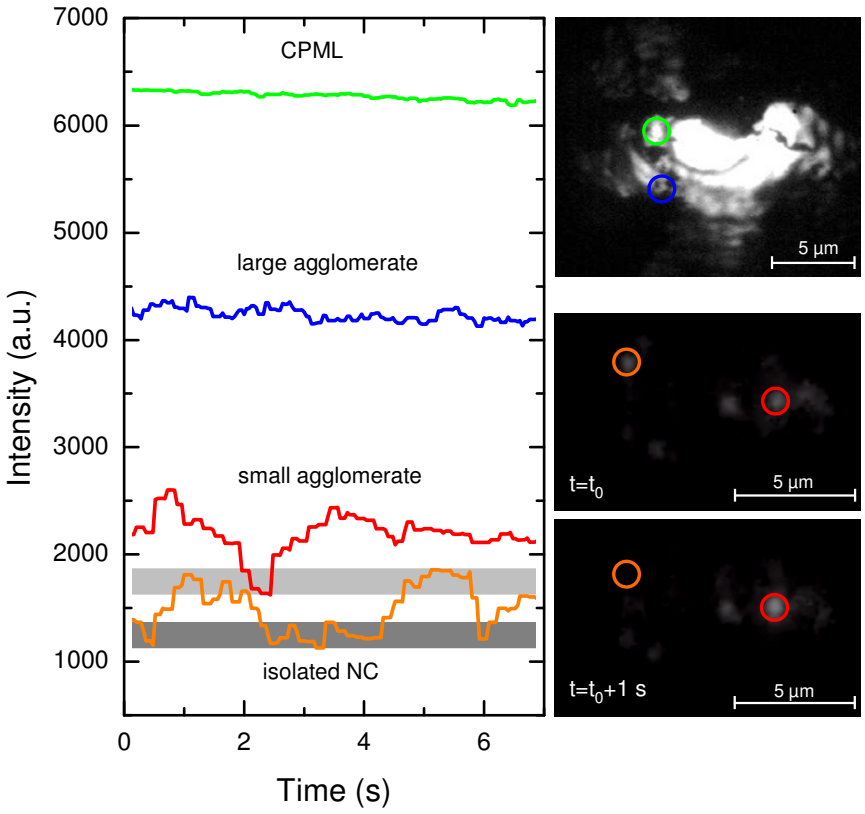

Figure 6.14: Examples of PL of NCs on a ZnSe buffer layer plotted on the same intensity scale. The left panel shows the temporal behavior of the PL intensity of the NC ensembles. The closely packed multi layer (green) displays high intensity and little fluctuations over time, apart from a general decrease in signal strength due to photo degradation. When decreasing the ensemble size, the fluctuations become more evident (blue). Only one snapshot of this field of view is shown on the right, since the fluctuations are hardly visible in the according video. The small agglomerate (red) displays a multi modal distribution of the PL intensity, while a single NC (orange) can be identified by it's "on-off" blinking behavior. The lowermost gray shaded area marks the detection background, while the light gray area above that marks the intensity observed when one NC is in the "on" state. This is also visible on the two lowermost snapshots, displaying the same field of view approximately one second apart.

The information accessible with this measurement include the size of the luminescent areas as well as the intensity, which enables the distinction between extended areas that are fully covered with a closely packed multi layer (CPML) of NCs, micrometer sized agglomerates, and smaller agglomerates, whose spatial extension is below the resolution limit. Recording the PL over a time of many seconds additionally allows for a distinction between these agglomerates and single NCs:

Both, small agglomerates and isolated NC are smaller in size than the spatial resolution, which causes a point-like appearance on an optical detector. However, the variations in PL intensity over time are averaged out in an ensemble of many NCs that individually either emit, or not. This results in fluctuations of the intensity on the order of the statistical noise level of $\sqrt{N}$ with N NCs in the ensemble.

Isolated NCs, that is, NCs that are separated by more than the spatial resolution of the μ-PL setup, are recorded either in their "on" or their "off"-state [84]. Their intensity fluctuations therefore show a bimodal distribution between the detection background level and the a maximal emission intensity corresponding to an individually detected NC. This leads to the observation of the "blinking" behavior also described in section 1.4.4. Figure 6.14 gives examples of the method described here. When decreasing the amount of NCs, whose emission is detected in conjunction, the signal strength decreases, as indicated on the intensity axis, which is valid for all time traces. From the CPML through large and small agglomerates, the reduction in intensity is accompanied by a reduction in the averaging effect, that leads to a multi modal distribution in the case of small agglomerates and finalizes in the bimodal blinking behavior. Judging the according video captures of the PL signal allows for a classification of the samples under investigation into CPML, agglomerate or isolated NC containing. In the latter case an areal NC density can be estimated additionally.

Buffer Layer Strain

For the incorporation of NCs in a matrix, without explicit emphasis on the isolated character of the NCs, the parameters chosen for the buffer layer growth were following empirical values suited for the optimization of a purely epitaxial growth. These values of experience suggested the deposition on a typically 45 nm thick ZnSe layer. Since one of the decisive parameters for a good NC deposition was identified as the buffer layer roughness, a more detailed investigation of the buffer layers was performed.

The growth of the ZnSe buffer layer on the GaAs wafer is strongly influenced by the lattice mismatch and the buffer layer thickness. Since the lattice parameters of the ZnSe-GaAs pair differ by only 0.3 % (GaAs 0.5653 nm, ZnSe (cubic) 0.567 nm), the buffer layer will initially grow pseudomorphically, that is, with the GaAs lattice constant. The critical thickness, above which the ZnSe starts to relax to resume growth according to its native lattice parameters is approximately 200 nm, while thicknesses exceeding 500 nm are considered to be fully relaxed [130]. For a comparative study of the wetting properties of strained and relaxed buffers, the limiting cases of "fully strained", represented by samples

of buffer thicknesses from 45 to 80 nm, and "fully relaxed" with 1 to 4 μm thickness were prepared. In the latter case, the surface shows a considerable roughness that should support the deposition of NCs.

The crystallographic (001) surfaces that are usually grown are terminated by only one of the two atomic species, selenium and zinc, exclusively. In order to include mixed surfaces in the survey, buffers resembling the (-110) or the (110) surfaces were prepared additionally. Purely zinc terminated surfaces were obtained by MBE and by etching a buffer surface with carbon disulfide (CS_2).

The crystalline perfection of the buffer layers was examined by HRXRD. It can be assumed, that the number of dislocations that break the periodicity of the lattice and therefore lead to the observable broadening of rocking curves, is also a measure for the imperfection of the buffer surface, in other words, the roughness that favors the NC deposition.

The rocking curves obtained from samples of varying buffer layers display a width of 5 to 50 arc seconds, when increasing the layer thickness from 5 to 100 nm, that is, within the strained regime. The relaxation initiated with further increasing thickness is linked to the introduction of dislocations. The defect density therefore rises in the intermediate regime, until it decreases again above thicknesses of 1 μm, as indicated by a reduction in the rocking curve FWHM from about 350 arc seconds down to 160 arc seconds at 4 μm buffer layer thickness (data not shown).

Results of Deposition Procedures

As already mentioned, the drop casting method produces uneven wettings, which holds for both, strained and relaxed substrates. Using suspensions of NC concentrations between 10^9 and 10^{13} μL^{-1} on strained surfaces, the final NC distribution ranges from small NC agglomerates to closely packed multi layers. In every case, the abundance in the outer regions of the sample is drastically reduced as compared with the center. The crystallographic orientation seems to be of no importance, since comparable results were obtained on strained ZnSe (001), (-110) and (100) surfaces.

Spin coating strained buffers produces a more homogeneous distribution of particles, which still tend to aggregate, even at low NC concentrations ($< 10^{11} \mu L^{-1}$) in the suspension. The agglomerate size is however small and more uniform, and the distribution across the surface is more homogeneous. Zinc terminated surfaces did not improve the result.

On relaxed surfaces, the drop casting method allows the deposition of isolated NC only when using low NC concentrations. Their distribution is inhomogeneous in this case, and isolated NC are mixed with agglomerates of various sizes.

The spin coating method on relaxed, selenium terminated surfaces produces reproducible results in the deposition of isolated NC. The used suspension concentration can be varied over a wide range without changing the result. The achieved values and their statistical errors are given in table 6.2. The obtained areal densities of $\sim 1 \times 10^7 \mathrm{cm}^{-2}$ falls below the minimum value attainable in the SK growth mode by one order of magnitude.

c in $\mu\mathrm{L}^{-1}$	areal density in 10^7 cm^{-2}
10^9	1.2 ± 0.2
10^{10}	1.5 ± 0.3
10^{11}	1.4 ± 0.2

Table 6.2: NC areal densities as a function of NC suspension concentration. The deposition was performed in a spin coating process with fixed acceleration parameters at 2000 rpm.

The effect of the high temperatures needed for MBE growth on NC ensembles was already tested. A similar experiment was carried out on samples exhibiting a low NC density, by monitoring the number of isolated NCs before and after heating the substrate. A substrate with a ZnSe buffer thickness of 1μm was impregnated with NCs in the spin coating procedure, resulting in an average density of isolated NC of 0.15 $\mu\mathrm{m}^{-2}$. The NC were again identified by their blinking PL behavior. The sample was then transferred to the MBE chamber and heated to 300°C for 10 minutes in ultra high vacuum. A repetition of the μ-PL experiment showed a density of isolated NC reduced by a factor of approximately 3, comparable to the result obtained from PL intensity measurements on NC ensembles before and after heating.

Buffer Layer: Optical Properties

According to the result of the various deposition procedures, using relaxed buffer layers combined with spin coating is the most promising method of NC deposition. This implies, that the parameters of growth that produce buffer layers that favor the deposition of isolated NCs differ from those that minimize the defect density. In order to judge the resulting background luminescence that has to be expected from the buffer layer, samples of different buffer layer thicknesses were tested for their PL. The observed defect luminescence can be attributed to a number of origins [43].

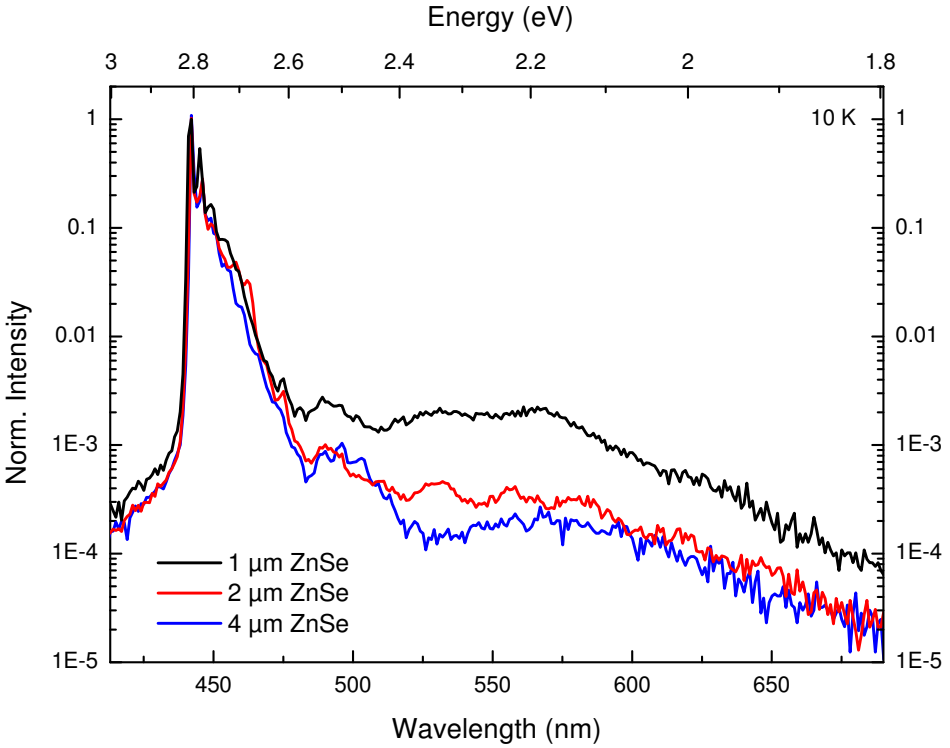

Figure 6.15: Buffer layer defect luminescence (log scale) as a function of buffer thickness.

An emission at 443 nm (2.8 eV) corresponds to the recombination of excitons and excitonic complexes in the ZnSe. The complexes are composed of the exciton bound to impurities acting as donors or acceptors. At lower energies, a pronounced spectral feature is the y-defect at 477 nm (2.6 eV), commonly attributed to extended defects and dislocations. Additional transitions between shallow donor and deep acceptor levels and their respective phonon replica have been summarized as the s-band around 496 nm (2.5 eV). The unavoidable contamination of MBE grown samples with copper traces, due to the employment of copper seals in the ultra high vacuum apparatus, gives rise to a broad emission feature between 515 nm and 540 nm (2.3-2.4 eV). Zinc vacancies can additionally lead to emission in this spectral region, when binding excitons. The abundance of these recombination centers is reduced with growing buffer layer thickness, in that a thicker layer approaches the full relaxation with reduced vacancy density. In an experiment with moderate spectral resolution, the buffer luminescence due to the aforementioned recombination mechanisms overlap. For experimental investigations of low NC densities, a buffer layer of lowest possible defect emission is therefore chosen, which translates into a layer thickness of 4 μm. The luminescence properties are furthermore influenced by the fabry-perot modes introduced by multiple reflections at the air-ZnSe and the ZnSe-GaAs

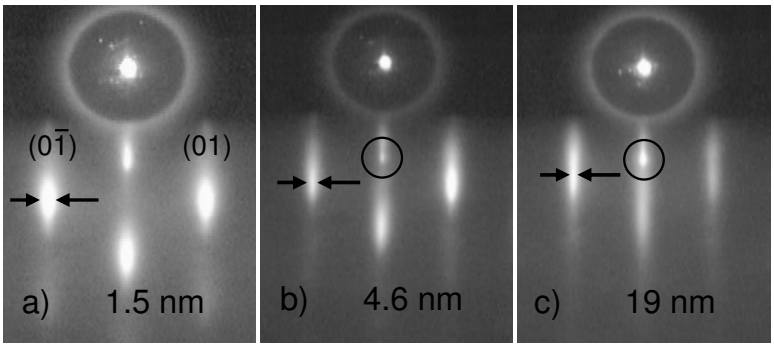

Figure 6.16: RHEED monitoring of the overgrowth of isolated NC. Increasing the cap layer thickness reduces the FWHM of the first order streak signal by a factor of 1.8. The overall development into a streak pattern and the appearance of the specular spot (circle) confirm the transition from three-dimensional to two-dimensional growth.

interface. These lead to a modulation of light intensity, when a spectrally broad emission from the sample is monitored. The same effect occurs, when white light is reflected from the sample, which enables an additional measurement of the cap layer thickness.

6.3.2 Low Density Hybrid Samples

Making use of the knowledge of suited parameters, gathered in the surveys described so far, leads to the fabrication of a low density hybrid sample in the following way:
A sample comprising a thick selenium terminated (001)-ZnSe buffer was wetted with CdSe/ZnS dots in pyridine, originally emitting at 530 nm at room temperature by spin coating. The resulting areal NC density was found to be 0.15 μm^{-2}. A cap layer was grown by MBE at 300°C, under a stochiometric zinc to selenium ratio of 1:1, and the crystallinity monitored by RHEED.

Structural Properties

Figure 6.16 displays the transition from an initially three dimensional growth to a two dimensional deposition of material when increasing the cap layer thickness to 19 nm. This is evidenced by the appearance of a specular spot, the reduction in FWHM of the streak features, and the overall transformation from a spot like to a streak like pattern. At a NC surface coverage of this low level, additional overgrowth experiments have shown, that comparable results are obtainable with both MEE and MBE. The low volume of the 19 nm cap layer, compared with the underlying 1 μm buffer prevent significant x-ray charac-

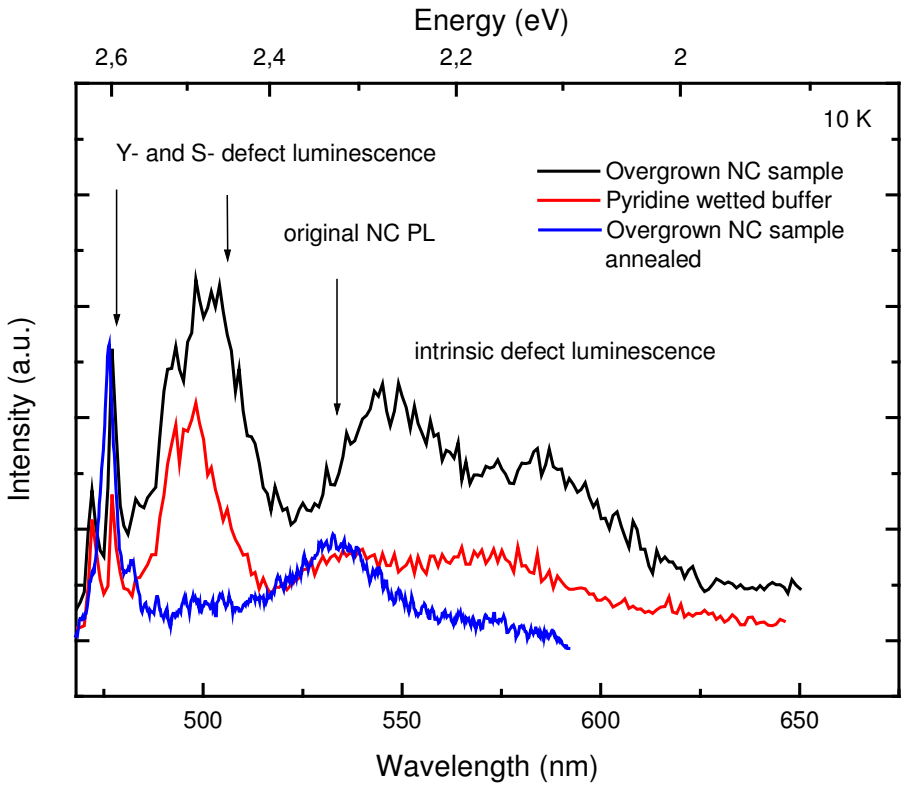

Figure 6.17: The PL of a sample comprising isolated NC (black) compared to a sample of overgrown pyridine (red). No clear identification of NC luminescence is possible. After a heat treatment, the defect luminescence intensity is reduced (blue). The intensity observed close to the original NC emission wavelength is broader and higher in intensity than expected for a single emitter and might therefore stem from a NC agglomerate or an artifact of modulated defect emission (see also text).

terizations. In order to achieve estimations of the cap layer quality, an additional sample comprising isolated NC, a 4 μm buffer, and a 400 nm cap was tested in HRXRD. The rocking curve indicates an about 1.6 fold increase in the defect density, when comparing the fully grown sample with the underlying buffer. An additional reciprocal space map confirms, that both ZnSe are oriented in the same way, without any tilt (not shown).

Optical Properties

The luminescence of the buried, isolated NCs was tested by collecting emission both, from a relatively large sample area in a standard PL, and with high collection efficiency in a μ-PL setup. The samples were kept at cryogenic temperatures and the excitation energy was chosen to be above the band gap of ZnSe. As stated earlier, the buffer layer properties that favor the deposition of single NCs, unfortunately also favors the formation

of defect luminescence centers. Consequently, the observed emission from the sample displays intensities that have to be attributed to the sources discussed in the previous subsection. Several investigated buffer layer thicknesses in the regime of full relaxation have led to similar results. An exchange of the NCs for a batch of different average size, in order to shift the luminescence of the incorporated emitters, likewise did not enable a clear distinction between defect related emission and NC luminescence. Figure 6.17 exemplifies the emission characteristics of isolated, overgrown NCs on relaxed buffer layers.

Annealing of Low NC Density Samples

The samples suited for the overgrowth of NC of low density exhibit a large number of structural defects, whose luminescence is hindering in the attempt to give experimental proof for the existence of buried NCs.

Since application of thermal energy to an imperfect crystal lattice is known to be capable of healing out structural defects, the attempt was made to reduce the defect density by tempering. Figure 6.18 shows the effect of such a procedure at 280°C for a duration of 30 minutes in the MBE chamber, applied to a sample comprising a strained buffer layer of 45 nm, spherical NCs, and a cap layer of 20 nm. An $\omega - 2\theta$-scan shows the x-ray intensity after reflection from the various interfaces in the sample and subsequent constructive or destructive interference. By dynamic diffraction theory, the intensity can be modeled and fitted to the experimental data with the layer thicknesses as fitting parameters. It is striking, that before the annealing procedure, the layer thickness in accordance with the diffraction pattern is 45 nm, while after the heat treatment 62 nm were derived. This can be explained by an effective healing of the structural defects, that mark the buffer-cap interface before the procedure. X-rays reflected by this boundary, and the GaAs-ZnSe boundary produce the 45 nm thickness signature. After the annealing, the buffer-cap interface fails to effectively diffract the x-rays, so that the buffer and cap layers become indistinguishable, and the result of 62 nm layer thickness is based on reflections from the GaAs-ZnSe interface, and the ZnSe-Air interface at the very top of the sample. The positive effect of the heat treatment is further corroborated by the reduction in the rocking curve FWHM from 100 to 63 arc seconds.

A prolonged and intensified tempering procedure was also applied to a sample with a relaxed buffer and evenly deposited NC of low density. The procedure was carried out at 350°C for a duration of 4 hours in an argon atmosphere of 300 mbar. The recorded PL is included in figure 6.17 as the blue curve. The reduced intensities at the spectral positions of the s defect, and the intrinsic defects seems to confirm the curing effect of

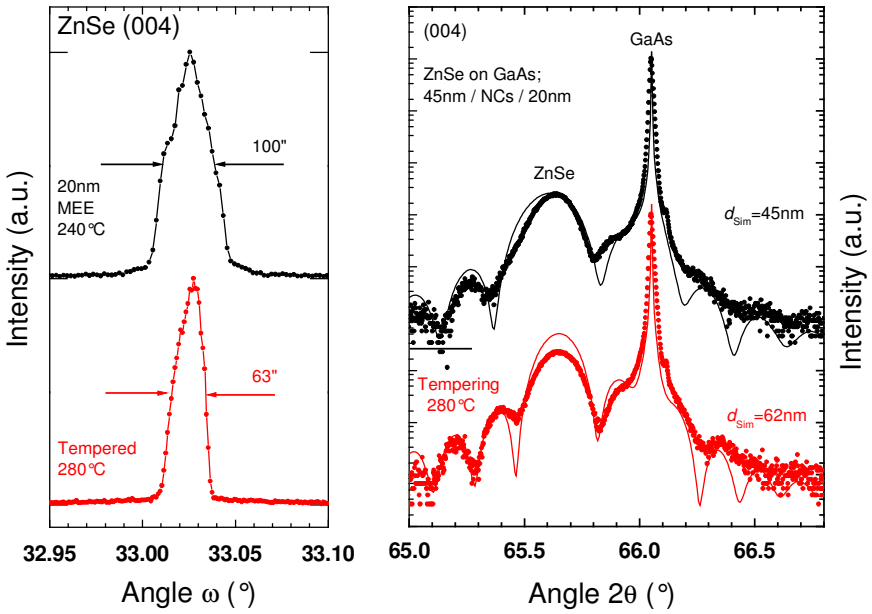

Figure 6.18: $\omega - 2\theta$-scan and rocking curves before and after annealing.

the treatment at elevated temperatures. With the reduced background, a PL peak close to the original NCs' PL at a low count rate becomes visible. However this emission is broader and higher in intensity than expected for a NC at the temperature of 10 K, and might very likely be an artifact introduced by Fabry-Perot modulated defect emission, or the emission stemming from a small agglomerate of NCs.

The blinking behavior, assumed to be the fingerprint of isolated nanoemitters, was failed to be observed so far.

6.3.3 Outlook on Hybrid Growth Technology

In this chapter the possibility of incorporating colloidal NCs in epitaxial structures has been demonstrated. Colloidal NCs can be transferred in an MBE compatible suspension with acceptable losses in PL intensity. The deposition of NCs of various areal densities on strained ZnSe buffer layers is easily achieved. A set of overgrowth parameters was found that produces cap layers of sufficiently high quality for further processing that relies on epitaxy. The NCs can be identified by means of structural investigations, after the incorporation. The luminescence of the NCs, though modified, can be detected in the hybrid structure.

Unfortunately, the buffer layer properties that favor the deposition of isolated NCs also favor background luminescence in the spectral region of interest. The low level of emitted light that has to be detected above an intense background of defect related emission has made the observation of isolated, overgrown NC impossible up to now.

Recent findings by Chen and coworkers [17] have shed a new light on the detection of blinking as a fingerprint of buried single emitters. Here it is reported, that nanocrystals surrounded with what the authors call a "giant" shell of a higher band gap material show suppressed blinking behavior. In their particular case, the suppression of blinking was observed for a 2-3 nm CdSe core, clad with a 15-20 nm shell of ZnS. Since in the hybrid samples under investigation here, not only a shell, but a full cap layer is grown onto the NCs, the surrounding material may well prevent the Auger-type photo induced ionization processes, commonly referred to as the origin of PL intermittency [62]. The chosen excitation scheme via the surrounding might serve as a method for the production of non-blinking colloidal NC emission. In such cases isolated NC would easily be mislabeled as small agglomerates, due to the absence of blinking.

A alternative experiment, that could help to clarify this issue, is μ-PL with higher spectral resolution. Here the lines of individual NC should become spectrally separable, at least, when the experiment is performed at cryogenic temperatures.

Furthermore, to overcome the ambiguity described above, correlation measurements of the emission might prove helpful, since even non-blinking NCs should still be single photon emitters that display antibunching of their emission.

As stated earlier, the usage of strained buffer layers, that exhibit a smaller defect related PL intensity, implicates a tendency of the NCs to aggregate. However, the possibility to incorporate agglomerates consisting of only a few NCs in an epitaxial host matrix of high crystalline quality offers a number of interesting possibilities.

The choice of emitter properties is instantly magnified by the fact that NC of various sizes and shapes, and even material compositions are accessible. If desirable, even a mixture of particles could be used.

This new technology might also assist in the effort to incorporate ions into epitaxial structures. This is the case, when the doping of a NC and the subsequent incorporation in a hybrid structure are more easily achieved, than the common ion implantation, that is usually accompanied by the creation of defects due to the excess energy deposited in the host's lattice.

The connection to well developed semiconductor technologies, such as the growth of Bragg mirror based cavities around the emitters, and electrical charge injection shows that a number of goals in a wide field of applications come into reach at this stage already.

The unambiguous identification and addressing of single buried emitters however is necessary for the usage of hybrid structures as a test bed for quantum effects. It is furthermore required for the use as single photon sources in applications as quantum computation or quantum cryptography. Further improvements of the technology introduced here might be accomplished by pushing the limit of the light collection efficiency. To that end, making use of a higher NA, low temperature microscope objective, or a customized anti-reflex coating on the sample surface, to reduce incoupling losses of the exciting laser light as well as to optimize the outcoupling of luminescence light from the buried emitters could be employed. In addition, the level of background luminescence has to be reduced. Post-growth annealing has proven to be a promising tool to achieve that.

7. Energy Transfer in Organic-Inorganic Hybrid Structures

The fact that energy can be transferred effectively from one fluorophore to another, makes the concept of using the benefits of multiple fluorescent species, by the construction of a multi-component energy transfer structure, appealing. In particular, a semiconductor nanocrystal displays high chemical stability, and size-dependent, absorption and emission properties; the latter enabling a tuning of the absorption to a convenient high energy region in the ultra-violet part of the spectrum.
Fluorescent proteins are available in a number of varieties. Since their luminescence properties can be functionalized to depend on, for example, the glucose content of the surrounding, they are widely used in the design of biosensors [77].
Organic dye molecules are well studied and easily incorporated in larger structures. Therefore they are well suited as standards or energy transfer reporters in the analysis of biomolecular conformation and interaction.

Building up a multi-component FRET system by making use of the structural properties of DNA as a nano scaffold, to control the inter-chromophore distances, should therefore enable the creation of a system that shows the strong UV absorption of the NC, the biological functionality of a protein, and the easy-to-detect emission of an organic dye. The sequential FRET from one chromophore via a second towards the final acceptor should result in an extended transfer range, as well as a larger Stokes shift.
By selectively bleaching one of the constituents luminescence, the system can in effect be broken down into the two-chromophore subsystems to allow a deeper insight into the pathways of energy migration.
As a complementary means of investigation, time-resolved measurements are carried out whose results are compared to a numerical simulation of the transfer dynamics.
In addition, the well established distance to transfer efficiency relation introduced by Th.

Förster [37] allows for an estimation of the spatial arrangement of the constituents.
In the next paragraphs, the candidates for such a three-chromophore multi-FRET system and their assembly are introduced.

7.1 Sample Preparation

In order to obtain a regulated distance between the participants in the intended multi-chromophore structure, a single stranded DNA (ssDNA), that is, a 24mer oligonucleotide, was attached to a fluorescent protein. The surface of a NC was saturated with these conjugates. Finally, the complementary single stranded DNA (CssDNA), labeled with an organic dye molecule, was reacted with this construct to obtain the structures under investigation here. The sample preparation, as well as measurements with a UV-Visible spectrophotometer (CARY-Eclipse, Varian), were performed by Huachang Lu in the group "Biologisch-Chemische Mikrostrukturtechnik" of the University of Dortmund, led by Prof. Dr. Christof M. Niemeyer.

7.1.1 Constituents of the Three-chromophore FRET System

CdSe/ZnS Core-shell Nanocrystals

CdSe/ZnS core shell NCs were obtained from organometallic precursors in a high temperature synthesis according to protocols described by Peng and coworkers [91], Hines [47], and Murray [81]. After the synthesis, the ligand shell of the NCs consists of trioctylphosphine (TOP $[CH_3(CH_2)_7]_3P$) and trioctylphosphine oxide (TOPO, $[CH_3(CH_2)_7]_3PO$), which, due to their hydrophobic nature are not bio-compatible, and have to be exchanged. The ligand exchange was carried out according to procedures introduced by H. Mattoussi [77], whereby a shell of dihydrolipoic acid (DHLA , $C_8H_{16}O_2S_2$), renders the NCs water-soluble. Changing the ligand reduces the quantum yield to a value of 3.3 % according to a comparative PL intensity measurement with Rhodamine 6G in ethanol, as a standard.

The peak of the NC ensemble PL is found at 517 nm, and the absorption peak corresponding to the first excitonic transition at 502 nm as shown in figure 7.2. The overall diameter consisting of the CdSe core, together with the ZnS shell, and the surrounding ligands is therefore approximately 4 nm. Before the subsequent linkage to the other three-chromophore FRET constituents, the NCs were kept in a TETBS buffer solution (=20

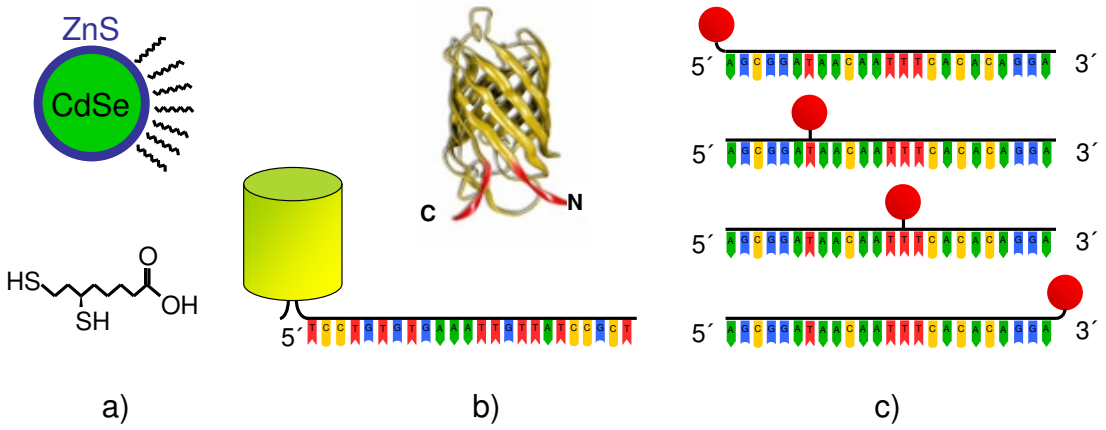

Figure 7.1: Components for the multi-FRET system. a) The CdSe/ZnS core-shell NC with part of the ligand shell sketched (DHLA molecule shown below). b) EYFP as a ribbon diagram and modeled as a cylinder with the attachment points below the cylinder and ssDNA attached. c) Atto647 attached to complementary CssDNA at four different points for inter-fluorophore distance control after hybridization.

mM Tris-buffered saline containing 150 mM NaCl, 5 mM EDTA, 0.005% Tween-20, pH 7.5).

Enhanced Yellow Fluorescent Protein - EYFP

The discovery of the green fluorescent protein (GFP) in the north pacific jelly fish aequorea victoria, in 1961 by O. Shimomura [109], has led to the development of a variety of luminescent proteins by mutation. The importance of Shimomura's discovery was recently appreciated by awarding the 2008 nobel price in chemistry to him, as well as Martin Chalfie and Roger Y. Tsien. Amongst the variations of GFP available today is the enhanced yellow fluorecent protein (EYFP), which was used here.

The protein was expressed in Escherichia coli and purified by affinity chromatography. To incorporate the EYFP molecule in a multi-FRET structure, it was linked to single stranded DNA, by the use of the heterobifunctional crosslinker sulfosuccinimidyl 4-[N-maleimidomethyl]-cyclohexane-1-carboxylate (sSMCC) [59]. To that end, amino-modified DNA oligomers were activated with the sSMCC and subsequently coupled with proteins containing exposed thiol groups. Because the two thiol containing cystein (cys) groups of the native EYFP are not accessible for covalent coupling with DNA oligomers, a CysEYFP mutant was created by site directed mutagenesis bearing an extra cysteine residue at the C-

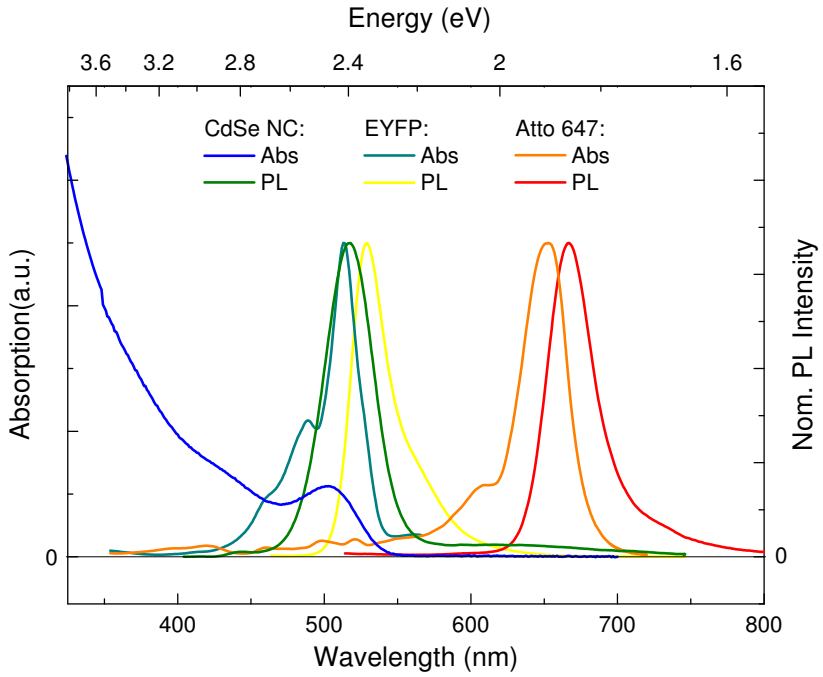

Figure 7.2: Absorption and luminescence properties of the components for a multi-FRET system.

terminal end, which is located at the protein's surface. The CysEYFP was then covalently coupled to the 5´-end of a 24mer oligonucleotide (sequence ssDNA: 5´-TCC TGT GTG AAA TTG TTA TCC GCT-3´) yielding conjugate CysEYFP-ssDNA (in the following simply referred to as EYFP-ssDNA) [60].

An additional modification of the protein was the inclusion of a hexahistidine tail at the N-terminus of the molecule. The affinity of the histidine to metals is used as one mechanism for the immobilization of the fluorescent proteins on the NC surface. In addition, the histidine binds to the deprotonated DHLA covering the NCs in suspension via electrostatic interaction.

The shape of the protein can be approximated by a cylinder with a diameter of 2.3-3.0 nm and a height of 4.0-4.2 nm. The attachment points for the linkages to both, DNA and NC are below the bottom of the cylinder.

The absorption and emission spectra of the EYFP are displayed in figure 7.2. The emission maximum is centered at 528 nm with an absorption band at 514 nm (Molar extinction coefficient $\varepsilon_{\mathrm{EYFP}} = 84000\,\mathrm{M^{-1}cm^{-1}}$) and a quantum yield of 62 %. The spectral position of the absorption peak makes EYFP an ideal acceptor of energy from the used NC emitting at 517 nm, since the large spectral overlap assures high energy transfer efficiency. The absorption maximum of the EYFP at 514 nm furthermore perfectly coincides with the

strongest line of an argon-ion laser, which is important for the possibility of photobleaching it. When the EYFP is exposed to intense light, close to the absorption maximum, for a sufficient amount of time, the luminescence and absorption features vanish, while the structure and functionality are preserved [112]. As optically inactive building blocks in control versions of the complexes studied here, photobleached EYFP was used, which was obtained by irradiating an EYFP solution with the emission of an argon-ion laser tuned to 514 nm for about eight hours at a power of 50 mW. By this method, the PL intensity was reduced below 1 % of the initial value.

Atto647

The organic dye Atto647 attached to the CssDNA, complementary to the one used to bind to the EYFP can be purchased from a number of commercial laboratories. In this case Atto647-DNA conjugates were purchased lyophilized from TIB MOLBIOL (Berlin, Germany), dissolved in H_2O at a concentration of 100 μM, and stored at -20 °C until use. In these conjugates, the Atto647-fluorophore is attached through a C6-linker to the 3´-end, through a C7-linker to the 5´-end, or through a C2-linker at two different thymine bases dT (underlined) of the 24mer oligonucleotide CssDNA (sequence: 5´-AGC GGA<u>T</u>AA CAA T<u>T</u>T CAC ACA GGA-3´), which is fully complementary to sequence ssDNA (see figure 7.1). Hybridization with the EYFP-ssDNA conjugates described above, produces one of four different conjugates: 3´-Atto-CssDNA, 5´-Atto-CssDNA, dT1-Atto-CssDNA, and dT2-Atto-CssDNA.

According to manufacturer's information, the DNA oligomers contained one Atto647 dye per DNA oligomer. The absorption band of the CssDNA-Atto647 conjugate is centered at 647 nm with a shoulder at 600 nm and a low absorption tail down to 380 nm. The molar extinction coefficient in the maximum amounts to $\varepsilon_{\mathrm{Atto647}} = 120000\,\mathrm{M^{-1}cm^{-1}}$. The quantum yield is 20 % with the luminescence peak centered at 667 nm. The corresponding spectra are shown in figure 7.2.

DNA

The four different supramolecular FRET systems with different numbers of separating base pairs were assembled by hybridization of CysEYFP-ssDNA with the Atto647-labeled oligomers. The resulting variation in donor-acceptor distances should be reflected in different FRET efficiencies. To this end, the Cys-EYFP-ssDNA conjugate and Atto-oligomers were mixed in TETBS at a final concentration of 0.5 μM. For higher hybridization efficien-

cies, the samples were heated up to 50°C for 5 min, slowly cooled to room temperature, and then stored at 4 °C until used in PLE measurements. As controls, the single fluorophore DNA conjugates were hybridized with complementary unlabeled DNA, and an EYFP-DNA conjugate (CysEYFP-CssDNA) containing the same DNA sequence as the Atto647-DNA conjugates was incubated with the Attooligomer species.

During the hybridization of the two single stranded DNA counterparts, the helical structure of a double stranded DNA is formed. The measurement of the circular dichroism, that is the measurement if the difference in absorption of right-handed polarized and left-handed polarized light confirmed that the DNA is of the right handed B-type [60]. In this conformation, the DNA has a diameter of 2 nm. Since short DNA is used here, that has a length of 8.2 nm, well below the persistence length of about 50 nm, the DNA helix is not folded, and can be modeled to fit into a cylinder of this diameter. The addition of one base pair will increase the height by 0.34 nm and turn the added base pair around the central cylinder axis by 36°, so that 10 base pairs complete one helical revolution.

Assembly of the Three-chromophore FRET System

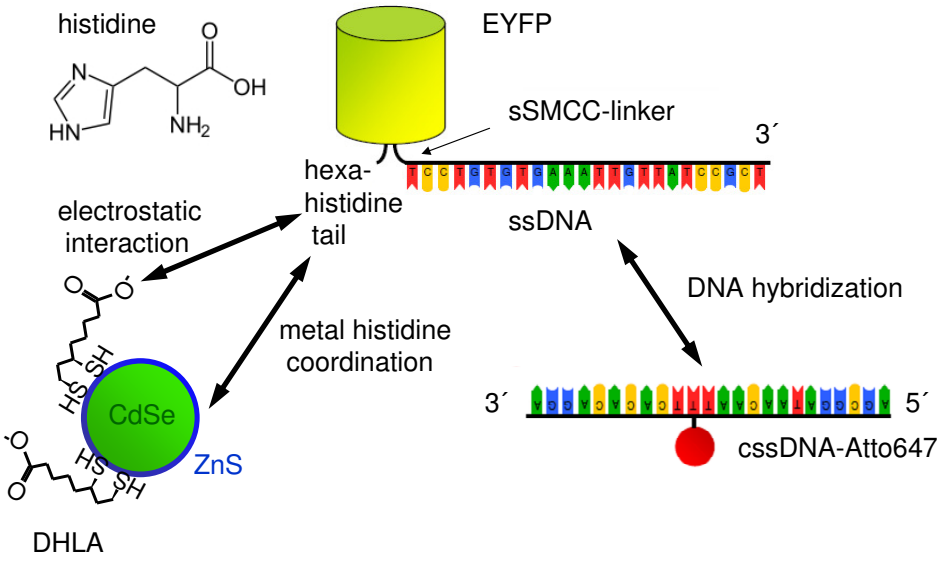

Figure 7.3: Assembly of a three chromophore system. The EYFP-DNA linkage is provided by a sSMCC molecule. The Protein is attached to the electrostatic histidine-DHLA interaction as well as the histidine-metal coordination. DNA hybridazation provides the distance controlled attachment of the Atto647 dye.

In the first part of the assembly, the ssDNA-EYFP conjugates were linked to the DHLA-NCs similar to the approach reported by Mattoussi and colleagues, in which polyhistidine-labeled proteins or short peptides were attached to DHLA-capped NCs [111]. The underlying mechanisms are the metal-histidine coordination, and electrostatic interaction. The binding is completed within a few minutes after mixing the two solutions.

In the second step of the assembly of the 3-chromophore FRET systems, the NC-ssDNA-EYFP conjugates were hybridized with dye labeled CssDNA of the complementary base pair sequence. Since the organic dye was attached to either the 3´-end, the 10-th base pair, the 17-th base pair, or the 5´-end of this DNA strand, the finally obtained four complexes comprise a NC, surrounded by 14 Proteins, which are bound to the surface. Attached to each EYFP is a short DNA segment, which carries a dye marker. The distance of the dye from both, the NC and the protein is specific for each of the four complexes. In the following, these sets of samples in order of ascending distance will be denoted **A, B, C,** and **D**.

7.2 Spectroscopic Investigations

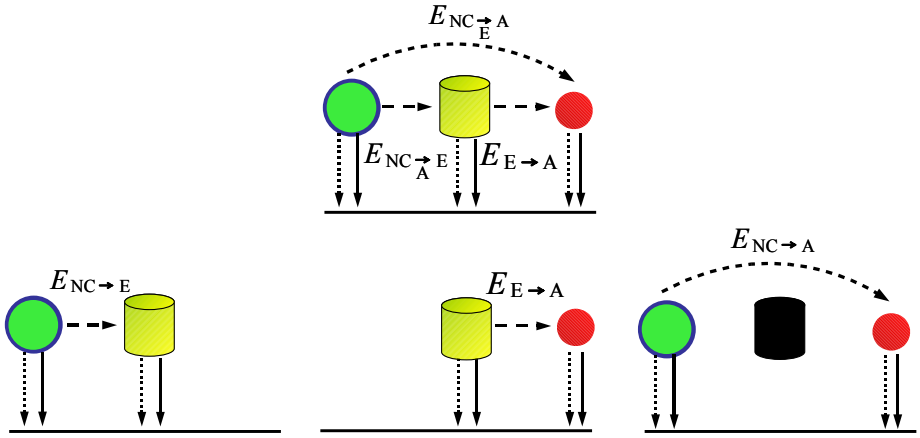

Figure 7.4: Pathways of energy migration in the three-chromophore system (top) and the subsystems displaying only a two chromophore energy transfer, namely the NC to EYFP (left), the EYFP to Atto647 (middle), and the NC to Atto647 transfer (right). FRET transitions are marked as dashed arrows, radiative recombination transitions as solid arrows, and the non-radiative recombination to the ground state as dotted arrows.

Besides the general proof for the presence of efficient energy transfer from the NC to the EYFP and the Atto647, the spectroscopic investigations carried out were aiming at a more detailed and quantitative analysis of the energy transfer processes involved. Figure

7.4 visualizes the transfer processes present in the created subsystems and the full three-chromophore system. For clarity, the variable names assigned to the different channels are summarized in table 7.1.

The individual transfer channels will be addressed discretely, that is, as a single-channel energy transfer between two chromophores, and as participants in the dual-channel FRET in the full, three-chromophore FRET system. Since the first building block of the superstructure is the NC-EYFP complex, its individual energy transfer properties will be addressed in most detail. On this example, the routines used to quantify the transfer efficiencies will be explained, before applying them to the other two-chromophore channels: The NC-Atto647, and the EYFP-Atto647 channels.

A distinction has to be made, regarding the efficiency in the presence or the absence of the respective third chromophore. The presence of the NC does not modify the protein to dye channel, because there is no transfer from the protein back to the NC, due to missing spectral overlap between the EYFP emission and the NC absorption. For the same reason the dye is only acting as an acceptor for transferred energy and not as a donor. The NC-Atto647 and the NC-EYFP channels however are influenced by the presence of the protein and the dye respectively.

Variable	Description
$E_{\mathrm{NC}\rightarrow\mathrm{E}}$	Efficiency of transfer from NC to EYFP in the 2-chromophore system
$E_{\mathrm{NC}\rightarrow\mathrm{A}}$	Efficiency of transfer from NC to Atto647 in the 2-chromophore system
$E_{\mathrm{E}\rightarrow\mathrm{A}}$	Efficiency of transfer from EYFP to Atto647 in the 2-chromophore system
$E_{\mathrm{NC}\underset{\mathrm{E}}{\rightarrow}\mathrm{A}}$	Efficiency of transfer from NC to Atto647 in the presence of EYFP (in the 3-chromophore system)
$E_{\mathrm{NC}\underset{\mathrm{A}}{\rightarrow}\mathrm{E}}$	Efficiency of transfer from NC to EYFP in the presence of Atto647 (in the 3-chromophore system)
$E_{\mathrm{NC}\rightarrow}$	Efficiency of transfer away from the NC
$E_{\rightarrow\mathrm{A}}$	Efficiency of transfer towards Atto647

Table 7.1: List of the variables used to denote the different energy transfer efficiencies.

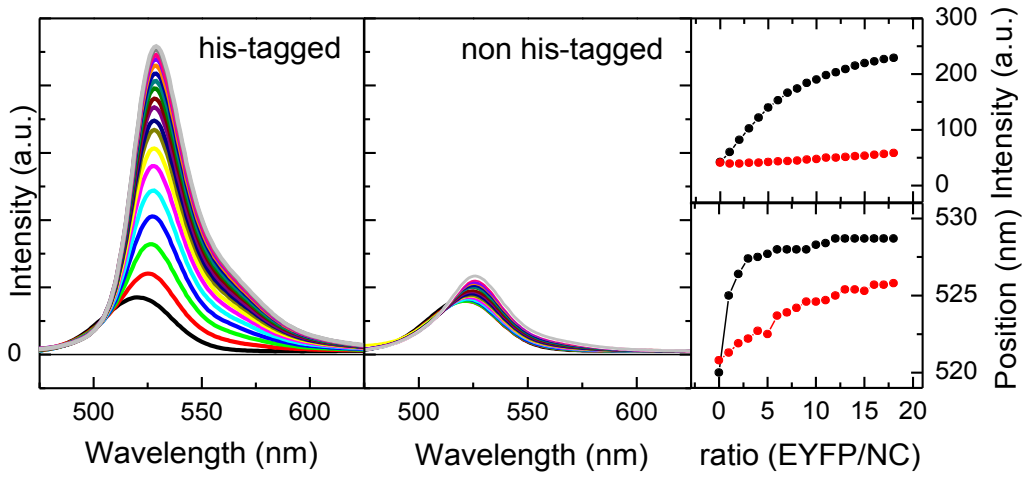

Figure 7.5: PL of NC-EYFP conjugate titrations. Left panel: the PL obtained when gradually adding up to 18 parts of his-tagged ssDNA-EYFP conjugates to 1 part of DHLA-NC. Middle panel: Equivalent titration without the his-tag. Right, top and bottom: The increase in PL intensity and the spectral peak shift when using his-tagged (black) and non his-tagged (red) EYFP as a function of EYFP/NC ratio.

For the final evaluation of the multi-chromophore system, the efficiencies $E_{\mathrm{NC}\rightarrow}$, referring to all energy transferred away from the NC, and $E_{\rightarrow\mathrm{A}}$ denoting the efficiency of transfer to the Atto647 dye, will be of importance.

7.2.1 The NC-EYFP Donor System

As a prerequisite for the aimed at assembly of a supra-molecular three-chromophore FRET system, the linkage between the NC and the fluorescent protein has to be accomplished and evaluated. To examine the efficiency of the protein-NC binding, and to determine the optimal loading factor of the NC surface, several titrations were carried out.

Firstly, the concentration dependence of a solution of ssDNA-EYFP conjugates was tested, by increasing the protein content in a buffer solution and monitoring the PL intensity. For the quantitative analysis, the resulting intensities can be subtracted from measurements on samples of respective concentration, in order to access the pure energy transfer driven changes in PL.

Secondly, a NC containing solution was titrated against a ssDNA-EYFP conjugates which were assembled using EYFP without the polyhistidine tag, engineered to provide the binding to the NC. No spectral shift or PL increase beyond the concentration driven

effects, measured before, were observed in this case (see figure 7.5), which strongly suggests that energy transfer due to unspecific bindings or reabsorption effects is negligible.

In a third titration, photobleached EYFP-ssDNA conjugates comprising the polyhistidine tag were used. In this case the NC PL showed an increase in intensity, without a simultaneous spectral shift. The increase in PL intensity can be attributed to an effect of hydrophilic shielding by the protein, which leads to a partial recovery of the quantum yield which was decreased in the ligand exchange process. This recovered quantum yield of 6.6 % was used in the following calculations.

With the interfering effects of concentration, unspecific binding or reabsorption, and NC-protein interaction quantified, a final, fourth titration was carried out to analyze the transfer in the NC-EYFP system. When increasing the amount of his-tagged ssDNA-EYFP in a NC containing solution, the PL shows a spectral shift towards the emission maximum of EYFP, as well as an increase in overall PL intensity (see figure 7.5). Both effects saturate, which can be attributed to the completion of a full shell of proteins around the NC. Additional ssDNA-EYFP ligands cannot bind to the NC surface anymore or are too far away from the donor chromophore center to participate in any energy transfer processes.

The maximum loading factor of the NC surface can also be estimated from geometric considerations. An former approach [77] suggests to calculate the volume of a layer around the NC with radius r_{NC}, with a thickness, that corresponds to the EYFP height h_{EYFP}. This ligand shell volume is then divided by the volume of one ssDNA-EYFP conjugate, which is approximated by a sphere with the EYFP height as the diameter. An additional filling factor of 0.65 is taken into account in equation 7.1, since gaps will form between the individual ligands.

$$N = 0.65 \cdot \frac{(r_{\mathrm{NC}} + h_{\mathrm{EYFP}})^3 - (r_{\mathrm{NC}})^3}{h_{\mathrm{EYFP}}^3} \tag{7.1}$$

As a modified approach given by equation 7.2, that relies on the available surface rather than the volume, the Protein ligands can be approximated as solid cylinders. The surface of the NC is compared to the area occupied by the cylinder bottom end face, taking into account a filling factor of 0.9 for surfaces that are maximally filled by circles, to obtain the maximum loading of the NC.

$$N = 0.9 \cdot \frac{4\pi r_{\mathrm{NC}}^2}{\pi r_{\mathrm{EYFP}}^2} \tag{7.2}$$

The values $r_{\mathrm{NC}} = 2$ nm, $h_{\mathrm{EYFP}} = 4.2$ nm, and $r_{\mathrm{EYFP}} = 1.15$ nm result in loading factors of 16, and 11 respectively, which can be seen as a upper and lower bound.

Based on these results, The EYFP/NC-ratio for the assembly of the multi-chromophore system was chosen to be 14:1, to assure a highly efficient energy transfer, while limiting the probability of leaving unconnected EYFP ligands in the solution. A narrow distribution of the loading factor around the chosen ratio of 14:1 can however not be excluded.

The titration experiments identify the NC/ssDNA-EYFP conjugates as a energy transfer system, in which the NC, which can be excited efficiently in the UV spectral range, transfers the excitations to one of the multiple ssDNA-EYFP complexes immobilized on its surface. A quantitative evaluation of the NC-EYFP subsystem will follow in section 7.2.4

7.2.2 FRET parameters

Prior to further studies, the Förster radii of the present transfer partners were determined, relying on the formalism derived in chapter 2.2.3. For the three donor-acceptor pairs, the emission of the respective donor was measured and normalized to an area under curve of unity, yielding the function $I_{\mathrm{Don,Norm}}(\lambda)$. The transmission of the respective acceptor of known concentration and molar extinction was then measured to gain the absorbance $\varepsilon_{\mathrm{Acc}}(\lambda)$. The obtained parameters were then used in the calculation of the spectral overlap integral J as:

$$J = \int I_{\mathrm{Don,Norm}}(\lambda)\varepsilon_{\mathrm{Acc}}(\lambda)\tilde{\lambda}^4 d\tilde{\lambda}$$

The results are inserted into the calculation of the Förster radius:

$$R_0 = \sqrt[6]{\frac{9000(ln10)\kappa^2\eta_{\mathrm{Don}}}{128\pi^5 n^4 N_{AV}} \cdot J}$$

Additional parameters used are: The respective donor quantum yield η_{Don}, the orientation factor $\kappa^2 = \frac{2}{3}$, the refractive index of the surrounding medium $n = 1.33$, and Avogadro's number N_{AV}. Table 7.2 lists the derived Förster radii.

FRET pair	Overlap integral J	Förster radius R_0
NC-EYFP	29.4	3.86
EYFP-Atto647	8.00	4.83
NC-Atto647	8.80	3.16

Table 7.2: Overlap integrals and Förster radii of the FRET pairs. The overlap integrals are given in units of $10^{-14}\mathrm{cm}^3\mathrm{M}^{-1}$ and the Förster radii in nm.

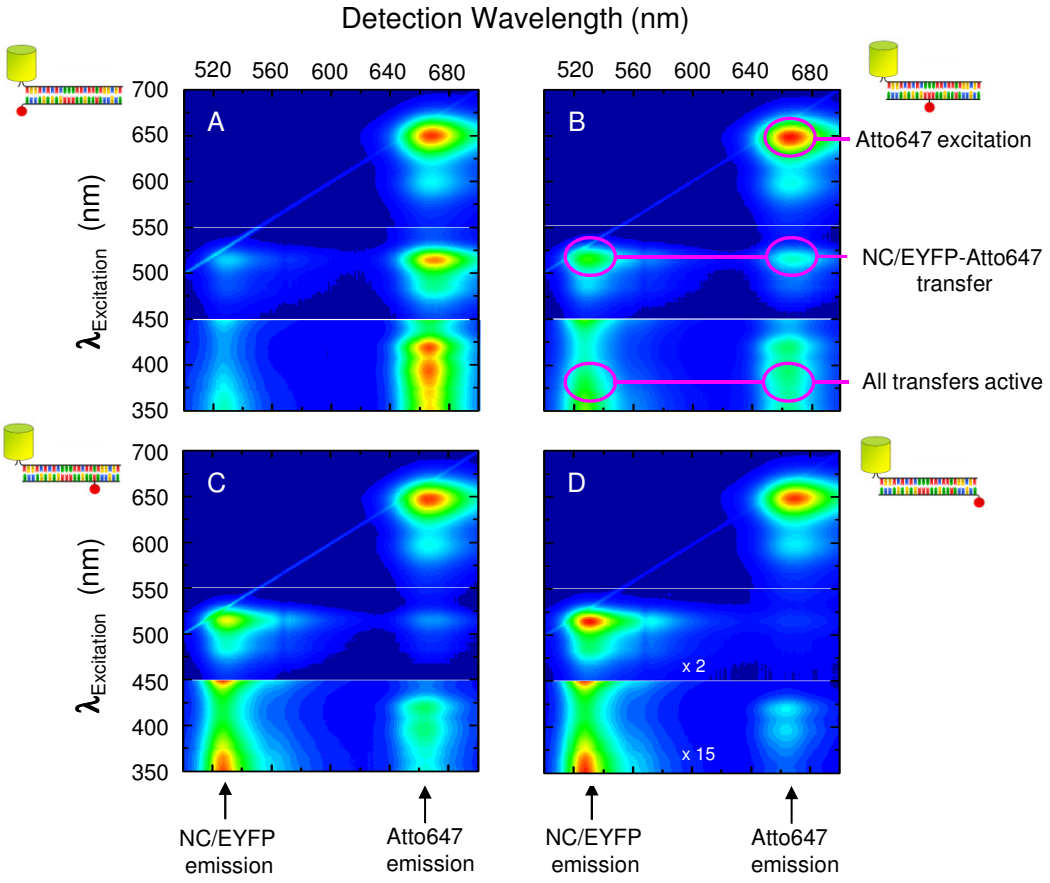

Figure 7.6: Full excitation-emission characteristics of 3Ch-FRET systems A-D. As sketched for the example of sample B, excitation wavelengths longer than 550 nm show the directly excited Atto647 emission. The 450 to 550 nm part (enhanced twofold) shows the transfer from the QD/EYFP subsystem to Atto647. The bottom part (enhanced 15x) shows direct Atto647 excitation, QD-Atto647 transfer and the sequential QD-EYFP-Atto647 transfer. The increasing distance between the QD-EYFP donor and the Atto647 acceptor (from **A**to **D**) leads to a decrease in Atto 647 emission and an increase in QD-EYFP emission, when exciting at 372 nm.

7.2.3 2d-PLE

While of less importance, when dealing with a single transfer channel between two chromophores, in order to study the 3-chromophore FRET systems, wavelength regions suited for quantitative analysis have to be determined. This is achieved by the analysis of 2d-PLE plots that display the PL intensity as a function of excitation and detection wavelength.

Figure 7.6 shows these emission landscapes for the four 3-chromophore FRET systems. The diagonal line present in all panels originates from scattered excitation light entering the detection spectrometer and can be used as a wavelength standard.

All of the four spectra show a high intensity feature at an excitation/detection wavelength coordinate of 652 nm/667 nm. This emission feature corresponds to the Atto647 dye emission, when exciting in its absorption maximum. The lower intensity feature around 600 nm/ 667 nm corresponds to a relative absorption maximum of the Atto647 at 600 nm.

The intensity visible at 528 nm, when tuning the excitation from 350 nm to 515 nm is due to the excitation of the NC/EYFP system and therefore develops as a combination of NC and EYFP absorption. Since this subsystem acts as a donor of energy, the intensity is quenched as a function of distance to the acceptor. This is evidenced by the gradual appearance of the donor emission, when the distanced is increased and therefore less energy is drawn from the NC/EYFP system (**A** to **D** in figure 7.6).

The complementary behavior can be observed in the emission of the acceptor in this energy transfer: The emission at the Atto647 recombination wavelength, when exciting the QD/EYFP subsystem. This effect is observable as a peak around 670 nm/520 nm whose intensity weakens from **A** to **D** due to decreasing energy transfer. A similar behavior can be observed for the same detection wavelength but for shorter excitation wavelength. In this region it is mainly the NC absorption that contributes to the energy stored in the NC/EYFP subsystem from which it is then transferred to the Atto647.

In addition, the Atto647 displays a secondary absorption band in the wavelength region between 380 and 420. The more detailed analysis will show that in this region, the observed emission stems from direct Atto647 excitation, energy transfer from the NC directly to the dye, and the sequential NC-protein-dye transfer.

These initial observations already demonstrate, that an energy transfer from the NC to the dye, both directly and mediated by the presence of the protein, is present in the sample at hand, and that it depends crucially on the donor-acceptor distance, as anticipated.

Moreover, a wavelength range suited for the quantitative analysis of the energy transfer processes involved can be identified from the presented graphs: The spectral region from 450-520 exhibits NC absorption, but the onset of the absorption of the EYFP prohibits the observation of the NC to Atto647 energy transfer. At higher excitation energies, the secondary absorption band of the Atto647 contributes significantly to the observed PLE intensities. The analysis of the FRET pathways from NC to Atto647 therefore has to focus on the excitation in the wavelength range below 380 nm, where both, EYFP and Atto647

absorptions are weak, while the NC to Atto647 transfer signature is strong enough for analysis. A further reduction of the excitation wavelength however has to be avoided, since the UV absorption features of protein and DNA gain significance there.

The following analysis of PL intensities of NC containing samples therefore refers to spectra obtained from excitation with 372 nm wavelength, unless otherwise stated. For the study of the EYFP-Atto647 subsystem, without NC, the EYFP absorption maximum at 514 nm was chosen.

7.2.4 Energy Transfer Efficiencies

The richness in features displayed in the 2d-PLE maps already shows, that a detailed analysis will require a number of comparative studies to break up the complex energy migration patterns, and reduce the multi-chromophore complex into equivalent, but unambiguous to analyze subsystems. A short road map of the forthcoming procedures is therefore given here:

Based on the derivations of mathematical expression for the description of two-chromophore FRET processes, introduced in chapter 2.2.3, formulae for the extraction of FRET efficiencies in a multi component system are introduced here [122]:

With the PL intensity of a fluorescent species acting as a donor, in the absence I_{Don}, and the presence $I_{\mathrm{Don,Acc}}$ of an acceptor given, the transfer efficiency E is defined as:

$$E = 1 - \frac{I_{\mathrm{Don,Acc}}}{I_{\mathrm{Don}}} \tag{7.3}$$

Complementary to that, the gain of the acceptors emission intensity in the presence of a donor $\frac{I_{\mathrm{Acc,Don}}}{I_{\mathrm{Acc}}}$ with the additional information of the ratio of absorbances at the donor excitation wavelength $A_{\mathrm{Don}}(\lambda_{exc})$ and $A_{\mathrm{Acc}}(\lambda_{exc})$ can be used to determine the same efficiency value E via:

$$E = \frac{A_{\mathrm{Acc}}(\lambda_{exc})}{A_{\mathrm{Don}}(\lambda_{exc})}\left[\frac{I_{\mathrm{Acc,Don}}}{I_{\mathrm{Acc}}} - 1\right] \tag{7.4}$$

Since these expressions are valid only in two-chromophore transfer processes, using them requires a breaking down of the complex three-chromophore system into its subsystems.

For a quantitative analysis of the energy transfer process, the contributions from the individual fluorophores to the conjugates' emission have to be analyzed. This can be accomplished, by fitting each conjugate's emission to a linear combination of the PL, measured from NC/bleached-EYFP, ssDNA-EYFP and CssDNA-Atto647 conjugates. Figure

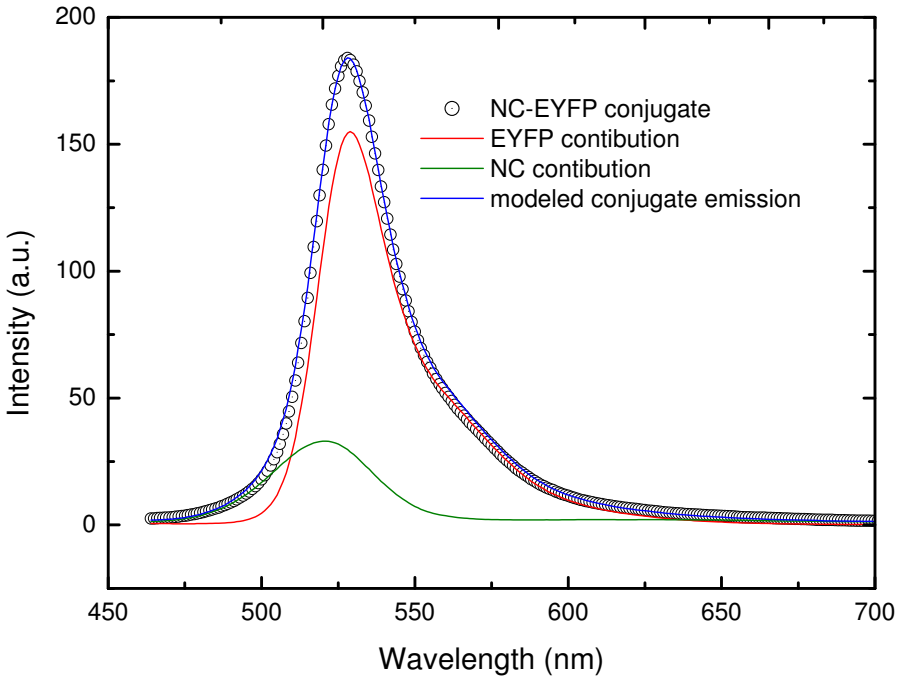

Figure 7.7: PL spectrum of an exemplary sample containing DHLA-NC and ssDNA-EYFP in a 1:9 ratio (black circles). The contributions of the NC (green) and ssDNA-EYFP (red) result in the blue fitting curve, when amplitudes of 33 and 155 are used respectively.

7.7 shows the principle of such a fit. The amplitude of the resulting single fluorophore contributions are then inserted as $I_{\mathrm{Don,Acc}}$ or I_{Don} in the efficiency calculation.

NC-EYFP Subsystem

The NC-EYFP subsystem can be assembled by leaving out the second assembly step, which means, that the NCs are surrounded by the shell of ssDNA-EYFP conjugates, but the hybridization with the dye labeled complementary CssDNA is omitted.

Fitting the obtained PL curves, enables the use of equation 7.3 with the amplitude of the NC contribution as $I_{\mathrm{Don,Acc}}$. Instead of using blank DHLA-NC, the NC surface is loaded with 14 bleached EYFP, to account for the partial quantum yield recovery of the NC, that was observed when attaching proteins to it's surface. The intensity of the DHLA-QD/bleached EYFP is therefore used as I_{Don}, to determine the transfer efficiency from the donor PL quenching.

EYFP-Atto647 Subsystem

The EYFP-Atto647 system is constructed by hybridizing the ssDNA-EYFP conjugates with Atto-labeled CssDNA, without the prior immobilization on the NC surface. Again intensities obtained from fits to the PL data are used to calculate efficiencies from donor quenching. This time, $I_{\mathrm{Don,Acc}}$ being the EYFP part of this PL measurement, and the Signal obtained from equally concentrated ssDNA-EYFP as I_{Don}.

NC-Atto647 Subsystem

Finally, the NC-Atto647 subsystem can be constructed by using photobleached EYFP as the bridging component between the NC and the dye-carrying DNA in an assembly process otherwise equal to that of the complete three-chromophore system. Here intensities obtained from PL fits were inserted in equation 7.4 to calculate efficiency values from the acceptor gain. $I_{\mathrm{Acc,Don}}$ is the Atto647 signal fraction in this sample, while I_{Acc} was obtained from CssDNA-Atto647 conjugates.

The efficiencies measured on these three single-channel (two-chromophore) FRET subsystems are listed in the first three lines of table 7.3

The first important result displayed in the topmost line, is that the efficiency of the NC to EYFP transfer of 72% is at a rather high value. The large spectral overlap of this fluorophore combination compensates the comparably low quantum yield of the DHLA capped NC (in comparison with the EYFP). Since this value was obtained by analyzing the PL of the NC, one has to keep in mind, that it reflects the transfer between one NC and the 14 fluorescent proteins attached to it, treated as a single entity. The ratio of the constituents of 1:14 can be accounted for by the following modification to Förster's law [20]:

$$E = \frac{N}{N + \left(\frac{r}{R_0}\right)^6} \tag{7.5}$$

Channel	A	B	C	D
$E_{\mathrm{NC\to E}}$	0.72 ± 0.02			
$E_{\mathrm{E\to A}} \equiv E_{\mathrm{E}\overrightarrow{\mathrm{NC}}\mathrm{A}}$	0.78 ± 0.02	0.43 ± 0.02	0.23 ± 0.02	0.072 ± 0.02
$E_{\mathrm{NC\to A}}$	0.31 ± 0.02	0.12 ± 0.02	0.028 ± 0.001	0.003 ± 0.002
$E_{\mathrm{NC}\overrightarrow{\mathrm{A}}\mathrm{E}}$	0.64 ± 0.02	0.69 ± 0.02	0.71 ± 0.02	0.72 ± 0.02
$E_{\mathrm{NC}\overrightarrow{\mathrm{E}}\mathrm{A}}$	0.11 ± 0.2	0.037 ± 0.007	0.008 ± 0.001	0.001 ± 0.001

Table 7.3: Single and dual channel FRET efficiencies in two- and three-chromophore systems.

Which is important for the translation of efficiencies E into distances r. Transforming the above equation into an expression for the distance, yields:

$$r = R_0 \sqrt[6]{N\left(\frac{1-E}{E}\right)} \tag{7.6}$$

which, taking into account the Förster radius for the NC/EYFP pair of $R_0 = 3.86$ nm, and $N = 14$ results in a distance of 5.1 nm between the NC and the EYFP chromophore center. This is in good agreement with the structural information available. The outer diameter of the NC amounts to 4 nm. According to literature ([78]), the polyhistidine residues add an additional 0.7 nm, when all six histidines are coordinated to the NC surface. Since the hexahistidine tail of the EYFP is located at the end face of the cylindrical protein, it can be expected, that the central axis is either oriented radially, which would add half of the EYFP height to the inter-chromophore distance, or is slightly tilted, thereby adding up to a value corresponding to half the cylinder diagonal to this distance. The two values define an interval between 2.3 and 2.6 nm, which sums up to a total of 5.0 to 5.3 nm for the overall inter-chromophore distance.

The single channel FRET efficiency from the EYFP to the Atto647 is of a similar magnitude in the sample which displays the closest proximity between the chromophores. Here the distance defining role of the DNA, at with the Atto647 is attached to different bases comes into play, as can be seen from the reduction of the transfer efficiency from 78 % to 7.2 % from sample **A** to sample **D**.

The single channel FRET efficiency from the NC to the Atto647 is of considerably smaller amount, due to reduced spectral overlap. Again a distance dependence is visible in the reduction of the transfer efficiency from 31 % to 0.3 % from sample **A** to sample **D**.

A more detailed interpretation of the implications, the observed efficiencies have on the possible structural conformations will be given at the end of this chapter.

The additional entries of table 7.3 refer to the expected values for three-chromophore transfer, calculated in a way described in the following.

Extending the nomenclature of the transfer efficiency, which was originally developed for transfer between two chromophores only, requires a distinction between the efficiencies derived from a true two component system and the efficiency of transfer between two components, when a third is present and taking part in the transfer as a competitor. Equations 7.9 and 7.10 take the presence of such a competitive transfer channel into account for the calculation of transfer efficiencies, and can be derived as follows.

The efficiency of transfer from the NC to the Atto dye, with the participation of the EYFP ($E_{\mathrm{NC}\xrightarrow{\mathrm{E}}\mathrm{A}}$) can be expressed by the transfer efficiency in the two-chromophore NC-Atto647 system ($E_{\mathrm{NC}\to\mathrm{A}}$) reduced by the fraction of transfer efficiency redirected to the competitive channel ($E_{\mathrm{NC}\to\mathrm{A}} \cdot E_{\mathrm{NC}\xrightarrow{\mathrm{A}}\mathrm{E}}$). Likewise, the nanocrystal to protein transfer in the three-chromophore system is the one of the two chromophore system reduced by the fraction, that is transferred to the Atto dye in the three chromophore system. This ansatz can be expressed as an equation system:

$$E_{\mathrm{NC}\xrightarrow{\mathrm{E}}\mathrm{A}} = E_{\mathrm{NC}\to\mathrm{A}} \cdot (1 - E_{\mathrm{NC}\xrightarrow{\mathrm{A}}\mathrm{E}}) \tag{7.7}$$

$$E_{\mathrm{NC}\xrightarrow{\mathrm{A}}\mathrm{E}} = E_{\mathrm{NC}\to\mathrm{E}} \cdot (1 - E_{\mathrm{NC}\xrightarrow{\mathrm{E}}\mathrm{A}}) \tag{7.8}$$

Inserting 7.8 in 7.7 yields the following expressions which connect the two-chromophore efficiencies with the three-chromophore systems' efficiencies.

$$E_{\mathrm{NC}\xrightarrow{\mathrm{E}}\mathrm{A}} = E_{\mathrm{NC}\to\mathrm{A}} \cdot \left[1 - E_{\mathrm{NC}\to\mathrm{E}}\left(1 - E_{\mathrm{NC}\xrightarrow{\mathrm{E}}\mathrm{A}}\right)\right]$$

$$= E_{\mathrm{NC}\to\mathrm{A}}\left[1 - \left(E_{\mathrm{NC}\to\mathrm{E}} - E_{\mathrm{NC}\to\mathrm{E}} \cdot E_{\mathrm{NC}\xrightarrow{\mathrm{E}}\mathrm{A}}\right)\right]$$

$$= E_{\mathrm{NC}\to\mathrm{A}} - E_{\mathrm{NC}\to\mathrm{A}} \cdot E_{\mathrm{NC}\to\mathrm{E}} + E_{\mathrm{NC}\xrightarrow{\mathrm{E}}\mathrm{A}} \cdot E_{\mathrm{NC}\to\mathrm{A}} \cdot E_{\mathrm{NC}\to\mathrm{E}} \Leftrightarrow$$

$$E_{\mathrm{NC}\xrightarrow{\mathrm{E}}\mathrm{A}} - E_{\mathrm{NC}\xrightarrow{\mathrm{E}}\mathrm{A}} \cdot E_{\mathrm{NC}\to\mathrm{A}} \cdot E_{\mathrm{NC}\to\mathrm{E}} = E_{\mathrm{NC}\to\mathrm{A}} - E_{\mathrm{NC}\to\mathrm{A}} \cdot E_{\mathrm{NC}\to\mathrm{E}} \Leftrightarrow$$

$$E_{\mathrm{NC}\xrightarrow{\mathrm{E}}\mathrm{A}} = \frac{E_{\mathrm{NC}\to\mathrm{A}} - E_{\mathrm{NC}\to\mathrm{A}} \cdot E_{\mathrm{NC}\to\mathrm{E}}}{1 - E_{\mathrm{NC}\to\mathrm{A}} \cdot E_{\mathrm{NC}\to\mathrm{E}}} \tag{7.9}$$

In a symmetric way the according relation for $E_{\mathrm{NC}\xrightarrow{\mathrm{A}}\mathrm{E}}$ can be derived:

$$E_{\mathrm{NC}\xrightarrow{\mathrm{A}}\mathrm{E}} = \frac{E_{\mathrm{NC}\to\mathrm{E}} - E_{\mathrm{NC}\to\mathrm{A}} \cdot E_{\mathrm{NC}\to\mathrm{E}}}{1 - E_{\mathrm{NC}\to\mathrm{A}} \cdot E_{\mathrm{NC}\to\mathrm{E}}} \tag{7.10}$$

The calculated values obtained for $E_{\mathrm{NC}\xrightarrow{\mathrm{E}}\mathrm{A}}$ and $E_{\mathrm{NC}\xrightarrow{\mathrm{A}}\mathrm{E}}$ are included in table 7.3. Since the protein to dye transfer is not modified by the presence of the NC, the according value is unchanged ($E_{\mathrm{E}\to\mathrm{A}} \equiv E_{\mathrm{E}\xrightarrow{\mathrm{NC}}\mathrm{A}}$).

To compare these values, expected for the three-chromophore system, to the realistically obtainable transfer efficiencies, the total energy balance has to be addressed. Therefore a donor depletion efficiency, reflecting all energy transferred away from the NC ($E_{\mathrm{NC}\to}$) and an acceptor pick up efficiency, comprising all energy received by the Atto647 ($E_{\to\mathrm{A}}$) are defined by equations 7.11 and 7.12.

$$E_{\mathrm{NC}\to} = E_{\mathrm{NC}\xrightarrow{\mathrm{A}}\mathrm{E}} + E_{\mathrm{NC}\xrightarrow{\mathrm{E}}\mathrm{A}} \tag{7.11}$$

$$E_{\to\mathrm{A}} = E_{\mathrm{NC}\xrightarrow{\mathrm{E}}\mathrm{A}} + E_{\mathrm{NC}\xrightarrow{\mathrm{A}}\mathrm{E}} \cdot E_{\mathrm{E}\to\mathrm{A}} \tag{7.12}$$

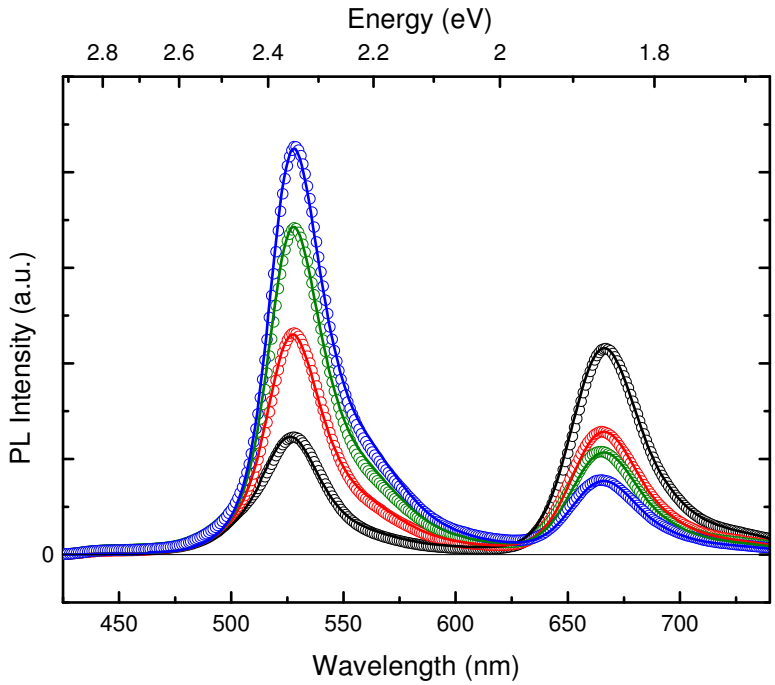

Figure 7.8: Distance dependence of PL intensities in the three-chromophore FRET system when excited with light of 372 nm. Shown are data points and fits to the data of samples with growing inter-chromophore distance (black (A) via red (B) and green (C) to blue (D)). In this order the transfer efficiency decreases, resulting in a gain in donor intensity detected at 528 nm and a simultaneous loss of acceptor PL intensity at 667.

Figure 7.8 shows the curves obtained when measuring and fitting the PL of the full three-chromophore systems **A-D** . The fits were conducted in the same way as described for the two-chromophore samples, with the addition of the respective third chromophore's aplitude as a third fit parameter. Using the according equations for donor PL loss and acceptor PL gain, the values listed in table 7.4 are calculated.

Efficiency	A	B	C	D
$E_{\mathrm{NC}\rightarrow,\mathrm{theo}}$	0.75 ± 0.02	0.73 ± 0.02	0.72 ± 0.02	0.72 ± 0.02
$E_{\mathrm{NC}\rightarrow,\mathrm{exp}}$	0.74 ± 0.01	0.72 ± 0.02	0.73 ± 0.02	0.74 ± 0.02
$E_{\rightarrow\mathrm{A},\mathrm{theo}}$	0.61 ± 0.02	0.33 ± 0.02	0.17 ± 0.02	0.053 ± 0.02
$E_{\rightarrow\mathrm{A},\mathrm{exp}}$	0.58 ± 0.04	0.30 ± 0.06	0.16 ± 0.02	0.048 ± 0.02

Table 7.4: NC quenching and Atto647 gain taking into account the direct as well as the sequential transfer channels theoretically via equations 7.11 and 7.12, and as measured on the donor quenching and acceptor gain.

A good agreement between calculated and measured values is achieved, displaying a transfer of almost three quarters of the energy, originally taken up by the NC, to the transfer partners in all of the samples. This reflects that the energy transferred away from the NC is constant and distributed among the two competing acceptors according to the respective distances. No leakage in the transfer of energy is introduced by tailoring the inter-chromophore distance, using DNA as a spacer.

For applications the amount of energy received by the acceptor, which is listed in the last two lines, is of major interest. The energy transfer efficiencies amount from ~ 60 % down to ~ 5 % in the system exhibiting sequential FRET, which is significantly higher than the values between 30 % and 0.3 % listed in table 7.3 for the two-chromophore FRET between NC and Atto647 alone.

Recalling the range of single step FRET, which typically is considered to be limited to 10 nm, is another way of appreciating the benefits of the sequential energy transfer described here, since as reviewed at the end of this chapter, the measured efficiencies can be translated into distances of up to 12.9 nm.

7.3 Temporal Evolution

7.3.1 Time-resolved PL Measurements

In addition to the time integrated PL intensities, the temporal evolution of the luminescence should reflect any energy migration in a system. To that end samples were excited with light of the same wavelength, as in steady state PL measurements (372 nm), and the emitted light analyzed both spectrally and temporally dispersed.

Initially, the participants of the sequential FRET were analyzed. Figure 7.9 (left) shows the decay of the conjugate comprising NC and bleached ssDNA-EYFP. This sample contains the PL modifications caused by the protein shell around the NC, but lacks the luminescence of the protein itself. The decay is multi-exponential and displays a fast initial part with a time constant in the hundred pico-second range. The behavior at larger delays from the exciting laser pulse is characterized by a relaxation time in the ns regime.

The middle panel of the same figure displays the modifications visible, when the photoactive EYFP species is used in the assembly of the NC/EYFP donor. It is striking, that the PL intensity rises until about 1 ns after the exciting laser pulse has arrived and decays from there on, which can be interpreted as the fingerprint of energy transfer. The EYFP is populated by the exciting laser only to a negligible amount, due to the small

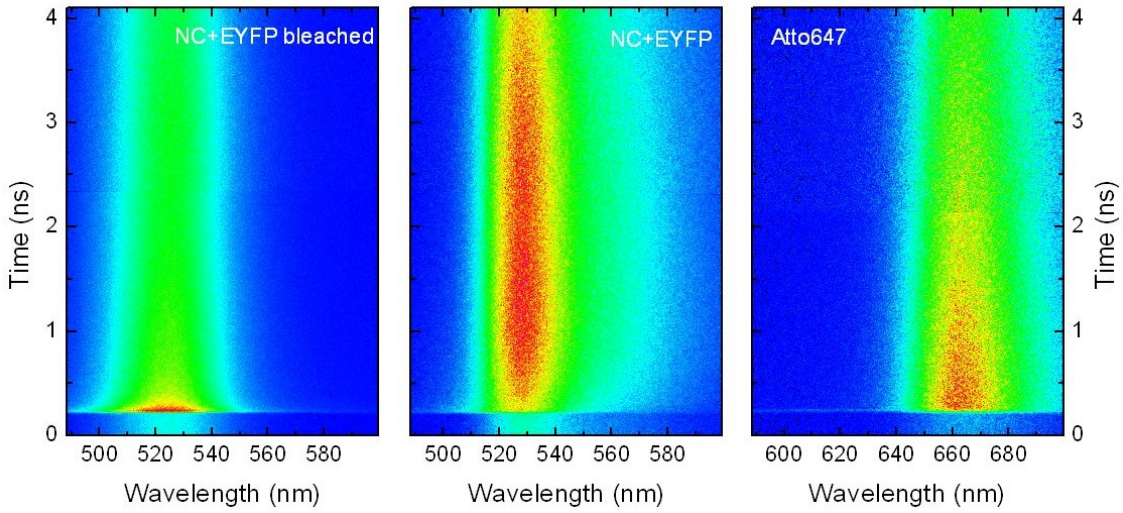

Figure 7.9: Time-resolved PL of NC-EYFP bleached, NC-EYFP and CssDNA-Atto647 conjugatess. The excitation wavelength used was 372 nm. The color scale is adjusted for each panel.

absorption coefficient at that particular wavelength. Excitations originally created in the NC are transferred to the protein efficiently. The radiative recombination of the EYFP is slow enough to allow for a build up of intensity during the time interval in which the NC is depleted, until finally the EYFP PL decays according to its intrinsic recombination probability.

The final building block of the multi-FRET system, the Atto647 dye decays in a mono-exponential way, as visible in the right panel of figure 7.9.

Following the tests on the constituents, the full three-chromophore systems **A-D** were investigated. Figure 7.10 shows the PL intensity of the samples.

Starting at sample **D**, which displays the largest separation between EYFP and Atto647, the signals obtained closely resemble the independent constituents' traces, since the energy transfer is weak. With decreasing distances, the NC/EYFP donor signal is quenched. The additional depopulation channel, which becomes available to the EYFP by the growing proximity of the Atto647, drains the excitations fast enough, to finally prohibit the rise-fall behavior observed in the pure NC/EYFP system. Simultaneously the Atto647 gains intensity as an acceptor of transferred energy. The effect is also observed in the temporal behavior, which develops the rise-fall transfer fingerprint.

In the following subsection, the PL dynamics will be modeled and the simulations compared to the data. For that purpose, the time- resolved intensities are binned over spectral regions corresponding to the intensity down to its half maximum value, that is,

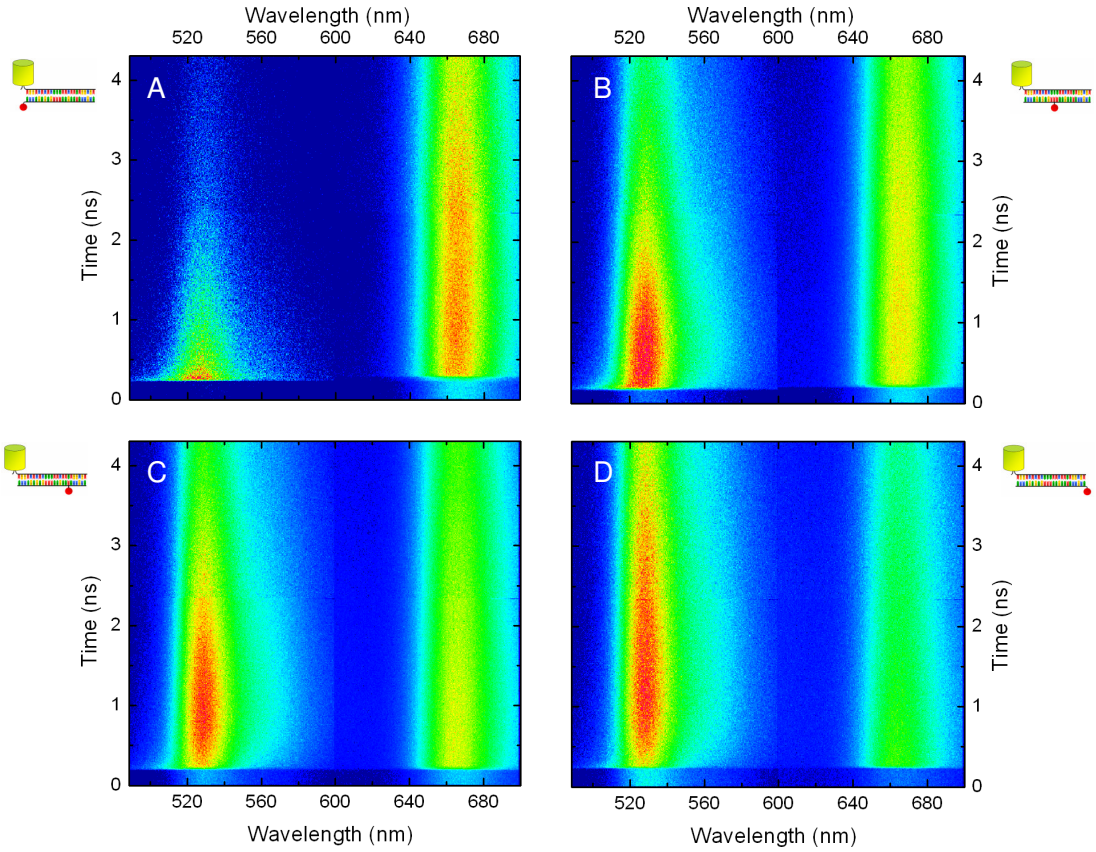

Figure 7.10: PL intensity maps of samples A to D. The combined NC/EYFP emission around 528 nm is strongly quenched in the sample of the closest proximity between the FRET partners. This intensity increases with decreasing transfer efficiency and recovers the rise-fall characteristic observable in the sample comprising only NCs and EYFP. The emission of the Atto647 dye loses relative intensity with growing distance to the donor.

the signal in the range from 625.7 nm to 678.5 nm is summed up to form the Atto part of the emission, and the signal from 521.3 nm to 547.5 nm is considered to form the sum of QD and EYFP emission. It can be derived from steady state PL, that this wavelength interval includes half of the area under the curve of the total PL intensity of the NC. The same is valid for the EYFP emission in this spectral region, so that the contributions can be summed up without any additional weighting factor for the comparison to the simulations.

7.3.2 Dynamic Modeling of Energy Transfer

As seen in the previous section, when using energy transfer efficiencies in a system comprising more than one energy transfer channel, great care has to be taken to distinguish

between the efficiency in the presence or the absence of one or the other transfer partner. This is due to the fact that efficiencies are renormalized when an additional, competitive channel is offered for the relaxation of an exited chromophore. The definition of the efficiency calculation for a state depopulated by radiative (k_{rad}), non-radiative (k_{nrad}) and two transfer channels (k_{trans1}, k_{trans2}) illustrates this relationship.

$$E_{trans1} = \frac{k_{trans1}}{k_{rad} + k_{nrad} + k_{trans1} + k_{trans2}} \tag{7.13}$$

The efficiency obtained for the first channel, even at a constant rate k_{trans1} is obviously depending on the value of k_{trans2}.

An alternative description of transfer processes makes use of the transition rates between all participating states directly.

While an efficiency weights the depopulation channels with respect to one another, the rate of a transfer between two chromophores is basically a transition probability, and therefore stays constant, even when a third transfer partner is introduced.
An additional benefit of the rate representation of energy transfer processes is the access to more complicated decays of the PL intensity.

In the simple case of a two-chromophore transfer, often the change in decay time is used to identify the strength of an energy migration. This relies on the inverse relations between decay time and the sum of all participating rates. Similar to the way the donor PL intensities in the presence and absence of an acceptor were used in 7.3 to attain efficiency values, the PL lifetimes can be used:

$$\tau_{Don} = \frac{1}{k_{rad} + k_{nrad}} \tag{7.14}$$

$$\tau_{Don,Acc} = \frac{1}{k_{rad} + k_{nrad} + k_{trans}} \tag{7.15}$$

The fluorescence lifetime, which is shortened, when a donor is depopulated by an additional transfer channel, then defines the efficiency:

$$E = 1 - \frac{\tau_{\mathrm{Don,Acc}}}{\tau_{\mathrm{Don}}} \tag{7.16}$$

However, the resulting, shortened decay time in presence of transfer, is still the argument of a single exponential function, and therefore only covers mono-exponential decay behavior of the PL intensity. As the qualitative PL overview graphs have already shown, this simple behavior is not observed.

The more complicated case of a sequential transfer describes the situation in which an energy donor undergoes a speeding up of its depletion by energy transfer to an acceptor,

but simultaneously receives energy from a third species acting as an additional donor. This is the case for the protein in the described three-chromophore system, which is deactivated by the Atto647 dye, while simultaneously being fed by the transfer from the NC.

In order to model the temporal evolution of the excitations present in the FRET system, typically a set of rate equations like 7.17 representing the changes of the NC, EYFP, and Atto647 excitation as a function of the population and depopulation rates, is solved. The resulting functions for NC(t), E (t) and A(t) are then used as fit functions in a least square fit to the data.

$$\frac{\partial NC}{\partial t} = NC(t) \cdot \left(-k_{\mathrm{NC,rad}} - k_{\mathrm{NC,nrad}} - k_{\mathrm{NC\to E}} \cdot M_E - k_{\mathrm{NC\to A}} \cdot M_A\right) \tag{7.17a}$$

$$\frac{\partial E}{\partial t} = E(t) \cdot \left(-k_{\mathrm{E,rad}} - k_{\mathrm{E,nrad}} - k_{\mathrm{E\to A}} \cdot \frac{M_A}{M_E}\right) + NC(t) \cdot k_{\mathrm{NC\to E}} \tag{7.17b}$$

$$\frac{\partial A}{\partial t} = A(t) \cdot \left(-k_{\mathrm{A,rad}} - k_{\mathrm{A,nrad}}\right) + E(t) \cdot k_{\mathrm{E\to A}} \cdot \frac{M_E}{M_A} + NC(t) \cdot k_{\mathrm{NC\to A}} \tag{7.17c}$$

Here the subscripts NC, A, and E refer to the three chromophores; The k variables denote radiative (rad) and non-radiative (nrad) rates as well as transfer rates like $k_{\mathrm{E\to A}}$. The M values refer to the molarities of the participating chromophores, normalized to the molarity of the NCs.

Since the parameter space spanned by such a set of functions is rather large, an iterative approach was chosen, that is, the population of a chromophore at a given time is calculated from the population within the preceding time interval. Accounting the loss and gain of the population within this time effectively replaces the time differential ∂t by a time interval Δt. Choosing Δt to be short compared with all other times involved in the systems dynamic, makes the numerical approach equivalent to solving the differential equation. Therefore, the variables for the populations of the individual chromophores were chosen to be represented by data arrays consisting of 30000 entries, each of which corresponding to a time interval of 1 ps.

The data entries for the $t = 0$ cell are first initialized in a way describing the initial condition, that on the arrival of the laser pulse all species are excited according to their absorbance at the excitation wavelength used.
For all further times $t > 0$, the population of the NCs is calculated from the previous time increment by taking into account the radiative and non-radiative depopulation, the transfer to the EYFP and the transfer to the Atto647 dye. A back-filling transfer channel from the EYFP to the NC was initially taken into account in the programming, but found to be negligible in the overall process.

The excited state of the EYFP is populated, apart from the initial laser pulse, by the transfer from the NC donor, while depopulation is governed by radiative and non-radiative rates as well as the transfer transition to the Atto647 dye.
The Atto647 dye itself acts as an acceptor of transferred energy from both the QD and the protein, while depopulation is possible only by non-radiative decay of excitation or photon emission.

The intensities of the PL signals are then calculated by multiplying the population with the relative concentration and the radiative decay rate. Since the signals of the NC and the EYFP overlap, the sum of both contributions is calculated and compared to the measured decay in the corresponding wavelength interval. The following short excerpt of the C-based code, used in the PL simulations, illustrates the approach.

```
Initialization:
NC[0]=pump*AN, EYFP[0]=pump*AE, Atto[0]=pump*AA.
Calculation for t>0:
NC[i]=NC[i-1]*(1-kNR-kNNR -kNE*ME-kNA*MA)+EYFP[i-1]*kEN*ME.
EYFP[i]= EYFP[i-1]*(1-kER-kENR-kEN-kEA*MA/ME)+NC[i-1]*kNE
Atto[i]= Atto[i-1]*(1-kAR-kANR)+kEA*EYFP[i-1]*ME/MA+kNA*NC[i-1].
Calculation of PL intensities:
NC_PL[i]=NC[i]*kNR*MN
EYFP_PL[i]=EYFP[i]*kER*ME
Atto_PL[i]=Atto[i]*kAR*MA
Variable definitions:
pump - intensity of the pump pulse in arbitrary units (set to 1)
AN - absorbance of the NC at the laser wavelength
AE - absorbance of the EYFP at the laser wavelength
AA - absorbance of the Atto647 at the laser wavelength
NC[i] - population of one NC unit at time index i
EYFP[i] - population of one EYFP unit at time index i
Atto[i] - population of one Atto647 dye unit at time index i
kNR - rate of radiative recombination of the NC
kNNR - rate of non-radiative recombination of the NC
kNE - rate of NC to EYFP transfer
kNA - rate of NC to Atto647 transfer
kER - rate of radiative recombination of the EYFP
kENR - rate of non-radiative recombination of the EYFP
kEN - rate of EYFP to NC (back)-transfer (=0)
kEA - rate of EYFP to Atto647 transfer
kAR - rate of radiative recombination of the Atto647
kANR - rate of non-radiative recombination of the Atto647
```

```
MN - molarity of the NC, (set to 1)
ME - molarity of the EYFP, relative to the NC concentration (=14)
MA - molarity of the Atto647 relative to the NC concentration(=14)
```

The necessary non-radiative recombination rates can be derived from the measured quantum yield in the absence of transfer, via its definition as:

$$\eta = \frac{k_{rad}}{k_{rad} + k_{nrad}} \qquad \Leftrightarrow \qquad k_{nrad} = k_{rad}\left(\frac{1}{\eta} - 1\right) \tag{7.18}$$

Likewise, the radiative recombination rates can be derived from measurements of the PL decay time, again in the absence of transfer:

$$\tau = \frac{1}{k_{rad} + k_{nrad}} = \frac{\eta}{k_{rad}} \tag{7.19}$$

The PL decay of the sample comprising NCs and photobleached EYFP was measured and found to display a fast initial decay in the first 100 ps, before a mono-exponential decay with a time constant of ~ 3.5 ns becomes visible. This decay time and the measured quantum yield of 6.6 % translate into a radiative decay rate of $0.019\,\mathrm{ns}^{-1}$.

Figure 7.11 displays the PL traces, prepared from the time- and wavelength-resolved PL maps of figure 7.10. The solid lines were calculated with the simulation program described above, using the rates given in table 7.5. The parameters used to obtain a consistent agreement are, for the NC: $\eta = 0.066$, $k_{rad} = 0.019\,\mathrm{ns}^{-1}$; EYFP: $\eta = 0.62$, $k_{rad} = 0.2\,\mathrm{ns}^{-1}$; and for the Atto647: η=0.2, $k_{rad} = 0.05\,\mathrm{ns}^{-1}$ and the NC to EYFP transfer rate $k_{\mathrm{NC}\to\mathrm{EYFP}} = 0.053\,\mathrm{ns}^{-1}$. The varying transfer rates in the four differently spaced multi-FRET systems are $k_{\mathrm{E}\to\mathrm{A}} = 1.15\,\mathrm{ns}^{-1}$, $0.245\,\mathrm{ns}^{-1}$, $0.10\,\mathrm{ns}^{-1}$, $0.031\,\mathrm{ns}^{-1}$; and $k_{\mathrm{NC}\to\mathrm{A}} = 0.0095\,\mathrm{ns}^{-1}$, $0.0028\,\mathrm{ns}^{-1}$, $0.0006\,\mathrm{ns}^{-1}$, $0.00008\,\mathrm{ns}^{-1}$ for samples **A-D**, respectively. Although the simulation allows for the calculation of the population of NC and EYFP individually, the obtained PL intensities are summed up, since the spectral overlap hinders a separation of the experimentally obtained traces.

The distance dependent appearance of the rise fall behavior, that is rise-fall behavior in the NC-EYFP system for large separations and for the Atto647 for small separations, can be successfully modeled with parameters consistent with the efficiency based analysis of the three-chromophore FRET system.

However it has to be mentioned here, that while the dynamics coincide well with the measured curves, the initial amplitudes have to be adjusted to values differing from those derived from the absorbances. This might hint towards a transfer processes on a faster time scale than the accessible, which modifies the initial population.

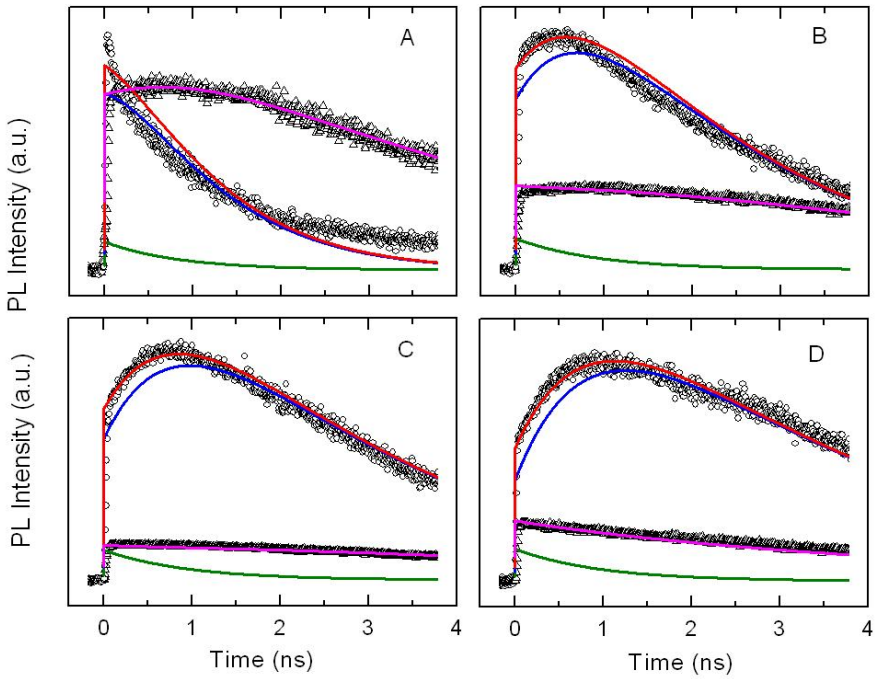

Figure 7.11: The temporal evolution of the spectrally resolved luminescence signal of the four FRET systems A to D, and their simulated behavior. The data points show the intensity recorded in the wavelength range of NC and EYFP emission (circles) and at the Atto647 emission wavelength (triangles). The simulated curves display the dynamics of NC (green), EYFP (blue), the sum of NC and EYFP (red), and Atto647 (magenta).

The small deviation of the simulated decay from the measured trace in the case of sample **A** can be explained by the presence of an initial fast decay in the NC sample,which is not taken into account in the modeling.

Rate	A	B	C	D
$k_{\mathrm{NC,rad}}$	0.019			
$k_{\mathrm{E,rad}}$	0.2			
$k_{\mathrm{NC\rightarrow E}}$	0.053			
$k_{\mathrm{A,rad}}$	0.05			
$k_{\mathrm{NC\rightarrow A}}$	0.0095	0.0028	0.0006	0.00008
$k_{\mathrm{E\rightarrow A}}$	1.15	0.245	0.10	0.031

Table 7.5: Radiative and transfer rates in ns^{-1}.

7.4 Estimating Spatial Conformation from Spectroscopic Fingerprints

The transfer efficiencies measured via the PL intensities, and confirmed by the simulated temporal behavior, enable the deduction of distances, by rewriting Förster's law as it was already used in section 7.2.4:

$$r = R_0 \sqrt[6]{N\left(\frac{1-E}{E}\right)} \tag{7.20}$$

With the knowledge of the spectral overlaps, which translate into the Förster radii listed in table 7.2, the inter-chromophore distances listed in table 7.6 can be derived. As already described, the NC-EYFP separation amounts to 5.1 nm, in good agreement with the parameters known for the individual components and the linkage in between. The EYFP-Atto647 distance, defined by the interjacent DNA, varies from 3.9 nm to 7.4 nm. The outstanding result is however, that by FRET measurements the NC-Atto647 distances of 5.6 nm up to 12.9 nm can be derived, well above the normal FRET range, which is considered to be below 10 nm.

The simultaneous presence of multiple FRET mechanisms allows for insights into the spatial arrangement of the system's components, since the geometry has to maintain all three derived distances. This can be interpreted as a result of the fact that three distances between three points in space define their respective coordinates. In a first approach, the distances corresponding to the measured efficiencies can be used in a triangulation of a possible arrangement of the three chromophores. Figure 7.12 shows the idea of a such a distance-to-position conversion in a planar representation (in a generalized problem with more than 3 chromophores, a three dimensional representation with spheres around the chromophores would have to be used).

The chromophore with access to two transfer channels (the NC) is positioned at an arbitrary point, and surrounded with two circles with radii representing the distances to the FRET partners. In the next step, the acceptor (Atto647) is placed on the circumference with the radius representing the NC-Atto647 distance. It is then surrounded with a circle

Distance	A	B	C	D
$d_{\mathrm{NC,E}}$	5.11 ± 0.06			
$d_{\mathrm{E,A}}$	3.91 ± 0.08	5.06 ± 0.07	5.91 ± 0.16	7.40 ± 0.44
$d_{\mathrm{NC,A}}$	5.61 ± 0.09	6.84 ± 0.2	8.86 ± 0.05	12.9 ± 1.1

Table 7.6: Donor-acceptor distances derived from the transfer efficiencies of the two chromophore systems.

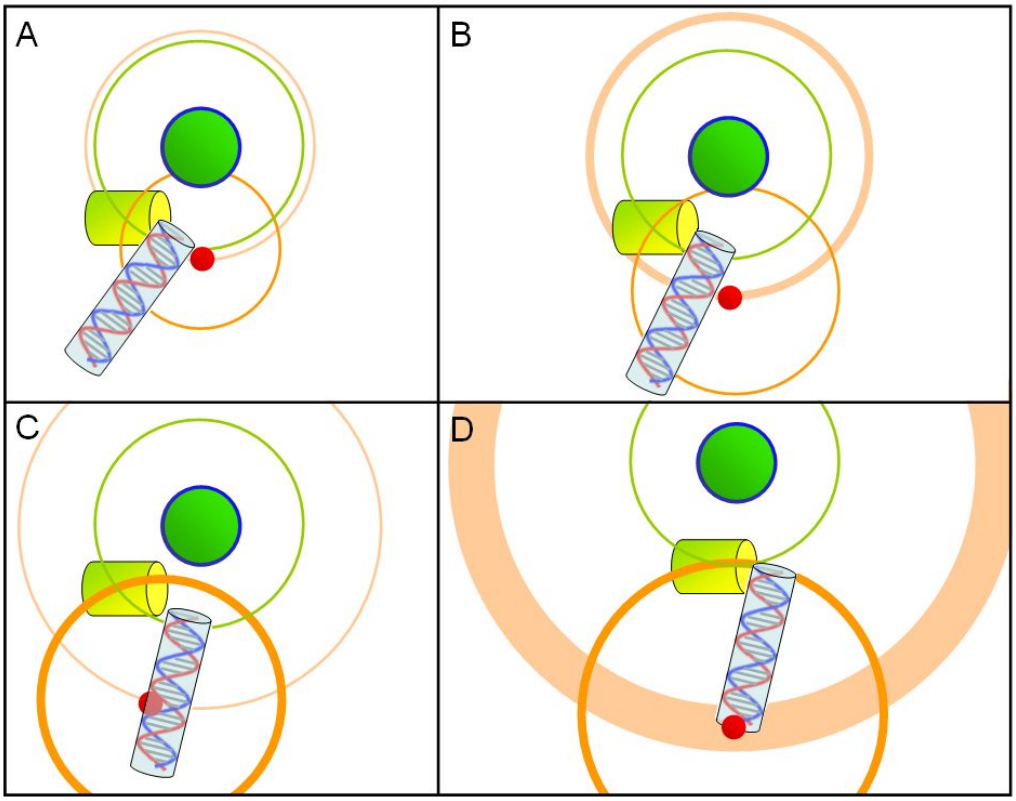

Figure 7.12: Possible spatial arrangement of the three chromophores in the multi-FRET system derived from the distances corresponding to measured FRET efficiencies. Around the NC (green) a circle with a radius corresponding to the NC-Atto647 distance is drawn (light brown). On that circle the Atto647 (red) is placed and surrounded by a circle corresponding to the EYFP-Atto647 distance (orange). The intersection of this circular line with a third, centered on the NC and representing the NC to EYFP distance (green) is the most likely position of the EYFP (yellow). The DNA which is attached to both, the EYFP and the Atto647, can be placed into the scheme by taking into account the respective attachment positions. The line thicknesses represent error bars of the distance calculations.

with the radius corresponding to the EYFP-Atto647 distance. The intersection of the NC-EYFP and the EYFP-Atto647 circles marks the position of the EYFP. The DNA, which attaches to EYFP at the 5´-end of the ssDNA and to the Atto647 at the 4 different thymin bases in the samples **A-D** should then fit in between the components.

While the uncertainties of such a triangulation are given by the error of the distance measurement, it can give an insight into the principal arrangement of the components. In this case, the only configuration in which the NC-Atto647 separation can be realized, while maintaining the EYFP-Atto647 and the NC-EYFP distances, is one in which the flexible EYFP/DNA link is bent in a way that allows the DNA and the attached Atto647 dye to point away from the QD. Taking into account additional information about the

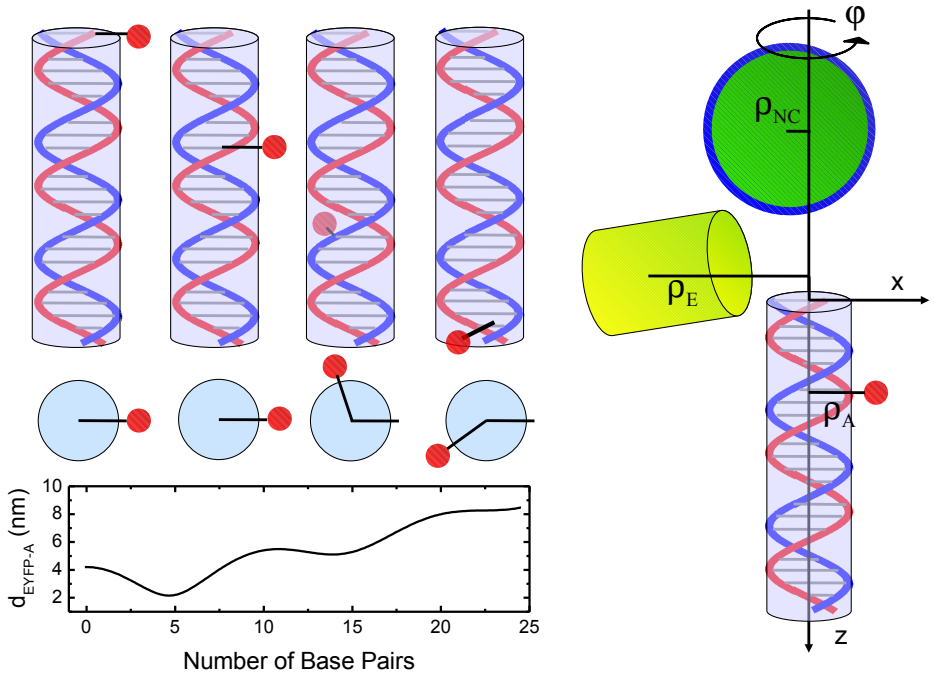

Figure 7.13: The attachment to different base pairs defines the distance in height and the angle between the protein and the atto dye (four sketches at top left). The fact that the Atto dye orbits the DNA cylinder results in a strong undulation of the inter chromophore distance as a funcion of the number of base pairs (left, bottom). Defining a cylindrical coordinate system with the center of the top lid of the DNA as the origin and the central axis of the DNA as the z-axis, allows an description of the NC and the EYFP coordinates by additional coordinates (z_E, φ_E, ρ_E and z_{NC}, φ_{NC}, ρ_{NC}). Only one of the 14 EYFP-DNA-Atto647 surrounding the NC is shown for simplicity.

chromophores allows a somewhat refined model. Picking up the picture of the NC being attached to the bottom end face of the EYFP, and taking into account that the DNA is attached to the same region of the protein, one can assume that the protein is being tilted to provide space for the flexible sSMCC linkage to the DNA.

The EYFP/QD subsystem displays an energy transfer efficiency that can be probed with high precision, thus allowing for a realistic estimation of a distance of 5.1 nm. The DNA helix of the EYFP/Atto647 subsystem provides well-defined values for the distance along, and the angle around the DNA axis. However, the aliphatic linker molecules in between EYFP and DNA or Atto647, respectively, introduce uncertainties because they are rather long and flexible. The number of possible configurations and orientations is increased even further, since the EYFP/Atto647 conjugates are likely bound flexible to the NC surface. However, one can expect that the high loading of the NC surface ($N \approx 14$) reduces the

range of possible configurations.

Because the persistence length of DNA is about 50 nm, the short ssDNA is considered to be a rigid linker, although the aliphatic spacers between DNA and both EYFP and NC should be considered flexible. Furthermore, the DNA is in its double helical B-configuration, and thus can be considered as a cylinder of 2 nm diameter, with neighboring base pairs separated by 0.34 nm and twisted by 36° with respect to each other. The relative position of the Atto647 and the EYFP can be described as a function of the number of base pairs separating them. The origin of a cylindrical coordinate system therefore is placed in the center of the circle resembling the top end face of the DNA cylinder. The position of the color center of the EYFP then is defined to be at a distance of ρ_E along the negative x-axis (i.e. φ_E is 180° in all systems) and displaced in height by z_E. The Atto647 position in the case of 0 BP between the two is fixed at a distance ρ_A in positive x direction. With growing number of base pairs between these two chromophores, the Atto647 orbits the central DNA axis with an angle $\varphi = N \cdot \frac{\pi}{5}$ and simultaneously descends along the z-axis as $z_A = N \cdot 0.34$ nm, with N indicating the number of base pairs. The position of the NC can be represented by a respective set of coordinates z_{NC}, φ_{NC}, ρ_{NC}.

The individual chromophore center positions in cylindrical coordinates are easily converted in a cartesian description, which allows for an easy distance calculation:

	x	y	z
NC	$\rho_{\mathrm{NC}} \cdot \cos(\varphi_{NC})$	$\rho_{\mathrm{NC}} \cdot \sin(\varphi_{NC})$	z_{NC}
EYFP	$-\rho_{\mathrm{E}}$	0	z_{E}
Atto647	$\rho_{\mathrm{A}} \cdot \cos(N \cdot \frac{\pi}{5})$	$\rho_{\mathrm{A}} \cdot \sin(N \cdot \frac{\pi}{5})$	$N \cdot 0.34$ nm

Table 7.7: chromophore positions in cartesian coordinates.

The absolute value of the vector, connecting two chromophores, then represents the distance between the two, as exemplified for the NC/Atto647 pair in equation 7.21.

$$d_{\mathrm{NC,A}} = \left[(x_{\mathrm{NC}} - x_{\mathrm{A}})^2 + (y_{\mathrm{NC}} - y_{\mathrm{A}})^2 + (z_{\mathrm{NC}} - z_{\mathrm{A}})^2\right]^{\frac{1}{2}} \tag{7.21}$$

The distances between the three multi-FRET constituents were calculated in order to compare them to those derived from the measured FRET efficiencies. The outcome of this "spectroscopic triangulation" is shown in figure 7.14. Recognizing the uncertainties introduced by the flexible linker molecules, the calculated distances are displayed only as a broad band, reflecting estimated errors of 1.3 nm, 0.5 nm, and 0.1 nm in the calculation of the NC/Atto647, the EYFP/Atto647, and the NC/EYFP distances, respectively. The free parameters used were: $z_{NC} = -3.5$ nm, $\varphi_{NC} = 270°$, $\rho_{NC} = 2.5$ nm; $z_E = 0$ nm, $\rho_E = 2.8$ nm; $\rho_A = 1.4$ nm, and are based on a least square fit to the data. Since one

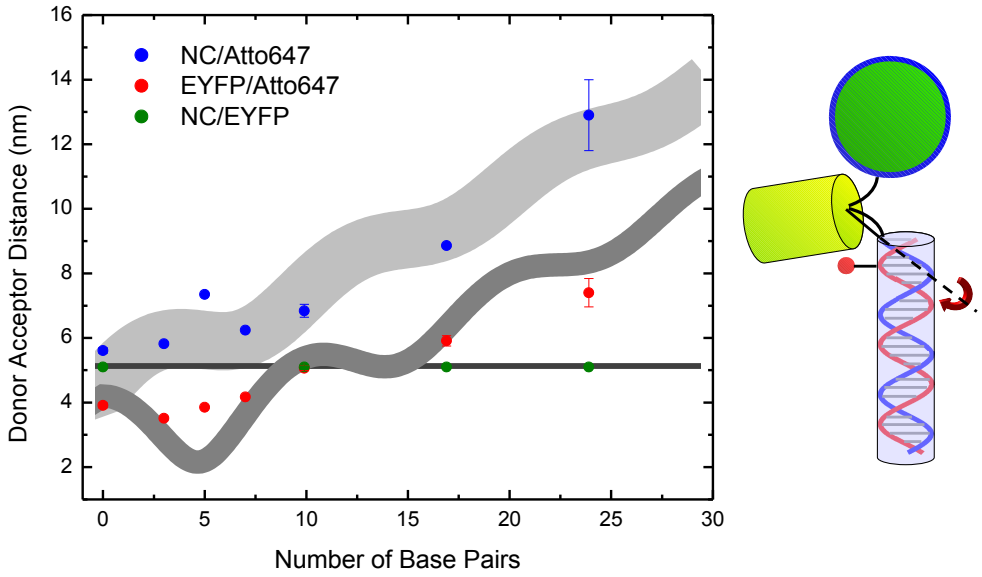

Figure 7.14: Donor-acceptor distance in the three chromophore system. The data points represent distances derived from measured transfer efficiencies. The gray areas correspond to the predictions of a model taking into account the helicity of the DNA, without the rotational degree of freedom in the EYFP-DNA link. The fit parameters are given in the text. The fact that the sSMCC molecule links the DNA to the protein with a rotational degree of freedom (right panel) might explain deviations from the expected undulation, especially in the case of an Atto647 molecule attached to the fifth base pair.

of the main predictions of the geometric model described above is a strong undulation in the case of only few base pairs separating the EYFP and the Atto647, three additional samples comprising these two chromophores only were created, with the DNA separating both by 3, 5 and 7 base pairs. The acquired data points are included in figure 7.14.

The overestimation of the undulations of the distances from the Atto647 dye is most likely due to a rotational degree of freedom, introduced by the protein-DNA linker as sketched in the right panel of figure 7.14. The possible turning around this link leads to an averaging effect that washes out the pronounced oscillating feature predicted by the simple geometric model. However, this simulation supports the hypothesis that the proteins are tilted on the NC surface, to allow the DNA to protrude from the NC, in order to place the Atto647 dye at a maximum possible distance. The full system, which includes 14 of the EYFP-DNA-Atto647 constructs around the NC, can therefore be imagined as a core-shell-shell like structure. The NC defines the core, with the next shell defined by the distance of the 14 EYFP molecules. The attachment points to the DNA define the inter-shell distance to the outermost Atto647 layer.

Summary

In the course of this work, optical investigations of nano structures were carried out to elucidate their emission dynamics. The main results are listed in the following:

CdSe and CdSe/CdS nanocrystals of varying shapes have been investigated for their optical properties. The dynamics observed in the time-resolved photoluminescence of the nanoparticles can be explained with level splittings and ground state symmetries:

- CdSe nanorods display a size-dependend crossing of levels in their energy diagramm.
- Above a critical radius of 3.7 nm, the lowest state is a dark state. With increasing temperature the above bright states are populated, evidenced by a speeding up of the luminescence decay, similar to the situation encountered in spherical CdSe nanocrystals.
- Below r_{crit}, the ground state is a bright state. The PL of this state slows down with rising temperature due to thermalization effects.
- CdSe nanorods were strongly coupled to the modes of microcavities and showed a Rabi splitting of $\hbar\Omega_{exp} = 37\mu$eV.

CeTe/CdS nanocrystals of the zinc-blende-type, exhibit a PL decay that is characterized by a stretched exponential behavior, due to several reasons:

- A broad distribution in decay times due to a nearly energy-degenerated superposition of dark states and bright states of varying oscillator strength.
- Variations in the electron-hole overlap caused by a (partly incomplete) CdTe/CdS core-shell structure
- The mono-exponential, almost temperature-independent decay of 315 ns observed is due to the decay of the optically forbidden ± 2 dark exciton state, a deep trap

decay or caused by indirect excitons formed in some of the CdTe/CdS core-shell nanocrystals.

Colloidal CdSe nanocrystals were successfully incorporated in an epitaxial matrix with the following key results:

- A set of overgrowth parameters was found that produces a high quality epitaxial capping layer.
- The NCs can be identified by means of structural investigations, after the incorporation.
- The modified luminescence of the NCs was detected from the hybrid structure.
- A combination of buffer layer growth and NC deposition was developed into a method for low NC density hybrid samples. Its effect on the defect density was determined.
- The detectable luminescence out of low density hybrid structures did not show the intermittency usually connected to the presence of isolated emitters.

CdSe nanodots were used as energy donors in an organic-inorganic FRET system, with the following results:

- The NCs are an efficient antenna for UV excitation of the system via FRET.
- Multiple simultaneous FRET processes can be elucidated by 2d-PLE, time-resolved PL studies and the modeling of the dynamics.
- A two-step multi-chromophore FRET outperforms the classic two-chromophore energy transfer in its spectral and spatial shifting abilities. Here up to 5% efficiency at 13 nm distance were confirmed.
- Analysis of simultaneously present transfer mechanisms allows an estimation of spatial confirmations. In this particular case, a core-shell-shell structure was found.

Bibliography

[1] Abliazov N.N., Areshkin A.G., Melekhin V.G., L.G. S., and Fedorov D.L. *Fluctuation Induced Broadening of Exciton Reflection Spectra in II-VI Solid Solutions.* Phys. Status Solidi B, volume 135:217, 1986

[2] Andreani L.C., Panzarini G., and Gérard J.M. *Strong-coupling regime for quantum boxes in pillar microcavities: Theory.* Phys. Rev. B, volume 60(19):13276–13279, 1999

[3] Artemyev M., Woggon U., Jaschinski H., Gurinovich L., and Gaponenko S. *Spectroscopic Study of Electronic States in an Ensemble of Close-Packed CdSe Nanocrystals.* Journal of Physical Chemistry B, volume 104(49):11617–11621, 2000

[4] Artemyev M., Woggon U., Wannemacher R., Jaschinski H., and Langbein W. *Light Trapped in a Photonic Dot: Microspheres Act as a Cavity for Quantum Dot Emission.* Nano Letters, volume 1(6):309–314, 2001

[5] Artemyev M.V., Bibik A.I., Gurinovich L.I., Gaponenko S.V., and Woggon U. *Evolution from individual to collective electron states in a dense quantum dot ensemble.* Phys. Rev. B, volume 60(3):1504–1506, 1999

[6] Ashcroft N.W. and Mermin N.D. *Festkörperphysik.* Teubner Verlag, Stuttgard, 1993

[7] Bauer E. *Phaenomenologische Theorie der Kristallabscheidung an Oberflaechen I.* Zeitschrift für Kristallographie, volume 110:372–394, 1958

[8] Bawendi M.G., Carroll P.J., Wilson W.L., and Brus L.E. *Luminescence properties of CdSe quantum crystallites: Resonance between interior and surface localized states.* The Journal of Chemical Physics, volume 96(2):946–954, 1992

[9] Borchert H., Talapin D., Gaponik N., McGinley C., Adam S., Lobo A., Moller T., and Weller H. *Relations between the Photoluminescence Efficiency*

of CdTe Nanocrystals and Their Surface Properties Revealed by Synchrotron XPS. Journal of Physical Chemistry B, volume 107(36):9662–9668, 2003

[10] Brun T.A. and Wang H. *Coupling nanocrystals to a high-Q silica microsphere: Entanglement in quantum dots via photon exchange.* Phys. Rev. A, volume 61(3):032307, 2000

[11] Brune M., Schmidt-Kaler F., Maali A., Dreyer J., Hagley E., Raimond J.M., and Haroche S. *Quantum Rabi Oscillation: A Direct Test of Field Quantization in a Cavity.* Phys. Rev. Lett., volume 76(11):1800–1803, 1996

[12] Brus L.E. *Electron-electron and electron-hole interactions in small semiconductor crystallites: The size dependence of the lowest excited electronic state.* The Journal of Chemical Physics, volume 80(9):4403–4409, 1984

[13] Buck J.R. and Kimble H.J. *Optimal sizes of dielectric microspheres for cavity QED with strong coupling.* Phys. Rev. A, volume 67(3):033806, 2003

[14] Camassel J., Auvergne D., Mathieu H., Triboulet R., and Marfaing Y. *Temperature dependance of the fundamental absorption edge in CdTe.* Solid State Communications, volume 13(1):63–68, 1973

[15] Carmichael H.J., Brecha R.J., Raizen M.G., Kimble H.J., and Rice P.R. *Subnatural linewidth averaging for coupled atomic and cavity-mode oscillators.* Phys. Rev. A, volume 40(10):5516–5519, 1989

[16] Chelikowsky J.R. and Cohen M.L. *Nonlocal pseudopotential calculations for the electronic structure of eleven diamond and zinc-blende semiconductors.* Phys. Rev. B, volume 14(2):556–582, 1976

[17] Chen Y., Vela J., Htoon H., Casson J.L., Werder D.J., Bussian D.A., Klimov V.I., and Hollingsworth J.A. *Giant Multishell CdSe Nanocrystal Quantum Dots with Suppressed Blinking.* Journal of the American Chemical Society, volume 130(15):5026–5027, 2008

[18] Cirac J.I., Zoller P., Kimble H.J., and Mabuchi H. *Quantum State Transfer and Entanglement Distribution among Distant Nodes in a Quantum Network.* Phys. Rev. Lett., volume 78(16):3221–3224, 1997

[19] Citrin D.S. *Long intrinsic radiative lifetimes of excitons in quantum wires.* Phys. Rev. Lett., volume 69(23):3393–3396, 1992

[20] Clapp A., Medintz I., Mauro J., Fisher B., Bawendi M., and Mattoussi H. *Fluorescence Resonance Energy Transfer Between Quantum Dot Donors and Dye-Labeled Protein Acceptors.* Journal of the American Chemical Society, volume 126(1):301–310, 2004

[21] Cooney R.R., Sewall S.L., Anderson K.E.H., Dias E.A., and Kambhampati P. *Breaking the Phonon Bottleneck for Holes in Semiconductor Quantum Dots.* Physical Review Letters, volume 98(17):177403, 2007

[22] Cooney R.R., Sewall S.L., Dias E.A., Sagar D.M., Anderson K.E.H., and Kambhampati P. *Unified picture of electron and hole relaxation pathways in semiconductor quantum dots.* Physical Review B (Condensed Matter and Materials Physics), volume 75(24):245311, 2007

[23] Cova S., Lacaita A., and Ripamonti G. *Trapping phenomena in avalanche photodiodes on nanosecond scale.* Electron Device Letters, IEEE, volume 12(12):685–687, 1991

[24] Crooker S.A., Barrick T., Hollingsworth J.A., and Klimov V.I. *Multiple temperature regimes of radiative decay in CdSe nanocrystal quantum dots: Intrinsic limits to the dark-exciton lifetime.* Applied Physics Letters, volume 82(17):2793–2795, 2003

[25] Danek M., Jensen K.F., Murray C.B., and Bawendi M.G. *Electrospray organometallic chemical vapor deposition—A novel technique for preparation of II–VI quantum dot composites.* Applied Physics Letters, volume 65(22):2795–2797, 1994

[26] de Oliveira C.R.M., de Paula A.M., Filho F.O.P., Neto J.A.M., Barbosa L.C., Alves O.L., Menezes E.A., Rios J.M.M., Fragnito H.L., Cruz C.H.B., and Cesar C.L. *Probing of the quantum dot size distribution in CdTe-doped glasses by photoluminescence excitation spectroscopy.* Applied Physics Letters, volume 66(4):439–441, 1995

[27] Donega03 C., Hickey S., Wuister S., Vanmaekelbergh D., and Meijerink A. *Single-step synthesis to control the photoluminescence quantum yield and size dispersion of CdSe nanocrystals.* JOURNAL OF PHYSICAL CHEMISTRY B, volume 107(2):489–496, 2003

[28] Duan L.M. and Kimble H.J. *Scalable Photonic Quantum Computation through Cavity-Assisted Interactions.* Phys. Rev. Lett., volume 92(12):127902, 2004

[29] Efros A.L., Rosen M., Kuno M., Nirmal M., Norris D.J., and Bawendi M. *Band-edge exciton in quantum dots of semiconductors with a degenerate valence band: Dark and bright exciton states.* Phys. Rev. B, volume 54(7):4843–4856, 1996

[30] Ekimov A.I., Hache F., Schanne-Klein M.C., Ricard D., Flytzanis C., Kudryavtsev I.A., Yazeva T.V., Rodina A.V., and Efros A.L. *Absorption and intensity-dependent photoluminescence measurements on CdSe quantum dots: assignment of the first electronic transitions.* J. Opt. Soc. Am. B, volume 10(1):100, 1993

[31] Empedocles S. and Bawendi M. *Quantum-Confined Stark Effect in Single CdSe Nanocrystallite Quantum Dots.* Science, volume 278:2114–2117, 1997

[32] Empedocles S.A., Norris D.J., and Bawendi M.G. *Photoluminescence Spectroscopy of Single CdSe Nanocrystallite Quantum Dots.* Phys. Rev. Lett., volume 77(18):3873–3876, 1996

[33] Esch V., Fluegel B., Khitrova G., Gibbs H.M., Xu J., Kang K., Koch S.W., Liu L.C., Risbud S.H., and Peyghambarian N. *State filling, Coulomb, and trapping effects in the optical nonlinearity of CdTe quantum dots in glass.* Phys. Rev. B, volume 42(12):7450–7453, 1990

[34] Fan X., Lonergan M.C., Zhang Y., and Wang H. *Enhanced spontaneous emission from semiconductor nanocrystals embedded in whispering gallery optical microcavities.* Phys. Rev. B, volume 64(11):115310, 2001

[35] Fisher B., Eisler H.J., Stott N., and Bawendi M. *Emission Intensity Dependence and Single-Exponential Behavior In Single Colloidal Quantum Dot Fluorescence Lifetimes.* Journal of Physical Chemistry B, volume 108(1):143–148, 2004

[36] Franzl T., Koktysh D.S., Klar T.A., Rogach A.L., Feldmann J., and Gaponik N. *Fast energy transfer in layer-by-layer assembled CdTe nanocrystal bilayers.* Applied Physics Letters, volume 84(15):2904–2906, 2004

[37] Förster T. *Zwischenmolekulare Energiewanderung und Fluoreszenz.* Annalen der Physik, volume 437(1-2):55–75, 1948

[38] Gammon D., Snow E.S., Shanabrook B.V., Katzer D.S., and Park D. *Fine Structure Splitting in the Optical Spectra of Single GaAs Quantum Dots.* Phys. Rev. Lett., volume 76(16):3005–3008, 1996

[39] Gao M., Kirstein S., Mohwald H., Rogach A., Kornowski A., Eychmuller A., and Weller H. *Strongly Photoluminescent CdTe Nanocrystals by Proper Surface Modification.* Journal of Physical Chemistry B, volume 102(43):8360–8363, 1998

[40] Gaponik N., Talapin D., Rogach A., Hoppe K., Shevchenko E., Kornowski A., Eychmuller A., and Weller H. *Thiol-Capping of CdTe Nanocrystals: An Alternative to Organometallic Synthetic Routes.* Journal of Physical Chemistry B, volume 106(29):7177–7185, 2002

[41] Gerard J.M. and Gayral B. *InAs quantum dots: artificial atoms for solid-state cavity-quantum electrodynamics.* Physica E: Low-dimensional Systems and Nanostructures, volume 9(1):131–139, 2001

[42] Gindele F., Westphaling R., Woggon U., Spanhel L., and Ptatschek V. *Optical gain and high quantum efficiency of matrix-free, closely packed CdSe quantum dots.* Applied Physics Letters, volume 71(15):2181–2183, 1997

[43] Gutowski J., Presser N., and Kudlek G. *Optical Properties of ZnSe Epilayers and Films.* Physical Status Solidi (A), volume 120(1):11–59, 1990

[44] Guyot-Sionnest P., Wehrenberg B., and Yu D. *Intraband relaxation in CdSe nanocrystals and the strong influence of the surface ligands.* The Journal of Chemical Physics, volume 123(7):074709, 2005

[45] Ham H. and Spector H.N. *Exciton linewidth due to scattering by polar optical phonons in semiconducting cylindrical quantum wire structures.* Phys. Rev. B, volume 62(20):13599–13603, 2000

[46] Herman M.A. and Sitter H. *Molecular beam epitaxy - fundamentals and current status.* Springer, Berlin, 1996

[47] Hines M.A. and Guyot-Sionnest P. *Synthesis and Characterization of Strongly Luminescing ZnS-Capped CdSe Nanocrystals.* Journal of Physical Chemistry, volume 100:468–471, 1996

[48] Hobel M. and Ricka J. *Dead-time and afterpulsing correction in multiphoton timing with nonideal detectors.* Review of Scientific Instruments, volume 65(7):2326–2336, 1994

[49] Hu J., Li L.s., Yang W., Manna L., Wang L.w., and Alivisatos A.P. *Linearly Polarized Emission from Colloidal Semiconductor Quantum Rods.* Science, volume 292(5524):2060–2063, 2001

[50] J. Perez-Conde A.K.B. *Electronic structure of CdTe nanocrystals: a tight-binding study.* Solid State Communications, volume 110(5):259, 1999

[51] Jaynes E. and Cummings F. *Comparison of quantum and semiclassical radiation theories with application to the beam maser.* Proceedings of the IEEE, volume 51(1):89–109, 1963

[52] Kapitonov A., Stupak A., Gaponenko S., Petrov E., Rogach A., and Eychmuller A. *Luminescence Properties of Thiol-Stabilized CdTe Nanocrystals.* Journal of Physical Chemistry B, volume 103(46):10109–10113, 1999

[53] Katari J.E.B., Colvin V.L., and Alivisatos A.P. *X-ray Photoelectron Spectroscopy of CdSe Nanocrystals with Applications to Studies of the Nanocrystal Surface.* Journal of Physical Chemistry, volume 98(15):4109–4117, 1994

[54] Kershaw S.V., Burt M., Harrison M., Rogach A., Weller H., and Eychmuller A. *Colloidal CdTe/HgTe quantum dots with high photoluminescence quantum efficiency at room temperature.* Applied Physics Letters, volume 75(12):1694–1696, 1999

[55] Kim S., Fisher B., Eisler H.J., and Bawendi M. *Type-II Quantum Dots: CdTe/CdSe(Core/Shell) and CdSe/ZnTe(Core/Shell) Heterostructures.* Journal of the American Chemical Society, volume 125(38):11466–11467, 2003

[56] Kittel C. *Einführung in die Festkörperphysik.* R.Oldenburg Verlag, München Wien, 9 edition, 1991

[57] Klingshirn C.F. *Semiconductor Optics.* Springer Verlag, Heidelberg, New York, 1995

[58] Kopitzki K. *Einführung in die Festkörperphysik.* Teubner Verlag, Stuttgard, 1993

[59] Kukolka F. and Niemeyer C.M. *Synthesis of fluorescent oligonucleotide–EYFP conjugate: Towards supramolecular construction of semisynthetic biomolecular antennae.* Org. Biomol. Chem., volume 2:2203–2206, 2004

[60] Kukolka F., Schoeps O., Woggon U., and Niemeyer C. *DNA-Directed Assembly of Supramolecular Fluorescent Protein Energy Transfer Systems.* Bioconjugate Chemistry, volume 18(3):621–627, 2007

[61] Kulakovich O., Strekal N., Yaroshevich A., Maskevich S., Gaponenko S., Nabiev I., Woggon U., and Artemyev M. *Enhanced Luminescence of CdSe Quantum Dots on Gold Colloids.* Nano Letters, volume 2(12):1449–1452, 2002

[62] Kuno M., Fromm D.P., Hamann H.F., Gallagher A., and Nesbitt D.J. *Nonexponential "blinking" kinetics of single CdSe quantum dots: A universal power law behavior.* The Journal of Chemical Physics, volume 112(7):3117–3120, 2000

[63] Labeau O., Tamarat P., and Lounis B. *Temperature Dependence of the Luminescence Lifetime of Single CdSe/ZnS Quantum Dots.* Phys. Rev. Lett., volume 90(25):257404, 2003

[64] Lai H.M., Leung P.T., Young K., Barber P.W., and Hill S.C. *Time-independent perturbation for leaking electromagnetic modes in open systems with application to resonances in microdroplets.* Phys. Rev. A, volume 41(9):5187–5198, 1990

[65] L.Bányai and Koch S. *Semiconductor Quantum Dots.* World Scientific, 1993

[66] Leatherdale C., Woo W.K., Mikulec F., and Bawendi M. *On the Absorption Cross Section of CdSe Nanocrystal Quantum Dots.* Journal of Physical Chemistry B, volume 106(31):7619–7622, 2002

[67] Lefebvre P., Richard T., Mathieu H., and Allegre J. *Influence of spin-orbit split-off band on optical properties of spherical semiconductor nanocrystals. The case of CdTe.* Solid State Communications, volume 98(4):303–306, 1996

[68] LeThomas N., Herz E., Schöps O., Woggon U., and Artemyev M.V. *Exciton Fine Structure in Single CdSe Nanorods.* Physical Review Letters, volume 94(1):016803, 2005

[69] LeThomas N., Woggon U., Schöps O., Artemyev M., Kazes M., and Banin U. *Cavity QED with Semiconductor Nanocrystals.* Nano Letters, volume 6(3):557–561, 2006

[70] Lindsey C.P. and Patterson G.D. *Detailed comparison of the Williams-Watts and Cole-Davidson functions.* The Journal of Chemical Physics, volume 73(7):3348–3357, 1980

[71] Loudon R. *The Quantum Theory of Light.* Clarendon Press, Oxford, 1983

[72] Luttinger J.M. and Kohn W. *Motion of Electrons and Holes in Perturbed Periodic Fields.* Phys. Rev., volume 97(4):869–883, 1955

[73] Mabuchi H. and Doherty A.C. *Cavity Quantum Electrodynamics: Coherence in Context.* Science, volume 298(5597):1372–1377, 2002

[74] Madelung O., editor. *Landolt-Börnstein, Numerical Data and Functional Relationships in Science and Technology*, volume 17 b. Springer Verlag, Berlin, Heidelberg, New York, 1982

[75] Mastai Y. and Hodes G. *Size Quantization in Electrodeposited CdTe Nanocrystalline Films.* Journal of Physical Chemistry B, volume 101(14):2685–2690, 1997

[76] Masumoto Y. and Sonobe K. *Size-dependent energy levels of CdTe quantum dots.* Phys. Rev. B, volume 56(15):9734–9737, 1997

[77] Mattoussi H., Mauro J., Goldman E., Anderson G., Sundar V., Mikulec F., and Bawendi M. *Self-Assembly of CdSe-ZnS Quantum Dot Bioconjugates Using an Engineered Recombinant Protein.* Journal of the American Chemical Society, volume 122(49):12142–12150, 2000

[78] Medintz I.L., Konnert J. H.and Clapp A.R., Stanish I., Twigg M.E., Mattoussi H., Mauro J.M., Deschamps J.R., and Karle J. *A Fluorescence Resonance Energy Transfer-Derived Structure of a Quantum Dot-Protein Bioconjugate Nanoassembly.* Proceedings of the National Academy of Sciences of the United States of America, volume 101(26):9612–9617, 2004

[79] Möller B., Woggon U., Artemyev M.V., and Wannemacher R. *Mode control by nanoengineering light emitters in spherical microcavities.* Applied Physics Letters, volume 83(13):2686–2688, 2003

[80] Mokari T. and Banin U. *Synthesis and Properties of CdSe/ZnS Core/Shell Nanorods.* Chemistry of Materials, volume 15(20):3955–3960, 2003

[81] Murray C.B., Norris D.J., and Bawendi M.G. *Synthesis and characterization of nearly monodisperse CdE (E = sulfur, selenium, tellurium) semiconductor nanocrystallites.* Journal of the American Chemical Society, volume 115(19):8706–8715, 1993

[82] Neuhauser R.G., Shimizu K.T., Woo W.K., Empedocles S.A., and Bawendi M.G. *Correlation between Fluorescence Intermittency and Spectral Diffusion in Single Semiconductor Quantum Dots.* Phys. Rev. Lett., volume 85(15):3301–3304, 2000

[83] Niles D.W. and Höchst H. *Band offsets and interfacial properties of cubic CdS grown by molecular-beam epitaxy on CdTe(110).* Phys. Rev. B, volume 41(18):12710–12719, 1990

[84] Nirmal M., Dabbousi B., Bawendi M., Macklin J., Trautman J., Harris T., and Brus L. *Fluorescence intermittency in single cadmium selenide nanocrystals.* Nature, volume 383(6603):802–804, 1996

[85] Nirmal M., Norris D.J., Kuno M., Bawendi M.G., Efros A.L., and Rosen M. *Observation of the "Dark Exciton" in CdSe Quantum Dots.* Phys. Rev. Lett., volume 75(20):3728–3731, 1995

[86] Patton B., Langbein W., and Woggon U. *Trion, biexciton, and exciton dynamics in single self-assembled CdSe quantum dots.* Phys. Rev. B, volume 68(12):125316, 2003

[87] Pellizzari T., Gardiner S.A., Cirac J.I., and Zoller P. *Decoherence, Continuous Observation, and Quantum Computing: A Cavity QED Model.* Phys. Rev. Lett., volume 75(21):3788–3791, 1995

[88] Peng X., Manna L., Yang W., Wickham J., Scher E., Kadavanich A., and Alivisatos A. *Shape Control of CdSe Nanocrystals.* Nature, volume 404:59–61, 2000

[89] Peng X., Schlamp M., Kadavanich A., and Alivisatos A. *Epitaxial Growth of Highly Luminescent CdSe/CdS Core/Shell Nanocrystals with Photostability and Electronic Accessibility.* Journal of the American Chemical Society, volume 119(30):7019–7029, 1997

[90] Peng X., Wickham J., and Alivisatos A. *Kinetics of II-VI and III-V Colloidal Semiconductor Nanocrystal Growth: "Focusing" of Size Distributions.* Journal of the American Chemical Society, volume 120(21):5343–5344, 1998

[91] Peng Z. and Peng X. *Formation of High-Quality CdTe, CdSe, and CdS Nanocrystals Using CdO as Precursor.* Journal of the American Chemical Society, volume 123(1):183–184, 2001

[92] Perez-Conde J., Bhattacharjee A.K., Chamarro M., Lavallard P., Petrikov V.D., and Lipovskii A.A. *Photoluminescence Stokes shift and exciton fine structure in CdTe nanocrystals.* Phys. Rev. B, volume 64(11):113303, 2001

[93] Peter E., Senellart P., Martrou D., Lemaitre A., Hours J., Gerard J.M., and Bloch J. *Exciton-Photon Strong-Coupling Regime for a Single Quantum Dot Embedded in a Microcavity.* Physical Review Letters, volume 95(6):067401, 2005

[94] Rabi I.I. *Space Quantization in a Gyrating Magnetic Field.* Phys. Rev., volume 51(8):652–654, 1937

[95] Rajh T., Micic O.I., and Nozik A.J. *Synthesis and characterization of surface-modified colloidal cadmium telluride quantum dots.* Journal of Physical Chemistry, volume 97(46):11999–12003, 1993

[96] Redigolo M.L., Arellano W.A., Barbosa L.C., Cruz C.H.B., Cesar C.L., and de Paula A.M. *Temperature dependence of the absorption spectra in CdTe-doped glasses.* Semiconductor Science and Technology, volume 14(1):58–63, 1999

[97] Reithmaier J.P., Sek G., Loffler A., Hofmann C., Kuhn S., Reitzenstein S., Keldysh L.V., Kulakovskii V.D., Reinecke T.L., and Forchel A. *Strong coupling in a single quantum dot-semiconductor microcavity system.* Nature, volume 432(7014):197–200, 2004

[98] Richard T., Lefebvre P., Mathieu H., and Allègre J. *Effects of finite spin-orbit splitting on optical properties of spherical semiconductor quantum dots.* Phys. Rev. B, volume 53(11):7287–7298, 1996

[99] Ripamonti G., Zappa F., and Cova S. *Effects of trap levels in single-photon optical time-domain reflectometry: evaluation and correction.* Lightwave Technology, Journal of, volume 10(10):1398–1402, 1992

[100] Rockenberger J., Troger L., Rogach A.L., Tischer M., Grundmann M., Eychmuller A., and Weller H. *The contribution of particle core and surface to strain, disorder and vibrations in thiolcapped CdTe nanocrystals.* The Journal of Chemical Physics, volume 108(18):7807–7815, 1998

[101] Rudin S. and Reinecke T.L. *Oscillator model for vacuum Rabi splitting in microcavities.* Phys. Rev. B, volume 59(15):10227–10233, 1999

[102] Sander F. Wuister Floris van Driel A.M. *Luminescence of CdTe nanocrystals.* Journal of Luminescence, volume 102-103:327–332, 2003

[103] Schlegel G., Bohnenberger J., Potapova I., and Mews A. *Fluorescence Decay Time of Single Semiconductor Nanocrystals.* Phys. Rev. Lett., volume 88(13):137401, 2002

[104] Schöps O., LeThomas N., Woggon U., and Artemyev M. *Recombination Dynamics of CdTe/CdS Core-Shell Nanocrystals.* Journal of Physical Chemistry B, volume 110(5):2074–2079, 2006

[105] Schreder B., Schmidt T., Ptatschek V., Winkler U., Materny A., Umbach E., Lerch M., Muller G., Kiefer W., and Spanhel L. *CdTe/CdS Clusters with*

"Core-Shell" Structure in Colloids and Films: The Path of Formation and Thermal Breakup. Journal of Physical Chemistry B, volume 104(8):1677–1685, 2000

[106] Sercel P.C. and Vahala K.J. *Polarization dependence of optical absorption and emission in quantum wires.* Phys. Rev. B, volume 44(11):5681–5691, 1991

[107] Shabaev A. and Efros A. *1D Exciton Spectroscopy of Semiconductor Nanorods.* Nano Letters, volume 4(10):1821–1825, 2004

[108] Shimizu K.T., Neuhauser R.G., Leatherdale C.A., Empedocles S.A., Woo W.K., and Bawendi M.G. *Blinking statistics in single semiconductor nanocrystal quantum dots.* Phys. Rev. B, volume 63(20):205316, 2001

[109] Shimomura O. *The discovery of aequorin and green fluorescent protein.* Journal of Microscopy, volume 217:3–15, 2005

[110] Stranski I.N. and Krastanow L.V. *Abhandlungen der Mathematisch-Naturwissenschaftlichen Klasse.* Akademie der Wissenschaften und der Literatur in Mainz, volume 146:797, 1939

[111] Susumu K., Uyeda H.T., Medintz I.L., and Mattoussi H. *Design of Biotin-Functionalized Luminescent Quantum Dots.* Journal of Biomedicine and Biotechnology, volume 2007:90651, 2007

[112] Swaminathan R., Hoang C., and Verkman A. *Photobleaching Recovery and Anisotropy Decay of Green Fluorescent Protein GFP-S65T in Solution and Cells: Cytoplasmic Viscosity Probed by Green Fluorescent Protein Translational and Rotational Diffusion.* Biophysical Journal, volume 72:1900–1907, 1997

[113] Talapin D., Haubold S., Rogach A., Kornowski A., Haase M., and Weller H. *A Novel Organometallic Synthesis of Highly Luminescent CdTe Nanocrystals.* Journal of Physical Chemistry B, volume 105(12):2260–2263, 2001

[114] Thompson R.J., Rempe G., and Kimble H.J. *Observation of normal-mode splitting for an atom in an optical cavity.* Phys. Rev. Lett., volume 68(8):1132–1135, 1992

[115] Thränhardt A., Ell C., Khitrova G., and Gibbs H.M. *Relation between dipole moment and radiative lifetime in interface fluctuation quantum dots.* Phys. Rev. B, volume 65(3):035327, 2002

[116] Türck V., Rodt S., Stier O., Heitz R., Engelhardt R., Pohl U.W., Bimberg D., and Steingrüber R. *Effect of random field fluctuations on excitonic*

transitions of individual CdSe quantum dots. Phys. Rev. B, volume 61(15):9944–9947, 2000

[117] uPrcell E. M. *Spontaneou Emission Probabilities at Radio Frequencies.* Physical Review, volume 69:681, 1946

[118] van der Meer B.W., Coker G., and Chen S. *Resonance Energy Transfer - Theory and Data.* VCH Publishers, Inc., New York, 1994

[119] van Sark W., Frederix P., Van den Heuvel D., Gerritsen H., Bol A., van Lingen J., de MelloDonega C., and Meijerink A. *Photooxidation and Photobleaching of Single CdSe/ZnS Quantum Dots Probed by Room-Temperature Time-Resolved Spectroscopy.* Journal of Physical Chemistry B, volume 105(35):8281–8284, 2001

[120] W. Wardzynski M.S. *Dependence of the exchange splitting in excitons on the interatomic distance.* Solid State Communications, volume 10(5):417–419, 1972

[121] Wang X., Yu W.W., Zhang J., Aldana J., Peng X., and Xiao M. *Photoluminescence upconversion in colloidal CdTe quantum dots.* Phys. Rev. B, volume 68(12):125318, 2003

[122] Watrob H., Pan C.P., and Barkley M. *Two-Step FRET as a Structural Tool.* Journal of the American Chemical Society, volume 125:7336–7343, 2003

[123] Wei S.H. and Zhang S.B. *Structure stability and carrier localization in $CdX(X = S, Se, Te)$ semiconductors.* Phys. Rev. B, volume 62(11):6944–6947, 2000

[124] Wei S.H., Zhang S.B., and Zunger A. *First-principles calculation of band offsets, optical bowings, and defects in CdS, CdSe, CdTe, and their alloys.* Journal of Applied Physics, volume 87(3):1304–1311, 2000

[125] Wilson-Rae I. and Imamoğlu A. *Quantum dot cavity-QED in the presence of strong electron-phonon interactions.* Phys. Rev. B, volume 65(23):235311, 2002

[126] Woggon U. *Optical Properties of Semiconductor Quantum Dots.* Springer Tracts in Modern Physic, 1996

[127] Woggon U., Giessen H., Gindele F., Wind O., Fluegel B., and Peyghambarian N. *Ultrafast energy relaxation in quantum dots.* Phys. Rev. B, volume 54(24):17681–17690, 1996

[128] Woggon U., Herz E., Schöps O., Artemyev M., Arens C., Rousseau N., Schikora D., Lischka K., Litvinov D., and Gerthsen D. *Hybrid Epitaxial-Colloidal Semiconductor Nanostructures.* Nano Letters, volume 5(3):483–490, 2005

[129] Woggon U., Wannemacher R., Artemyev M., Möller B., LeThomas N., Anikeyev V., and Schöps O. *Dot-in-a-dot: electronic and photonic confinement in all three dimensions.* Appl. Phys. B, volume 77(5):469, 2003

[130] Wolf K., Jilka S., Rosenauer A., Schutz G., Stanzl H., Reisinger T., and Gebhardt W. *High-resolution X-ray diffraction investigations of epitaxially grown ZnSe/GaAs layers.* Journal of Physics D: Applied Physics, volume 28(4A):A120–A124, 1995

[131] Wuister S., Koole R., deMelloDonega C., and Meijerink A. *Temperature-Dependent Energy Transfer in Cadmium Telluride Quantum Dot Solids.* Journal of Physical Chemistry B, volume 109(12):5504–5508, 2005

[132] Wuister S., van Driel F., and Meijerink A. *Luminescence and growth of CdTe quantum dots and clusters.* PHYSICAL CHEMISTRY CHEMICAL PHYSICS, volume 5(6):1253–1258, 2003

[133] Yoshie T., Scherer A., Hendrickson J., Khitrova G., Gibbs H.M., Rupper G., Ell C., Shchekin O.B., and Deppe D.G. *Vacuum Rabi splitting with a single quantum dot in a photonic crystal nanocavity.* Nature, volume 432(7014):200–203, 2004

[134] Yu W., Qu L., Guo W., and Peng X. *Experimental Determination of the Extinction Coefficient of CdTe, CdSe, and CdS Nanocrystals.* Chemistry of Materials, volume 15(14):2854–2860, 2003

[135] Zhu K.D. and Li W.S. *Effect of quantum lattice fluctuations on quantum coherent oscillations in a coherently driven quantum dot-cavity system.* Physics Letters A, volume 314(5-6):380–385, 2003

List of Figures

Abbreviations and Symbols

symbol	**meaning**
$\boldsymbol{a}$	acceleration vector
a_B	exciton Bohr radius
AOM	acousto-optic modulator
APD	avalanche photo diode
β-ZnS	beta zink selenide
BP	base pair
c	speed of light in vacuum (299792458 ms^{-1})
c	concentration
CCD	charge coupled device
CdSe	cadmium selenide
CdTe	cadmium telluride
CPML	closely packed multi layer
CW	continuous wave (excitation)
$\delta(t)$	Dirac delta function
DLP	Degree of linear polarization
DOS	Density of states
e	unit charge ($1.602176 \cdot 10^{-19}$ C)
E_g	gap energy
ε	relative dielectric constant
ε_0	static dielectric constant
eV	electron volt ($1.602176 \cdot 10^{-19}$ J)
η	quantum yield

$\boldsymbol{F}$	force vector
f	focal length of lens
fcc	face centered cubic
FRET	Förster (or Fluorescence) resonance energy transfer
fs	femtosecond
FWHM	full width at half maximum
$\boldsymbol{G}$	reciprocal lattice vactor
h	Planck's constant ($6.62606896 \cdot 10^{-34}$ Js)
hh	Heavy hole
$\hbar$	reduced Planck constant ($\equiv \frac{h}{2\pi}$ =$1.054571628 \cdot 10^{-34}$ Js)
$\widehat{H}$	Hamilton operator
HRXRD	High Resolution X-ray Diffraction
HRTEM	High Resolution Transmission Electron Microscopy
J	spectral overlap integral
$\mathbf{k_i}$	wave vector with band index i
κ	dipole-dipole orientation factor
λ	wavelength
lh	Light hole
MBE	Molucular beam epitaxy
MC	Monochromator
MEE	Migration enhanced epitaxy
MHz	megahertz
ML	monolayer
$\mu-$	(prefix) micro ($\times 10^{-6}$)
μ PL	micro-photoluminescence
μ	reduced mass
m_0	electron mass ($9.109381 \cdot 10^{-31}$ kg)
m_e	effective electron mass
m_{hh}	effective heavy-hole mass
m_{lh}	effective light-hole mass

m_{eff}	effective mass
MOCVD	metal-organic chemical vapor deposition
n	index of refraction
NA	numerical aperture
NC	Nano crystal
nm	nanometer (10^{-9} m)
ns	nanosecond
PHC	photon counting
PL	Photoluminescence
PLE	Photoluminescence excitation
PMMA	Poly(methyl methacrylate)
ps	picosecond
QD	Quantum dot
R_0	Förster radius
RHEED	Reflection High Energy Electron Diffraction
$\boldsymbol{R}_j$,$\boldsymbol{r}_i$	spatial coordinates of ion cores and electron with index j or i
Ry	Rydberg energy (13.6056923 eV)
T	temperature
τ	delay time
TCSPC	time correlated single photon counting
$\boldsymbol{v}_g$	group velocity
Z_j	effective charge of the ion core with index j
ZPL	zero phonon line
ZnS	zinc sulfide
ZnSe	zinc selenide

Acknowledgements

This work was conducted in a number of collaborations and with support from many people all of whom I would like to thank for their help and support.

First of all I would like to thank Prof. Dr. Ulrike Woggon for guidance, support and encouragement. It was a pleasure to be introduced to a variety of communities and acquire and apply knowledge and skills under her supervision.

I thank Prof. K. Lischka for the fruitful collaboration with members of his group and for agreeing to referee this thesis.

I cordially acknowledge Prof. A. Eychmüller for kindly accepting to referee this work.

I would like to thank Dr. B. Siegmann for refereeing this thesis.

For the preparation of excellent nanocrystal samples and useful discussions on their chemistry I would like to thank Dr. Mikhail Artemyev, MSc Erik Herz, and Dr. Yurij Fedutik.

I gratefully acknowledge the collaboration with Dr. Christof Arens on the hybrid colloidal epitaxial growth project, supervised by Dr. Detlef Schikora from the group of Prof. Klaus Lischka.

The important structural sample analysis by TEM was conducted by Dr. D. Litvinov at the electron microscopy lab of Prof. D. Gerthsen, who I am indebted to.

The collaboration with the group of Prof. Christof Niemeyer brought me together with Dr. Florian Kukolka and Dr. Huachang Lu, who I would like o thank here.

Of great help both scientifically and beyond were all former and current members of the group EIIb of the department of physics in Dortmund, who I would like to acknowledge: Brian Patton, Gerrit Kocherscheidt, Stephan Schneider, Björn Möller, Wolfgang Langbein, Paola Borri, Sabine Dommers, Olga Dyatlova, Vasily Temnov, Alexander Achtstein, Vitali Anikeyev, Marco Allione and Nicolas LeThomas, who I am especially indebted to for the effective mass approximation based calculations. I would also like to thank Jordi Gomez Bresco for carefully proof reading this thesis.

The workshops and administrative staff of the TU Dortmund are gratefully acknowledged, especially the great help of Michaela Wäscher, Beate Schwertfeger, Susanne Fricke, Klaus Wiegers, Gisela Pike, Dirk Schemionek and Harald Köppen.